



저작자표시-비영리-변경금지 2.0 대한민국

이용자는 아래의 조건을 따르는 경우에 한하여 자유롭게

- 이 저작물을 복제, 배포, 전송, 전시, 공연 및 방송할 수 있습니다.

다음과 같은 조건을 따라야 합니다:



저작자표시. 귀하는 원저작자를 표시하여야 합니다.



비영리. 귀하는 이 저작물을 영리 목적으로 이용할 수 없습니다.



변경금지. 귀하는 이 저작물을 개작, 변형 또는 가공할 수 없습니다.

- 귀하는, 이 저작물의 재이용이나 배포의 경우, 이 저작물에 적용된 이용허락조건을 명확하게 나타내어야 합니다.
- 저작권자로부터 별도의 허가를 받으면 이러한 조건들은 적용되지 않습니다.

저작권법에 따른 이용자의 권리는 위의 내용에 의하여 영향을 받지 않습니다.

이것은 [이용허락규약\(Legal Code\)](#)을 이해하기 쉽게 요약한 것입니다.

[Disclaimer](#)

공학박사 학위논문

**Effect of Shape Modulation of Soft
Magnetic Composite on the
Electromagnetic Wave Absorbing
Performance**

형상 제어된 연자성 복합체가 전자파 흡수체에
미치는 영향

2023년 8월

서울대학교 대학원
재료공학부
장 미 세

Effect of Shape Modulation of Soft Magnetic Composite on the Electromagnetic Wave Absorbing Performance

지도 교수 박 종 래

이 논문을 공학박사 학위논문으로 제출함
2023년 4월

서울대학교 대학원
재료공학부
장 미 세

장미세의 공학박사 학위논문을 인준함
2023년 6월

위 원 장 _____ 남기태 (인)

부위원장 _____ 박종래 (인)

위 원 _____ 선정운 (인)

위 원 _____ 양승재 (인)

위 원 _____ 권영태 (인)

Abstract

Effect of Shape Modulation of Soft Magnetic Composite on the Electromagnetic Wave Absorbing Performance

Mi Se Chang

Department of Materials Science and Engineering

The Graduate School

Seoul National University

Advances in wireless transmission and aerospace technologies have led to the widespread use of electromagnetic waves (EMW) in both the civil and military fields. Despite the natural convenience of wireless communication, this technology is limited by EMW interference, multipath propagation, and EMW pollution, which deteriorates the reliability of data transmission and threatens human health. Considering the employment of miniaturized electronic devices and various form factors, EMW-absorbing materials need to be flexible, light weight, and exhibit high thermal conductivity for heat dissipation of the absorbed EMW energy. These EMW functional materials presents demands in strong EMW absorption in a broadband frequency range. For absorption in the designed EMW frequency band, it is also necessary to select appropriate absorbing materials depending on the purpose.

This research aimed to investigate the relationship between complex

permeability and soft magnetic materials through various shape-modulation techniques applied to FeCo alloys. Shape modulation was identified as a crucial factor in enhancing complex permeability, validated using Snoek's Law. Previous attempts at shape modulation using wet-chemical methods had limitations in achieving one-dimensional structures with securely bonded particles.

The objective was to explore the correlation between shape modulation and complex permeability, with a focus on achieving a broadband electromagnetic wave absorption material (EWAM) and identifying optimal structures for maximum loading in composites. Strategies were employed to enhance initial permeability and the ferromagnetic resonance frequency (f_{FMR}) by considering Snoek's limit. Additionally, shape modulation of FeCo alloys was utilized to mitigate high viscosity in nanomaterial fillers for EW absorbing composites while retaining high complex permeability. By incorporating BN nanoparticles, the complex permittivity and absorbing performance of shape-modulated FeCo electromagnetic wave absorbing composites were regulated. Among the examined structures, FeCo nanobelts exhibited the highest initial permeability and f_{FMR} , followed by FeCo nanochains and FeCo hollow-spheres.

Part I offers a comprehensive overview of electromagnetic wave (EW) absorbing materials, highlighting a critical technique called shape modulation to improve initial permeability, as well as f_{FMR} to enhance the absorbing capabilities. Part I also addresses additional challenges encountered in the field, such as the high viscosity of nanomaterials that restricts their use as filler materials in electromagnetic wave (EW) absorbing composites. Furthermore, it discusses the limited heat dissipation capabilities of EW absorbing composites. Part II offers solutions to overcome these challenges.

Part II presents novel methods aimed at resolving the aforementioned challenges discussed in Part I. In Chapter 3, the technique of shape modulation is introduced, where FeCo alloys are transformed into a one-dimensional structure using a thermal-plasma technique, resulting in improved absorbing performance of the EWAM. Chapter 4 expands upon the shape modulation approach introduced in Chapter 3 by fabricating a two-dimensional FeCo alloy, further enhancing the material's absorbing capabilities. Additionally, Chapter 3 addresses the issue of heat dissipation by incorporating BN nanoparticles into the EW absorbing composite. Lastly, Chapter 4 employs further shape modulation to address the high viscosity of nanomaterials, achieving this by fabricating hollow-spherical FeCo alloy structures.

In summary, this study aimed to investigate the relationship between shape modulation and complex permeability, focusing on developing a broadband electromagnetic wave absorption material (EWAM) and identifying optimal structures for maximum loading in composites. Strategies were employed to enhance initial permeability and f_{FMR} while considering Snoek's limit. This study provides valuable insights into shape modulation techniques for FeCo alloys, paving the way for advancements in electromagnetic wave absorber applications.

Keyword : Soft magnetic material, FeCo alloy, Shape-modulation, Complex permeability, Snoek's Limit, Electromagnetic wave absorption

Student Number : 2018-33245

Table of Contents

Part I. Background Information on Electromagnetic Wave Absorbing Materials (EWAM)..... 1

Chapter 1. Introduction	2
1.1. Overview of EWAMs.....	2
1.1.1. What are Electromagnetic Waves?.....	2
1.1.2. Demands and Applications for Next Generation EWAM	5
1.2. Working principles of EWAMs.....	8
1.2.1. EW Absorbing Material vs. EW Shielding Material	8
1.2.2. Transmission Line Theory and Impedance Matching	11
1.2.3. Magnetic and Dielectric Loss Mechanisms	14
1.2.4. Reflection Loss Calculations	18
1.2.5. Soft Magnetic Materials for Magnetic Loss in EWAMs	20
1.2.6. Aim of this Research.....	20
1.3. References.....	22

Chapter 2. Introduction to Shape-Modulated Soft Magnetic Material as EWAM.....	33
2.1. Introduction to Soft Magnetic Material	33
2.1.1. Ferromagnetic Resonance in Soft Magnetic Material	33
2.2. Issues of Soft Magnetic Material for EM Wave Absorbers	37
2.2.1. 1 st Issue: Limited Broadband Absorption.....	37

2.2.1.1. Limited Broadband Absorption in Soft Magnetic Materials	37
2.2.1.2. Why Do We Need Broadband EW Absorbers?	41
2.2.1.3. For broadband Absorption: What can be controlled? Enhancing the Initial Permeability and Ferromagnetic Resonance Frequency.....	45
2.2.1.4. Theoretical Consideration of Magnetic Anisotropy	48
2.2.1.5. Snoek's Limit and Shape Anisotropy.....	50
2.2.1.6. Phase Diagram of FeCo and Slater-Pauling Rule...	53
2.2.1.7. Shape Anisotropy of Magnetic Material.....	58
2.2.1.8. State-of-the-Art (SOA) of 1 st Issue: Shape-Modulated FeCo Nanomaterials.....	60
2.2.1.9. Issues to be solved – 1 st Issue.....	62
2.2.2. 2 nd Issue: High Viscosity of Nanomaterials	64
2.2.2.1. Limited Loading Ratio of Filler Material.....	64
2.2.2.2. State-of-the-Art (SOA) of 2 nd Issue	68
2.2.2.3. Issues to be solved – 2 nd Issue	70
2.2.3. 3 rd Issue: Long-time Exposure to Radiation	72
2.2.3.1. Theoretical Consideration of Thermal Dissipation	72
2.2.3.2. Issues to be solved – 3 rd Issue.....	73
2.3. References	77

Part II. Shape-Modulated Hybrid FeCo Composite Material

Chapter 3. SiO₂-Coated 0D-1D FeCo Nanochains	86
3.1. Introduction	86
3.1.1. Synthesis of FeCo Nanochains: Radio-Frequency Thermal Plasma.....	86
3.1.2. Working Principles of FeCo@SiO ₂ Nanochains as EWAMs.....	91
3.2. Experimental Section	93
3.2.1. Materials.....	93
3.2.2. Preparation of FeCo nano-chained particles.....	93
3.2.3. Synthesis of FeCo@SiO ₂ using APTMS.....	93
3.2.4. Synthesis of FeCo@SiO ₂ using TEOS.....	94
3.2.5. Characterization	94
3.3. Results and Discussion	96
3.3.1. Structural Morphology Characterization of FeCo Nanochain	96
3.3.2. Elemental Composition and Aspect Ratio Investigation of Fe _x Co _{1-x} alloys.....	99
3.3.3. Crystallographic and Magnetic Properties Fe _x Co _{1-x} alloys	102
3.3.4. Electromagnetic Properties of Fe _x Co _{1-x} alloys: Complex Permeability and Permittivity Spectra	108
3.3.5. Structural Morphology Characterization of Fe _{0.6} Co _{0.4} @SiO ₂ Insulation.....	112
3.3.6. Crystallographic and Magnetic Properties Fe _{0.6} Co _{0.4} @SiO ₂	

Nanochain.....	114
3.3.7. Electromagnetic Properties of $\text{Fe}_{0.6}\text{Co}_{0.4}@\text{SiO}_2$: Complex Permeability and Permittivity Spectra	117
3.3.8. Electromagnetic Wave Absorbing Performance: Reflection Loss and Loss Tangent Calculation	121
3.3.9. Large-scale Production of FeCo/Epoxy Composite Film	128
3.4. Conclusion.....	130
3.5. References	136
 Chapter 4. Boron Nitride Incorporated 1D-2D FeCo Nanobelts	140
4.1. Introduction	140
4.1.1. Synthesis of FeCo Nanobelts: Planetary Ball-Mill.....	140
4.1.2. Shape Anisotropy of FeCo Nanobelts.....	142
4.2. Experimental Section	145
4.2.1. Materials.....	145
4.2.2. Preparation of FeCo Nanochains, FeCo Nanobelts, and FCBN	145
4.2.3. Fabrication of FCBN-TPU EMW Absorbing Membrane	146
4.2.4. Characterization	147
4.3. Results and Discussion	148
4.3.1. Structural Morphology Characterization of FeCo Nanobelt and FeCo/BN Nanobelt (FCBN)	148
4.3.2. Thermal and Magnetic Properties of FeCo Nanobelts and FCBN ..	154
4.3.3. Electromagnetic Properties of FeCo Nanochains, Nanobelts, and FCBN	157
4.4.4. Electromagnetic Wave Absorbing Performance: Reflection Loss	

Calculation and Bandwidth Comparison	163
4.4.5. Electromagnetic Wave Absorbing Performance: Input Impedance and Attenuation Constant	172
4.4.6. EMW-Absorbing Mechanisms.....	175
4.4.7. Reliability Study.....	180
4.4. Conclusion.....	183
4.5. References	187
 Chapter 5. Boron Nitride Incorporated 0D-1D@3D FeCo Nanoparticles	192
5.1. Introduction	192
5.1.1. Limitation of Loading Factor of Nano-Filler Material in EW absorbers	192
5.1.2. Synthesis of Shape-Modulated FeCo Particles: Ultrasonic Spray Pyrolysis.....	195
5.2. Experimental Section	199
5.2.1. Materials.....	199
5.2.2. Synthesis of FeCo spherical, cubic, and hollow-spherical particles via ultrasonic spray pyrolysis.....	199
5.2.3. Synthesis of FeCo/BN spherical, cubic, and hollow-spherical particles via ultrasonic spray pyrolysis	200
5.2.4. Fabrication of FeCo/BN/TPU EW Absorbing Composite.....	200
5.2.5. Characterization	201
5.3. Results and Discussion	204
5.3.1. Structural Morphology Characterization of FeCo and FeCo/BN	

Particles	204
5.3.2. Theoretical Consideration of Relationship Between Precursor Material and Shape Modulation	208
5.3.3. Crystallographic and Magnetic Properties of FeCo Particles	211
5.3.4. Thermal Properties of FeCo/BN Particles	214
5.3.5. Electromagnetic Properties of FeCo and FeCo/BN Particles: Complex Permeability and Permittivity Spectra.....	216
5.3.6. Electromagnetic Wave Absorbing Performance: Reflection Loss Calculation and EAB.....	220
5.3.7. Loading Factor Investigation of FeCo Nanochain, FeCo Spherical Particle, and FeCo Hollow-Spherical Particle	224
5.3.8. Bulk Density and Viscosity Measurements of FeCo Nanochain, FeCo Spherical Particle, and FeCo Hollow-Spherical Particle	227
5.4.9. Electromagnetic Properties of FeCo Hollow-Spherical Particles of 70 wt% Loading Factor	229
5.4. Conclusion.....	231
5.5. References	233
 Part III. Conclusion	236
 Chapter 6. Concluding Remarks.....	237
 Abstract in Korean	240

List of Tables

Table 2.1. List of Researches Using Soft Magnetic Materials as Filler Material.

Table 4.1. Effective bandwidth (< -10 dB) and reflection loss value at different thicknesses of the FeCo nanochain, FeCo nanobelts, and FCBN composite materials.

Table 4.2. Comparison of flaky-shaped materials reported in the literature.

Table 5.1. Table showing variables for each precursor material.

Table 5.2. Effective bandwidth (< -10 dB) and reflection loss value (< -20 dB) at different thicknesses of the EMW absorbing membranes manufactured by FeCo/BN-Nitrate, FeCo/BN-Chloride, and FeCo/BN-Acetate.

List of Figures

Figure 1.1. Oscillating electric and magnetic fields in the electromagnetic wave.

Figure 1.2. Frequency range of electromagnetic spectrum.

Figure. 1.3. Global microwave absorbers market revenue, by application, 2015-2025 (USD Million)

Figure 1.4. Applications of EWAMs in military defense, textile, healthcare, and telecommunication technologies.

Figure 1.5. Schematic showing the difference between (a) electromagnetic wave shielding material and (b) electromagnetic wave absorbing material.

Figure 1.6. Schematic illustration of (a) transmission line (b) electromagnetic wave absorber.

Figure 1.7. Images of magnetic loss mechanisms including (a) Eddy current loss and (b) resonance loss.

Figure 1.8. Images of dielectric loss mechanisms.

Figure 1.9. Plot of calculated Reflection Loss of an absorber material. Having a broad bandwidth with just over -10 dB is more significant than having a narrow bandwidth.

Figure 2.1. Schematic illustration of external EM wave incident on absorber material at ferromagnetic resonance frequency.

Figure 2.2. Real part of complex permeability shows a rapid drop and imaginary part shows a sharp peak at ferromagnetic resonance frequency, indicating maximum EM wave absorption.

Figure 2.3. The ferromagnetic resonance frequency is proportionally related to the coercivity of the magnetic material.

Figure 2.4. (a) Hysteresis loop of soft and hard magnetic material. (b) Ferromagnetic resonance peak of soft and hard magnetic material.

Figure 2.5. Schematic illustration of stealth aircraft absorbing (a) frequency of only long wavelength and (b) frequency of both short and long wavelength.

Figure 2.6. Illustration of cell phone using various frequencies. Cell phones and other wireless communication devices operate using binary code and multiple channels with different frequencies

Figure 2.7. Enhancing the initial permeability and blue-shifting the ferromagnetic resonance frequency will improve the absorption behavior.

Figure 2.8. Magnetic material with a strong easy axis will tend to align with an external magnetic field in that direction, whereas if it has a strong hard axis, it will tend to resist alignment with the external magnetic field.

Figure 2.9. When a magnetic material is magnetized, the magnetic poles induced on the opposite sides of the material generates an internal field opposing the external field, called the demagnetizing field, H_d

Figure 2.10. According to the Slater-Pauling rule, the magnetic moment of transition metal alloys can be estimated based on the electron configuration of the constituent elements.

Figure 2.11. Phase Diagram of FeCo alloy.

Figure 2.12. As the cobalt contents increases, the crystal structure of α -FeCo transitions to a ordered α' -phase and this ordering produces an increase in the saturation magnetization.

Figure 2.13. A magnetic sphere experiences zero shape anisotropy, therefore $H_\theta = H_\phi$. For a magnetic rod, magnetization deviates into the easy plane, resulting in $H_\theta > H_\phi$.

Figure 2.14. Schematic illustration of FeCo nanochains and nanobelts covered in Part II, Chapter 3 and 4 respectively.

Figure 2.15. Complex permeability of an EWAM. Increasing the loading ratio of filler material in a composite can increase the complex permeability.

Figure 2.16. Graph of intrinsic viscosity vs. aspect ratio of nanomaterials. Viscosity increases with decreasing aspect ratio. (*Minerals 2023, 13(1), 91*)

Figure 2.17. Schematic illustration of hollow FeCo particles covered in Part II of Chapter 5.

Figure 2.18. Schematic illustration of EWAM with good absorbing and heat dissipating performance.

Figure 2.19. The incorporation of boron nitride nanoparticles in the FeCo nanomaterials is covered in Part II of Chapter 4 and Chapter 5.

Figure 3.1. In a RF thermal plasma, micron-sized solid precursors are immediately heated to evaporation point and mass production of nanoparticles are synthesized

Figure 3.2. When the RF power supply is activated, it produces an alternating current that flows through the induction coil. This alternating current creates a rapidly changing magnetic field around the coil.

Figure 3.3. Schematic illustration of the thermal plasma preparation via RF-thermal plasma synthesis of nano-chained FeCo composition.

Figure 3.4 (a) Eddy current formation for the 1-D magnetic anisotropy formed in nano-chained FeCo. The precession motion of the FeCo nanoparticles is expressed by the external field, H . And (b) electromagnetic wave absorber with the most ideal $1/4\lambda$ phase difference.

Figure 3.5. Scanning electron microscope (SEM) Transmission electron microscope (TEM) images of nano-chained $\text{Fe}_x\text{Co}_{1-x}$ synthesized by the RF-ITP: (a)-(c) $x = 0.6$ and (d)-(f) $x = 0.3$.

Figure 3.6. (a) TEM image of one $\text{FeCo}@SiO_2$ nanochain. (b) Diffraction pattern of interface of FeCo nanochain confirms clear crystal structure.

Figure 3.7. Graph of the combined appropriate weight ratio of Fe to Co, *i.e.* 7:3 to 3:7.

Figure 3.8. Graph of distinctive aspect ratios versus composition with varying weight ratio of Fe to Co, *i.e.* 7:3 to 3:7 calculated from the region in images.

Figure 3.9. XRD patterns of the $\text{Fe}_x\text{Co}_{1-x}$ alloys ($x = 0.3, 0.4, 0.5, 0.6, 0.7$), respectively.

Figure 3.10. In-situ TEM observation of the inter-particle diffusion of $\text{Fe}_{0.6}\text{Co}_{0.4}$ nano-particles. (a) A completely spherical $\text{Fe}_{0.6}\text{Co}_{0.4}$ nano-particle with a size of under 100 nm at 873 K. Sequential images for particle accompanied by the diffusion and process of the forming a neck to rods or chained as linear increasing temperature with 30 °C/min from 873 K to 973 K in (b) and 1073 K in (c).

Figure 3.11. Magnetic properties identified for various weight percentages of Co elements.

Figure 3.12. (a) Complex permeability of nano-chained $\text{Fe}_x\text{Co}_{1-x}$ and FeCo spherical micro powder. And (b) complex permittivity of $\text{Fe}_{0.6}\text{Co}_{0.4}$ nano-rods and FeCo spherical micro powder

Figure 3.13. TEM images in different magnification of the insulation coated $\text{Fe}_{0.6}\text{Co}_{0.4}$; 100 nm scale (a) and (b), 10 nm scale (c) and (d). Each coating material show a different thickness of SiO_2 of 29.21 nm and 2.00 nm, respectively. (e) TEM image of $\text{Fe}_{0.6}\text{Co}_{0.4}@APTMS$ and the corresponding the energy dispersive X-Ray using the EDS element mapping analysis.

Figure 3.15. XRD patterns of $\text{Fe}_{0.6}\text{Co}_{0.4}@TEOS$ and $\text{Fe}_{0.6}\text{Co}_{0.4}@APTMS$. The well-defined peaks revealed a degree of crystallinity after coated.

Figure 3.16. Magnetic hysteresis loop of $\text{Fe}_{0.6}\text{Co}_{0.4}$, $\text{Fe}_{0.6}\text{Co}_{0.4}@TEOS$, and $\text{Fe}_{0.6}\text{Co}_{0.4}@APTMS$, the inset show the corresponding low-field H_c values.

Figure 3.17. (a) Complex permittivity and (b) complex permeability of different condition samples of $\text{Fe}_{0.6}\text{Co}_{0.4}$; as synthesized, $@TEOS$, and $@APTMS$ at 30 wt. %.

Figure 3.18. The widen frequency dependence of complex permittivity (a) and complex permeability (b) of $\text{Fe}_{0.6}\text{Co}_{0.4}$; as synthesized and $@APTMS$ at 50 wt.% nano-chained FeCo filler loading.

Figure 3.19. (a) 3-D mapping for the overall relationship between reflection loss and frequency (~ 26 GHz) for $\text{Fe}_{0.6}\text{Co}_{0.4}$ and (b) corresponding 2-D mapping for the thickness influence of $\text{Fe}_{0.6}\text{Co}_{0.4}$.

Figure 3.20. (a) 3-D mapping for the overall relationship between reflection loss and frequency (~ 26 GHz) for $\text{Fe}_{0.6}\text{Co}_{0.4}@SiO_2$ and (b) corresponding 2-D mapping for the thickness influence of $\text{Fe}_{0.6}\text{Co}_{0.4}@SiO_2$.

Figure 3.21. 3-D mapping of overall relationship between reflection loss and frequency (5-18 GHz) of the FeCo spherical micro particles which show only shallow absorption valleys and maximum reflection loss of -11.46 dB at 16.6 GHz.

Figure 3.22. The frequency dependence of $\tan\delta_\epsilon$ and $\tan\delta_\mu$ for (a) $\text{Fe}_{0.6}\text{Co}_{0.4}$ and (b) $\text{Fe}_{0.6}\text{Co}_{0.4}@SiO_2$.

Figure 3.23. Photo of scalable synthesis of electromagnetic wave absorber embodied FeCo nano-chained through composite manufacturing.

Figure 3.24. 3-D graph showing this work compared to other works. This work guarantee that high-throughput production of nanoparticles with beneficial 1-dimensional morphologies and unprecedented magnetic properties can be used to fabricate high-efficiency EWAMs with minimal thickness.

Figure 3.25. Tables showing experimental and estimated value of various

factors.

Figure 3.26. Graph showing estimated and calculated values of FeCo alloys with different aspect ratios relative to the anisotropic function and the derived equation and coefficients from the graph.

Figure 4.1. Nanomanufacturing strategy of the FCBN. (a) Schematics showing the shape modulation process to fabricate the FCBN, where one-dimensional FeCo nanochains are synthesized with a high-temperature thermal plasma system. Subsequently, the BN nanoparticles are incorporated with the FeCo nanobelts manufactured through a planetary ball mill. (b) Illustration to compare the effect of shape anisotropy in between the FeCo nanochains and FeCo nanobelts. SEM images (right) and corresponding illustrations (left) of (c) FeCo nanochains, (d) nanochains ball-milled into FeCo nanobelts, (e) ball-milled FeCo nanobelts with the addition of BN nanoparticles.

Figure 4.2. Structural characterization of the manufactured FeCo nanomaterials. TEM images of (a) as-synthesized FeCo nanochain, (b) ball-milled FeCo nanobelt, and (c) FeCo nanobelts intercalated with boron nitride nanoparticles.

Figure 4.3. SEM image of FCBN and their corresponding EDS mapping for boron (B), nitrogen (N), iron (Fe), and cobalt (Co) atoms. BN nanoparticles are fully intercalated between the FeCo nanobelts.

Figure 4.4. (a) TEM image of boron nitride nanoparticles. (b) Measured size histogram of boron nitride nanoparticles show that the nanoparticles have an average dimension of 30 nm.

Figure 4.5. XRD analysis of three different samples, including the FeCo nanochains, FeCo nanobelts, and FCBN.

Figure 4.6. Thermal conductivity measurement of three different samples, including the FeCo nanochains, FeCo nanobelts, and FCBN.

Figure 4.7. Magnetic hysteresis loop data of three different samples, including the FeCo nanochains, FeCo nanobelts, and FCBN.

Figure 4.8. Overall characteristics for the EMW absorbance at the S (2–4 GHz), C (4–8 GHz), X (8–12 GHz), and Ku (12–18 GHz) band frequencies. (a-b) Electromagnetic characteristics of (a) complex permeability (μ) and (b) permittivity (ϵ). The samples were prepared with FeCo nanochains, FeCo nanobelts, and FCBN. Solid lines represent the real parts (μ' , ϵ'), whereas the dot lines indicate the imaginary parts (μ'' , ϵ'').

Figure 4.9. Enhancement in (a) real permeability at low frequency range and (b) imaginary permeability of FeCo nanochain, FeCo nanobelts, and FCBN.

Figure 4.10. Comparison of FeCo nanochains and FCBN represented in the magnetic (δ_μ) and dielectric (δ_ϵ) loss tangent ($\tan\delta_\mu = \mu''/\mu'$, $\tan\delta_\epsilon = \epsilon''/\epsilon'$).

Figure 4.11. EMW absorbing performance of FeCo nanochain at various thicknesses and frequencies and calculated with equations (9-10).

Figure 4.12. EMW absorbing performance of FeCo nanobelt at various thicknesses and frequencies and calculated with equations (9-10).

Figure 4.13. EMW absorbing performance of FCBN at various thicknesses and frequencies and calculated with equations (9-10).

Figure 4.14. Two- and three-dimensional mapping of the overall relationship between reflection loss and frequency up to 18 GHz for FCBN.

Figure 4.15. Two- and three-dimensional mapping of the overall relationship between reflection loss and frequency up to 18 GHz for (a) FeCo nanochain and (b) FeCo nanobelt.

Figure 4.16. Comparison of the bandwidth at thicknesses 1.4 mm and 1.5 mm for FeCo nanochains and FCBN. FCBN shows wider bandwidth than FeCo nanochain for all thicknesses.

Figure 4.17. Frequency dependence of relative input impedance ($|Z_{in}/Z_o|$) for FeCo nanochains, FeCo nanobelts, and FCBN.

Figure 4.18. Comparison of the attenuation constants (α) between FeCo nanochains and FCBN.

Figure 4.19. Schematic of possible EMW absorption process in FCBN-TPU composite membrane. Three different absorption systems, including the magnetic loss, multiple reflection, and dielectric loss, allow an improved EMW absorbance and successful impedance matching.

Figure 4.20. Graphs showing (a) $\mu''(\mu')^{-2}f^{-1}$ (eddy current loss) versus frequency of FeCo nanochains and FCBN and (b) ratio of Co value for FCBN and FeCo nanochain versus frequency.

Figure 4.21. Cole-Cole plots of (a) FeCo nanochains and (b) FCBN. The dotted line indicates the semicircles in the Cole-Cole curves.

Figure 4.22. (a) Photographs showing the FCBN composite with a dimension of 30 mm in width x 30 mm in height x 15 mm in thickness. The manufactured

membrane displays high flexibility. (b-c) Complex permeability and permittivity values measured (b) before and (c) after 1,000-cycle bending. The insert photographs indicate the FCBN-TPU composite membrane loaded into the 90° bending machine.

Figure 4.23. 3-D graph showing comparison of this work to other works. FCBN shows the largest bandwidth at small thickness.

Figure 4.24. Validation of anisotropic function through the experimental value of FeCo nanobelt.

Figure 5.1. EW absorbing composite (FeCo/TPU) fabrication process. Composite with 50 wt% FeCo nanochain well-casted compared to inhomogeneous casting of 70 wt% composite.

Figure 5.2. Schematic illustration of formation of FeCo/BN particles from three different precursors including Fe/Co Nitrate, Fe/Co Chloride, and Fe/Co Acetate via Ultrasonic Spray Pyrolysis. Droplets of aerosol carried by carrier gas into hot chamber and droplets are dried, contracted, precipitated, thermolized and sintered.

Figure 5.3. Schematic illustration of overall process of Ultrasonic Spray Pyrolysis involving the three different precursors, Fe/Co Nitrate, Fe/Co Chloride, and Fe/Co Acetate, where spherical, cubic, and hollow-sphere particles are formed respectively.

Figure 5.4. Structural characterization of as-synthesized FeCo. (a-c) High magnification SEM images of one particle and (d-f) Low magnification SEM images of overview of FeCo-Nitrate, FeCo-chloride, and FeCo-Acetate respectively.

Figure 5.5 TEM observation images, and corresponding elemental mapping of iron, cobalt, and nitrogen: (a) FCBN-Nitrate, (b) FCBN-Chloride, and (c) FCBN-Acetate particles.

Figure 5.6. Manufacturing strategy for the shape-modulated FeCo particles. (a-c) Schematics demonstrating a series of shape-modulation processes produced from the different metal salt precursors. (a) Sphere-shaped FeCo particle manufactured through the aerosol reaction of iron nitrate and cobalt nitrate. (b) FeCo cube particle synthesized from the pyrolysis process of iron chloride and cobalt chloride. (c) FeCo hollow sphere particle using iron acetate and cobalt acetate.

Figure 5.7. Characterization results from XRD analysis. XRD data captures the pure FeCo body-centered cubic (BCC) peaks at 44.8°, 65.2°, and 82.6°.

Figure 5.8. Magnetic hysteresis loop data of the three different samples, including FeCo-Nitrate, FeCo-Chloride, and FeCo-Acetate.

Figure 5.9. Thermal conductivity measurement of the three different as-synthesized FeCo particles and the BN-incorporated samples.

Figure 5.10. Electromagnetic characterization of the as-synthesized FeCo particles. (a) Complex permeability and (b) complex permittivity for FeCo-Nitrate, FeCo-Chloride, and FeCo-Acetate.

Figure 5.11. Electromagnetic characterization of the as-synthesized FeCo particles. (a) Complex permeability and (b) complex permittivity for FeCo/BN-Nitrate, FeCo/BN-Chloride, and FeCo/BN-Acetate.

Figure 5.12. EMW absorption characteristics at the S (2 – 4 GHz), C (4 – 8 GHz), X (8 – 12 GHz), Ku (12 – 18 GHz), and K (18 – 26 GHz) band frequencies. (a-c) 2-D mappings of reflection loss calculation at the various thickness of EMW absorbing membranes manufactured by (a) FeCo/BN-Nitrate, (b) FeCo/BN-Chloride, and (c) FeCo/BN-Acetate particles.

Figure 5.13. Overall microstructure and flow characteristics of FeCo nanochain, FeCo-Nitrate, and FeCo-Acetate shown by (a) SEM images and (b) photos of uncured FeCo/TPU composites.

Figure 5.14. Physical characteristics of FeCo nanochain, FeCo-Acetate, FeCo-Nitrate analyzed by (a) Bulk density measurements and (b) Viscosity measurements.

Figure 5.15. Electromagnetic characterization of FeCo-Acetate/TPU (70 wt%).

Figure 6.1. Summary of results in Chapter 3, 4, and 5.

Part I

Background Information on Electromagnetic Wave Absorbing Materials (EWAM)

Chapter 1. Introduction

1.1. Overview of EWAMs

1.1.1. What are Electromagnetic Waves?

Most of the mass and energy in the entire universe occurs in the form of electromagnetic radiation¹. Human life is strongly immersed in it, where modern communication technologies are particularly dependent on one of its forms². As our daily life has been pervaded by electromagnetic (EM) radiation, such pollution has also been prolonging malfunctioning of neighboring devices and harmful effects on human life³.

EM radiation is a form of energy that is transmitted through space in the form of electromagnetic waves⁴. The waves are composed of oscillating electric and magnetic fields that are perpendicular to each other and to the direction of the wave's propagation (see **Figure 1.1**)⁵. EM radiation includes wide range of frequencies and wavelengths⁶. The spectrum ranges from radio waves with long wavelengths and low frequencies, to microwaves, infrared radiation, visible light, ultraviolet radiation, X-rays, and gamma rays, which have shorter wavelengths and higher frequencies (see **Figure 1.2**)⁷.

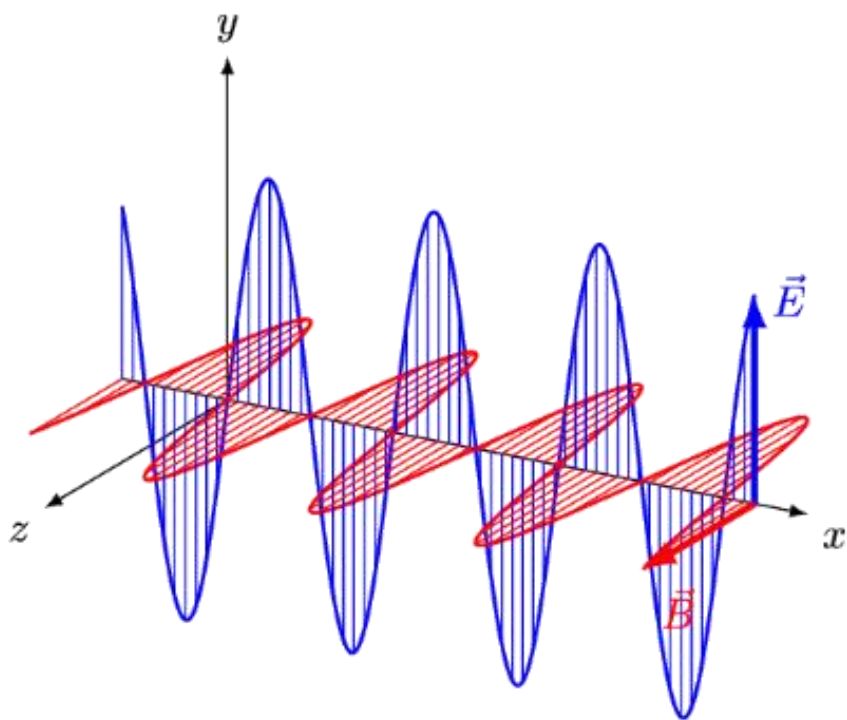


Figure 1.1. Oscillating electric and magnetic fields in the electromagnetic wave.

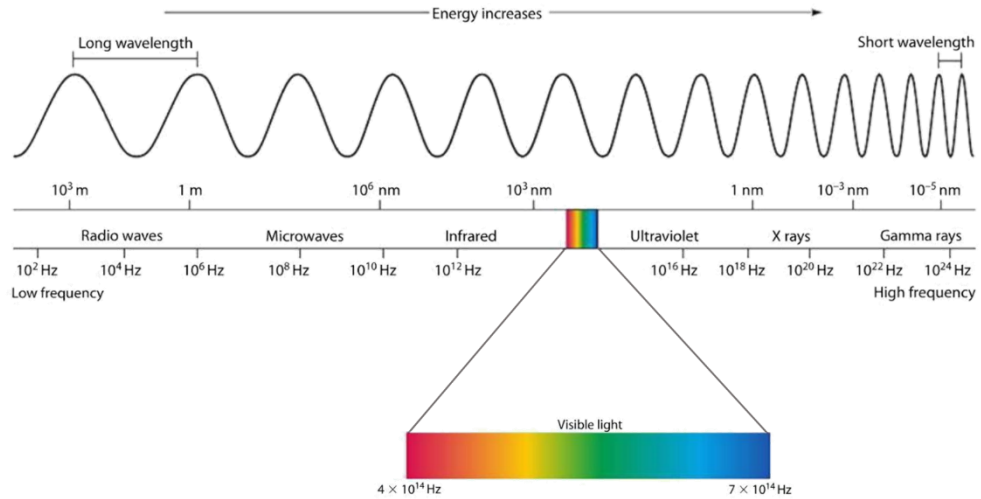


Figure 1.2. Frequency range of electromagnetic spectrum.

1.1.2. Demands for Next Generation EWAMs

EM radiation with diverse frequencies result from various occurrences such as natural radiators, unintentional radiators, and intentional radiators⁸. Therefore, EM wave absorption is needed over a wide range of frequencies⁹⁻¹¹. The increasing demand for microwave absorbers and the advancements in technology are expected to create significant market avenues for future generations of microwave absorbers^{12, 13}. The market is expected to be driven by aerospace/defense industries and electronics/telecommunication technologies (see **Figure 1.3**).^{14, 15} The telecommunication industry is expected to contribute greatly to the growth of the market, with increasing demand for 5G wireless communication networks.¹⁶⁻¹⁸ In addition, healthcare industry is expected to provide growth opportunities, particularly for medical devices and therapies.^{19, 20} Overall, the market for future generations of microwave absorbers is expected to grow significantly in the coming years, driven by advancements in technology and increasing demand from a variety of industries (see **Figure 1.4**).²¹⁻²³

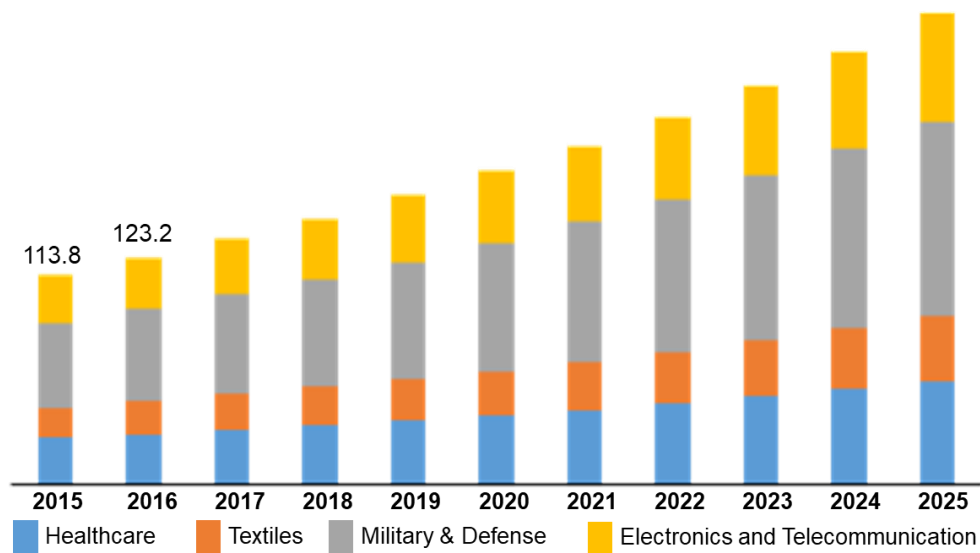


Figure. 1.3. Global microwave absorbers market revenue, by application, 2015-2025 (USD Million)

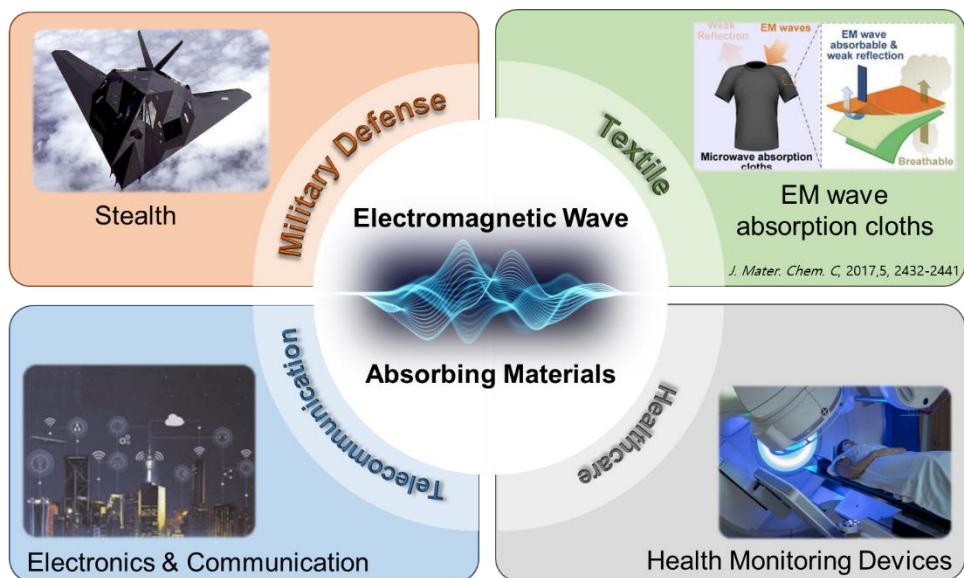


Figure 1.4. Applications of EWAMs in military defense, textile, healthcare, and telecommunication technologies.

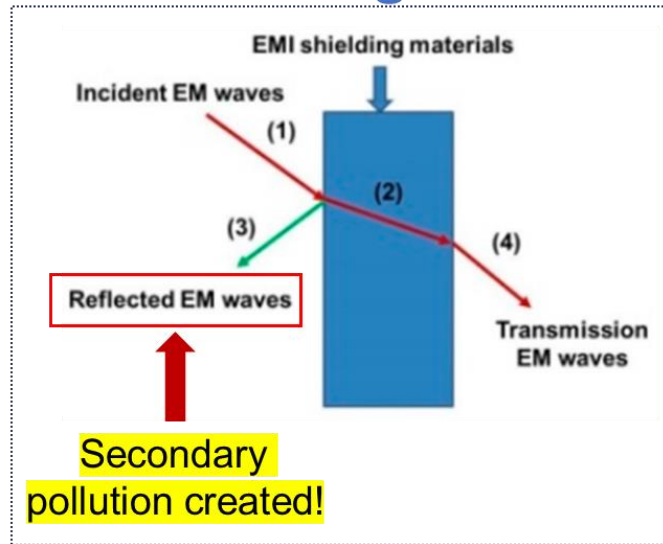
1.2. Working Principles of EWAMs

1.2.1. EW Absorbing Material vs. EW Shielding Material

Electromagnetic wave shielding materials and electromagnetic wave absorbing materials are both used to protect against electromagnetic interference (EMI), but they function in different ways. Electromagnetic wave shielding materials are designed to block or reflect electromagnetic waves, preventing them from penetrating a specific area.^{24, 25} These materials can be used to shield electronic devices from electromagnetic interference. Some common examples of electromagnetic wave shielding materials include metals such as copper, aluminum, and steel.²⁶⁻²⁸ However, secondary reflection can occur when electromagnetic shielding materials reflect electromagnetic waves, causing them to bounce off surfaces and reflect back into the surrounding environment.^{29, 30} This can potentially cause interference with other electronic devices or systems in the area, which can lead to further electromagnetic pollution (see **Figure 1.5 (a)**).³¹ The risk of secondary reflection can be mitigated by using electromagnetic wave absorbing materials instead. Electromagnetic wave absorbing materials are designed to reduce the electromagnetic radiation that is reflected, by converting it into heat or other forms of energy (see **Figure 1.5 (b)**). Such EWAMs are commonly used in radar technology to minimize the radar cross section (RCS) of detectable objects such as stealth aircraft.³² One approach is to coat the surface of the aircraft with EWAM, which absorbs and dissipates electromagnetic energy, reducing the amount of radiation reflected back towards the radar system.³³ EWAMs are also commonly used in telecommunication applications to improve the performance of electronic devices.³⁴ ³⁵ EWAMs can help reduce the amount of electromagnetic radiation that is reflected

by neighboring electronic components and circuits.³⁶

(a) EW Shielding Material



(b) EW Absorbing Material

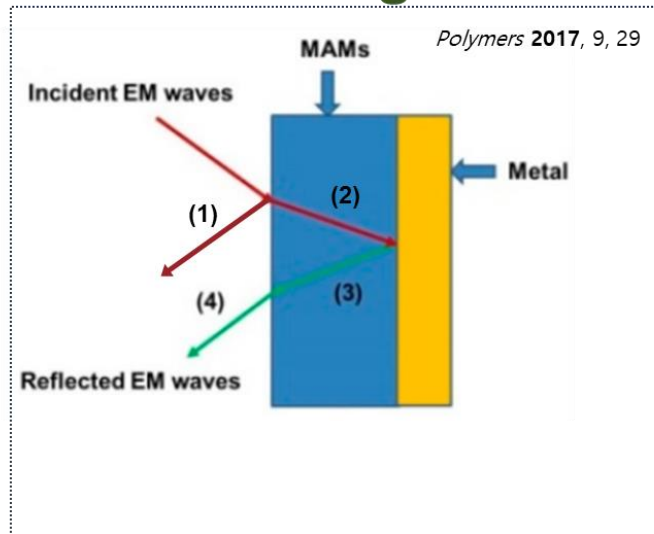


Figure 1.5. Schematic showing the difference between (a) electromagnetic wave shielding material and (b) electromagnetic wave absorbing material.

1.2.2. Transmission Line Theory and Impedance Matching

Transmission line theory studies the behavior of electrical signals as they propagate through conductive lines such as cables and wires.^{37, 38} Transmission lines are used to transfer electrical signals from one location to another, and are found in a wide range of applications including telecommunications³⁹, power distribution⁴⁰, and electronic circuitry⁴¹. These electrical cables, however, can radiate electromagnetic energy in the high frequency range, particularly at connectors and joints.^{42, 43} Such phenomenon can cause signal distortion⁴⁴, attenuation⁴⁵, and other types of interference in electronic systems⁴², which can degrade their performance and reliability.⁴⁶ To reduce the amount of interference generated within the electrical cables, impedance is considered, which is a measure of the resistance of the line to the flow of electrical signals.⁴⁷ Impedance matching in transmission lines refers to the process of making the impedance of the load equal to the characteristic impedance of the transmission line.^{48, 49} When the impedance of the load matches the characteristic impedance of the transmission, maximum power is transferred from the source to the load with minimum reflection losses (see **Figure 1.6 (a)**).⁵⁰ The input impedance of transmission line can be expressed by the following equation, which is a complex quantity that depends on the length of the line, frequency of the signal, characteristic impedance of the line, and the load impedance:⁵¹

$$Z_{in,N} = Z_{c,N} \frac{Z_{in(N-1)} + Z_{c,N} \tanh \gamma_N l_N}{Z_{c,N} + Z_{in(N-1)} \tanh \gamma_N l_N} \quad (1)$$

Where Z_c = characteristics impedance

Z_L = load impedance

$Z_{in,0} = Z_L$

The input impedance can be adjusted by varying the load impedance to ensure that

it matches the characteristic impedance.

An EW absorber is designed based on the principles of transmission line theory.⁵² For example, a Salisbury screen consists of a layer of absorbing material backed by a metallic plate.^{53, 54} The absorbing material must have an input impedance comparable to the impedance of air (377Ω) in order to absorb as much incident as possible.^{47, 55} The absorbing material is carried out using transmission line theory, where each layer of material is equivalent to the characteristic impedance after the transmission line (see **Figure 1.6 (b)**).⁵⁶ The input impedance of EMW absorber can be expressed by the following equation, including the complex permeability and complex permittivity of the absorber material:⁵⁷

$$Z_{in,N} = \sqrt{\frac{\mu_{r(N-1)}}{\epsilon_{r(N-1)}}} \tanh \left[j \frac{2\pi f d}{c} \sqrt{\mu_{r(N-1)} \epsilon_{r(N-1)}} \right] \quad (2)$$

Where μ_r = complex permeability

ϵ_r = complex permittivity

f = frequency

d = thickness

c = speed of light

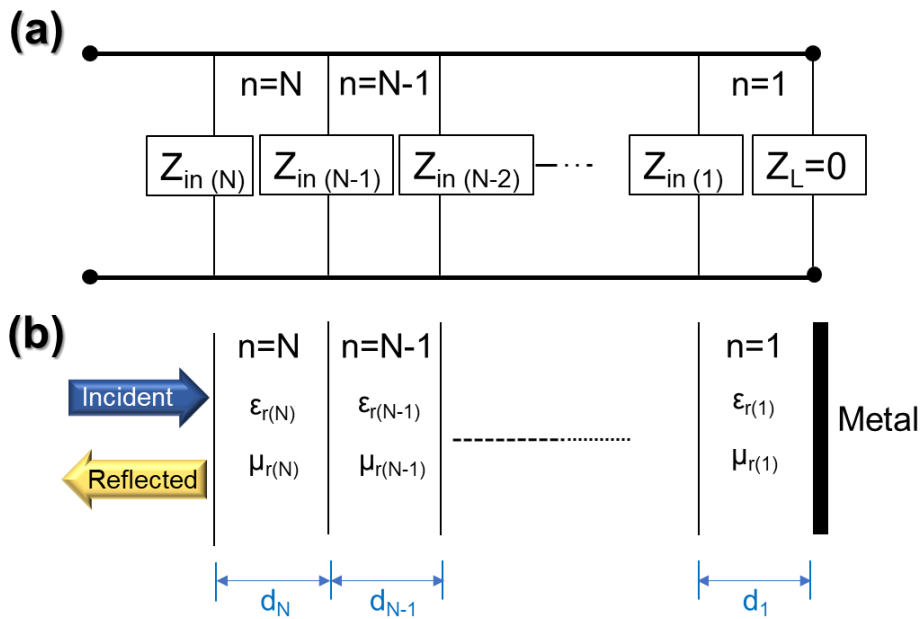


Figure 1.6. Schematic illustration of (a) transmission line (b) electromagnetic wave absorber.

1.2.3. Magnetic and Dielectric Loss Mechanisms

As an EW absorber absorbs electromagnetic waves, it converts the absorbed radiation into heat and dissipates energy.⁵⁸ This phenomenon occurs in materials that are capable of absorbing the magnetic and electric field. Magnetic materials such as magnetic alloys and ferrites are responsible for absorbing the magnetic field while materials with high dielectric constants such as SiO₂ and Al₂O₃ are responsible for absorbing the electrical field.⁵⁹ The absorption and loss of the magnetic field can be expressed by the complex permeability, which is a parameter used to describe the magnetic properties of a material in the presence of an alternating magnetic field. It is a complex number that is defined as the ratio of the magnetic flux density to the magnetic field as shown in the following equation:⁶⁰

$$\mu_r = \frac{B}{H} = \mu'_r - j\mu''_r \quad (3)$$

Here, μ'_r is the real part of the complex permeability, which represents the material's ability to store magnetic energy, and μ''_r is the imaginary part, which represents the material's ability to dissipate magnetic energy.⁶¹ There are various kinds of loss factors that can affect the magnetic loss performance of an EW absorber, including the eddy current loss and resonance loss.⁶² Eddy currents are circulating currents that are induced within a conductor when it is exposed to a changing magnetic field. These currents generate resistive loss (I^2R) by transforming the energy into heat (see **Figure 1.7 (a)**). Another kind of loss is related to the natural resonance of the magnetic material in the EW absorber. Resonance occurs when the frequency of the incoming electromagnetic wave matches the natural resonant frequency of the EWAM. At this frequency, the absorber absorbs maximum energy, resulting in a higher absorption rate (see **Figure 1.7 (b)**).⁶³

Dielectric loss is another factor that can affect the performance of EWAMs.⁶⁴ When EM radiation is absorbed, the internal field generated induces translational motions of free or bound charges such as electrons or ions, or rotates dipoles. Inertial, elastic, and frictional forces resist these induced motions causing losses by converting into heat.⁶⁵ Similar to magnetic loss, dielectric loss can be explained by the complex permittivity. Again, it is a complex number defined as the ratio of the electric flux density (D) to the electric field strength (E) in the material, given by:⁶⁶

$$\epsilon_r = \frac{D}{E} = \epsilon'_r - j\epsilon''_r \quad (4)$$

Here, ϵ'_r is the real part of the complex permittivity, which represents the material's ability to store electrical energy, and ϵ''_r is the imaginary part, which represents the material's ability to dissipate electrical energy. Major loss factors include conduction loss and polarization loss, where electrical energy is dissipated into heat through the resistance as mentioned above (see **Figure 1.8**).⁶⁷

(a) Eddy current loss



(b) Resonance loss

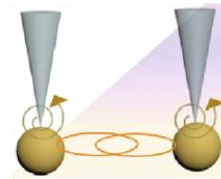
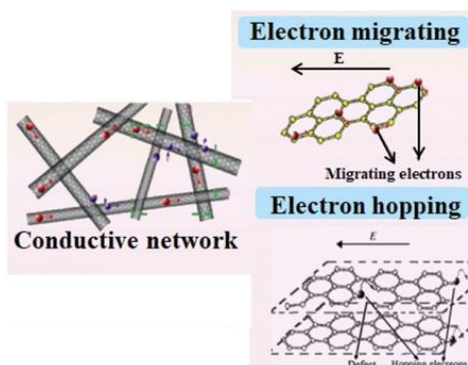


Figure 1.7. Images of magnetic loss mechanisms including (a) Eddy current loss and (b) resonance loss.

Conduction loss



Polarization loss

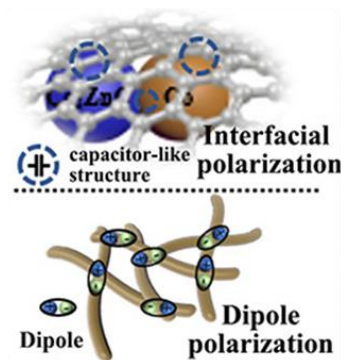


Figure 1.8. Images of dielectric loss mechanisms.

1.2.4. Reflection Loss Calculations

EWAMs in the form of composite material, composed from magnetic and dielectric materials absorb incoming EM radiation, and molecules are activated to convert it into heat energy. When an electromagnetic wave travels in free space (377Ω) with impedance Z_o , and encounters the surface of an EWAM with impedance Z_{in} , reflection occurs. To obtain zero-reflection, the reflection coefficient, $\Gamma = \frac{Z_{in}-Z_o}{Z_{in}+Z_o}$ must be 0 and the input impedance of the absorbing material, Z_{in} must be equal to impedance of free space, Z_o or 377Ω (also known as impedance matching).⁶⁸ The input impedance of the absorber depends on the complex permeability, μ_r and complex permittivity, ϵ_r of the material, as well as the thickness of the absorber as mentioned in equation (2). Impedance matching is an important concept as it helps to maximize the absorption of electromagnetic energy by minimizing the amount of reflected energy. The reflection loss (RL) can be calculated by the following equation and give information on how much energy is reflected back from the absorber:⁶⁹

$$RL = 20 \log_{10} \Gamma = 20 \log_{10} \left| \frac{Z_{in} - Z_o}{Z_{in} + Z_o} \right| \quad (5)$$

The RL is calculated in decibels (dB), and low RL indicates that the absorber is effective at absorbing energy and minimizing reflections. As seen in **Figure 1.9**, RL of -10 dB and -20 dB is comparable to 90% absorption and 99% absorption respectively.⁷⁰ However, having a broad bandwidth with just over -10 dB is more significant than having a narrow bandwidth due to the applications of absorber materials involved in broad frequency range.⁷¹

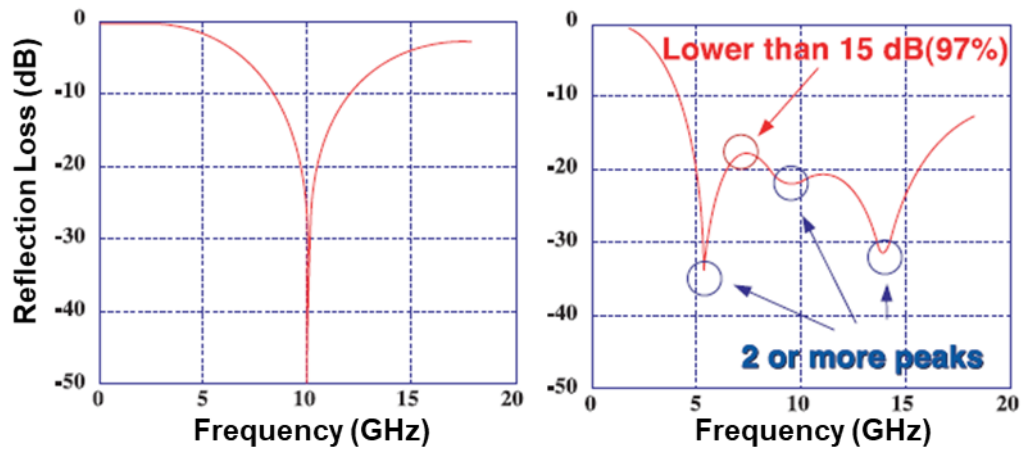


Figure 1.9. Plot of calculated Reflection Loss of an absorber material. Having a broad bandwidth with just over -10 dB is more significant than having a narrow bandwidth.

1.2.5. Soft Magnetic Materials for Magnetic Loss in EWAMs

Soft magnetic materials are commonly used as electromagnetic wave absorbing materials owing to their ability to attenuate electromagnetic waves.⁷² Soft magnetic materials have high magnetic permeability and low coercivity, meaning that they can easily align their magnetic domains with an applied magnetic field and then quickly return to their original state when the field is removed.⁷³ Soft magnetic materials such as ferrite and magnetic alloys are commonly used to provide magnetic loss within the absorber.⁷⁴ These materials can be processed into thin sheets, powders, or coatings, and can be tailored to have specific properties for applications in EW absorber.^{52, 75, 76} Magnetic materials with high complex permeability are commonly used in absorbers for maximum storage of magnetic energy when contacted with EM radiation. However, generally magnetic materials have limited complex permeability and addressing this limitation by engineering the materials is one of the vigorously studied area.⁷⁶ Various methods such as grain size control⁷⁶, alloying and doping⁷⁷, and multilayered structures⁷⁸ are being extensively studied to enhance the complex permeability of the magnetic material. One of the most spotlighted methods for enhancing the complex permeability of magnetic materials is shape modulation, primarily due to the renowned Snoek's Law.⁷⁹

1.2.6. Aim of this Research

The aim of this research is to investigate the relationship between the complex permeability and the soft magnetic material by engineering FeCo alloys through various shape-modulation. Shape modulation is a key factor to enhance the complex permeability and is verified in this research with the aid of Snoek's Law. Previous

studies have attempted to shape-modulate FeCo powders into a chain-like structure solely using wet-chemical methods. However, this approach has limitations in terms of designing one-dimensional structures where particles are securely bonded or firmly attached to each other. The objective of this study is to explore the relationship between shape modulation of magnetic materials and complex permeability, with a focus on achieving a broadband EWAM as well as the optimum structure for maximum loading in the composite as filler material. By gaining a better understanding of this relationship, this research may contribute to the development of new strategies for shape-modulating FeCo alloys for applications in EW absorber.

1.3. References

1. Lv, H.; Yang, Z.; Pan, H.; Wu, R., Electromagnetic absorption materials: Current progress and new frontiers. *Progress in Materials Science* **2022**, *127*, 100946.
2. Namai, A.; Sakurai, S.; Nakajima, M.; Suemoto, T.; Matsumoto, K.; Goto, M.; Sasaki, S.; Ohkoshi, S.-i., Synthesis of an Electromagnetic Wave Absorber for High-Speed Wireless Communication. *Journal of the American Chemical Society* **2009**, *131* (3), 1170-1173.
3. Drossos, A.; Santomaa, V.; Kuster, N., The dependence of electromagnetic energy absorption upon human head tissue composition in the frequency range of 300-3000 MHz. *IEEE Transactions on Microwave Theory and Techniques* **2000**, *48* (11), 1988-1995.
4. Genuis, S. J., Fielding a current idea: exploring the public health impact of electromagnetic radiation. *Public Health* **2008**, *122* (2), 113-124.
5. Ma, G.; Sun, J.; Aslani, F.; Huang, Y.; Jiao, F., Review on electromagnetic wave absorbing capacity improvement of cementitious material. *Construction and Building Materials* **2020**, *262*, 120907.
6. Ruiz-Perez, F.; López-Estrada, S. M.; Tolentino-Hernández, R. V.; Caballero-Briones, F., Carbon-based radar absorbing materials: A critical review. *Journal of Science: Advanced Materials and Devices* **2022**, *7* (3), 100454.
7. Cao, M.-S.; Wang, X.-X.; Zhang, M.; Shu, J.-C.; Cao, W.-Q.; Yang, H.-J.; Fang, X.-Y.; Yuan, J., Electromagnetic Response and Energy Conversion for Functions and Devices in Low-Dimensional Materials. *Advanced Functional Materials* **2019**, *29* (25), 1807398.
8. Ma, M. T.; Kanda, M.; Crawford, M. L.; Larsen, E. B., A review of

- electromagnetic compatibility/interference measurement methodologies. *Proceedings of the IEEE* **1985**, 73 (3), 388-411.
9. Ra'di, Y.; Simovski, C. R.; Tretyakov, S. A., Thin Perfect Absorbers for Electromagnetic Waves: Theory, Design, and Realizations. *Physical Review Applied* **2015**, 3 (3), 037001.
 10. Li, Q.; Zhang, Z.; Qi, L.; Liao, Q.; Kang, Z.; Zhang, Y., Toward the Application of High Frequency Electromagnetic Wave Absorption by Carbon Nanostructures. *Advanced Science* **2019**, 6 (8), 1801057.
 11. Ren, F.; Yu, H.; Wang, L.; Saleem, M.; Tian, Z.; Ren, P., Current progress on the modification of carbon nanotubes and their application in electromagnetic wave absorption. *RSC Advances* **2014**, 4 (28), 14419-14431.
 12. Zhang, X.-J.; Guo, A.-P.; Wang, G.-S.; Yin, P.-G., Recent progress in microwave absorption of nanomaterials: composition modulation, structural design, and their practical applications. *IET Nanodielectrics* **2019**, 2 (1), 2-10.
 13. Zeng, X.; Cheng, X.; Yu, R.; Stucky, G. D., Electromagnetic microwave absorption theory and recent achievements in microwave absorbers. *Carbon* **2020**, 168, 606-623.
 14. Sawant, K. K.; Satapathy, A.; Mahimkar, K.; Krishnamurthy, S.; Kaur, A.; Kandasubramanian, B.; Raj, A. A. B., Recent Advances in MXene Nanocomposites as Electromagnetic Radiation Absorbing Materials. *Journal of Electronic Materials* **2023**, 52 (6), 3576-3590.
 15. Yin, X.; Kong, L.; Zhang, L.; Cheng, L.; Travitzky, N.; Greil, P., Electromagnetic properties of Si–C–N based ceramics and composites. *International Materials Reviews* **2014**, 59 (6), 326-355.
 16. Wang, T.; Huang, B. In *Millimeter-wave techniques for 5G mobile*

communications systems: Challenges, framework and way forward, 2014 XXXIth URSI General Assembly and Scientific Symposium (URSI GASS), 16-23 Aug. 2014; 2014; pp 1-4.

17. Hao, H.; Hui, D.; Lau, D., Material advancement in technological development for the 5G wireless communications. *Nanotechnology Reviews* **2020**, *9* (1), 683-699.

18. Lee, S.; Fujita, M.; Toyoda, M.; Takano, K.; Hara, S.; Watanabe, I.; Kasamatsu, A.; Ito, H. In *Sub-Terahertz Electromagnetic-Wave Absorber for Future Wireless Communication*, 2022 IEEE International Symposium on Radio-Frequency Integration Technology (RFIT), 29-31 Aug. 2022; 2022; pp 101-103.

19. Agarwal, K.; Guo, Y. X. In *Interaction of electromagnetic waves with humans in wearable and biomedical implant antennas*, 2015 Asia-Pacific Symposium on Electromagnetic Compatibility (APEMC), 26-29 May 2015; 2015; pp 154-157.

20. Zhao, Y.; Hao, L.; Zhang, X.; Tan, S.; Li, H.; Zheng, J.; Ji, G., A Novel Strategy in Electromagnetic Wave Absorbing and Shielding Materials Design: Multi-Responsive Field Effect. *Small Science* **2022**, *2* (2), 2100077.

21. Zhou, J.; Zhang, G.; Luo, J.; Hu, Y.; Hao, G.; Guo, H.; Guo, F.; Wang, S.; Jiang, W., A MOFs-derived 3D superstructure nanocomposite as excellent microwave absorber. *Chemical Engineering Journal* **2021**, *426*, 130725.

22. Liu, Z.; Wu, C.; Wang, Y.; Xian, G.; Zhu, Z.; Xie, N.; Wang, Y.; Liu, Y.; Kong, L., MXene/CoS heterostructures self-assembled through electrostatic interaction as superior microwave absorber. *Journal of Alloys and Compounds* **2022**, *900*, 163452.

23. Hou, X.; Wang, W.; Gao, X.; Ran, K.; Huang, Y.; Zhang, Z.;

- Fang, Y.; Wang, S.; He, D.; Ye, W.; Zhao, R.; Xue, W., Salt template assisted synthesis of Fe@graphene for high-performance electromagnetic wave absorption. *Carbon* **2022**, *199*, 268-278.
24. Wang, G.; Ong, S. J. H.; Zhao, Y.; Xu, Z. J.; Ji, G., Integrated multifunctional macrostructures for electromagnetic wave absorption and shielding. *Journal of Materials Chemistry A* **2020**, *8* (46), 24368-24387.
 25. Xia, Y.; Gao, W.; Gao, C., A Review on Graphene-Based Electromagnetic Functional Materials: Electromagnetic Wave Shielding and Absorption. *Advanced Functional Materials* **2022**, *32* (42), 2204591.
 26. Geetha, S.; Satheesh Kumar, K. K.; Rao, C. R. K.; Vijayan, M.; Trivedi, D. C., EMI shielding: Methods and materials—A review. *Journal of Applied Polymer Science* **2009**, *112* (4), 2073-2086.
 27. Oussaid, R., Study of the materials improvement in electromagnetic compatibility. *Journal of Electrical Systems Special*, (01) **2009**, 53-56.
 28. Pandey, R.; Tekumalla, S.; Gupta, M., EMI shielding of metals, alloys, and composites. In *Materials for Potential EMI Shielding Applications*, Elsevier: 2020; pp 341-355.
 29. Wang, X.-X.; Shu, J.-C.; Cao, W.-Q.; Zhang, M.; Yuan, J.; Cao, M.-S., Eco-mimetic nanoarchitecture for green EMI shielding. *Chemical Engineering Journal* **2019**, *369*, 1068-1077.
 30. Wang, M.; Tang, X.-H.; Cai, J.-H.; Wu, H.; Shen, J.-B.; Guo, S.-Y., Construction, mechanism and prospective of conductive polymer composites with multiple interfaces for electromagnetic interference shielding: a review. *Carbon* **2021**, *177*, 377-402.
 31. Jia, X.; Li, Y.; Shen, B.; Zheng, W., Evaluation, fabrication and

dynamic performance regulation of green EMI-shielding materials with low reflectivity: A review. *Composites Part B: Engineering* **2022**, 109652.

32. Ahmad, H.; Tariq, A.; Shehzad, A.; Faheem, M. S.; Shafiq, M.; Rashid, I. A.; Afzal, A.; Munir, A.; Riaz, M. T.; Haider, H. T.; Afzal, A.; Qadir, M. B.; Khaliq, Z., Stealth technology: Methods and composite materials—A review. *Polymer Composites* **2019**, 40 (12), 4457-4472.

33. Liu, J.; Zhao, Z.; Zhang, L., Toward the application of electromagnetic wave absorption by two-dimension materials. *Journal of Materials Science: Materials in Electronics* **2021**, 32 (21), 25562-25576.

34. Wu, Z.; Cheng, H. W.; Jin, C.; Yang, B.; Xu, C.; Pei, K.; Zhang, H.; Yang, Z.; Che, R., Dimensional design and core-shell engineering of nanomaterials for electromagnetic wave absorption. *Advanced Materials* **2022**, 34 (11), 2107538.

35. Cheng, Y.; Zhu, W.; Lu, X.; Wang, C., Recent progress of electrospun nanofibrous materials for electromagnetic interference shielding. *Composites Communications* **2021**, 27, 100823.

36. Zhou, S.; Zhang, G.; Nie, Z.; Liu, H.; Yu, H.; Liu, Y.; Bi, K.; Geng, W.; Duan, H.; Chou, X., Recent advances in 3D printed structures for electromagnetic wave absorbing and shielding. *Materials Chemistry Frontiers* **2022**, 6 (13), 1736-1751.

37. Eleftheriades, G. V., EM transmission-line metamaterials. *Materials today* **2009**, 12 (3), 30-41.

38. Alibakhshikenari, M.; Virdee, B. S.; Azpilicueta, L.; Naser-Moghadasi, M.; Akinsolu, M. O.; See, C. H.; Liu, B.; Abd-Alhameed, R. A.; Falcone, F.; Huynen, I., A comprehensive survey of “metamaterial transmission-line

based antennas: Design, challenges, and applications”. *Ieee Access* **2020**, 8, 144778-144808.

39. Vandenbosch, G.; Demuynck, F.; Van de Capelle, A., The transmission line models: Past, present, and future (invited review article). *International Journal of Microwave and Millimeter-Wave Computer-Aided Engineering* **1993**, 3 (4), 319-325.

40. Karimi, S.; Musilek, P.; Knight, A. M., Dynamic thermal rating of transmission lines: A review. *Renewable and Sustainable Energy Reviews* **2018**, 91, 600-612.

41. Fan, J.; Ye, X.; Kim, J.; Archambeault, B.; Orlandi, A., Signal integrity design for high-speed digital circuits: Progress and directions. *IEEE Transactions on Electromagnetic Compatibility* **2010**, 52 (2), 392-400.

42. Kikuchi, H., Overview of power-line radiation and its coupling to the ionosphere and magnetosphere. *Space Science Reviews* **1983**, 35 (1), 33-41.

43. Pavlidou, N.; Vinck, A. H.; Yazdani, J.; Honary, B., Power line communications: state of the art and future trends. *IEEE Communications magazine* **2003**, 41 (4), 34-40.

44. Yigit, M.; Gungor, V. C.; Tuna, G.; Rangoussi, M.; Fadel, E., Power line communication technologies for smart grid applications: A review of advances and challenges. *Computer Networks* **2014**, 70, 366-383.

45. Devi, N.; Ray, S. S., Electromagnetic interference cognizance and potential of advanced polymer composites toward electromagnetic interference shielding: A review. *Polymer Engineering & Science* **2022**, 62 (3), 591-621.

46. Divakaran, S. K.; Krishna, D. D.; Nasimuddin, RF energy harvesting systems: An overview and design issues. *International Journal of RF and Microwave*

Computer-Aided Engineering **2019**, 29 (1), e21633.

47. Wang, T.; Chen, G.; Zhu, J.; Gong, H.; Zhang, L.; Wu, H., Deep understanding of impedance matching and quarter wavelength theory in electromagnetic wave absorption. *Journal of Colloid and Interface Science* **2021**, 595, 1-5.
48. Couraud, B.; Vauche, R.; Daskalakis, S. N.; Flynn, D.; Deleruyelle, T.; Kussener, E.; Assimonis, S., Internet of things: A review on theory based impedance matching techniques for energy efficient RF systems. *Journal of Low Power Electronics and Applications* **2021**, 11 (2), 16.
49. Wang, B.; Cao, Z., A review of impedance matching techniques in power line communications. *Electronics* **2019**, 8 (9), 1022.
50. Rathod, V. T., A review of electric impedance matching techniques for piezoelectric sensors, actuators and transducers. *Electronics* **2019**, 8 (2), 169.
51. Xia, L.; Feng, Y.; Zhao, B., Intrinsic mechanism and multiphysics analysis of electromagnetic wave absorbing materials: New horizons and breakthrough. *Journal of Materials Science & Technology* **2022**.
52. Zhang, S.; Cheng, B.; Jia, Z.; Zhao, Z.; Jin, X.; Zhao, Z.; Wu, G., The art of framework construction: hollow-structured materials toward high-efficiency electromagnetic wave absorption. *Advanced Composites and Hybrid Materials* **2022**, 5 (3), 1658-1698.
53. Wang, Y., Research progress on radar absorbing materials. *Channels* **2008**, 4, 5G.
54. Rhee, J.; Yoo, Y.; Kim, K.; Kim, Y.; Lee, Y., Metamaterial-based perfect absorbers. *Journal of Electromagnetic Waves and Applications* **2014**, 28 (13), 1541-1580.

55. Sultanov, F.; Daulbayev, C.; Bakbolat, B.; Daulbayev, O., Advances of 3D graphene and its composites in the field of microwave absorption. *Advances in Colloid and Interface Science* **2020**, 285, 102281.
56. Panwar, R.; Lee, J. R., Recent advances in thin and broadband layered microwave absorbing and shielding structures for commercial and defense applications. *Functional composites and structures* **2019**, 1 (3), 032001.
57. Jia, Z.; Lan, D.; Lin, K.; Qin, M.; Kou, K.; Wu, G.; Wu, H., Progress in low-frequency microwave absorbing materials. *Journal of Materials Science: Materials in Electronics* **2018**, 29, 17122-17136.
58. Houbi, A.; Aldashevich, Z. A.; Atassi, Y.; Telmanovna, Z. B.; Saule, M.; Kubanych, K., Microwave absorbing properties of ferrites and their composites: A review. *Journal of Magnetism and Magnetic Materials* **2021**, 529, 167839.
59. Kim, S.-S.; Kim, S.-T.; Yoon, Y.-C.; Lee, K.-S., Magnetic, dielectric, and microwave absorbing properties of iron particles dispersed in rubber matrix in gigahertz frequencies. *Journal of Applied Physics* **2005**, 97 (10).
60. Bartley, P. G.; Begley, S. B. In *A new technique for the determination of the complex permittivity and permeability of materials*, 2010 IEEE Instrumentation & Measurement Technology Conference Proceedings, 3-6 May 2010; 2010; pp 54-57.
61. Ebara, H.; Inoue, T.; Hashimoto, O., Measurement method of complex permittivity and permeability for a powdered material using a waveguide in microwave band. *Science and Technology of Advanced Materials* **2006**, 7 (1), 77.
62. Wang, H.; Xiang, L.; Wei, W.; An, J.; He, J.; Gong, C.; Hou, Y., Efficient and Lightweight Electromagnetic Wave Absorber Derived from Metal Organic Framework-Encapsulated Cobalt Nanoparticles. *ACS Applied Materials & Interfaces* **2017**, 9 (48), 42102-42110.

63. Cheng, J.; Zhang, H.; Ning, M.; Raza, H.; Zhang, D.; Zheng, G.; Zheng, Q.; Che, R., Emerging Materials and Designs for Low- and Multi-Band Electromagnetic Wave Absorbers: The Search for Dielectric and Magnetic Synergy? *Advanced Functional Materials* **2022**, 32 (23), 2200123.
64. Qin, M.; Zhang, L.; Wu, H., Dielectric Loss Mechanism in Electromagnetic Wave Absorbing Materials. *Advanced Science* **2022**, 9 (10), 2105553.
65. Somaratna, J.; Ravikumar, D.; Neithalath, N., Response of alkali activated fly ash mortars to microwave curing. *Cement and Concrete Research* **2010**, 40 (12), 1688-1696.
66. Abbas, S. M.; Dixit, A. K.; Chatterjee, R.; Goel, T. C., Complex permittivity, complex permeability and microwave absorption properties of ferrite–polymer composites. *Journal of Magnetism and Magnetic Materials* **2007**, 309 (1), 20-24.
67. Wang, L.; Li, X.; Li, Q.; Zhao, Y.; Che, R., Enhanced Polarization from Hollow Cube-like ZnSnO₃ Wrapped by Multiwalled Carbon Nanotubes: As a Lightweight and High-Performance Microwave Absorber. *ACS Applied Materials & Interfaces* **2018**, 10 (26), 22602-22610.
68. Giannakopoulou, T.; Kontogeorgakos, A.; Kordas, G., Single-layer microwave absorbers: influence of dielectric and magnetic losses on the layer thickness. *Journal of Magnetism and Magnetic Materials* **2003**, 263 (1), 173-181.
69. Liu, Y.; Zhao, K.; Drew, M. G. B.; Liu, Y., A theoretical and practical clarification on the calculation of reflection loss for microwave absorbing materials. *AIP Advances* **2018**, 8 (1).
70. Oh, J.-H.; Oh, K.-S.; Kim, C.-G.; Hong, C.-S., Design of radar

absorbing structures using glass/epoxy composite containing carbon black in X-band frequency ranges. *Composites Part B: Engineering* **2004**, 35 (1), 49-56.

71. Jayalakshmi, C. G.; Inamdar, A.; Anand, A.; Kandasubramanian, B., Polymer matrix composites as broadband radar absorbing structures for stealth aircrafts. *Journal of Applied Polymer Science* **2019**, 136 (14), 47241.

72. Zhao, Z.; Jia, Z.; Wu, H.; Gao, Z.; Zhang, Y.; Kou, K.; Huang, Z.; Feng, A.; Wu, G., Morphology-dependent electromagnetic wave absorbing properties of iron-based absorbers: one-dimensional, two-dimensional, and three-dimensional classification. *Eur. Phys. J. Appl. Phys.* **2019**, 87 (2), 20901.

73. Flohrer, S.; Herzer, G., Random and uniform anisotropy in soft magnetic nanocrystalline alloys (invited). *Journal of Magnetism and Magnetic Materials* **2010**, 322 (9), 1511-1514.

74. Liu, J.; Zhang, L.; Wu, H., Electromagnetic wave-absorbing performance of carbons, carbides, oxides, ferrites and sulfides: review and perspective. *Journal of Physics D: Applied Physics* **2021**, 54 (20), 203001.

75. Zhang, S.; Cheng, B.; Gao, Z.; Lan, D.; Zhao, Z.; Wei, F.; Zhu, Q.; Lu, X.; Wu, G., Two-dimensional nanomaterials for high-efficiency electromagnetic wave absorption: An overview of recent advances and prospects. *Journal of Alloys and Compounds* **2022**, 893, 162343.

76. Cheng, J.; Zhang, H.; Xiong, Y.; Gao, L.; Wen, B.; Raza, H.; Wang, H.; Zheng, G.; Zhang, D.; Zhang, H., Construction of multiple interfaces and dielectric/magnetic heterostructures in electromagnetic wave absorbers with enhanced absorption performance: A review. *Journal of Materiomics* **2021**, 7 (6), 1233-1263.

77. Yang, W.; Jiang, B.; Che, S.; Yan, L.; Li, Z.-x.; Li, Y.-f., Research

progress on carbon-based materials for electromagnetic wave absorption and the related mechanisms. *New Carbon Materials* **2021**, *36* (6), 1016-1030.

78. Cao, M.; Han, C.; Wang, X.; Zhang, M.; Zhang, Y.; Shu, J.; Yang, H.; Fang, X.; Yuan, J., Graphene nanohybrids: excellent electromagnetic properties for the absorbing and shielding of electromagnetic waves. *Journal of Materials Chemistry C* **2018**, *6* (17), 4586-4602.

79. Snoek, J. L., Dispersion and absorption in magnetic ferrites at frequencies above one Mc/s. *Physica* **1948**, *14* (4), 207-217.

Chapter 2. Introduction to Shape-Modulated Soft Magnetic Material as EWAM

2.1. Introduction to Soft Magnetic Material

2.1.1. Ferromagnetic Resonance in Soft Magnetic Material

When designing effective electromagnetic wave absorbers, ferromagnetic resonance frequency (F_{fmr}) is an important mechanism in order to maximize absorption of electromagnetic waves.⁵ Ferromagnetic resonance is a phenomenon that occurs in materials that exhibit ferromagnetism, such as iron, cobalt, and nickel.⁶ At the F_{fmr} , the magnetic moments in the magnetic material undergo precession around the direction of the applied magnetic field. This precession can be thought as a kind of oscillation, with a frequency that depends on the material's magnetic properties and the strength of the magnetic field.⁷ When an external electromagnetic wave is incident on the absorber material at F_{fmr} (if frequency of external electromagnetic wave matches the natural precession frequency of magnetization), the oscillating magnetic field of the wave interacts with the precessing magnetic moments of the material, causing maximum energy to be absorbed (see **Figure 2.1**).⁸ The F_{fmr} can be observed in the imaginary part of the complex permeability (see **Figure 2.2**).⁹ At frequencies below F_{fmr} , the imaginary part is comparably small, demonstrating that the material does not absorb EM waves strongly. As the frequency of the incident EM wave approaches the F_{fmr} , the imaginary part increases sharply, showing a stronger absorption of the wave. At the F_{fmr} itself, the imaginary part of the complex permeability reaches a maximum, indicating that the material is absorbing the wave very strongly. Beyond the F_{fmr} , the imaginary part decreases,

illustrating the diminishing of the absorbed wave. The F_{fmr} can be therefore identified in the imaginary part of the complex permeability as a sharp peak and this information is useful for designing EW absorbers that can effectively absorb specific frequencies of interest.¹⁰⁻¹¹

At F_{fmr} , the real part of the complex permeability of an absorbing material typically drops rapidly shown in **Figure 2.2**. This is because, at this point, the energy absorption is maximized, leading to a transfer of energy from the EM wave to the material.¹² This energy transfer causes the magnetic moments in the material to precess and align with the external magnetic field, resulting in a decrease in the effective magnetic permeability of the material. The drop in the real part is often more pronounced in magnetic materials with magnetic anisotropy, which exhibit a strong dependence on the angle between the magnetic moment and the externally applied magnetic field.¹³ This effect leads to a sharper drop in the real part at the F_{fmr} and a more distinct peak in the imaginary part, resulting in a stronger absorption of EW waves at the F_{fmr} . By controlling the magnetic anisotropy of the magnetic material, it is possible to tailor the absorption properties to specific frequencies and applications.¹⁴

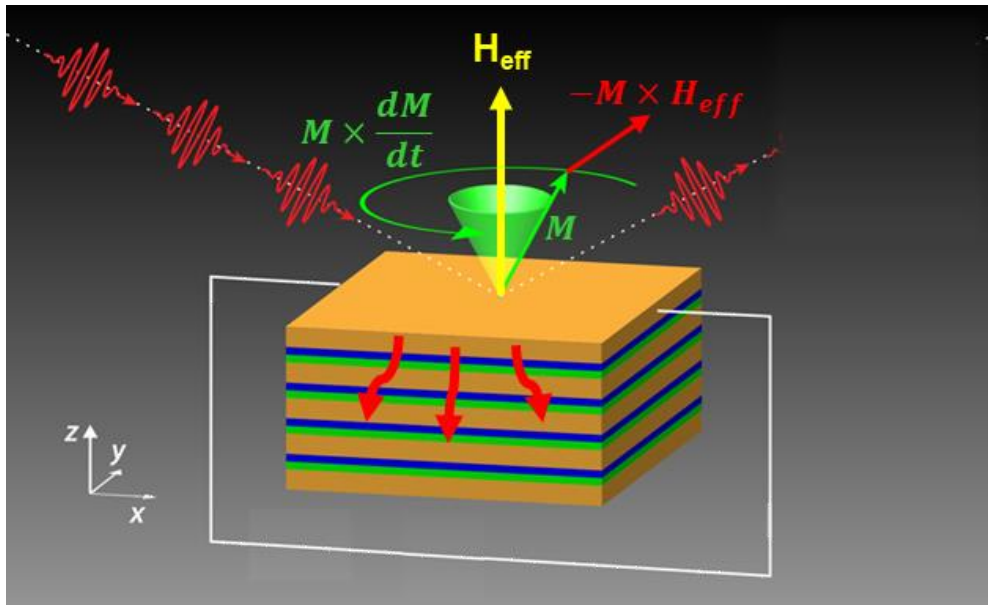


Figure 2.1. Schematic illustration of external EM wave incident on absorber material at ferromagnetic resonance frequency.

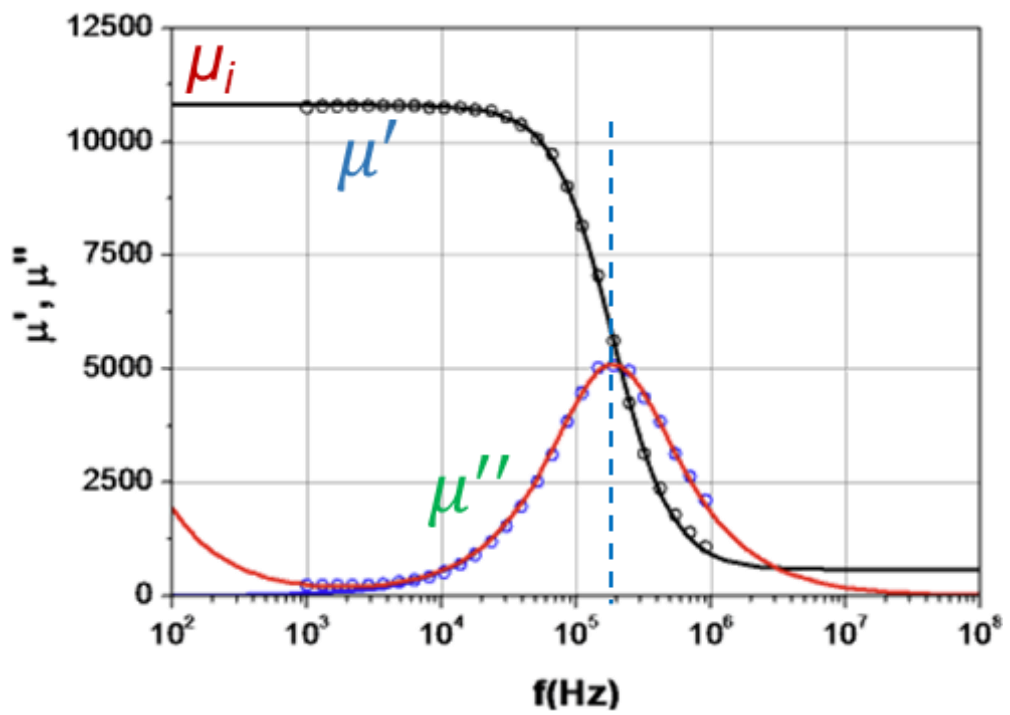


Figure 2.2. Real part of complex permeability shows a rapid drop and imaginary part shows a sharp peak at ferromagnetic resonance frequency, indicating maximum EM wave absorption.

2.2. Issues of Soft Magnetic Material for EM Wave Absorbers

2.2.1. 1st Issue: Limited Broadband Absorption

2.2.1.1. Limited Broadband Absorption in Soft Magnetic Materials

Although soft magnetic materials can be useful in EW absorbers due to their ability to efficiently store magnetic energy, there are some issues that can arise when using these materials in absorber applications. One of the main challenges is achieving broad bandwidth absorption. Soft magnetic materials typically have a narrow bandwidth of absorption, which limits their effectiveness in absorbing electromagnetic waves over a wide range of frequencies.¹⁵ Factors limiting wide-band absorption of the soft magnetic materials include the correlation between f_{FMR} and the coercivity of the material. As indicated in **Figure 2.3**, f_{FMR} is proportional to the coercivity of magnetic materials.⁴ Therefore, f_{FMR} of soft magnetic materials with small coercivity occur at a lower frequency compared to hard magnetic materials with large coercivity (see **Figure 2.4 (a)** and **(b)**). However, in soft magnetic materials, the ferromagnetic resonance spectrum typically has a long tail (see **Figure 2.4 (b)**), which arises due to the presence of spin waves. Spin waves are collective excitations of the magnetic moments in a material, which they propagate through the material, with their amplitude decaying over time due to various damping mechanisms. Spin waves are more perceptible in soft magnetic materials because they have a low magnetocrystalline anisotropy. This low magnetocrystalline anisotropy allows the magnetic moments of the electrons to move relatively easily, facilitating the propagation of spin waves. Such propagation of spin waves through the material gives rise to the presence of FMR tail, as the spectrum is closely related to the precession of spins in the material in response to a resonant electromagnetic

field.¹⁶ In contrast, hard magnetic materials have a high magnetocrystalline anisotropy, which means that the magnetization is strongly pinned along a particular direction. This makes it difficult for the magnetic moments to move and for spin waves to propagate.¹⁷ Thus, though hard magnetic materials exhibit its f_{FMR} peak at a higher frequency, the tail of the spectrum drops off rapidly with increasing frequency. Which makes it a more suitable candidate for absorbing materials requiring high absorption performance at high frequency range. Soft magnetic materials are more suitable for broadband absorption applications due to its f_{FMR} tail. Since soft magnetic materials exhibit a f_{FMR} at a low frequency, blue-shifting the ferromagnetic resonance peak and the tail can lead to broadband absorption at wider frequency ranges.

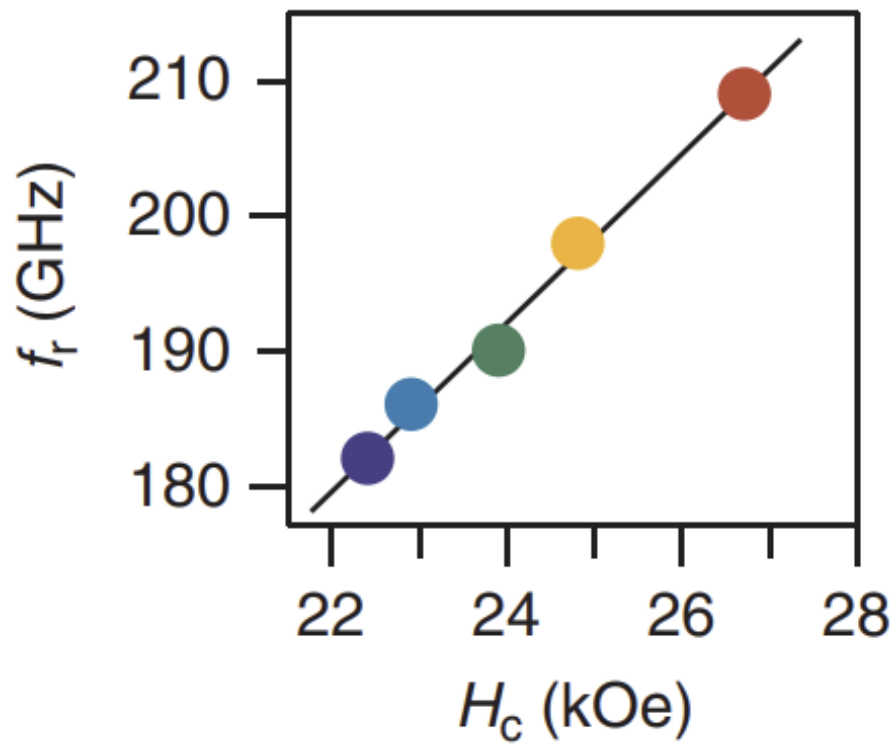


Figure 2.3. The ferromagnetic resonance frequency is proportionally related to the coercivity of the magnetic material. ⁴

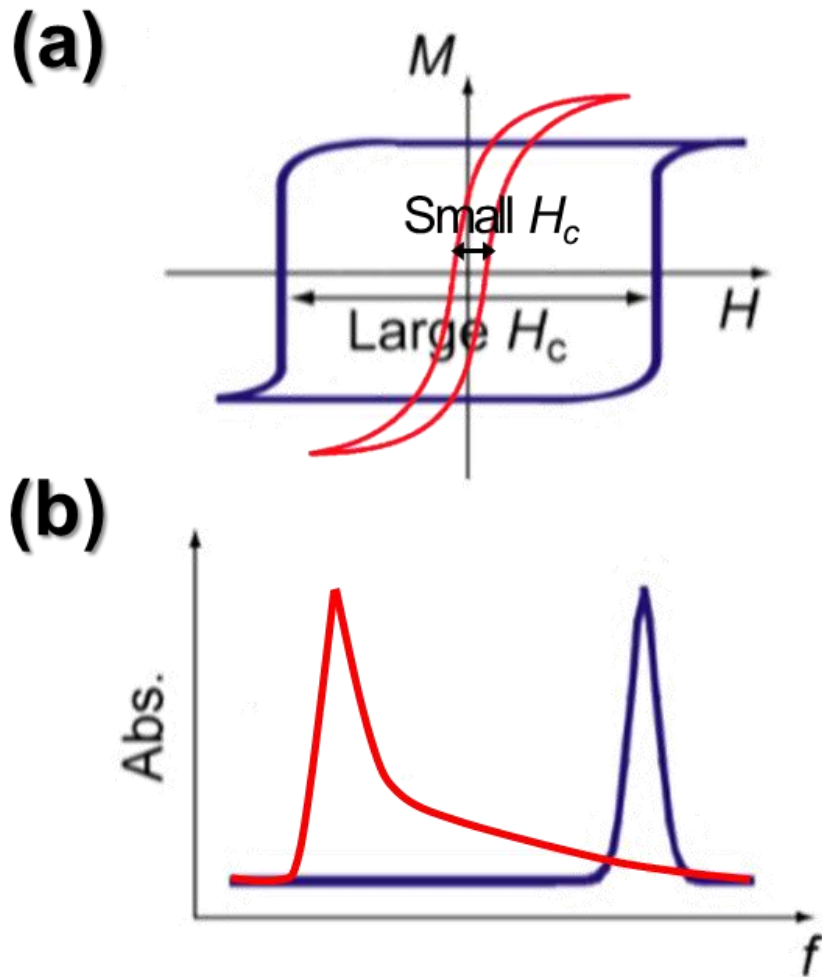


Figure 2.4. (a) Hysteresis loop of soft and hard magnetic material. (b) Ferromagnetic resonance peak of soft and hard magnetic material.

2.2.1.2. Why Do We Need Broadband EW Absorbers?

Broadband wave absorbers are essential in various applications including military and telecommunication applications. For example, in military applications, broadband wave absorbers are used in radar absorbing materials (RAMs) to minimize the amount of radar energy that is reflected back to the radar system.¹⁸ RAMs are used in objects such as Stealth aircraft to reduce the radar cross-section (RCS) of an object, making it less visible to radar systems.¹⁹ The RCS is a measure of how much radar energy is reflected back to the radar system when it is illuminated by radar waves.²⁰ Broadband wave absorbers are commonly used in stealth aircraft to reduce their RCS and make them less detectable by radar. Though stealth aircraft are designed to have a low RCS, several techniques can be used to detect it. One approach is to use multiple radar systems operating at different frequencies and from different angles.²¹⁻²² But, if a stealth aircraft is capable of absorbing radars with a wide range of frequencies as seen in **Figure 2.5 (b)**, then it reduces the amount of radar energy reflected back to the radar system, making the aircraft less visible.²³⁻²⁴ **Figure 2.5 (a)** illustrates the opposite situation, where the stealth aircraft only absorbs the radar with a shorter wavelength while reflecting back the radar with longer wavelength, which makes it possible to provide a more complete picture of the aircraft's RCS. Overall, broadband wave absorbers are an essential component of RAMs because they can effectively absorb a wide range of frequencies, reducing the RCS of an object and making it less visible to radar systems.

In addition to military applications, broadband wave absorbers are also used in other areas, such as telecommunications,²⁵ where they can be used to reduce unwanted electromagnetic interference²⁶ and improve signal quality.²⁷ For example, cell phones receive signals that are composed of series of radio waves. Cell phones

and other wireless communication devices operate using binary code and multiple channels with different frequencies as seen in **Figure 2.6**.²⁸ Each channel can support a certain amount of data transmission, and different frequencies can be used for different types of communication. For instance, the electromagnetic spectrum incident on the phone is broken up into many different channels, with each channel having a specific wavelength for a 1, and another for a 0. Channel 38, for example, can have a frequency of 2.44387 GHz for a 1 and 2.44313 GHz for a 0 while channel 54 can have 2.42987 GHz for a 1 and 2.42913 GHz for a 0. When a channel is crowded by other users, cell phones use frequency hopping to improve signal quality and reduce interference.²⁹ As the phone rapidly switches between many different frequencies, it wants to avoid interference from the remaining frequencies, therefore requiring a broadband EW absorber.

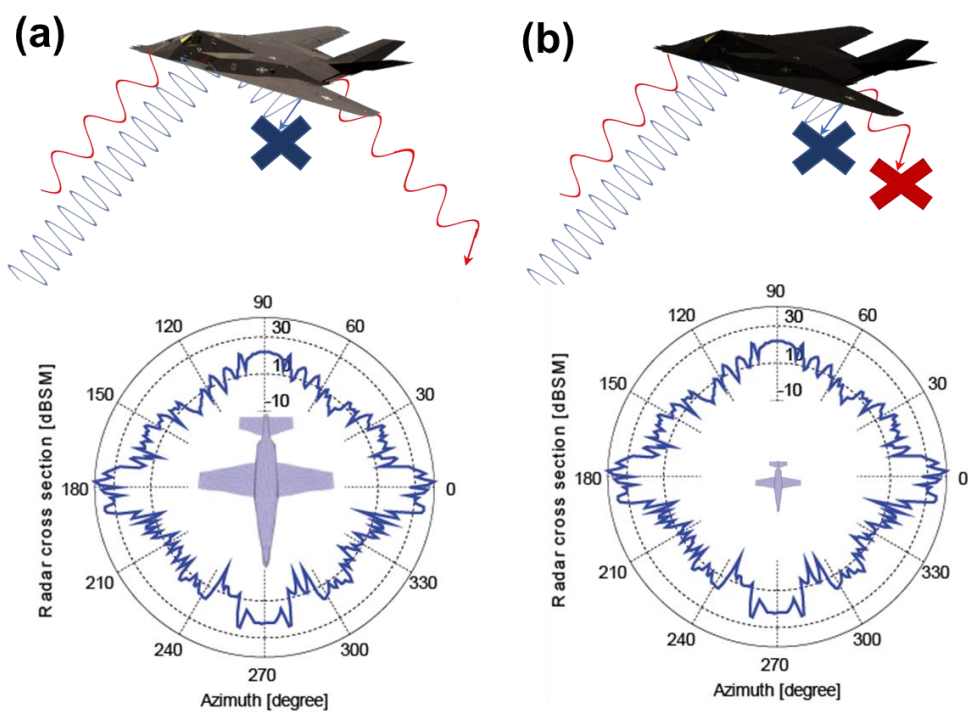


Figure 2.5. Schematic illustration of stealth aircraft absorbing (a) frequency of only long wavelength and (b) frequency of both short and long wavelength.

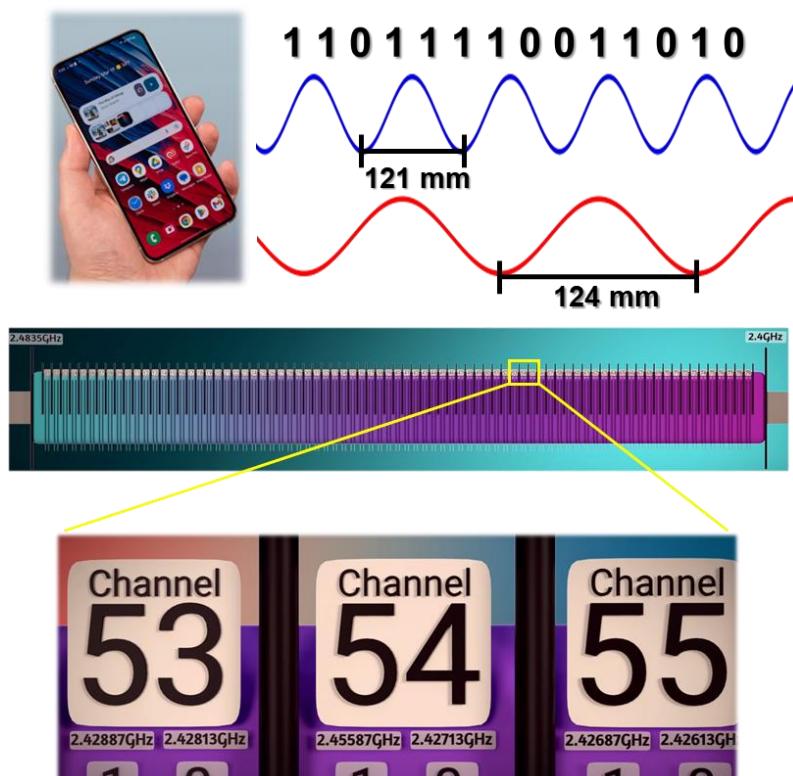


Figure 2.6. Illustration of cell phone using various frequencies. Cell phones and other wireless communication devices operate using binary code and multiple channels with different frequencies

2.2.1.3. For broadband Absorption: What can be controlled?

Enhancing the Initial Permeability and Ferromagnetic Resonance Frequency

As mentioned previously, initial permeability and f_{FMR} are the two important factors that can affect the electromagnetic wave absorption performance. By enhancing the initial permeability and by blue-shifting the f_{FMR} (see **Figure 2.7**), the real part and the imaginary part of the complex permeability can be improved and thus give rise to a broadband electromagnetic wave absorbing material.

In order to improve the above two factors, material selection at specific bands in the radio wave spectrum is important. Different bands in the radio wave spectrum use different materials for electromagnetic wave absorption because the frequency of the EW determines the type of materials that are most effective for absorbing them. In high frequency bands, from 26 to 40 GHz, also called the Ka band, uses hard ferrites as the absorbing material because of the reasons explained in section 2.2.1.1.³⁰ Bands such as L, S, C, X, Ku, and K (1 GHz to 26 GHz) utilizes soft magnetic materials as absorbing materials.³¹ The relationship between initial permeability and f_{FMR} can be expressed by Snoek's law, which is a fundamental limitation that arises from the fact that the magnetic properties of a material are determined by the way in which its magnetic moments interact with each other:³²

$$(\mu_i - 1)f_{\text{FMR}} = \frac{\gamma}{2\pi} M_s \quad (6)$$

Where γ = gyromagnetic constant

M_s = Saturation magnetization

The initial permeability and f_{FMR} is very limited in this equation as the left-side of equation 6 is generally equal to a constant depending on the magnetization of the

material. Therefore, in order to increase the left-side of the equation, techniques such as shape anisotropy³³ are used, which adds an anisotropic parameter to the equation, which will be explained in the next section.

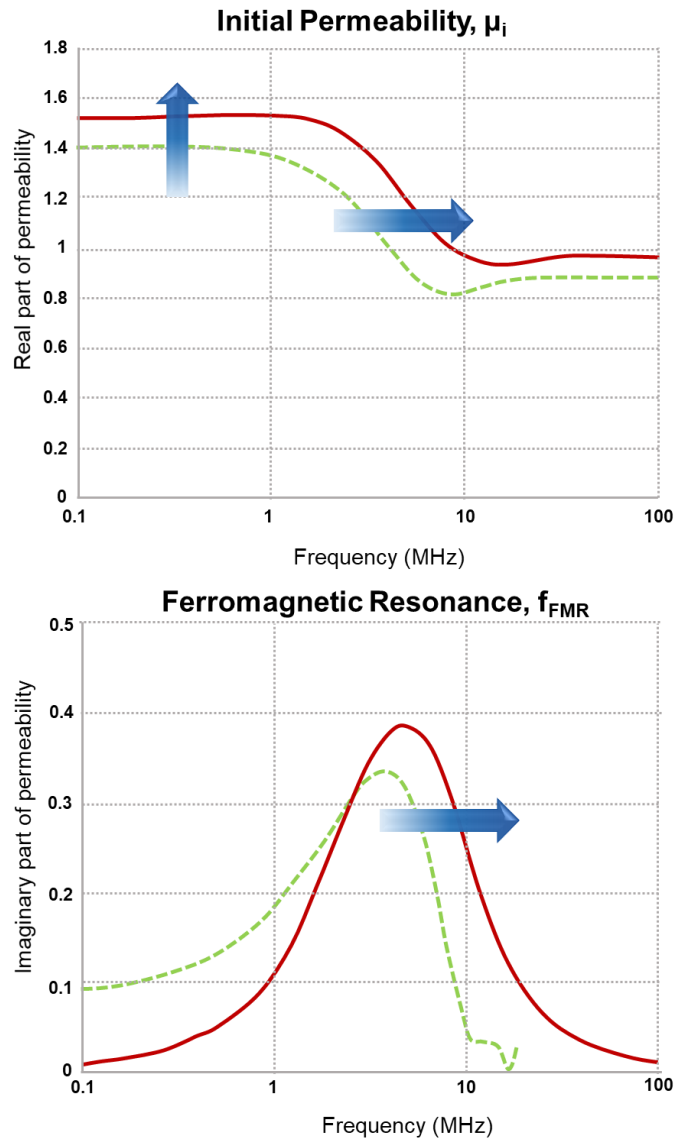


Figure 2.7. Enhancing the initial permeability and blue-shifting the ferromagnetic resonance frequency will improve the absorption behavior.

2.2.1.4. Theoretical Consideration of Magnetic Anisotropy

Shape-modulation is one of the important techniques that give rise to magnetic anisotropy in magnetic materials. Magnetic anisotropy is the property of a magnetic material that causes it to have a preferred direction of magnetization.³⁴ This means that the material will be more easily magnetized in one direction than in others. The easy axis is the direction in which magnetic moments of the material align most easily.³⁵ It is often the direction with the lowest energy barrier for magnetization, and therefore the direction in which the material is most likely to be magnetized. The hard axis, on the other hand, is the direction in which the magnetic moments of the material are most difficult to align. It is often the direction with the highest energy barrier for magnetization, and therefore the direction in which the material is least likely to be magnetized.³⁶ The distinction between the easy axis and hard axis is important because it can determine the behavior of the material in response to an external magnetic field.³⁷ For example, if a magnetic material has a strong easy axis, it will tend to align with an external magnetic field in that direction, whereas if it has a strong hard axis, it will tend to resist alignment with the external magnetic field (see **Figure 2.8**).³

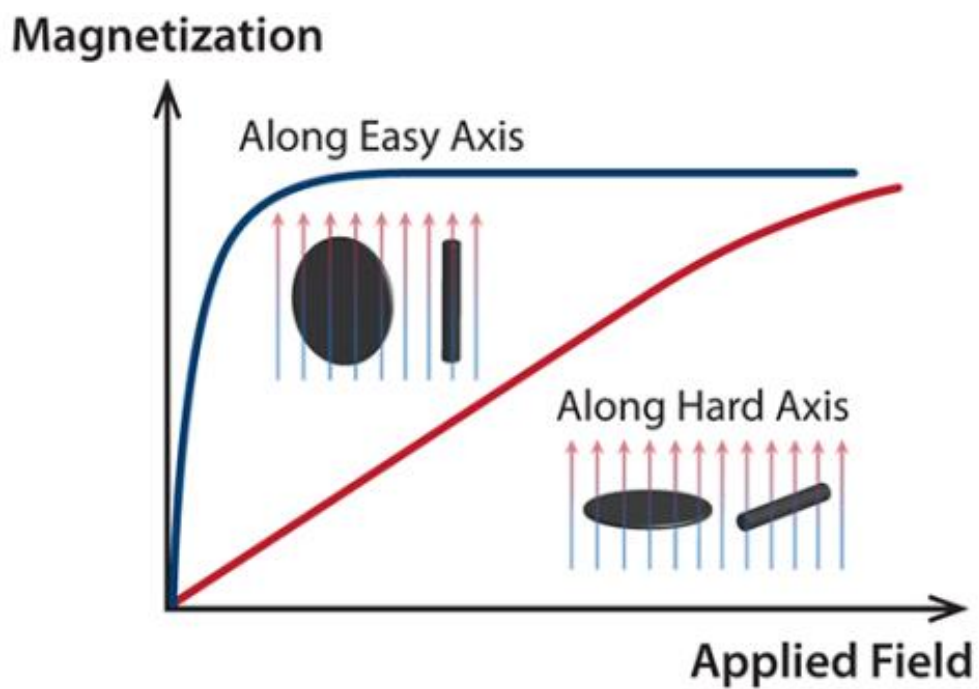


Figure 2.8. Magnetic material with a strong easy axis will tend to align with an external magnetic field in that direction, where whereas if it has a strong hard axis, it will tend to resist alignment with the external magnetic field.³

2.2.1.5. Snoek's Limit and Shape Anisotropy

In magnetic materials, a demagnetizing field arises due to the magnetization of the material itself. When a magnetic material is magnetized, the magnetic poles induced on the opposite sides of the material generates an internal field opposing the external field. This self-created field is called the demagnetizing field, H_d and can be expressed as $H_d = -NM$ (see **Figure 2.9**).³⁸⁻³⁹ The demagnetizing field can be quantified by a demagnetizing factor, which depends on the shape of the magnetized object. The factor can be expressed by three orthogonal directions, usually denoted as N_x , N_y , N_z . The three directions add up to 1, $N_x + N_y + N_z = 1$. When the induced poles have a small separation, strong H_d is generated resulting in a large demagnetizing factor close to 1. When the poles are separated largely, weak H_d is generated giving rise to a small demagnetizing factor close to 0. The demagnetizing field reduces the actual field experienced by the material, lowering the total magnetization.⁴⁰

The Kittel equation describes the f_{FMR} of a ferromagnetic material by relating the resonant frequency of the material to the applied magnetic field and the magnetic properties of the material. The f_{FMR} of a magnetic material without any anisotropy is given by the following equation:⁴¹

$$f_{\text{FMR}} = \frac{\gamma}{2\pi} \mu_o H_{\text{ext}} \quad (7)$$

Where μ_o = vacuum permeability = $4\pi \times 10^{-7}$ H/m

H_{ext} = applied external magnetic field

The Landau-Lifshitz-Gilbert (LLG) equation is a partial differential equation that describes the dynamics of magnetization in a magnetic material under the influence of an external magnetic field. The LLG equation can be used to model the behavior

of magnetic materials under a wide range of conditions, including those involving changes in applied magnetic field. By deriving and solving the complicated LLG equation, initial permeability under external field of H_{ext} can be written as:⁴²

$$\mu_i - 1 = \frac{M_s}{H_{ext}} \quad (8)$$

When equations 7 and 8 are multiplied, an expression for both initial permeability and f_{FMR} can be found in the following equation, which is also known as the Snoek's limit:

$$(\mu_i - 1)f_{FMR} = \frac{\gamma}{H_{ext}} M_s \quad (8)$$

Snoek's limit provides a theoretical upper bound on the f_{FMR} and the permeability of a magnetic material at high frequencies. The limit suggests that high μ_i and high f_{FMR} cannot be reached simultaneously due to the constants on the right hand side of the equation, but can be raised by introducing shape anisotropy to the equation. Initial permeability and f_{FMR} of magnetic material with shape anisotropy can be re-written as the modified Snoek's limit:⁴³

$$(\mu_i - 1)f_{FMR} = \frac{\gamma}{2\pi} \sqrt{\frac{H_\theta}{H_\phi}} M_s \quad (8)$$

Where H_θ = effective field in-plane

H_ϕ = effective field out-of-plane

The modified Snoek's limit now depends on both the in-plane and out-of-plane components of the effective magnetic field. If the effective field in-plane is much larger than the field out-of-plane, both μ_i and f_{FMR} can be raised, which can be done by shape modulation of the magnetic material.

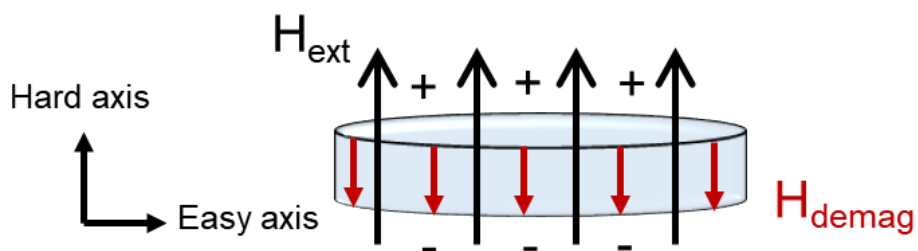


Figure 2.9. When a magnetic material is magnetized, the magnetic poles induced on the opposite sides of the material generates an internal field opposing the external field, called the demagnetizing field, H_d

2.2.1.6. Phase Diagram of FeCo and Slater-Pauling Rule

Two factors of the modified Snoek's limit can be set as a variable. The first factor is the saturation magnetization value. Using a magnetic material with high saturation magnetization will enhance the initial permeability and f_{FMR} according to equation 7. According to the Slater-Pauling rule in **Figure 2.10**, the magnetic moment of transition metal alloys can be estimated based on the electron configuration of the constituent elements. The magnetic moment of elements near Ni depend on (3d + 4s) electrons/atom, expressed in the following equation:⁴⁴⁻⁴⁵

$$\mu_H = (10.6 - n)\mu_B \quad (8)$$

Both Fe and Co are transition metals with unpaired electrons in their 3d orbitals, which contribute significantly to their magnetic properties. When these elements combine to form an alloy, the unpaired 3d electrons can interact and align their magnetic moments resulting in a higher total magnetic moment compared to the individual elements. When the cobalt contents is very small in the FeCo alloy, the atoms are randomly arranged in the disordered α -phase in the corners and centers of the cubic cell (see **Figure 2.11**).⁴⁶ As the cobalt contents increases, the crystal structure transitions to a ordered α' -phase, which has the CsCl structure. At this phase, Fe atoms arrange themselves in the corner and the Co atoms in the center of the cubic cell. This ordering produces an increase in the saturation magnetization as

shown in **Figure 2.12**.⁴⁷

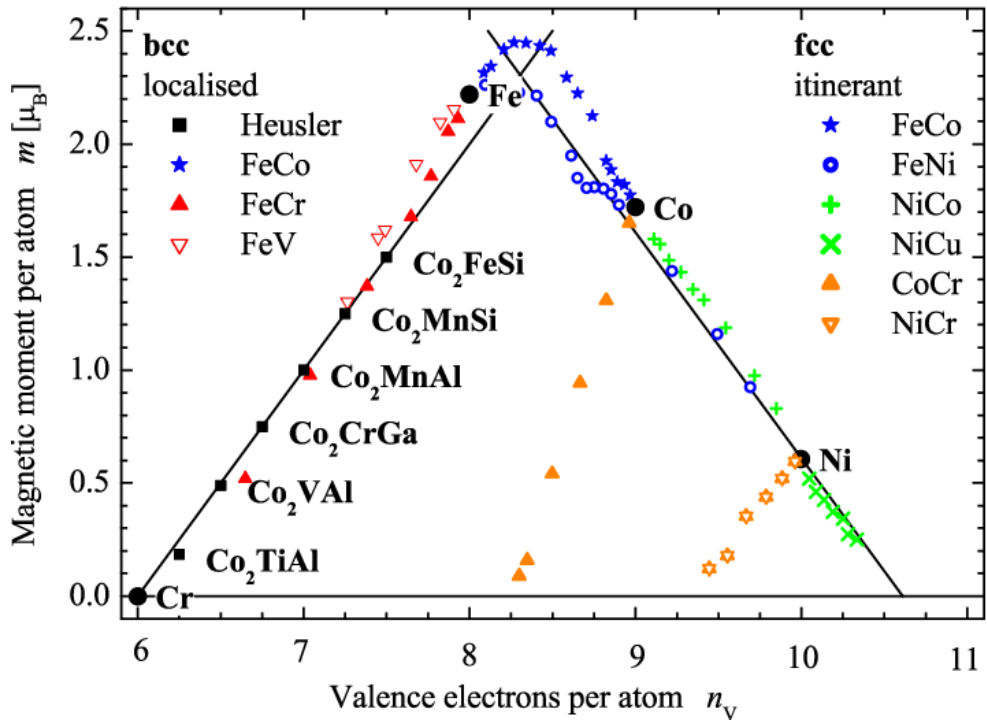


Figure 2.10. According to the Slater-Pauling rule, the magnetic moment of transition metal alloys can be estimated based on the electron configuration of the constituent elements.

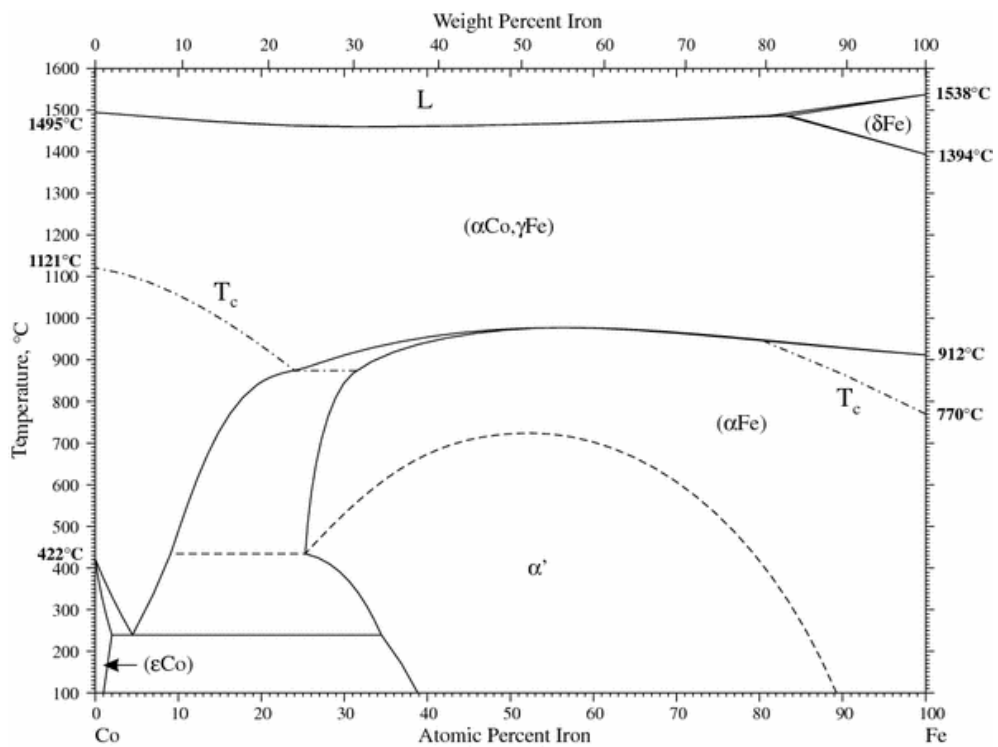


Figure 2.11. Phase Diagram of FeCo alloy.

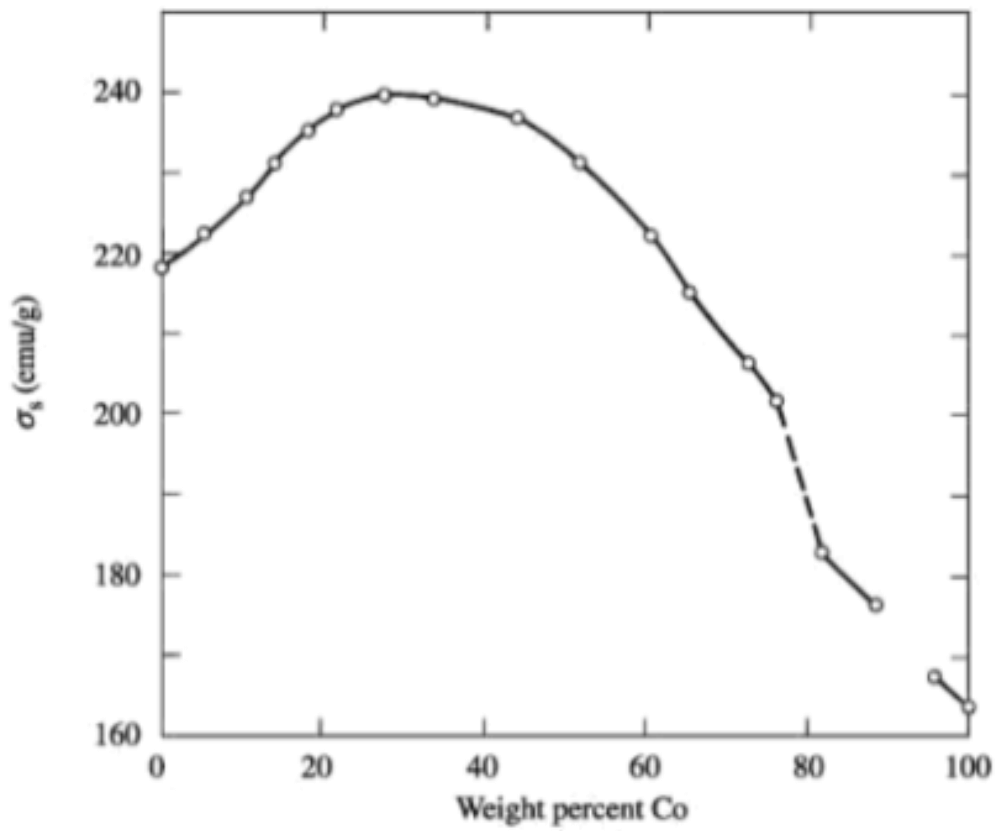


Figure 2.12. As the cobalt contents increases, the crystal structure of α -FeCo transitions to a ordered α' -phase and this ordering produces an increase in the saturation magnetization.

2.2.1.7. Shape Anisotropy of Magnetic Material

The second factor is the effective anisotropic fields, $\sqrt{H_\theta/H_\phi}$. As mentioned in section 2.2.1.4, the precession of magnetization around the easy axis can be influenced by the anisotropy fields acting on the magnetization. The shape anisotropy arises due to the shape of the magnetic material, such as elongated particles or thin films. The shape anisotropy tends to align the magnetization along the longest dimension of the material. As seen in **Figure 2.13**, a magnetic sphere experiences zero shape anisotropy, therefore $H_\theta = H_\phi$. For a magnetic rod, magnetization deviates into the easy plane, resulting in $H_\theta > H_\phi$. This means that the anisotropy field that tends to align magnetization tangentially within the easy plane is stronger than the anisotropy field that tries to force the magnetization to align perpendicular to the plane. The relative strengths of these anisotropy fields determine the preferred orientation of the magnetization within the magnetic rod. Overall, the large saturation magnetization value and effective anisotropy field generated from shape modulation are critical factors to increase the initial permeability and f_{FMR} .

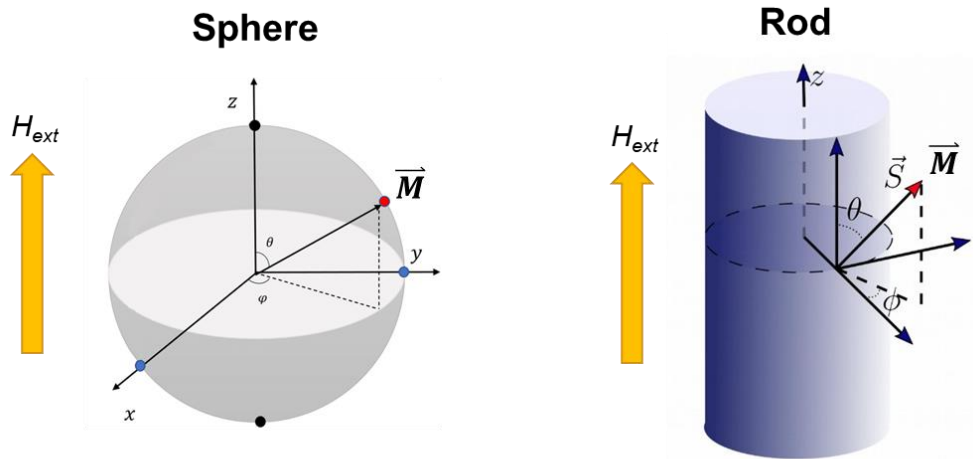


Figure 2.13. A magnetic sphere experiences zero shape anisotropy, therefore $H_{\theta} = H_{\phi}$. For a magnetic rod, magnetization deviates into the easy plane, resulting in $H_{\theta} > H_{\phi}$.

2.2.1.8. State-of-the-Art (SOA) of 1st Issue: Shape-Modulated FeCo Nanomaterials

Shape modulation of magnetic materials has emerged as a promising approach for the development of EWAMs with enhanced properties. By controlling the shape of magnetic particles, it is possible to enhance their magnetic anisotropy, complex permeability, and thus the absorbing properties. The state-of-the-art in this field includes the exploration of various approaches to control the shape of magnetic particles. The magnetic material in this section will be focused on shape modulation of FeCo alloys tailored for use in EW absorbers. Recent studies have shown that the shape of magnetic particles plays a crucial role in determining the electromagnetic properties of EWAMs and can be synthesized through different methods. For example, Zhang et al. fabricated FeCo nanochains assembled within the polyvinylpyrrolidone (PVP) polymer matrix via wet-chemical process under an external magnetic field (SmCo magnet, ~ 0.5 T). The FeCo/PVP nanochains show a real permeability value of approximately 1.6 at 2 GHz, which decreases over the increasing frequency. The electromagnetic absorbing bandwidth (EAB) of the FeCo/PVP nanochain turns out to be approximately 2 GHz at thickness of 2 mm.⁴⁸ Cui et al. also successfully fabricated FeCo/PVP core-shell nanochains@GO composite through a similar wet chemical process under external magnetic field. The real permeability has a value of 1.25 at 2 GHz with an EAB of 4.9 GHz at thickness of 2 mm.⁴⁹ Despite these advancements, there are still challenges in synthesizing 1-dimensional FeCo nanomaterials due to its crystal growth behavior, which is why external magnetic field is used to diffuse individual FeCo particles into a long chain. However, external magnets used during the wet-chemical method is very limited due to the lacking strength of the externally created magnetic field and the viscous media,

which creates weak binding between the FeCo particles.

2.2.1.9. Issues to be solved – 1st Issue

Overall, soft magnetic materials are widely used in EW absorbing applications including RAMs and telecommunications. One of the critical properties required for many of these applications is broad-band absorption, which refers to the ability of the material to absorb energy over a wide range of frequencies. Achieving broad-band absorption in soft magnetic materials without anisotropy is challenging, as it requires a balance between the μ_i and the f_{FMR} according to the Snoek's law. Moreover, the small μ_i and the f_{FMR} affects the absorbing performance of the material due to lack of magnetic anisotropy. Therefore, there is a need for innovative solutions to address these issues by developing shape-modulated soft magnetic material to enhance the μ_i and the f_{FMR} through a new route that is distinguishable from the former wet-chemical method.

To solve the 1st issue, in this study, 1-dimensional FeCo nanochains are fabricated based on a dry method, which involves the modification nanoparticles in a gas phase. The fabrication and application of FeCo nanochains as EWAMs will be discussed in Part II of Chapter 3. Additionally, the as-synthesized FeCo nanochains are further modified into a 2-dimensional belt-like structure in order to further enhance the μ_i and the f_{FMR} , and consequently proving the Snoek's Law. The fabrication and application of FeCo nanobelts as EWAMs will be discussed in Part II of Chapter 4 (See **Figure 2.14**).

Part II
Chapter 3
0D-1D hybrid
FeCo nanochain



Part II
Chapter 4
1D-2D hybrid
FeCo nanobelt



Figure 2.14. Schematic illustration of FeCo nanochains and nanobelts covered in Part II, Chapter 3 and 4 respectively.

2.2.2. 2nd Issue: High Viscosity of Nanomaterials

2.2.2.1. Limited Loading Ratio of Filler Material

In EW absorbers, the loading ratio of filler material refers to the proportion of the filler material added to the composite structure.⁵⁰ The filler material is typically the magnetic and dielectric materials mentioned previously that is added to enhance the absorption properties of the composite. The loading ratio of the filler material is an important parameter that affects the performance of the EW absorber. Generally, a higher loading ratio of filler material results in increased absorption of electromagnetic waves, as the filler material can interact more strongly with the incoming waves.⁵¹ As complex permeability of a composite material is a measure of the ability of the material to store magnetic energy in the presence of an external magnetic field, increasing the loading ratio of filler material in a composite can increase the complex permeability as seen in **Figure 2.15**.²

Recently, nanomaterials have been attractive as filler materials because of their small size and large surface area-to-volume ratio, which generates more active chemical sites for dielectric/magnetic interaction and thus enables them to efficiently absorb electromagnetic radiation in a thin layer.⁵²⁻⁵³ Moreover, the use of nanomaterials in thin EW absorbers can also lead to improved mechanical and thermal properties, such as increased strength, flexibility and thermal stability. However, nanomaterials can have high viscosity due to their small size and large surface area-to-volume ratio, which can result in strong interparticle forces and surface effects that contribute to high viscosity. At the nanoscale, the surface area of particles becomes a significant proportion of their total volume. This means that the surface atoms or molecules of nanoparticles are more exposed and can interact more strongly with other particles or the surrounding medium, resulting in stronger

interparticle forces. These interparticle forces, such as Van der Waals forces, electrostatic forces, and steric hindrance, can cause nanoparticles to agglomerate and form clusters, which can increase their viscosity. The high viscosity of nanomaterials can pose challenges in their processing and handling, especially when used as filler materials in EW absorbers. The high viscosity causes difficulty in increasing the loading ratio of the filler material in the matrix material. Shape modulation of nanomaterials can help in reducing their viscosity. Viscosity of a suspension depends on the shape of the particle where particle movements are affected by the rotational and translational abilities. Uniform spherical particles have a symmetrical shape and can rotate freely about their own axis, resulting in lower viscosity. Platy or rod-like particles have anisotropic shapes and require an area comparable to the length of their longest axis. When platy or rod-like particles are packed closely together, their contact areas can be larger, resulting in stronger interparticle interactions and increased viscosity (See **Figure 2.16**).¹ Therefore, in order to reduce the viscosity of platy or rod-like particles, it is important to ensure that there is sufficient spacing between them.

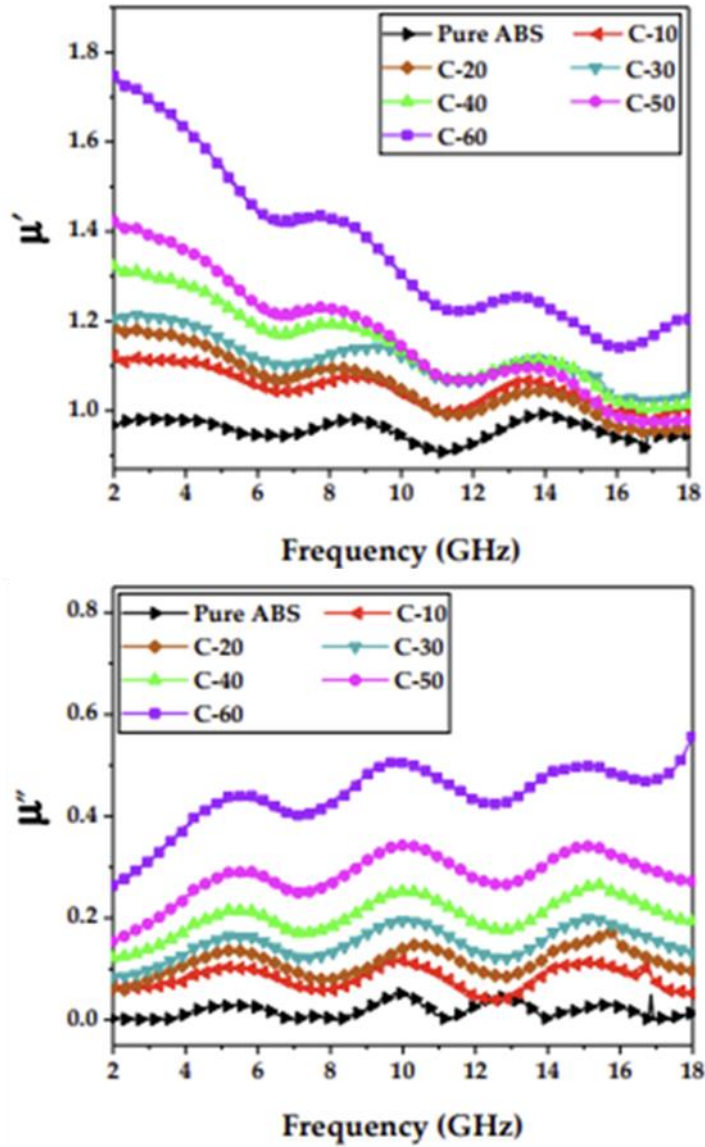


Figure 2.15. Complex permeability of an EWAM. Increasing the loading ratio of filler material in a composite can increase the complex permeability.²

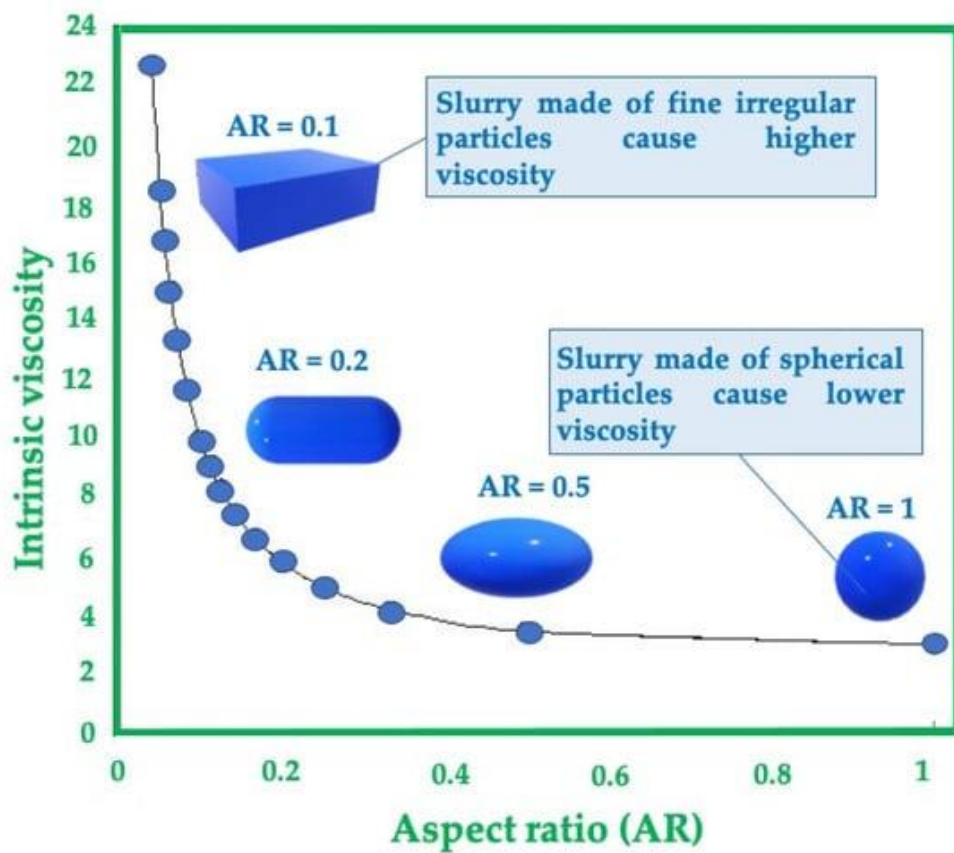


Figure 2.16. Graph of intrinsic viscosity vs. aspect ratio of nanomaterials. Viscosity increases with decreasing aspect ratio.¹

2.2.2.2. State-of-the-Art (SOA) of 2nd Issue

The loading ratio of filler material in EW absorbers is an essential parameter that affects the absorber's performance. As mentioned in **Figure 2.15**, by increasing the magnetic filler material in the EW absorber (in this case, carbonyl iron powder), the complex permeability value increases dramatically, which enhances the absorbing performance of the absorber. However, because of the high viscosity of the nanomaterials, the loading ratio of filler material of soft magnetic materials are very limited as shown in **Table 2.1**.⁵⁴⁻⁵⁵ As shown in the table, the loading ratio of the different studies generally reaches up to only 40 to 50%. When the loading factor is increased beyond 50%, the processing of the composite becomes difficult as the suspension of the composite becomes very viscous, making it difficult to cast into a very thin composite film.

Table 2.1. List of Researches Using Soft Magnetic Materials as Filler Material.

Absorbing material	Reflection Loss (dB)	Frequency (GHz)	Thickness (mm)	Loading factor (%)
Porous Co/C nanocomposite	-35.3	6	4.0	40
Co/CNTs nanohybrid	-49.16	14.2	2.5	30
Co/C composite	-32.4	12.0	2.0	30
Co@CNTs	-48	13.2	2	30
Co@C nanofiber	-40	7.1	2.4	50
Fe₃O₄/carbon fiber mat	-47	10.0	2.5	30

2.2.2.3. Issues to be solved – 2nd Issue

The loading ratio of filler material in EW absorbers is a critical parameter that significantly affects the absorber's performance. An optimal loading ratio can improve the absorber's complex permeability, and thus improve the absorbing performance. Yet there is a limit to dramatically increasing the loading ratio because of the high viscosity of nanomaterials. Therefore shape modulation of soft magnetic material can be used to reduce the viscosity of the nanomaterial. However, it is important to maintain a high complex permeability value even after undergoing shape modulation of the magnetic material. In order to achieve high complex permeability value and also reduce the viscosity of the nanomaterial simultaneously, a new route of fabrication is introduced in Part II of Chapter 5 as seen in **Figure 2.17**. In this Chapter, a composite containing hybrid FeCo particle with high complex permeability and low viscosity is synthesized. The newly developed hollow FeCo particle not only possesses a low viscosity owing to its hollow 0-dimensional structure, but also maintains a high complex permeability value owing to its 1-dimensional channels interconnecting to form the hollow spherical structure.

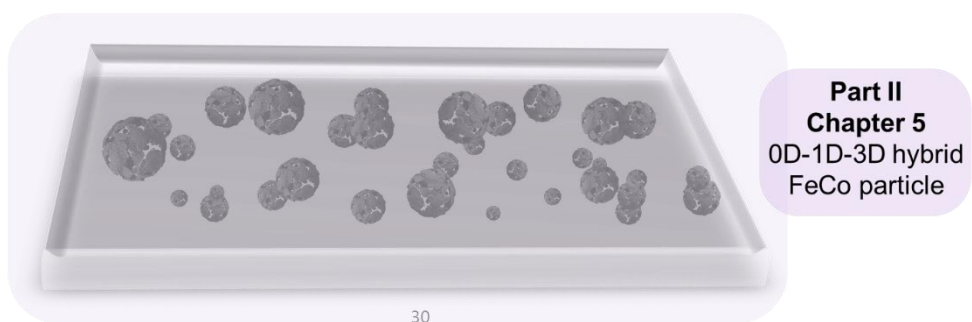


Figure 2.17. Schematic illustration of hollow FeCo particles covered in Part II pf Chapter 5.

2.2.3. 3rd Issue: Long-time Exposure to Radiation

2.2.3.1. Theoretical Consideration of Thermal Dissipation

Electromagnetic wave absorbers are inevitably exposed to electromagnetic radiation for long periods of time, which can cause overheating of EW absorbers in certain situations.⁵⁶ The degree of overheating depends on the frequency, intensity, and duration of the radiation exposure, as well as the characteristics of the absorber material itself. When EM radiation is absorbed by the absorber, the energy of the radiation is converted into heat energy. However, if the absorber material is unable to dissipate this heat effectively, it can become overheated, which can lead to degradation, reduced performance, or even failure of the material.⁵⁷

To prevent overheating, it is important to optimize the design of the absorber material itself to improve its thermal properties, such as its thermal conductivity or specific heat capacity.⁵⁸ Generally, when magnetic materials with high electrical conductivity are used in EW absorbers, various dielectric materials are also considered to control the complex permittivity of the absorber material. When selecting the dielectric material, it is important to select a material with appropriate dielectric properties as well as thermal conductivity properties.

2.2.3.2. Issues to be solved – 3rd Issue

Dielectric materials are materials that do not conduct electricity easily, but can store electrical energy in an electric field. They have a high resistance to the flow of electric charge. When an EM wave passes through a dielectric material, it induces an electric field within the material, causing charges to accumulate on its surface. The accumulated charges must rearrange themselves with the changing electric field, and the rearrangement requires energy, which is lost in the form of heat. The heat generated through dielectric loss can cause the temperature of the material to increase, therefore heat dissipating materials with high thermal conductivity are needed in EW absorbers to prevent the material from overheating. Thermal conductivity is a measure of a material's ability to conduct heat. Materials with high thermal conductivity can transfer heat away from the absorbed electromagnetic waves more quickly, reducing the likelihood of heat buildup and improving the overall performance of the absorber. Common heat dissipating materials used in EW absorbers include metals such as aluminum and copper, ceramic materials such as alumina and silicon carbide, and matrix materials such as silica and epoxy.⁵ The choice of heat dissipating material will depend on the specific application and the desired level of performance.

In this study, a matrix material is required in order to control the complex permittivity of the network-like magnetic material. Due to the inter-connection generated by the chain-like magnetic material, the electrical conductivity is inevitably increased, which over-enhances the complex permittivity. Therefore, selecting a dielectric material with appropriate dielectric properties and thermal conductivity is important for balancing the absorbing and thermal dissipation properties of an EW absorber. Here, boron nitride is used as a dielectric material

owing to the combination of its high thermal conductivity and excellent dielectric properties, which make it a good choice for EW absorbers that require both efficient heat dissipation and EW absorption (see **Figure 2.18**)⁵⁹. The incorporation of boron nitride nanoparticles in the FeCo nanomaterials is covered in Part II of Chapter 4 and Chapter 5 as seen in **Figure 2.19**.

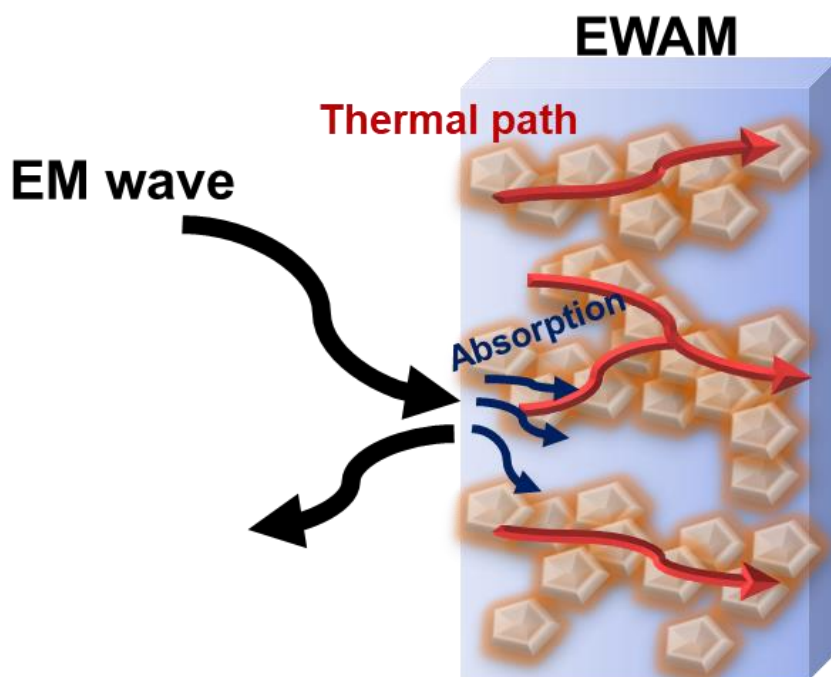


Figure 2.18. Schematic illustration of EWAM with good absorbing and heat dissipating performance.

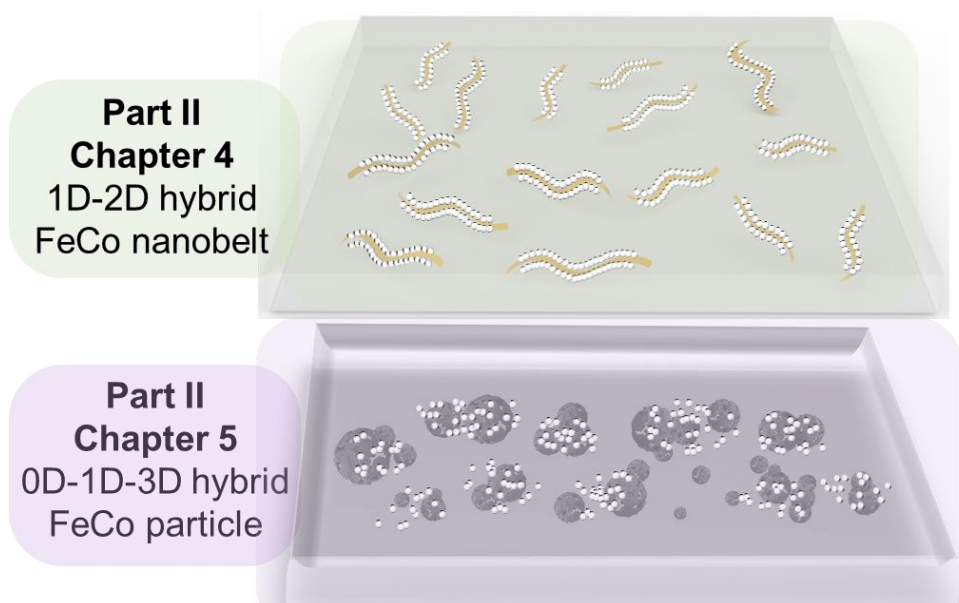


Figure 2.19. The incorporation of boron nitride nanoparticles in the FeCo nanomaterials is covered in Part II of Chapter 4 and Chapter 5.

2.3. References

1. Ulusoy, U., A Review of Particle Shape Effects on Material Properties for Various Engineering Applications: From Macro to Nanoscale. *Minerals* **2023**, *13* (1), 91.
2. Lai, W.; Wang, Y.; He, J., Effects of Carbonyl Iron Powder (Cip) Content on the Electromagnetic Wave Absorption and Mechanical Properties of Cip/Abs Composites. *Polymers* **2020**, *12* (8), 1694.
3. Kim, Y.; Zhao, X., Magnetic Soft Materials and Robots. *Chemical Reviews* **2022**, *122* (5), 5317-5364.
4. Namai, A.; Yoshikiyo, M.; Yamada, K.; Sakurai, S.; Goto, T.; Yoshida, T.; Miyazaki, T.; Nakajima, M.; Suemoto, T.; Tokoro, H.; Ohkoshi, S.-i., Hard Magnetic Ferrite with a Gigantic Coercivity and High Frequency Millimetre Wave Rotation. *Nature Communications* **2012**, *3* (1), 1035.
5. Bai, H.; Yin, P.; Lu, X.; Zhang, L.; Wu, W.; Feng, X.; Wang, J.; Dai, J., Recent Advances of Magnetism-Based Microwave Absorbing Composites: An Insight from Perspective of Typical Morphologies. *Journal of Materials Science: Materials in Electronics* **2021**, *32* (21), 25577-25602.
6. Rouhi, M.; Hajizadeh, Z.; Taheri-Ledari, R.; Maleki, A.; Babamoradi, M., A Review of Mechanistic Principles of Microwave Absorption by Pure and Composite Nanomaterials. *Materials Science and Engineering: B* **2022**, *286*, 116021.
7. Elmahaishi, M. F.; Azis, R. a. S.; Ismail, I.; Muhammad, F. D., A Review on Electromagnetic Microwave Absorption Properties: Their Materials and Performance. *Journal of Materials Research and Technology* **2022**, *20*, 2188-2220.

8. Damon, R. W., Relaxation Effects in the Ferromagnetic Resonance. *Reviews of Modern Physics* **1953**, 25 (1), 239-245.
9. Yamaguchi, M.; Hyeon Kim, K.; Ikedaa, S., Soft Magnetic Materials Application in the Rf Range. *Journal of Magnetism and Magnetic Materials* **2006**, 304 (2), 208-213.
10. Goodenough, J. B., Summary of Losses in Magnetic Materials. *IEEE Transactions on Magnetics* **2002**, 38 (5), 3398-3408.
11. Yusuf, J. Y.; Soleimani, H.; Noorhana, y.; Sanusi, Y. K.; Adebayo, L. L.; Sikiru, S.; Wahaab, F. A., Recent Advances and Prospect of Cobalt Based Microwave Absorbing Materials. *Ceramics International* **2020**, 46 (17), 26466-26485.
12. Houbi, A.; Aldashevich, Z. A.; Atassi, Y.; Bagasharova Telmanovna, Z.; Saule, M.; Kubanych, K., Microwave Absorbing Properties of Ferrites and Their Composites: A Review. *Journal of Magnetism and Magnetic Materials* **2021**, 529, 167839.
13. Yadav, R. S.; Anju; Kuřitka, I., Spinel Ferrite and Mxene-Based Magnetic Novel Nanocomposites: An Innovative High-Performance Electromagnetic Interference Shielding and Microwave Absorber. *Critical Reviews in Solid State and Materials Sciences* **2022**, 1-39.
14. Zheng, W.; Ye, W.; Yang, P.; Wang, D.; Xiong, Y.; Liu, Z.; Qi, J.; Zhang, Y., Recent Progress in Iron-Based Microwave Absorbing Composites: A Review and Prospective. *Molecules* **2022**, 27 (13), 4117.
15. Panwar, R.; Lee, J. R., Recent Advances in Thin and Broadband Layered Microwave Absorbing and Shielding Structures for Commercial and Defense Applications. *Functional Composites and Structures* **2019**, 1 (3), 032001.
16. Kraus, L., 15 - Ferromagnetic Resonance in Individual Wires: From Micro-

to Nanowires. In *Magnetic Nano- and Microwires*, Vázquez, M., Ed. Woodhead Publishing: 2015; pp 449-486.

17. Jalili, H.; Aslibeiki, B.; Ghotbi Varzaneh, A.; Chernenko, V. A., The Effect of Magneto-Crystalline Anisotropy on the Properties of Hard and Soft Magnetic Ferrite Nanoparticles. *Beilstein Journal of Nanotechnology* **2019**, *10*, 1348-1359.

18. Yu, Q.-T.; Zeng, Y.-S.; Ma, G.-J., A Radar-Infrared Compatible Broadband Absorbing Surface: Design and Analysis*. *Chinese Physics B* **2021**, *30* (7), 078402.

19. Alves, M. A.; Port, R. J.; Rezende, M. C. In *Simulations of the Radar Cross Section of a Stealth Aircraft*, 2007 SBMO/IEEE MTT-S International Microwave and Optoelectronics Conference, 29 Oct.-1 Nov. 2007; 2007; pp 409-412.

20. Peixoto, G. G.; Paula, A. L. d.; Andrade, L. A.; Lopes, C. M. A.; Rezende, M. C. In *Radar Absorbing Material (Ram) and Shaping on Radar Cross Section Reduction of Dihedral Corners*, SBMO/IEEE MTT-S International Conference on Microwave and Optoelectronics, 2005., 25-25 July 2005; 2005; pp 460-463.

21. Ahmad, H.; Tariq, A.; Shehzad, A.; Faheem, M. S.; Shafiq, M.; Rashid, I. A.; Afzal, A.; Munir, A.; Riaz, M. T.; Haider, H. T.; Afzal, A.; Qadir, M. B.; Khaliq, Z., Stealth Technology: Methods and Composite Materials—a Review. *Polymer Composites* **2019**, *40* (12), 4457-4472.

22. Kumar, A.; Singh, S., Development of Coatings for Radar Absorbing Materials at X-Band. *IOP Conference Series: Materials Science and Engineering* **2018**, *330* (1), 012006.

23. Ren, S.; Yu, H.; Wang, L.; Huang, Z.; Lin, T.; Huang, Y.; Yang, J.; Hong, Y.; Liu, J., State of the Art and Prospects in Metal-Organic Framework-Derived Microwave Absorption Materials. *Nanomicro Lett.* **2022**, *14* (1), 68.

24. Munir, A., Microwave Radar Absorbing Properties of Multiwalled Carbon

- Nanotubes Polymer Composites: A Review. *Adv. Polym. Tech.* **2017**, *36* (3), 362-370.
25. Afghahi, S. S. S.; Jafarian, M.; Atassi, Y., Novel Approach for Designing a Thin and Broadband Microwave Absorber in Ku Band Based on Substituted M-Hexaferrites. *Journal of Magnetism and Magnetic Materials* **2016**, *419*, 62-67.
26. Okano, Y.; Ogino, S.; Ishikawa, K., Development of Optically Transparent Ultrathin Microwave Absorber for Ultrahigh-Frequency Rf Identification System. *IEEE Transactions on Microwave Theory and Techniques* **2012**, *60* (8), 2456-2464.
27. Kim, G.; Kim, S.; Lee, B., Design of Wideband Microwave Absorbers Using Reactive Salisbury Screens with Maximum Flat Reflection. *J. Electromagn. Eng. Sci* **2019**, *19* (2), 71-81.
28. Arora, K.; Singh, J.; Randhawa, Y. S., A Survey on Channel Coding Techniques for 5g Wireless Networks. *Telecommunication Systems* **2020**, *73* (4), 637-663.
29. Verdone, R.; Zanella, A.; Zuliani, L., Performance of a Cellular Network Based on Frequency Hopping with Dynamic Channel Allocation and Power Control. *IEEE Transactions on Wireless Communications* **2005**, *4* (1), 46-56.
30. Durmus, Z.; Durmus, A.; Kavas, H., Synthesis and Characterization of Structural and Magnetic Properties of Graphene/Hard Ferrite Nanocomposites as Microwave-Absorbing Material. *Journal of Materials Science* **2015**, *50* (3), 1201-1213.
31. Wang, C.; Lv, R.; Huang, Z.; Kang, F.; Gu, J., Synthesis and Microwave Absorbing Properties of Feco Alloy Particles/Graphite Nanoflake Composites. *Journal of Alloys and Compounds* **2011**, *509* (2), 494-498.
32. Snoek, J. L., Dispersion and Absorption in Magnetic Ferrites at Frequencies above One Mc/S. *Physica* **1948**, *14* (4), 207-217.

33. Rozanov, K. N.; Koledintseva, M. Y., Application of Generalized Snoek's Law over a Finite Frequency Range: A Case Study. *Journal of Applied Physics* **2016**, *119* (7).
34. Ma, F.; Qin, Y.; Li, Y.-Z., Enhanced Microwave Performance of Cobalt Nanoflakes with Strong Shape Anisotropy. *Applied Physics Letters* **2010**, *96* (20).
35. Han-Shin, C.; Sung-Soo, K., M-Hexaferrites with Planar Magnetic Anisotropy and Their Application to High-Frequency Microwave Absorbers. *IEEE Transactions on Magnetics* **1999**, *35* (5), 3151-3153.
36. Shi, X.; You, W.; Li, X.; Wang, L.; Shao, Z.; Che, R., In-Situ Regrowth Constructed Magnetic Coupling 1d/2d Fe Assembly as Broadband and High-Efficient Microwave Absorber. *Chemical Engineering Journal* **2021**, *415*, 128951.
37. Zhang, T.; Peng, X.; Li, J.; Yang, Y.; Xu, J.; Wang, P.; Jin, D.; Jin, H.; Hong, B.; Wang, X.; Ge, H., Structural, Magnetic and Electromagnetic Properties of SrFe₁₂O₁₉ Ferrite with Particles Aligned in a Magnetic Field. *Journal of Alloys and Compounds* **2017**, *690*, 936-941.
38. Qiao, L.; Han, R.; Wang, T.; Tang, L.; Li, F., Greatly Enhanced Microwave Absorbing Properties of Planar Anisotropy Carbonyl-Iron Particle Composites. *Journal of Magnetism and Magnetic Materials* **2015**, *375*, 100-105.
39. Khani, O.; Shoushtari, M. Z.; Ackland, K.; Stamenov, P., The Structural, Magnetic and Microwave Properties of Spherical and Flake Shaped Carbonyl Iron Particles as Thin Multilayer Microwave Absorbers. *Journal of Magnetism and Magnetic Materials* **2017**, *428*, 28-35.
40. Shimba, K.; Tezuka, N.; Sugimoto, S., Magnetic and Microwave Absorption Properties of Polymer Composites with Amorphous Fe-B/Ni-Zn Ferrite Nanoparticles. *Materials Science and Engineering: B* **2012**, *177* (2), 251-256.

41. Gao, B.; Qiao, L.; Wang, J.; Liu, Q.; Li, F.; Feng, J.; Xue, D., Microwave Absorption Properties of the Ni Nanowires Composite. *Journal of Physics D: Applied Physics* **2008**, *41* (23), 235005.
42. Qiao, L.; Han, X.; Gao, B.; Wang, J.; Wen, F.; Li, F., Microwave Absorption Properties of the Hierarchically Branched Ni Nanowire Composites. *Journal of Applied Physics* **2009**, *105* (5).
43. Kumar, S.; Dubey, D. P.; Shannigrahi, S.; Chatterjee, R., Complex Permittivity, Permeability, Magnetic and Microwave Absorbing Properties of Ni²⁺ Substituted Mechanically Milled U-Type Hexaferrites. *Journal of Alloys and Compounds* **2019**, *774*, 52-60.
44. Slater, J. C., The Ferromagnetism of Nickel. Ii. Temperature Effects. *Physical Review* **1936**, *49* (12), 931-937.
45. Pauling, L., The Nature of the Interatomic Forces in Metals. *Physical Review* **1938**, *54* (11), 899-904.
46. Kawahara, K., Effect of Additive Elements on Cold Workability in Feco Alloys. *Journal of Materials Science* **1983**, *18* (6), 1709-1718.
47. Qiu, S. L.; Marcus, P. M.; Moruzzi, V. L., Magnetic Structure in Fecr and Feco. *Journal of Applied Physics* **1999**, *85* (8), 4839-4841.
48. Zhang, X.; Li, Y.; Liu, R.; Rao, Y.; Rong, H.; Qin, G., High-Magnetization Feco Nanochains with Ultrathin Interfacial Gaps for Broadband Electromagnetic Wave Absorption at Gigahertz. *ACS Applied Materials & Interfaces* **2016**, *8* (5), 3494-3498.
49. Cui, E.; Pan, F.; Xiang, Z.; Liu, Z.; Yu, L.; Xiong, J.; Li, X.; Lu, W., Engineering Dielectric Loss of Feco/Polyvinylpyrrolidone Core-Shell Nanochains@Graphene Oxide Composites with Excellent Microwave Absorbing

Properties. *Advanced Engineering Materials* **2021**, 23 (1), 2000827.

50. Dong, R.-E.; Hassan, A.; Mehrez, S.; Hermawan, I.; Anqi, A. E.; Mahariq, I.; Fayed, M., Hierarchical 3d MnO₂ and 1d MnFe₂O₄ Wrapped with MnO₂ Nanocomposites toward High-Performance Bi-Layer Microwave Absorber. *Ceramics International* **2023**, 49 (5), 8099-8111.

51. Khadour, M.; Atassi, Y.; abdallah, M., Preparation and Characterization of a Flexible Microwave Absorber Based on Mn_{0.1}Ni_{0.45}Zn_{0.45}Fe₂O₄ in a Thermoset Polyurethane Matrix. *SN Applied Sciences* **2020**, 2 (2), 236.

52. Green, M.; Chen, X., Recent Progress of Nanomaterials for Microwave Absorption. *Journal of Materiomics* **2019**, 5 (4), 503-541.

53. Sadiq, I.; Naseem, S.; Ashiq, Muhammad N.; Khan, M. A.; Niaz, S.; Rana, M. U., Tunable Microwave Absorbing Nano-Material for X-Band Applications. *Journal of Magnetism and Magnetic Materials* **2016**, 401, 63-69.

54. Yan, L.; Xiang, J.; Guan, G.; Zhang, H.; Zhang, Y.; Zhang, K., Tunable High-Performance Microwave Absorption of Cobalt Nanoparticles Wrapped in N-Self-Doped Carbon Nanofibers at Ultralow Filler Loadings. *J. Alloys Compd.* **2023**, 933, 167808.

55. Zhao, H.; Cheng, Y.; Zhang, Z.; Yu, J.; Zheng, J.; Zhou, M.; Zhou, L.; Zhang, B.; Ji, G., Rational Design of Core-Shell Co@C Nanotubes Towards Lightweight and High-Efficiency Microwave Absorption. *Compos. Part B* **2020**, 196, 108119.

56. Fan, Y.; Jin, L.; Ji, W.; Wang, J.; Zhu, L.; Zhao, W., Microwave-Induced Carbonization of Rapeseed Shell for Bio-Oil and Bio-Char: Multi-Variable Optimization and Microwave Absorber Effect. *Energy Conversion and Management* **2019**, 191, 23-38.

57. Zhou, M.; Xu, X.; Wan, G.; Mou, P.; Teng, S.; Wang, G., Rationally Tailoring Interface Characteristics of ZnO/Amorphous Carbon/Graphene for Heat-Conduction Microwave Absorbers. *Nano Research* **2022**, *15* (10), 8677-8687.
58. Wu, L.; Liu, X.; Wan, G.; Peng, X.; He, Z.; Shi, S.; Wang, G., Ni/Cnts and Carbon Coating Engineering to Synergistically Optimize the Interfacial Behaviors of TiO₂ for Thermal Conductive Microwave Absorbers. *Chemical Engineering Journal* **2022**, *448*, 137600.
59. Zivkovic, I.; Murk, A. Boron Nitride Loading for Thermal Conductivity Improvement of Composite Microwave Absorbers *Electronics Letters* [Online], 2012, p. 1130-1131.

Part II

Shape-Modulated Hybrid FeCo Composite Material

Chapter 3. SiO₂-Coated 0D-1D FeCo Nanochains

3.1. Introduction

3.1.1. Synthesis of FeCo Nanochains: Radio-frequency (RF) Thermal Plasma

Radio-frequency (RF) thermal plasma is a type of plasma generated using radio waves as the primary source of energy. Plasma, often referred to as the fourth state of matter, is a highly ionized gas composed of positively charged ions, negatively charged electrons, and neutral particles. It is created when a gas is heated to very high temperatures or subjected to strong electric fields. The plasma is generated by applying a high-frequency alternating current (AC) electric field to a gas. The RF electric field causes the gas molecules to oscillate rapidly, and collisions between these molecules lead to the generation of heat. As the temperature of the gas increases, some of the gas molecules become ionized, and form a plasma.³ The RF thermal plasma has several characteristics that make it useful in various applications, including having a clean high-temperature field being free from electrode material contamination where micron-sized solid precursors are immediately heated to evaporation point and mass production of nanoparticles are synthesized as seen in **Figure 3.1.**⁴⁻⁶

In RF thermal plasma systems, an induction coil is often used to generate and sustain the plasma. The induction coil is typically a helical-shaped conductor made of copper. It is placed around the region where the plasma is generated, such as the reactor chamber. The coil is connected to an RF power supply that generates the high-frequency AC used to produce the plasma. When the RF power supply is activated, it produces an alternating current that flows through the induction coil.

This alternating current creates a rapidly changing magnetic field around the coil (See **Figure 3.2**).² The changing magnetic field generated by the coil induces an electric field within the surrounding region. This electric field interacts with the gas or plasma. The electric field induced by the coil exerts a force on the charged particles present in the gas, especially the free electrons. The electrons experience a Lorentz force due to their electric charge and motion in the presence of the magnetic field. This force causes the electrons to move in a cyclical motion within the plasma, leading to their acceleration. As the accelerated electrons collide with gas molecules, they transfer energy to the gas particles, resulting in heating. The heating and ionization processes increase the plasma's temperature and ionization level.⁷⁻⁸

The magnetic field generated in the plasma may act as an external magnetic field when Fe and Co precursor micro-powders are inserted into the system, leading to the formation of FeCo nanochains (See **Figure 3.3**). When magnetic particles are placed in a magnetic field, each particle experiences a magnetic force. The particles align themselves in such a way that their magnetic moments are oriented in the direction of the magnetic field. This alignment occurs due to the attractive forces between the particles' magnetic moments and the applied field.⁹⁻¹¹

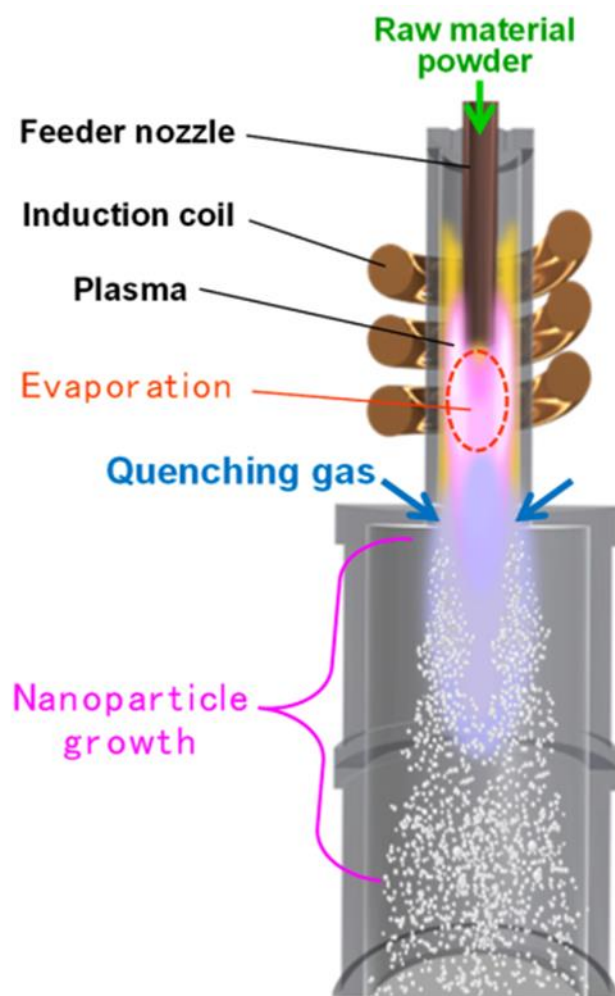


Figure 3.1. In a RF thermal plasma, micron-sized solid precursors are immediately heated to evaporation point and mass production of nanoparticles are synthesized¹

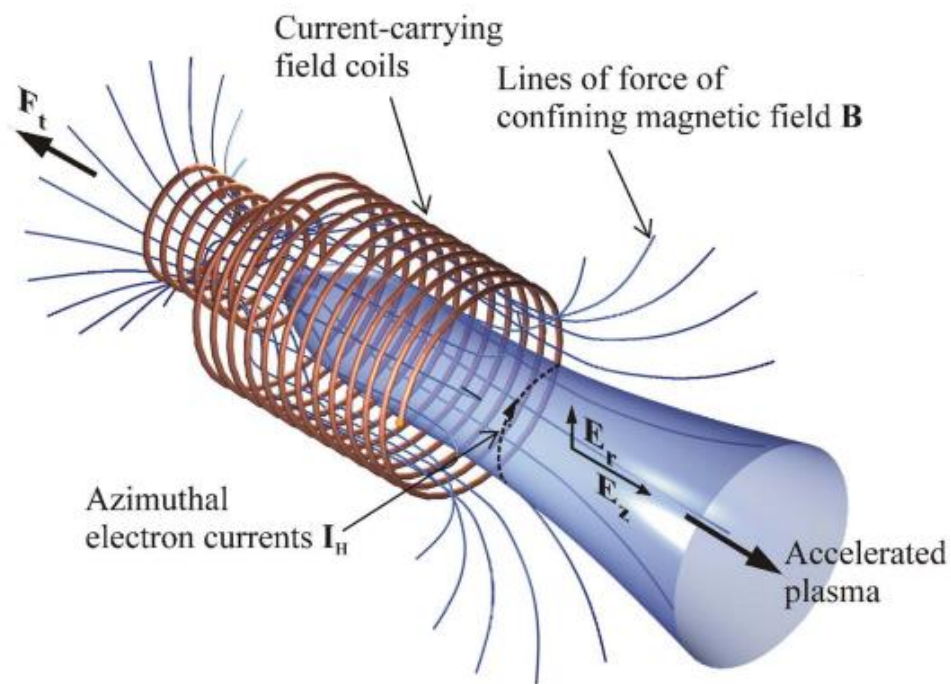


Figure 3.2. When the RF power supply is activated, it produces an alternating current that flows through the induction coil. This alternating current creates a rapidly changing magnetic field around the coil. ²

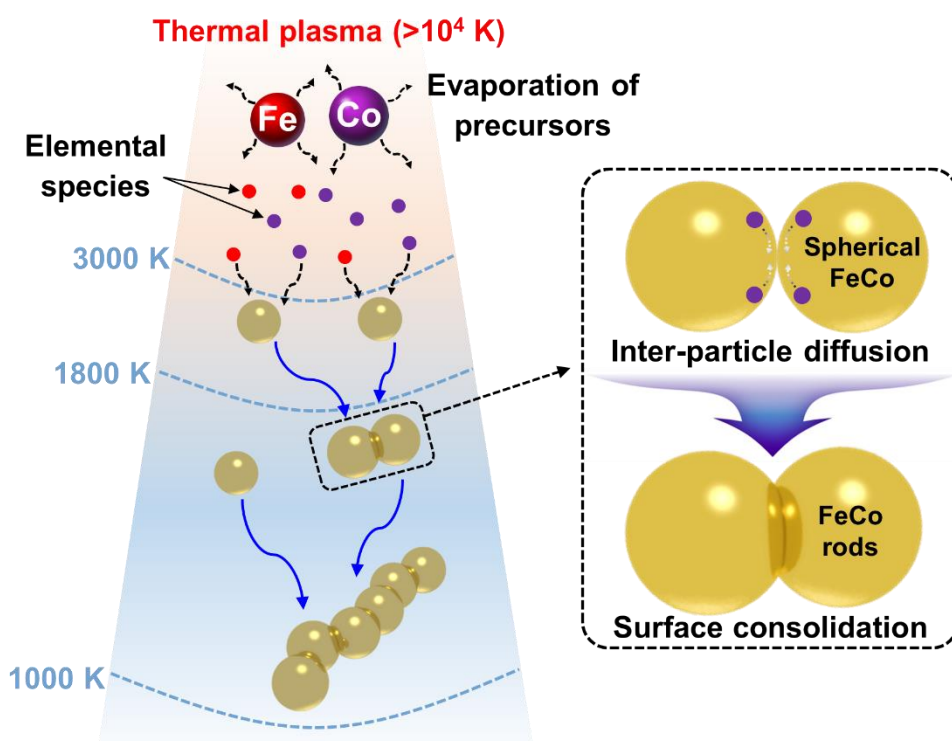


Figure 3.3. Schematic illustration of the thermal plasma preparation via RF-thermal plasma synthesis of nano-chained FeCo composition.

3.1.2. Working Principles of FeCo@SiO₂ Nanochains as EWAMs

Figure 3.4 (a) and **(b)** schematically show how the incident electromagnetic waves are dissipated by the absorber. Incident microwaves are partially reflected at the surface or interface of the materials; the rest are absorbed in the FeCo particles. **Figure 3.4 (a)** shows the heat dissipation of a beam incident on an electromagnetic wave absorber with a certain thickness. In general, for soft magnetic materials under alternating magnetization conditions, eddy currents are generated by the movement of the magnetic domains, which causes internal heat and which is called iron loss. Also, the precession motion of the FeCo nano-particles is expressed by the external field (H). The transmitted electromagnetic waves are partly absorbed in the FeCo nano-chained electromagnetic wave absorber and the rest are simultaneously reflected by the FeCo nano-chained particles and absorbed again. The electromagnetic waves emitted from the absorber and the first reflected electromagnetic wave at the interface or surface is designed to cancel each other according to $1/4\lambda$ destructive interference, as schematically illustrated in **Figure 3.4 (b)**.

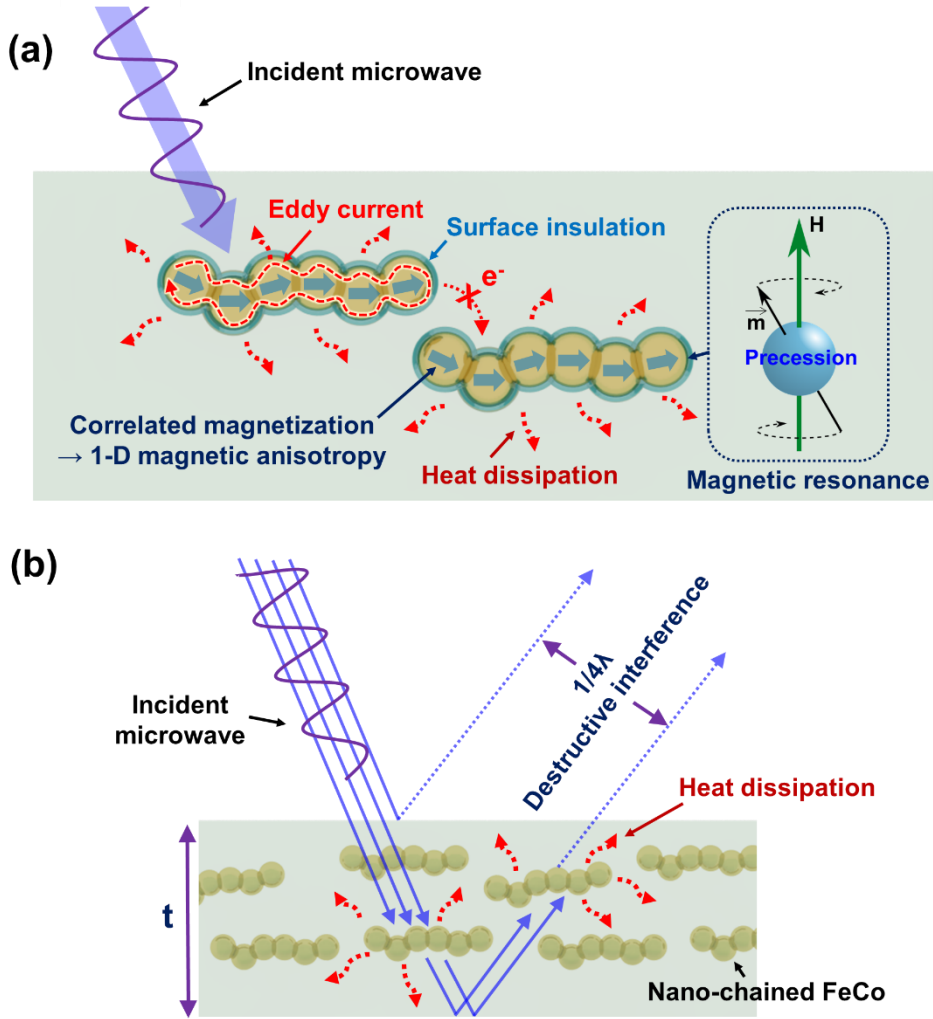


Figure 3.4 (a) Eddy current formation for the 1-D magnetic anisotropy formed in nano-chained FeCo. The precession motion of the FeCo nano-particles is expressed by the external field, H . And (b) electromagnetic wave absorber with the most ideal $1/4\lambda$ phase difference.

3.2. Experimental Section

3.2.1. Materials

All chemicals, of analytical grade, including absolute ethyl alcohol ($\text{C}_2\text{H}_5\text{OH}$, 99.9%), (3-Aminopropyl) trimethoxysilane ($\text{H}_2\text{N}(\text{CH}_2)_3\text{Si}(\text{OCH}_3)_3$, 97%, APTMS), ammonium hydroxide (NH_4OH , 25%), and tetraethyl orthosilicate ($\text{Si}(\text{OC}_2\text{H}_5)_4$, 98%, TEOS), were purchased from Sigma-Aldrich.

3.2.2. Preparation of FeCo nano-chained particles

TEKNA PL-35LS (Tekna Plasma Systems, INC.), a radio-frequency inductively-coupled thermal plasma (RF-ITP) system, was used to synthesize the FeCo compositions. The morphology and structure of the as-synthesized FeCo were modified in sequence. First, the nucleation and growth of FeCo nanoparticles took place gently; successful surface consolidations among FeCo nanoparticles rapidly occurred at the quenching zone and eventually resulted in nano-chained morphology. These results were collected and used for the insulation coating process.

3.2.3. Synthesis of FeCo@SiO₂ using APTMS

A solution of 400 ml of anhydrous ethanol and 4 ml of APTMS was stirred vigorously at room temperature in advance. Gradually, as-synthesized nano-chained FeCo composition was added to the mixture solution and mechanically blended and stirred at a speed of 300 rpm for 45 minutes at room temperature. Anhydrous ethanol/APTMS solution was carefully discarded and FeCo@APTMS was collected through a 200 nm pore PTFE filter paper (J020A047A) with vacuum pumping in air. Consequently, FeCo@SiO₂ nano-chained particles were rinsed two times with

ethanol and then completely dried in a 60 °C vacuum oven for 20 hours.

3.2.4. Synthesis of FeCo@SiO₂ using TEOS

Solutions of NH₄OH-H₂O and TEOS-absolute ethyl alcohol were prepared and each solution was magnetically stirred for 15 minutes at 60 °C. Then, NH₄OH-H₂O and TEOS-ethanol were mixed as done earlier and directly added to the prepared FeCo compositions in solution with mechanical stirring for 3 hours at room temperature. Finally, the FeCo@SiO₂ was gently washed with ethanol two times and then entirely dried at 60 °C in a vacuum oven for 20 hours.

3.2.5. Characterization

The obtained morphological features were characterized by field emission transmission electron microscopy (FE-TEM, Tecnai G2 F30 S-Twin, USA). Also, energy-dispersive X-ray spectroscopy (EDS, Tecnai G2 F30 S-Twin, USA) was used for elemental analysis and chemical characterization of samples. The motions of the surface consolidations and the diffusion were vividly observed using a field emission gun (FEG)-TEM (JEM 2100F, JEOL LTD.). The crystal structure of the novel material was detected by X-ray diffraction (XRD, Rigaku D/Max-2500VL/PC). The magnetic properties of specimens were precisely detected by a vibrating sample magnetometer (VSM, Riken Denshi, BHV-525). To measure the electromagnetic parameters (ϵ' , ϵ'' , μ' , μ'') of the products, a vector network analyzer (Keysight N5222B) was used. In the range of 0.5-18 GHz, a Keysight 85051B verification kit and a 10 cm coaxial airline were integrated with the N5222B. A ring-shaped specimen with outer radius of 7 mm, inner radius of 3.04 mm, and thickness of 2 mm was loaded for measurements. In the range of 18-26 GHz, the Keysight

K11644A calibration kit and a WR-42 waveguide were integrated with the N5222B. Rectangular specimens with dimensions of $10.7 \times 4.3 \times 2.0 \text{ mm}^3$ were loaded for measurements. Each sample was individually prepared by mixing specific weights of FeCo particles with YD-128 epoxy resin, a tetramethylphtalic anhydride curing agent, and MeTHPA catalyst from Kukdo Chemical. The mixture can be modified into various forms before curing, e.g. cubes or casted films. Fig. 8(g) shows a large scale film with 225 cm^2 area. The mixture was cured into specimens for 2 hours at 80°C , 1 hour at 120°C , and 2 hours at 150°C in a vacuum oven.

3.3 Results and Discussion

3.3.1 Structural Morphology Characterization of FeCo Nanochain

It is inferred from Equation (8) that achieving high M_s is a prime consideration for moving to the gigahertz range. For the Fe-Co system, M_s dramatically varies with Co content, so it is important to precisely control the composition to achieve maximum M_s . Fortunately, this is easy to achieve via thermal plasma synthesis. Since the extremely-high-temperature (>104 K) thermal plasma vaporizes all precursors regardless of the original compositional state, this vapor composed of elemental species with composition given by the precursors will condense into alloyed particles in a single phase, assuming the constituent elements can form a solid solution. Consequently, using thermal plasma synthesis, we can systematically control the composition of synthesized FeCo particles simply by changing the mixing ratio of precursors, i.e. Fe-to-Co. To obtain FeCo alloy particles with optimal composition that shows highest M_s , Fe to Co ratio in the mixed powder precursor was varied from 7:3 to 3:7, and morphological features of as-synthesized $\text{Fe}_x\text{Co}_{1-x}$ nano-particles with different compositions were observed by scanning electron microscopy (SEM) and transmission electron microscopy (TEM), with results shown in **Figure 3.5 (a)–(c) ($x=0.3$)** and **2(d)–(f) ($x=0.6$)**, respectively. In both cases, numerous chain-shaped FeCo particles can be identified in the low-magnification SEM and TEM images shown in **Figure 3.5 (a), (b), (d), and (e)**. A clear crystal structure was confirmed at the interface where the nano-chained FeCo was formed (See **Figure 3.6**).

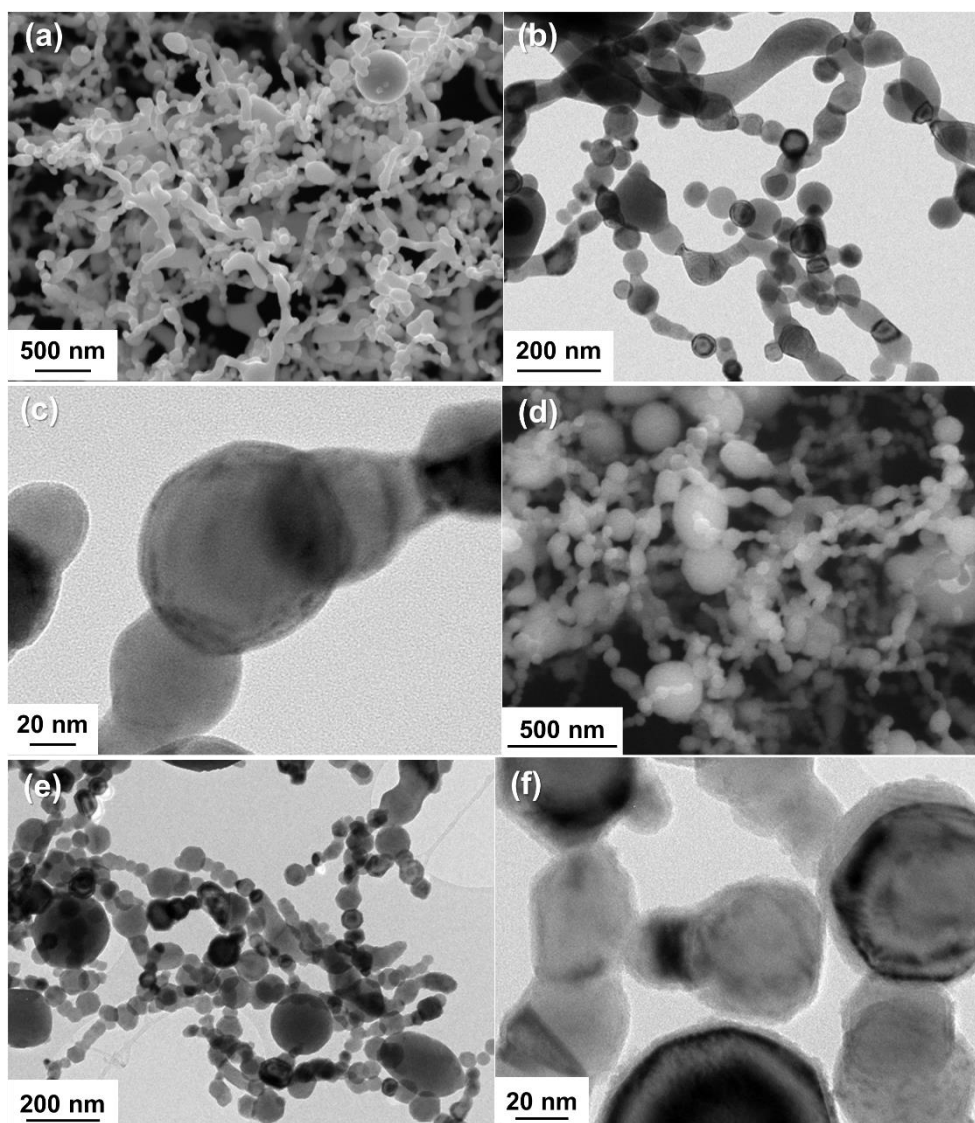


Figure 3.5. Scanning electron microscope (SEM) Transmission electron microscope (TEM) images of nano-chained $\text{Fe}_x\text{Co}_{1-x}$ synthesized by the RF-ITP: (a)-(c) $x=0.6$ and (d)-(f) $x=0.3$.

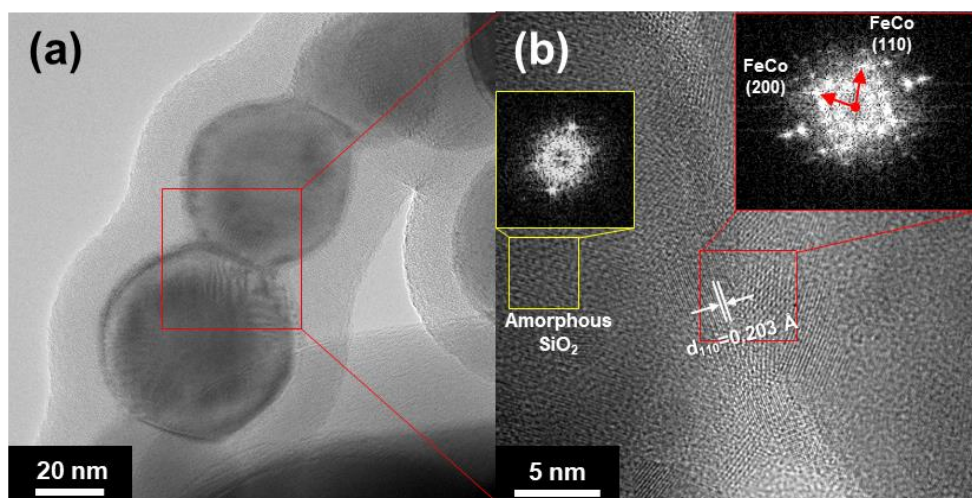


Figure 3.6. (a) TEM image of one FeCo@SiO₂ nanochain. (b) Diffraction pattern of interface of FeCo nanochain confirms clear crystal structure.

3.3.2. Elemental Composition and Aspect Ratio Investigation of $\text{Fe}_x\text{Co}_{1-x}$ alloys

From the EDS analysis results shown in **Figure 3.7**, the Co content in the FeCo alloys gradually increased from 29.6 wt. % to 72.44 wt. % as the mixing weight ratios, i.e. Fe to Co, in the precursor were varied from 7:3 to 3:7. It is noteworthy that nano-chained shapes of FeCo particles were observed regardless of the composition ratio of Fe- and Co-elements. While the actual mixing weight ratios, i.e. Fe to Co, of 7:3 to 3:7, are clearly different, the aspect ratio of FeCo alloys appears to be higher than 4 for all configurations, as shown in **Figure 3.8**.

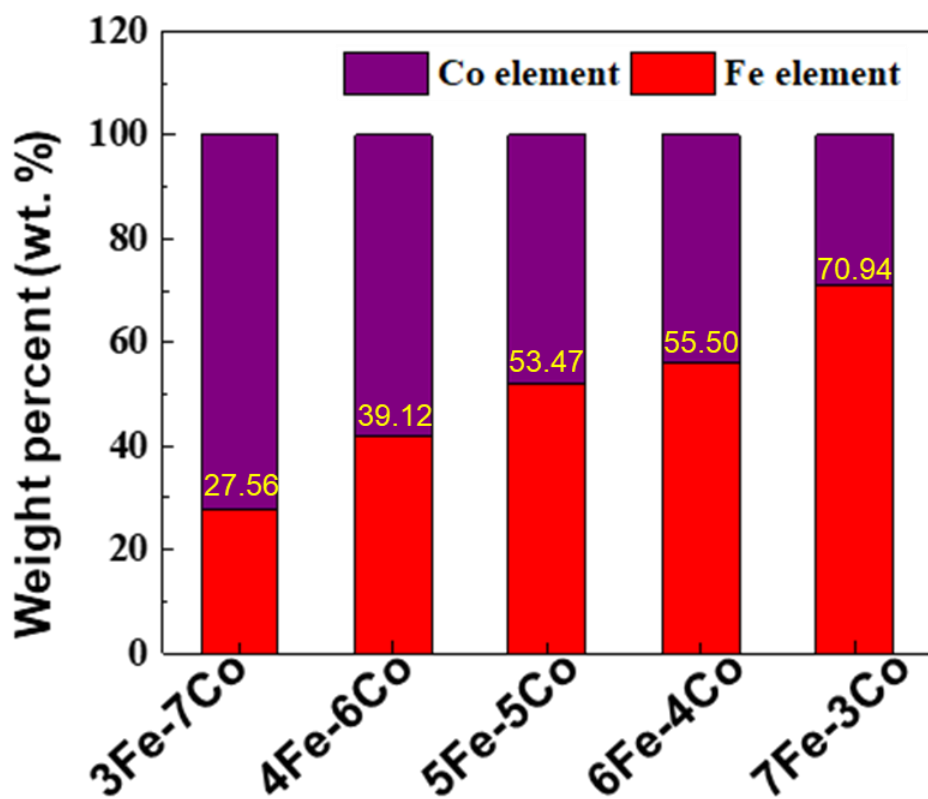


Figure 3.7. Graph of the combined appropriate weight ratio of Fe to Co, *i.e.* 7:3 to 3:7.

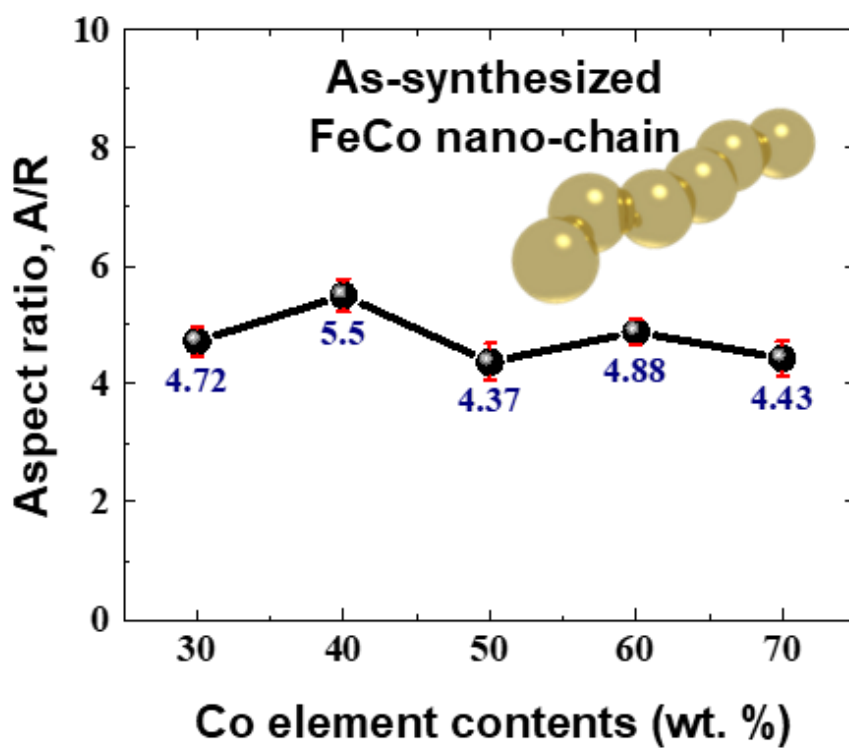


Figure 3.8. Graph of distinctive aspect ratios versus composition with varying weight ratio of Fe to Co, i.e. 7:3 to 3:7 calculated from the region in images.

3.3.3. Crystallographic and Magnetic Properties $\text{Fe}_x\text{Co}_{1-x}$ alloys

Meanwhile, X-ray diffraction (XRD) was used to observe the synthetic composition according to the crystal structure and precursor of FeCo alloy. Typical XRD patterns of FeCo alloy for all samples ($\text{Fe}_x\text{Co}_{1-x}$, $x = 0.3, 0.4, 0.5, 0.6$, and 0.7) can be observed in **Figure 3.9**. Diffraction peaks very similar to the standard pattern of FeCo alloy were detected regardless of the composition ratio. The characteristic diffraction peaks at $2\theta = 44.8^\circ, 65.2^\circ$, and 82.6° , corresponding to FeCo alloy, indicate that the body-centered cubic (BCC) structures of (110), (200), and (211) planes can be indexed (JCPDS card #44-1433). However it can be seen that weak diffraction intensity were detected in the cases of Co contents of $x = 0.3$ and 0.4 . In other words, Co element with the face-centered cubic (FCC) structure is indexed in addition to the BCC structure of the FeCo alloy. The relatively low characteristic diffraction peaks are located at $2\theta = 44.2^\circ, 51.5^\circ$, and 75.8° , corresponding to Co element with FCC structures of (111), (200), and (220) planes (JCPDS card # 89-7093).

It can be assumed that during the initial synthesis stage of RF-ITP, self-aggregation of the remaining Co elements occurred after the alloy was formed due to the addition of excess Co elements. Consequently, by controlling the mixing ratio of the precursors for thermal plasma synthesis, systematic control of the composition and magnetic properties of $\text{Fe}_x\text{Co}_{1-x}$ alloy particles was accomplished while high aspect ratio chained morphologies of the nanoparticles were secured. It is presumed that, during the thermal plasma synthesis, spherical FeCo nanoparticles are first formed through nucleation and growth processes; then, the high temperature zone of plasma thermal plasma accelerates plasma diffusion of constituent elements, leading to surface-consolidation between particles at the moment of collision; as a result, 1-

dimensional nano-chained particles are fabricated. It is of particular interest that FeCo nanoparticles act as precursors for chain formation. So, we additionally performed in-situ thermal TEM analysis to observe how the morphology of initially-spherical $\text{Fe}_{0.6}\text{Co}_{0.4}$ particles changed in real time as the temperature increased. Three different TEM images taken at 0, 240, and 360 s, retrieved from the original in-situ TEM results, are shown in **Figure 3.10**. This is direct evidence of the inter diffusion among nearby FeCo nanoparticles, which involves self-diffusion and growth steps of the FeCo alloy.¹²⁻¹⁴ It can be seen from **Figure 3.10** that FeCo particles gradually linked to each other as the temperature increased from 273 K to 1073 K within 360 s. In the TEM image, it can be clearly seen that particles with relatively small size or distorted shape disappeared or merged with large well-formed particles as temperature increased.¹⁵⁻¹⁶ Surprisingly, it can also be visually proven in **Figure 3.10 (c)** that necking is formed on the surface between the FeCo particles after all the reactions are completed. In the thermal plasma synthesis process, right after the formation of spherical FeCo particles, massive inter-particle collisions take place at the quenching zone just below the hot zone (104 K). Because the temperature of the quenching zone is in the regime of 1000-1800 K, the diffusion coefficients of Fe and Co elements in the FeCo alloys are highly intensified, and surface diffusion between FeCo particles will occur at the moment of collision, which subsequently results in surface consolidation and necking between particles. The diffusion coefficients of Fe and Co element in FeCo binary alloy are more active than those of γ -Fe or Co alloys.¹⁷⁻¹⁹ Finally, successive collision and surface consolidation between particles resulted in chained FeCo nanoparticles with aspect ratio in a range of 4.4-5.5.

The M_s and H_c values of the FeCo alloys, depending on the Co content (wt. %), were also measured by VSM at room temperature. In **Figure 3.11**, changes

in the values of M_s and H_c of soft magnetic FeCo alloy according to the amount of Co element added in the alloy were confirmed and the tendency and relationship of the two parameters were examined. It can be seen that the values of M_s decrease as the content of Co element increases; M_s shows a maximum value of 230.4 emu/g with the composition $Fe_{0.7}Co_{0.3}$. This result is consistent with the highest value of M_s of the $Fe_{70}Co_{30}$ alloy reported in the literature. It is noteworthy that only a slight decrease in M_s to 227 emu/g was observed for $Fe_{0.6}Co_{0.4}$ alloy particles; however, these particles showed the highest aspect ratio of 5.5, as can be seen in **Figure 3.11**. Dramatic decreases of M_s from similar experimental values of 209.54 emu/g for $Fe_{0.5}Co_{0.5}$ and 209.31 emu/g for $Fe_{0.4}Co_{0.6}$ to 151.1 emu/g for $Fe_{0.3}Co_{0.7}$ are attributed to large precipitation of FCC Co particles, which have M_s values less than 124 emu/g. On the other hand, H_c increases as the Co content increases, and the maximum value of H_c (408.22 Oe) is achieved by the alloy consisting of 70 wt. % Co element; this maximum value is attributed to precipitation of FCC Co particles, which have uniaxial crystalline anisotropy higher than that of the BCC FeCo alloys, as can be seen in **Figure 3.11**.

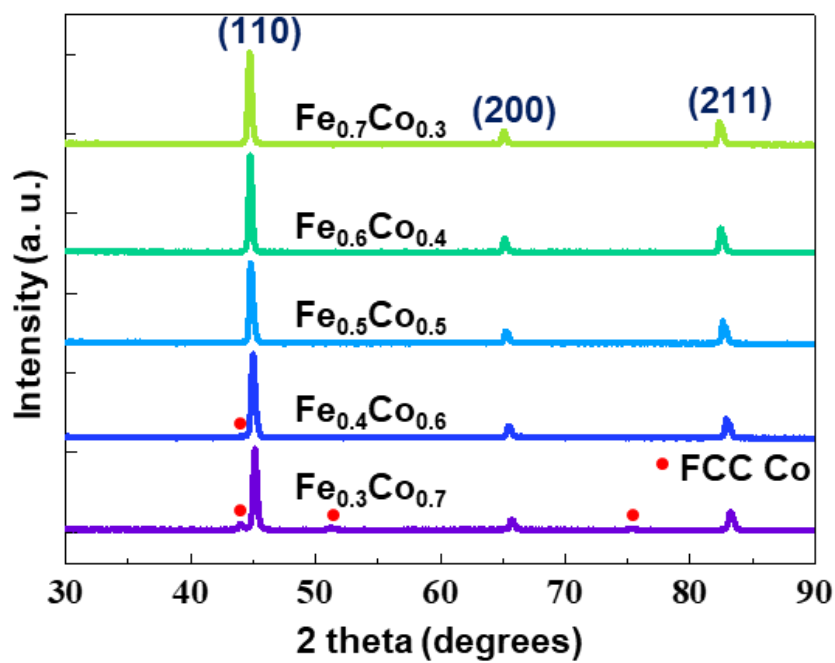


Figure 3.9. XRD patterns of the Fe_xCo_{1-x} alloys (x = 0.3, 0.4, 0.5, 0.6, 0.7), respectively.

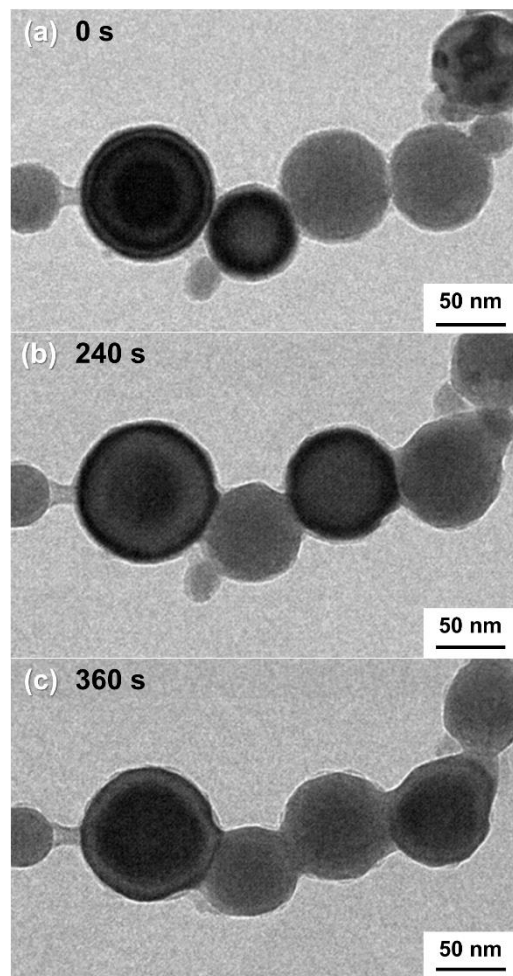


Figure 3.10. In-situ TEM observation of the inter-particle diffusion of Fe_{0.6}Co_{0.4} nano-particles. (a) A completely spherical Fe_{0.6}Co_{0.4} nano-particle with a size of under 100 nm at 873 K. Sequential images for particle accompanied by the diffusion and process of the forming a neck to rods or chained as linear increasing temperature with 30 °C/min from 873 K to 973 K in (b) and 1073 K in (c).

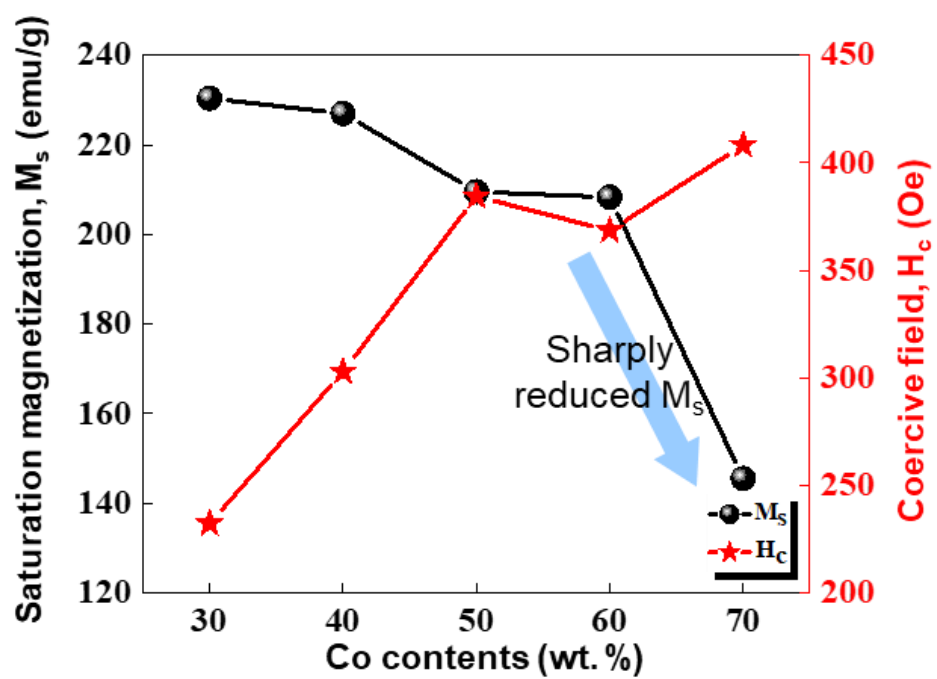


Figure 3.11. Magnetic properties identified for various weight percentages of Co elements.

3.3.4. Electromagnetic Properties of $\text{Fe}_x\text{Co}_{1-x}$ alloys: Complex Permeability and Permittivity Spectra

To understand the electromagnetic properties of FeCo nano-chained particles at high frequency regime, the complex permeability and complex permittivity versus the frequency were studied, as shown in **Figure 3.12 (a)** and **(b)**. Frequency dependency values of the real part (μ') and the imaginary part (μ'') of the complex permeability, which correspond to the magnetic storage ability and attenuation ability, respectively, are plotted in **Figure 3.12 (a)**. At $x=0.3$ to 0.7 of Co content, the $\text{Fe}_{0.6}\text{Co}_{0.4}$ alloy showed maximum values in all frequency bands. Based on previous results²⁰⁻²², distinguished shaped materials can be associated with unique magnetic behaviors and absorption performance, and the $\text{Fe}_{0.6}\text{Co}_{0.4}$ alloy with the largest aspect ratio value, visible in **Figure 3.8**, can be explained as the reason for the excellent permeability. In relation to the results showing the influence of shape, the micro spherical FeCo alloy and the nano-chained FeCo alloy were compared and it was found that the nano-chained FeCo alloy having aspect ratio values between 4.4 and 5.5 had better values of μ' regardless of the composition. The μ'' values of each alloy at the 10 GHz frequency band can be seen in the inset. It was confirmed that the $\text{Fe}_{0.6}\text{Co}_{0.4}$ alloy with μ' value of 1.348 has outstanding permeability, making it a suitable candidate absorption material. The μ'' value of the micro spherical FeCo alloy is almost constant, with an averaged value of 0.29, whereas nano-chained FeCo alloys show a phenomenon in which this value of μ'' goes up from 0.15 to 0.49, increasing as the frequency increases.²³ The sources of the magnetic loss in microwave frequency range are eddy current loss, natural resonance, and exchange resonance.²⁴ Among them, the natural resonance is reported as the dominant factor of the increased magnetic loss in a chain of magnetic nanoparticles.²⁵ **Figure 3.12 (b)**

indicates the complex permittivity real parts (ϵ') and imaginary parts (ϵ'') of the two samples, the micro spherical FeCo alloy and nano-chained $\text{Fe}_{0.6}\text{Co}_{0.4}$ alloys, indicating the exceptionally complex permeability: both similar behaviors and distinctly dissimilar values of ϵ' were investigated. There were gradual drops of ϵ' value from 11.87 to 11.01 for nano-chained $\text{Fe}_{0.6}\text{Co}_{0.4}$ alloys and from 6.35 to 5.87 for the micro spherical FeCo alloy. The values of ϵ'' for both micro-spherical and nano-chained particles were negligibly small. The gradual decrease of ϵ' with frequency is advantageous for broad-band impedance matching. However, the decrement of ϵ' for FeCo particles was only 7.91% for the 1-18 GHz range. Higher ϵ' values for nano-chained FeCo particles, compared to those for FeCo micro spheres, were attributable to the increased surface area and enhanced electrical conductivity due to the larger aspect ratio.

To validate Snoek's law, a comparison was made between the real and imaginary parts of the complex permeability of FeCo micropowder and five different FeCo nanochains in the low frequency range (see **Figure 3.13**). As depicted in **Figure 3.13 (a)**, the FeCo micropowder exhibits the lowest permeability value of 1.9 at 0.5 GHz, whereas $\text{Fe}_{0.6}\text{Co}_{0.4}$ demonstrates the highest value of 1.94. In Figure 3.13 (b), the imaginary permeability value of $\text{Fe}_{0.6}\text{Co}_{0.4}$ reaches its peak at 0.49 at 11 GHz, surpassing the lowest value of 0.29 observed in FeCo micropowder. These findings further support the validation of Snoek's law, as they demonstrate an enhancement in both the real and imaginary permeability values.

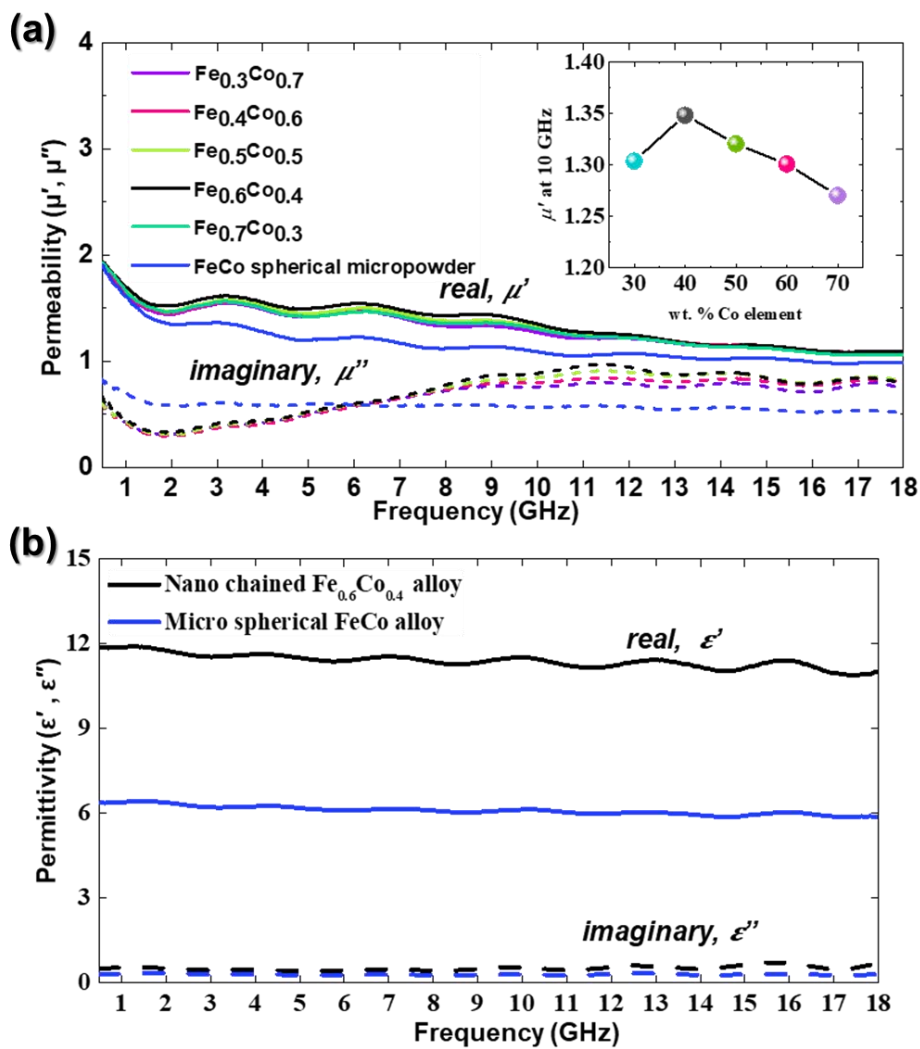


Figure 3.12. (a) Complex permeability of nano-chained $\text{Fe}_x\text{Co}_{1-x}$ and FeCo spherical micro powder. And (b) complex permittivity of $\text{Fe}_{0.6}\text{Co}_{0.4}$ nano-rods and FeCo spherical micro powder

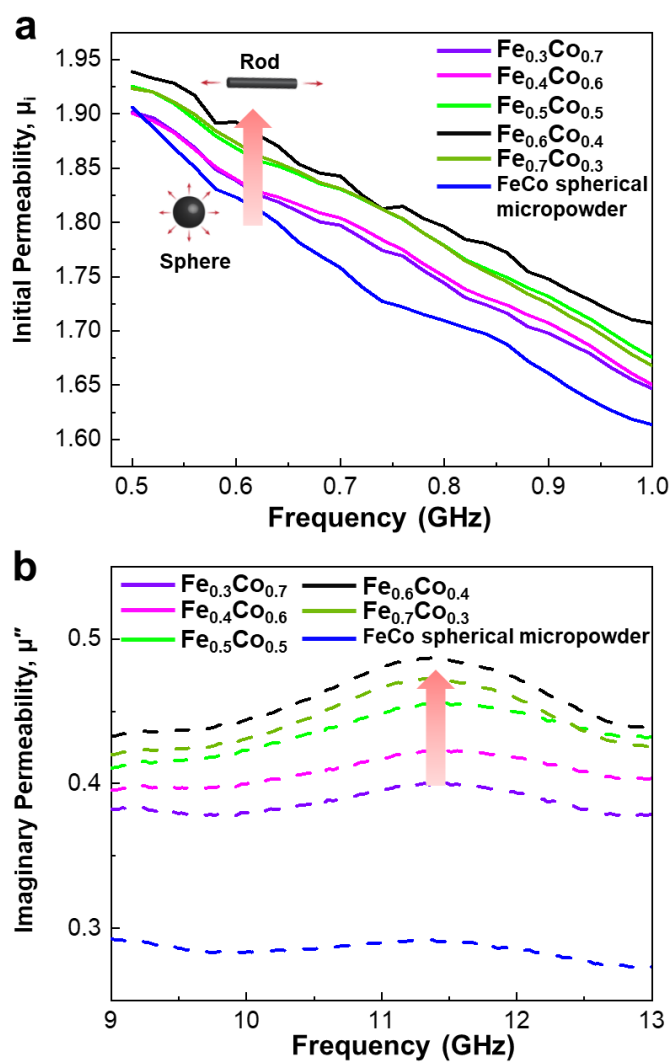


Figure 3.13. Enhancement in (a) real permeability at low frequency range and (b) imaginary permeability of nano-chained $\text{Fe}_x\text{Co}_{1-x}$ and FeCo spherical micro powder..

3.3.5. Structural Morphology Characterization of $\text{Fe}_{0.6}\text{Co}_{0.4}@\text{SiO}_2$ Insulation

In **Figure 3.5 (a)–(f)**, it can be seen that rod-like or chain-shaped FeCo alloys are intertwined with each other, which resulted in electrical conduction between the particles and increased ϵ' . In general, the value of ϵ' of magnetic particles shows a constant value over the frequency regime of interest (1-26 GHz), and so adjusting the permittivity is important for impedance matching at the targeted frequency to ensure minimum absorbing film thickness. For this purpose, we performed uniform insulation coating on FeCo nano-chained particles through a sol-gel process. **Figure 3.14 (a)–(d)** shows the TEM results for $\text{Fe}_{0.6}\text{Co}_{0.4}@\text{SiO}_2$ particles after completion of the insulating coating. The data in **Figure 3.14 (a)** and **(b)** are meaningful because there was no deformation of the chain-shaped FeCo particles as they initially formed because insulating coating was performed at room temperature. It can be clearly seen from **Figure 3.14 (c)** and **(d)** that SiO_2 is consistently coated to thicknesses of 29.21 nm (@TEOS in **Figure 3.14 (c)**) and 2.00 nm (@APTMS in **Figure 3.14 (d)**) on the surface of FeCo particles. It should be noted that SiO_2 with thickness of 2.00 nm uniformly and fairly thinly distributed on the FeCo surface can be confirmed, as shown in **Figure 3.14 (d)**. To further identify SiO_2 , one of the FeCo particles was individually monitored by EDS analysis; its components correspond to Fe-, Co-, Si-, and O- elemental mapping results, as can be seen in **Figure 3.14 (e)**.

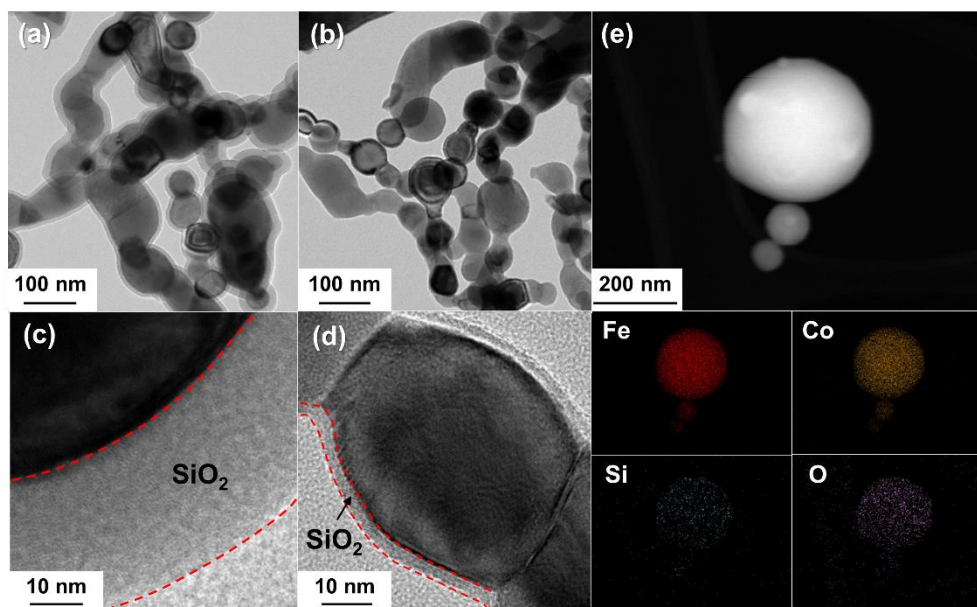


Figure 3.14. TEM images in different magnification of the insulation coated Fe_{0.6}Co_{0.4}; 100 nm scale (a) and (b), 10 nm scale (c) and (d). Each coating material show a different thickness of SiO₂ of 29.21 nm and 2.00 nm, respectively. (e) TEM image of Fe_{0.6}Co_{0.4}@APTMS and the corresponding the energy dispersive X-Ray using the EDS element mapping analysis.

3.3.6. Crystallographic and Magnetic Properties $\text{Fe}_{0.6}\text{Co}_{0.4}@\text{SiO}_2$ Nanochain

XRD was measured to observe the composition of the material after coating. Both $\text{Fe}_{0.6}\text{Co}_{0.4}@\text{SiO}_2$ with a thickness of 29.21 nm and $\text{Fe}_{0.6}\text{Co}_{0.4}@\text{SiO}_2$ with a thickness of 2.00 nm were examined with results shown in **Figure 3.15**. Only the sharp and strong patterns from the FeCo phase of BCC structure after coating can be verified; no other diffraction peaks indexing the structure of SiO_2 can be found.

The magnetic properties of as-synthesized $\text{Fe}_{0.6}\text{Co}_{0.4}$, $\text{Fe}_{0.6}\text{Co}_{0.4}@\text{TEOS}$ (SiO_2 with a thickness of 29.21 nm), and $\text{Fe}_{0.6}\text{Co}_{0.4}@\text{APTMS}$ (SiO_2 with a thickness of 2.00 nm) were estimated by VSM at room temperature and showed three different hysteresis loops, as can be seen in **Figure 3.16**. When the SiO_2 thickness was 2.00 nm, M_s was reduced only by 3.76% compared to the as-synthesized $\text{Fe}_{0.6}\text{Co}_{0.4}$ composition, while, in the case of the thickness of 29.21 nm, M_s dramatically decreased by 49.06% due to the large incorporation of SiO_2 layers. In contrast, as shown in the inset, each sample's intrinsic characteristic, given by the H_c value, was found to be approximately 338.3 Oe, unaffected both before and after coating.

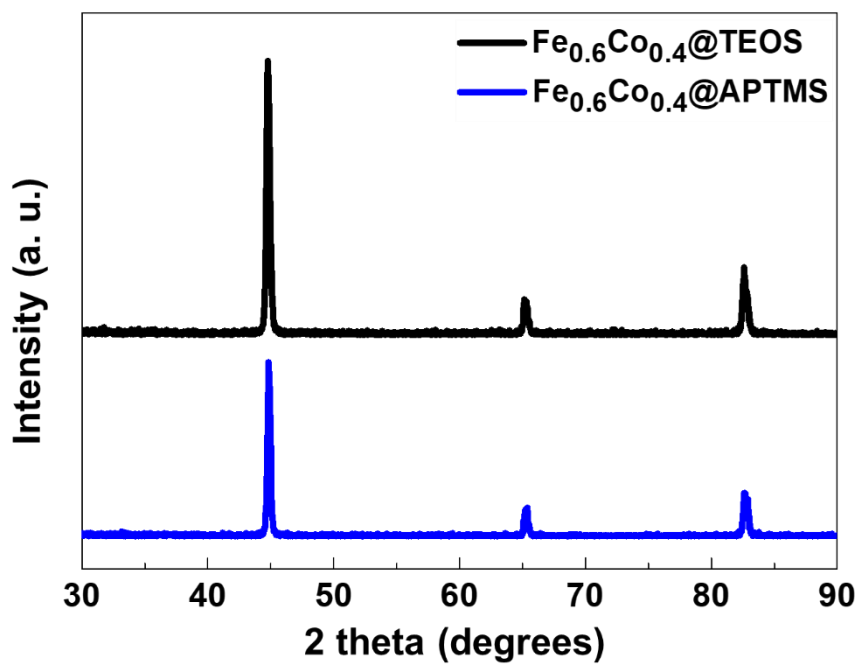


Figure 3.15. XRD patterns of $\text{Fe}_{0.6}\text{Co}_{0.4}@TEOS$ and $\text{Fe}_{0.6}\text{Co}_{0.4}@APTMS$. The well-defined peaks revealed a degree of crystallinity after coated.

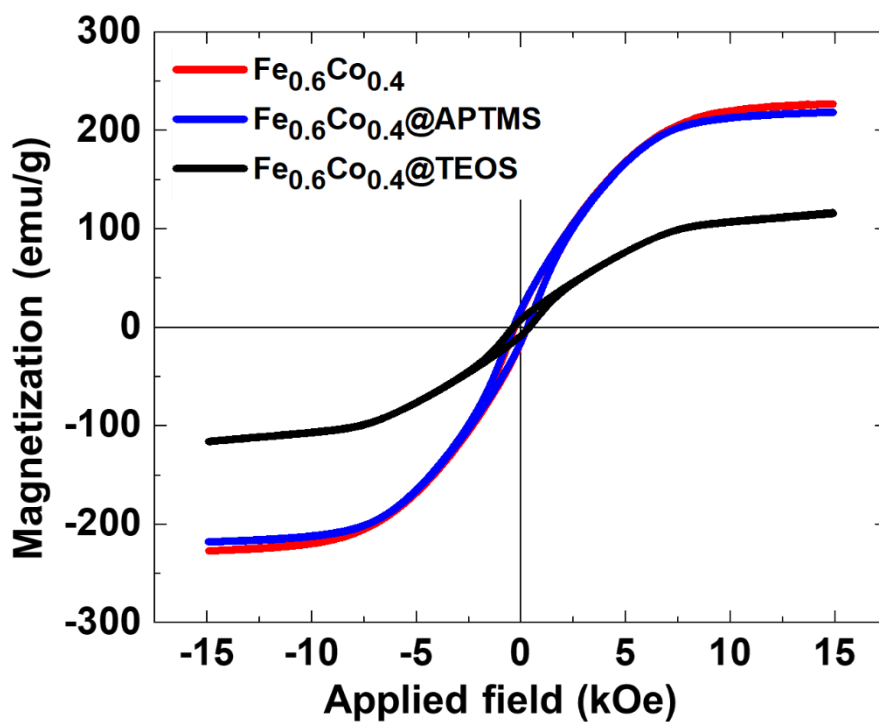


Figure 3.16. Magnetic hysteresis loop of $\text{Fe}_{0.6}\text{Co}_{0.4}$, $\text{Fe}_{0.6}\text{Co}_{0.4}@\text{TEOS}$, and $\text{Fe}_{0.6}\text{Co}_{0.4}@\text{APTMS}$, the inset show the corresponding low-field H_c values.

3.3.7. Electromagnetic Properties of $\text{Fe}_{0.6}\text{Co}_{0.4}@\text{SiO}_2$: Complex Permeability and Permittivity Spectra

Figure 3.17 (a) and **(b)** compares the complex permittivity and permeability spectra of the insulated FeCo particles ($\text{FeCo}@\text{TEOS}$, $\text{FeCo}@\text{APTMS}$) with the spectrum of the raw FeCo particles up to 18 GHz. For a fair comparison, all three samples contain the same amount of FeCo particles (30 wt. %), in spite of the different SiO_2 coating thicknesses. No differences can be identified between the permeability of the samples shown in **Figure 3.17 (b)**, which indicates that the insulating coating does not affect the values of μ' and μ'' , H_c as shown in **Figure 3.16**. The permeability significantly depends on the magnetization and morphology of the magnetic particles, and our insulation coating method does not change the 1-dimensional nano-chained morphology of the FeCo particles after the coating; also, magnetic properties such as M_s and H_a are preserved. On the other hand, the permittivity dramatically increases with 29.21-nm-thickness SiO_2 coating, while it decreases with 2.00-nm-thickness coating. A thin SiO_2 coating insulates individual FeCo particles and reduces electrical connections between them, which leads to decreased permittivity. However, a thick coating increases the surface area of the particles and hence the permittivity also increases. These results show that the permittivity of the FeCo particles can be controlled by adjusting the SiO_2 coating thickness, without affecting the permeability. As the goal of this study is to apply FeCo particles for high frequency electromagnetic wave absorbers, a decreased permittivity is preferred for impedance matching. **Figure 3.18 (a)** and **(b)** compares the raw FeCo particles (black lines) with the $\text{FeCo}@\text{APTMS}$ (blue lines) up to 26 GHz. Each sample contains 50 wt. % of FeCo particles. As can be seen in **Figure 3.17 (a)** and **(b)**, a 2-nm-thick SiO_2 coating leads a decreased permittivity, which is

preserved up to 26 GHz. Since two different measurement systems are used for the wavelength band of 0.5-18 GHz and 18-26 GHz, there is a discontinuity at 18 GHz in the measurement graph (green dotted line).

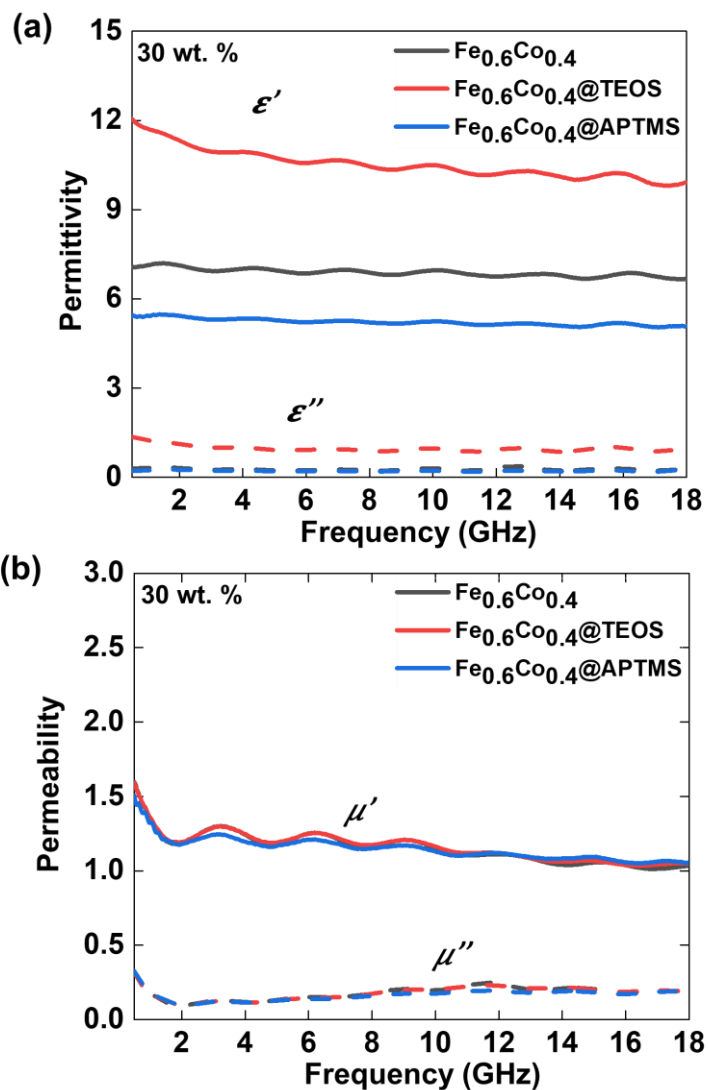


Figure 3.17. (a) Complex permittivity and (b) complex permeability of different condition samples of $\text{Fe}_{0.6}\text{Co}_{0.4}$; as synthesized, @TEOS, and @APTMS at 30 wt. %.

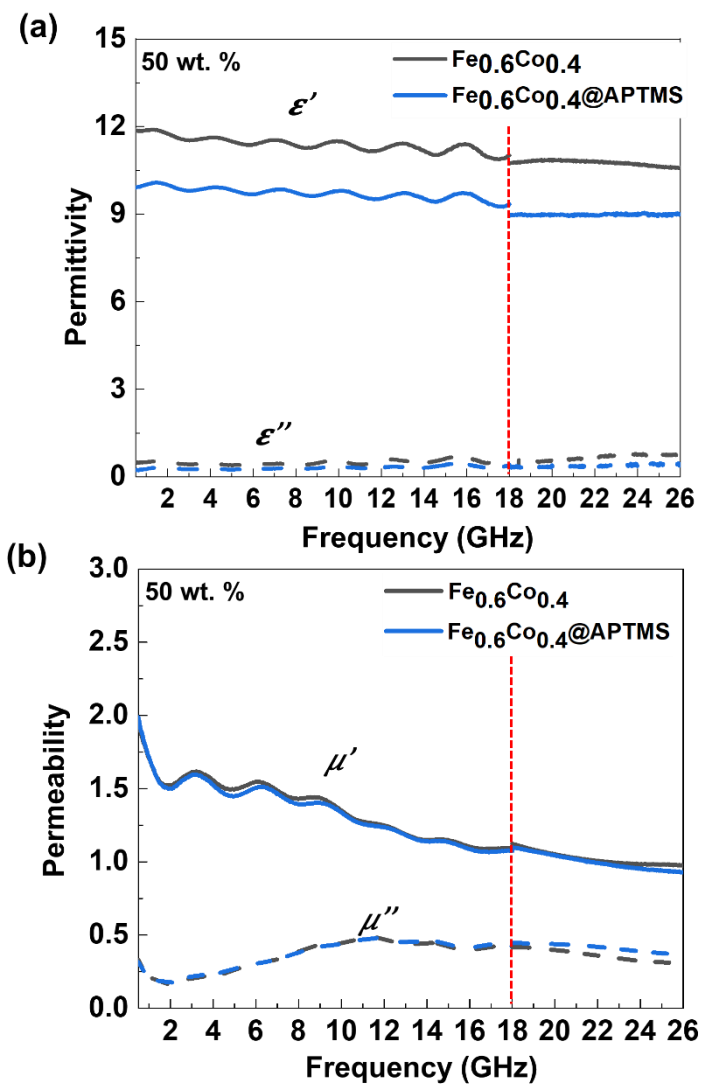


Figure 3.18. The wide frequency dependence of complex permittivity (a) and complex permeability (b) of $\text{Fe}_{0.6}\text{Co}_{0.4}$; as synthesized and $@APTMS$ at 50 wt.% nano-chained FeCo filler loading.

3.3.8. Electromagnetic Wave Absorbing Performance: Reflection Loss and Loss Tangent Calculation

Finally, the electromagnetic wave absorbing performances of the raw FeCo particles and of FeCo@APTMS are evaluated by calculating their reflection loss (RL) at various thicknesses d and frequencies f .²⁶⁻²⁷ RL can be calculated as follows:

$$Z_{in} = Z_o \sqrt{\frac{\mu_r}{\varepsilon_r}} \tanh \left(j \frac{2\pi f d}{c} \sqrt{\mu_r \varepsilon_r} \right) \quad (9)$$

$$RL = 20 \log_{10} \left| \frac{Z_{in} - Z_o}{Z_{in} + Z_o} \right| \quad (10)$$

, where the relative permeability is $\mu_r = \mu' - j\mu''$, the relative permittivity is $\varepsilon_r = \varepsilon' - j\varepsilon''$, and Z_o , Z_{in} , and c indicate the impedance of free space, the respective indices of refraction, and the speed of light in vacuum, respectively.

Figure 3.19 (a) and **(b)** presents the calculated RL values of the raw FeCo particles in 3D and 2D, respectively, while **Figure 3.20 (a)** and **(b)** presents those of FeCo@APTMS. The electromagnetic wave absorbing performance can be evaluated in two ways: (1) according to the maximum RL – how much of the electromagnetic wave is absorbed in the material at certain frequency and (2) according to the absorption bandwidth – the frequency bandwidth where RL exceeds -10 dB (90% absorption).

Remarkably, FeCo particles showed wide and deep RL valleys across the 8-26 GHz range (**Figure 3.19 (a)**); maximum RL was observed to be -42.63 dB at 21 GHz. Electromagnetic wave absorption properties of the FeCo particles are extraordinary when compared with those of FeCo spherical micro particles, which show only shallow absorption valleys (**Figure 3.21**) and maximum RL of -11.46 dB

at 16.6 GHz. Moreover, previous pioneer works were considered as comparative results for evaluating our absorber property.²⁸⁻²⁹ Here, the highly intensified electromagnetic wave absorption properties of FeCo particles are attributed to their high permeability, originating from the uniquely high aspect ratio of the nano-chained morphology.

As is evident in **Figure 3.22 (a)**, the magnetic loss tangent (δ_μ) of raw FeCo shows an abrupt increase up to 18 GHz, reaching a maximum value of 0.3; these values are preserved up to 26 GHz, as indicated in **Figure 3.22 (a)**. The high value of δ_μ of FeCo particles at high frequency (10-26 GHz) indicates exceptional electromagnetic wave absorption performance.

More importantly, FeCo@APTMS particles showed an even more intense maximum RL of -43.49 dB at 16.74 GHz. In particular, FeCo@APTMS particles showed additional RL peaks at 21.42 and 24.72 GHz with intensities of -40.64 and -38.87 dB, respectively. The increased maximum RL and existence of additional RL peaks for FeCo@APTMS are attributable to decreased permittivity and enhanced impedance matching due to the presence of surface insulation coating. Compared with FeCo, FeCo@APTMS also shows a wider absorbing bandwidth, especially at high frequencies over 12 GHz. More red peaks (increased RL) and wider green/blue regions (wider RL bandwidth) can be observed in **Figure 3.20 (b)** compared to **Figure 3.19 (b)**. For example, the EWAM of 1-mm-thick 50 wt. % FeCo@APTMS represents has less than -10 dB bandwidth in 10 GHz range (from 14 to 24 GHz). When the film thickness is decreased to 0.6 mm, EWAM based on FeCo@APTMS is absolutely expected to cover whole frequency band for 5th-generation telecommunication (26-30 GHz). Again, the unprecedentedly-wide absorption bandwidth for FeCo@APTMS at high frequency is attributable to the enhanced

impedance matching at high frequency (**Figure 3.22 (a)** and **(b)**).

The value of δ_μ of FeCo@APTMS shows behavior similar to that of FeCo (**Figure 3.22 (b)**). It has an abrupt increase up to 18 GHz, reaching a maximum value of 0.3; then, the values are preserved up to 26 GHz. Obviously, due to its lowered permittivity, FeCo@APTMS showed a dielectric loss tangent (δ_e) lower than that of raw FeCo; however, the value of δ_e is only a tenth of δ_μ , and its effect on the absorption performance was negligible. This validates the idea that the coating process not only controls the permittivity of FeCo materials but also improves the wave absorbing performance.

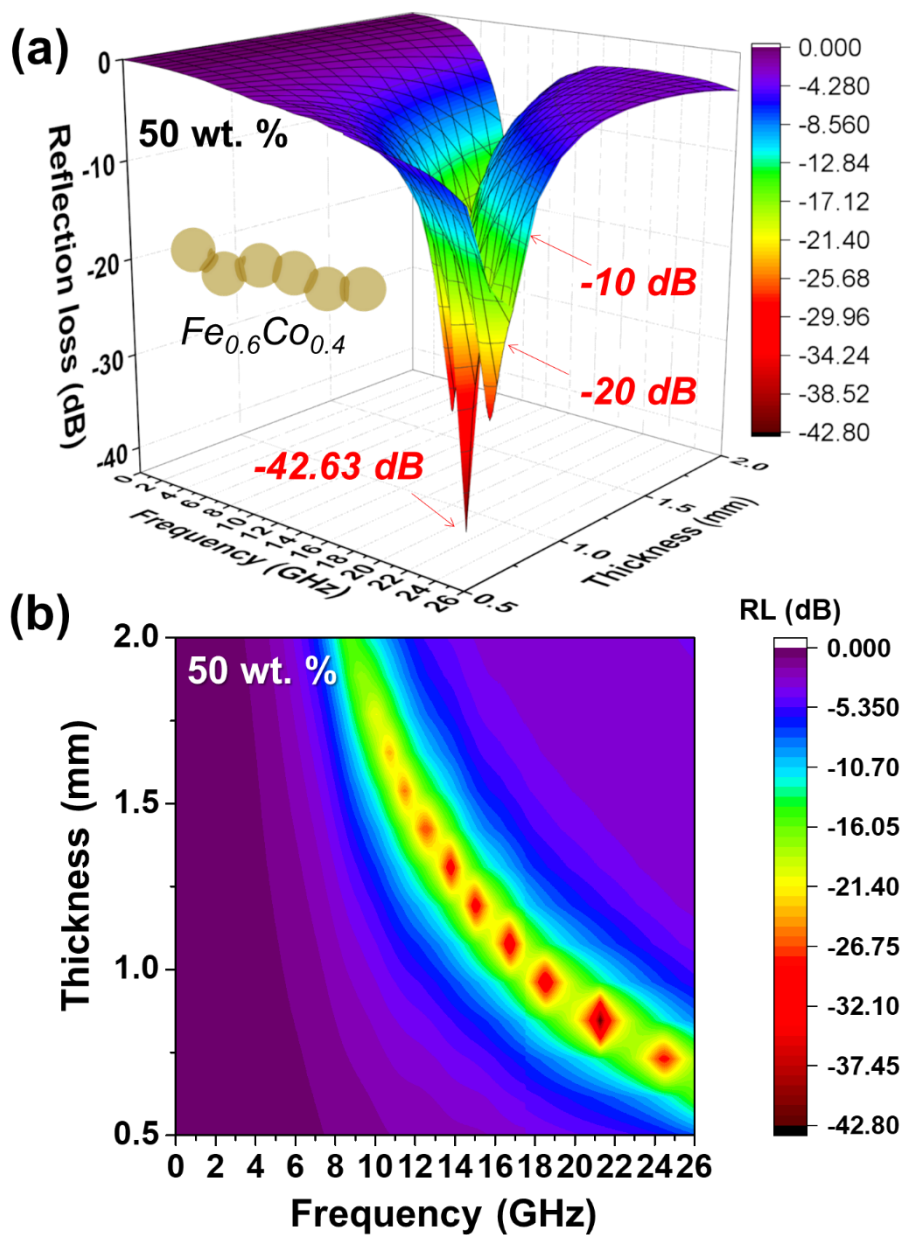


Figure 3.19. (a) 3-D mapping for the overall relationship between reflection loss and frequency (~26 GHz) for $\text{Fe}_{0.6}\text{Co}_{0.4}$ and (b) corresponding 2-D mapping for the thickness influence of $\text{Fe}_{0.6}\text{Co}_{0.4}$.

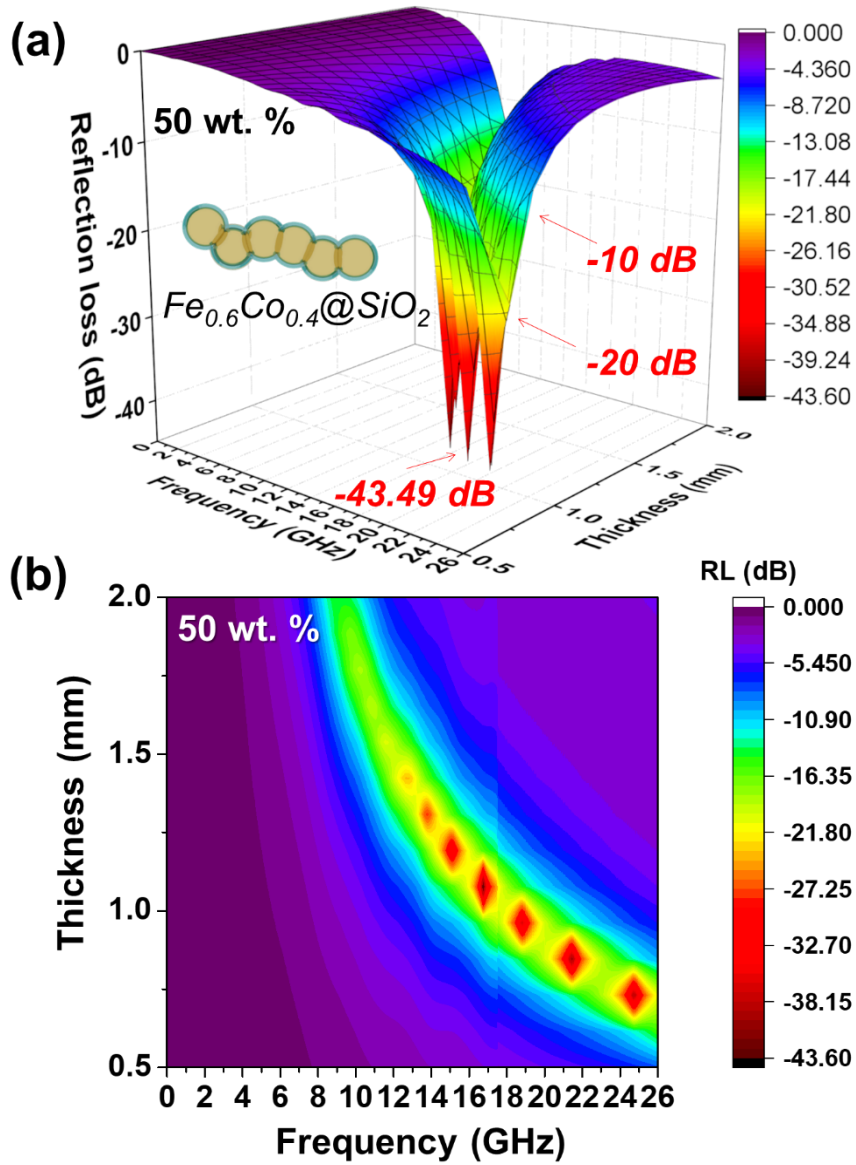


Figure 3.20. (a) 3-D mapping for the overall relationship between reflection loss and frequency ($\sim 26 \text{ GHz}$) for $\text{Fe}_{0.6}\text{Co}_{0.4}@/\text{SiO}_2$ and (b) corresponding 2-D mapping for the thickness influence of $\text{Fe}_{0.6}\text{Co}_{0.4}@/\text{SiO}_2$.

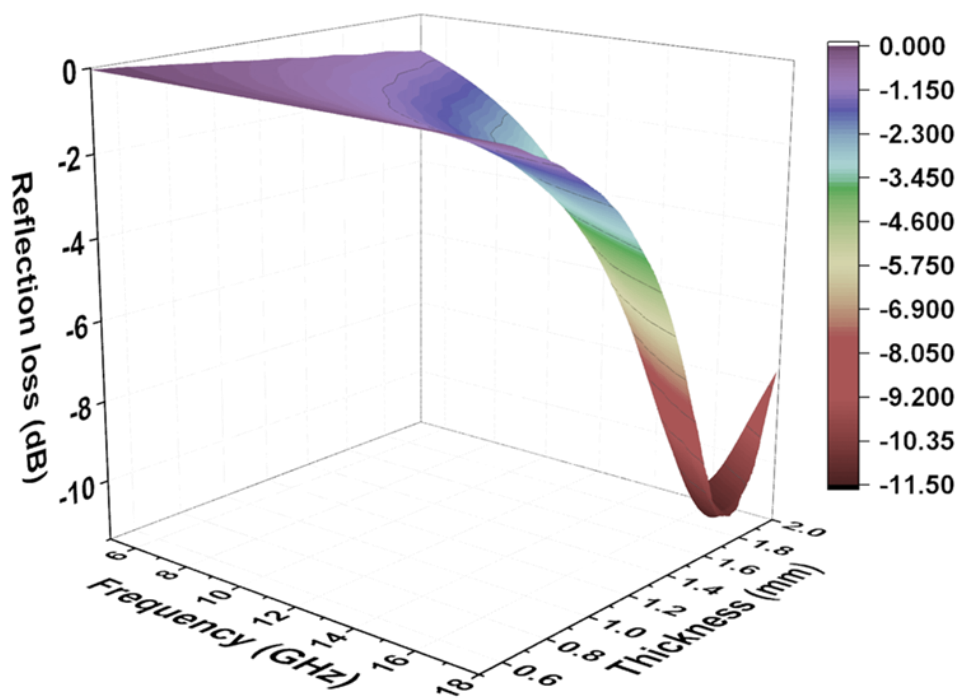


Figure 3.21. 3-D mapping of overall relationship between reflection loss and frequency (5-18 GHz) of the FeCo spherical micro particles which show only shallow absorption valleys and maximum reflection loss of -11.46 dB at 16.6 GHz.

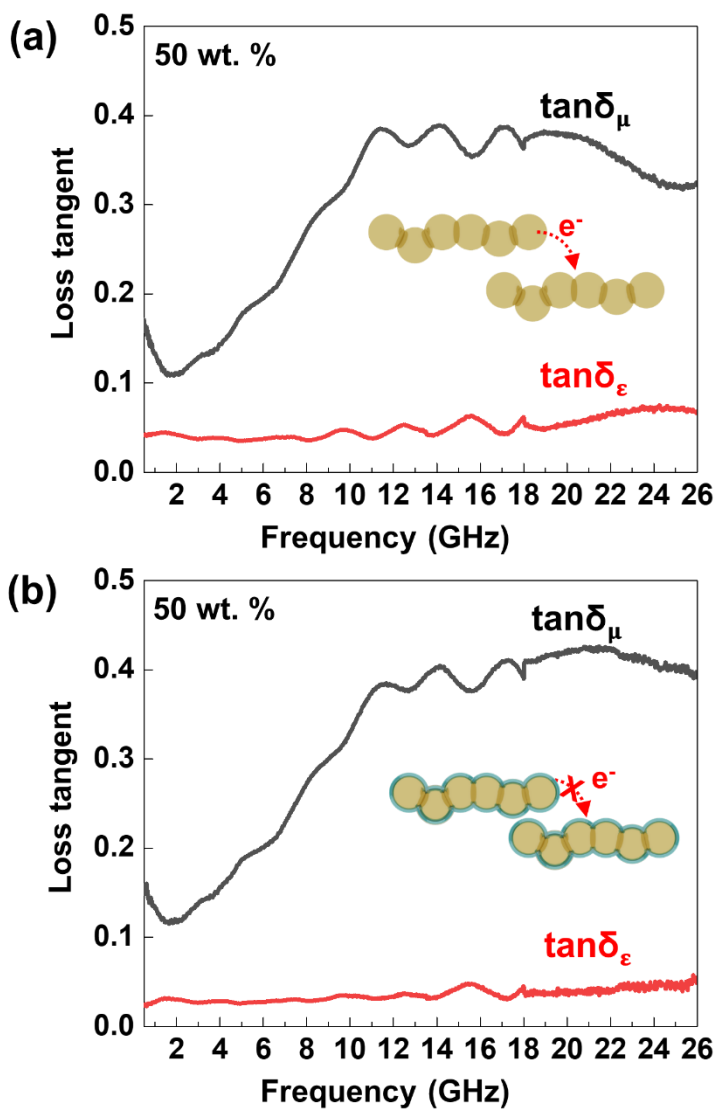


Figure 3.22. The frequency dependence of $\tan\delta_\epsilon$ and $\tan\delta_\mu$ for (a) $\text{Fe}_{0.6}\text{Co}_{0.4}$ and (b) $\text{Fe}_{0.6}\text{Co}_{0.4}@\text{SiO}_2$.

3.3.9. Large-scale Production of FeCo/Epoxy Composite Film

One important advantage of thermal plasma synthesis is that it provides exceptionally-high throughput in the fabrication of metallic nanoparticles. The large-scale industrial RF-ITP system has a production capacity of >10 kg/hour. Taking advantage of the large-scale production of FeCo nanoparticles by using RF-ITP, we additionally demonstrated a large-area electromagnetic wave absorbing film. As shown in **Figure 3.22**, an electromagnetic wave absorber film with areal size of $15 \times 15 \text{ cm}^2$ was produced by simple screen-printing process. This demonstrates the possibility of large-scale production of EWAMs, making them practically applicable to diverse devices.

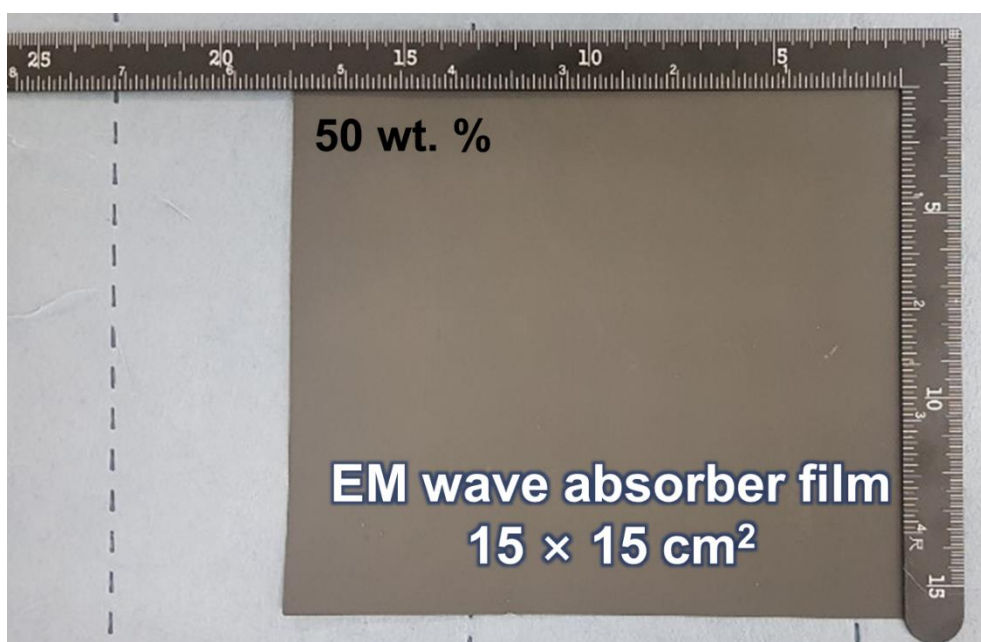


Figure 3.23. Photo of scalable synthesis of electromagnetic wave absorber embodied FeCo nano-chained through composite manufacturing.

3.4. Conclusion

In summary, high-purity FeCo nanoparticles with 1-dimensional chained shapes were prepared by highly-productive thermal plasma synthesis while using mixtures of Fe- and Co-elements as precursors. It was presumed that, during the RF-ITP synthesis, spherical FeCo nanoparticles were first formed through a nucleation and growth process; then, the high temperature zone of the thermal plasma accelerated diffusion of the constituent elements, leading to surface-consolidation between particles at the moment of collision and unusual nano-chained morphologies of FeCo particles. Inter-particle diffusion and the formation of chains were visually supported through in-situ thermal TEM analysis.

Systematic control of the composition and magnetic properties of $\text{Fe}_x\text{Co}_{1-x}$ nano-chained particles has been accomplished by changing the mixing ratio (Fe-to-Co) of the precursors, i.e. 7:3 to 3:7. The highest M_s of 230.4 emu/g was obtained at the composition of $\text{Fe}_{70}\text{Co}_{30}$, while the aspect ratio of nano-chained FeCo was kept within 4-6 in the composition of interest. With high M_s of 227 emu/g and aspect ratio of 5.5, $\text{Fe}_{0.6}\text{Co}_{0.4}$ nano-chained particles exhibited overwhelmingly intensified complex permeability, 19.45% higher than that of $\text{Fe}_{0.6}\text{Co}_{0.4}$ spherical micro-particles; this improvement is attributed to the moving of Sneek's limit far above the GHz range.

In addition, precisely-controlled and uniform surface SiO_2 coating on FeCo nano-chained particles effectively modulated the complex permittivity. In particular, $\text{Fe}_{0.6}\text{Co}_{0.4}@\text{SiO}_2$ with 2.00 nm thickness provided optimally reduced permittivity, which opens possibilities of improved impedance matching at frequencies of 10-26 GHz with minimal absorbing film thickness. Noticeably, a composite

electromagnetic wave absorber comprising $\text{Fe}_{0.6}\text{Co}_{0.4}$ nano-chained particles with 2.00 nm thick surface insulation demonstrated the lowest RL value of -43.49 dB at 16.74 GHz and -10 dB (90% absorbance) bandwidth of 19.28 GHz; a thickness of 0.85 mm was also achieved.

It can be assumed that nano-chained FeCo particles with high aspect ratio can cover a wide frequency, and this gives us a way to reduce the layer thickness of the magnetic absorbent and also to obtain economic benefits. Our results guarantee that low-cost and high-throughput production of nanoparticles with beneficial 1-dimensional morphologies and unprecedented magnetic properties can be used to fabricate high-efficiency EWAMs with minimal thickness targeted to the GHz range (refer to **Figure 3.24**).

To investigate the relationship between shape modulation and complex permeability, a function associated with shape modulation was derived using an empirical calculation method (See **Figure 3.25** and **3.26**). Initially, the permeability value was estimated using the equation, $\mu = \mu_i + A \tanh(kf)$, where A represents the slope, k is equal to 10^6 (MHz), and f denotes the frequency (as depicted in **Figure 3.25**). Furthermore, the f_{FMR} of spherical FeCo and FeCo nanochains with varying compositions was also estimated, considering that the f_{FMR} of FeCo alloys typically falls within the MHz range. Using the estimated μ_i values, experimental values were plotted on a graph relative to the anisotropic function based on the aspect ratio, as illustrated in **Figure 3.26**. From this plot, an empirical formula was derived, as depicted in **Figure 3.26**, with the corresponding coefficients provided. In essence, this newly formulated function enables the verification of the relationship between shape modulation and permeability, thereby validating Snoek's law. Moreover, this function allows for the calculation of any three of the following factors— μ_i , M_s , and

f_{FMR} —given that two of these factors are known.

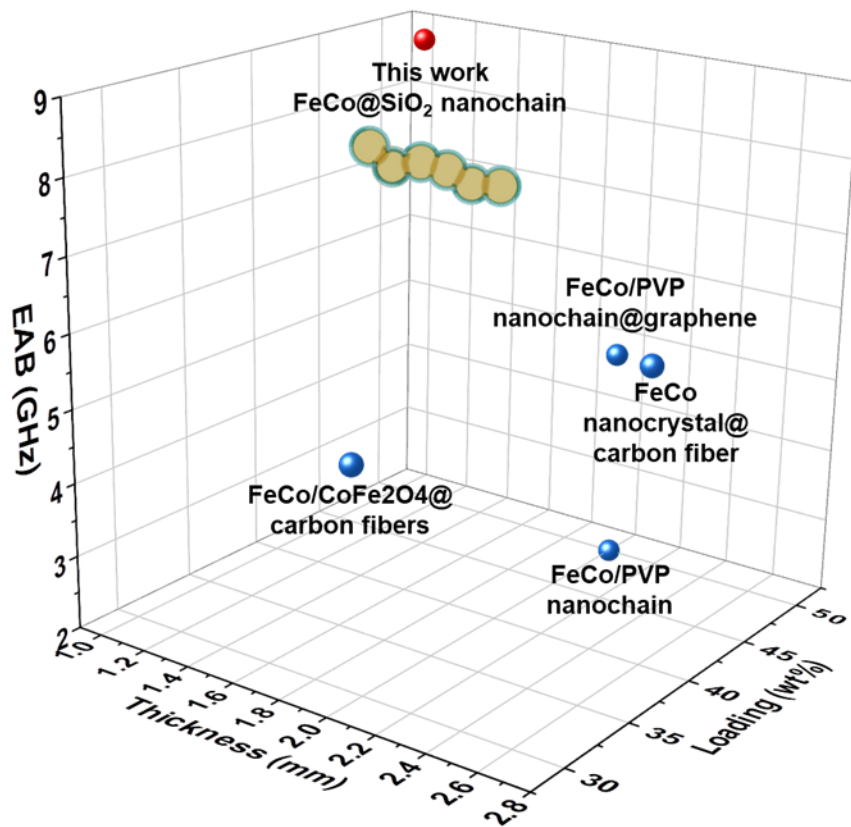
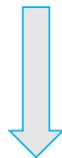


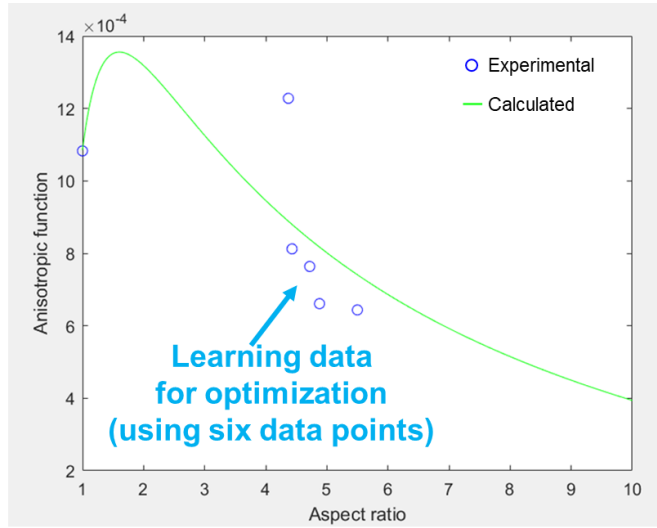
Figure 3.24. 3-D graph showing this work compared to other works. This work guarantee that high-throughput production of nanoparticles with beneficial 1-dimensional morphologies and unprecedented magnetic properties can be used to fabricate high-efficiency EWAMs with minimal thickness.

	$H_0/H_\phi = 1$	$H_0 > H_\phi$				
Shape	Spherical	Nanochain				
Composition	Fe0.6Co0.4	Fe0.3Co0.7	Fe0.4Co0.6	Fe0.5Co0.5	Fe0.7Co0.3	Fe0.6Co0.4
Hypothetical FMR (MHz)	100	138	144.9	155.04	161.9	168.9
Experimental Ms (emu/g)	227	145.5	209.54	208.31	230.4	227
Aspect ratio	1	4.43	4.88	4.37	4.72	5.5



$\mu = \mu_i + A \tanh(kf)$						
Coefficients	Spherical	Fe0.3Co0.7	Fe0.4Co0.6	Fe0.5Co0.5	Fe0.7Co0.3	Fe0.6Co0.4
μ_i	24.578	24.6573	24.6643	24.6679	24.6597	24.6821
A	-23.419	-23.344	-23.3332	-23.3297	-23.3378	-23.3158
k	10^6					

Figure 3.25. Tables showing experimental and estimated value of various factors.



Anisotropic Function:

$\frac{\mu_i}{f_{FMR}M_s} = F(AR) = \left(\alpha \frac{\ln(\beta \cdot AR)}{AR} + \gamma \right)$	
Coefficients	value
Alpha	0.0054
Beta	1.6050
Gamma	-0.0015

Figure 3.26. Graph showing estimated and calculated values of FeCo alloys with different aspect ratios relative to the anisotropic function and the derived equation and coefficients from the graph.

3.5. References

1. Shigeta, M.; Hirayama, Y.; Ghedini, E., Computational Study of Quenching Effects on Growth Processes and Size Distributions of Silicon Nanoparticles at a Thermal Plasma Tail. *Nanomaterials* **2021**, *11* (6), 1370.
2. Bathgate, S. N.; Bilek, M. M. M.; McKenzie, D. R., Electrodeless Plasma Thrusters for Spacecraft: A Review. *Plasma Science and Technology* **2017**, *19* (8), 083001.
3. Samal, S., Thermal Plasma Technology: The Prospective Future in Material Processing. *Journal of cleaner production* **2017**, *142*, 3131-3150.
4. Taylor, P. R.; Pirzada, S. A., Thermal Plasma Processing of Materials: A Review. *Advanced Performance Materials* **1994**, *1*, 35-50.
5. Szépvölgyi, J.; Mohai, I.; Károly, Z.; Gál, L., Synthesis of Nanosized Ceramic Powders in a Radiofrequency Thermal Plasma Reactor. *J. Eur. Ceram. Soc.* **2008**, *28* (5), 895-899.
6. Seo, J. H.; Kim, D. U.; Nam, J. S.; Hong, S. H.; Sohn, S. B.; Song, S. M., Radio Frequency Thermal Plasma Treatment for Size Reduction and Spheroidization of Glass Powders Used in Ceramic Electronic Devices. *J. Am. Ceram. Soc.* **2007**, *90* (6), 1717-1722.
7. Li, M.; Tang, H.-B.; Ren, J.-X.; York, T. M., Modeling of Plasma Processes in the Slowly Diverging Magnetic Fields at the Exit of an Applied-Field Magnetoplasma dynamic Thruster. *Physics of Plasmas* **2013**, *20* (10).
8. Colombo, V.; Deschenaux, C.; Ghedini, E.; Gherardi, M.; Jaeggi, C.; Leparoux, M.; Mani, V.; Sanibondi, P., Fluid-Dynamic Characterization of a Radio-Frequency Induction Thermal Plasma System for Nanoparticle Synthesis. *Plasma*

Sources Sci. Technol. **2012**, 21 (4), 045010.

9. Crusius, A.; Schlickeiser, R., Synchrotron Radiation in a Thermal Plasma with Large-Scale Random Magnetic Fields. *Astron. Astrophys.* **1988**, 196, 327-337.
10. Svidzinski, V.; Kim, J.; Spencer, J.; Zhao, L.; Galkin, S.; Evstatiev, E., Hot Plasma Dielectric Response to Radio-Frequency Fields in Inhomogeneous Magnetic Field. *Physics of Plasmas* **2016**, 23 (11), 112101.
11. Cohen, R.; Rognlien, T., Electron Kinetics in Radio-Frequency Magnetic Fields of Inductive Plasma Sources. *Plasma Sources Sci. Technol.* **1996**, 5 (3), 442.
12. Hirano, K.-i.; Cohen, M., Diffusion of Cobalt in Iron-Cobalt Alloys. *Transactions of the Japan Institute of Metals* **1972**, 13 (2), 96-102.
13. Fishman, S. G.; Gupta, D.; Lieberman, D. S., Diffusivity and Isotope-Effect Measurements in Equiatomic Fe-Co. *Phys. Rev. B* **1970**, 2 (6), 1451-1460.
14. Fishman, S. G.; Jeffery, R. N., Effect of High Pressure on Self-Diffusion in Concentrated Feco Alloys. *Phys. Rev. B* **1971**, 3 (12), 4424-4427.
15. Nitta, H.; Iijima, Y.; Tanaka, K.; Yamazaki, Y.; Lee, C.-G.; Matsuzaki, T.; Watanabe, T., Self-Diffusion in Unidirectionally Solidified Fe–50 At.% Co Alloys at 833–1123 K. *Materials Science and Engineering: A* **2004**, 382 (1-2), 243-249.
16. Varotsos, P.; Alexopoulos, K., Calculation of Diffusion Coefficients at Any Temperature and Pressure from a Single Measurement. I. Self Diffusion. *Phys. Rev. B* **1980**, 22 (6), 3130.
17. Graham, D.; Tomlin, D., Self-Diffusion in Iron. *Philosophical Magazine* **1963**, 8 (93), 1581-1585.
18. Naghavi, S. S.; Hegde, V. I.; Wolverton, C., Diffusion Coefficients of Transition Metals in Fcc Cobalt. *Acta Mater.* **2017**, 132, 467-478.
19. Zhang, B., Calculation of Self-Diffusion Coefficients in Iron. *AIP Adv.* **2014**,

4 (1), 017128.

20. Lv, H.; Liang, X.; Ji, G.; Zhang, H.; Du, Y., Porous Three-Dimensional Flower-Like Co/Coo and Its Excellent Electromagnetic Absorption Properties. *ACS Appl. Mater. Interfaces* **2015**, 7 (18), 9776-9783.
21. Wang, J.; Zhou, H.; Zhuang, J.; Liu, Q., Magnetic Γ -Fe₂O₃, Fe₃O₄, and Fe Nanoparticles Confined within Ordered Mesoporous Carbons as Efficient Microwave Absorbers. *PCCP* **2015**, 17 (5), 3802-3812.
22. Jing, L.; Wang, G.; Duan, Y.; Jiang, Y., Synthesis and Electromagnetic Characteristics of the Flake-Shaped Barium Titanate Powder. *J. Alloys Compd.* **2009**, 475 (1-2), 862-868.
23. Buznikov, N.; Iakubov, I.; Rakhmanov, A.; Sboyshakov, A., High-Frequency Magnetic Permeability of Nanocomposite Film. *J. Magn. Magn. Mater.* **2005**, 293 (3), 938-946.
24. Wang, G.; Gao, Z.; Wan, G.; Lin, S.; Yang, P.; Qin, Y., High Densities of Magnetic Nanoparticles Supported on Graphene Fabricated by Atomic Layer Deposition and Their Use as Efficient Synergistic Microwave Absorbers. *Nano Res.* **2014**, 7, 704-716.
25. Liu, J.; Cao, M.-S.; Luo, Q.; Shi, H.-L.; Wang, W.-Z.; Yuan, J., Electromagnetic Property and Tunable Microwave Absorption of 3d Nets from Nickel Chains at Elevated Temperature. *ACS Appl. Mater. Interfaces* **2016**, 8 (34), 22615-22622.
26. Lv, H.; Guo, Y.; Wu, G.; Ji, G.; Zhao, Y.; Xu, Z. J., Interface Polarization Strategy to Solve Electromagnetic Wave Interference Issue. *ACS Appl. Mater. Interfaces* **2017**, 9 (6), 5660-5668.
27. Xu, H.; Yin, X.; Zhu, M.; Han, M.; Hou, Z.; Li, X.; Zhang, L.; Cheng, L.,

Carbon Hollow Microspheres with a Designable Mesoporous Shell for High-Performance Electromagnetic Wave Absorption. *ACS Appl. Mater. Interfaces* **2017**, *9* (7), 6332-6341.

28. Yin, P.; Zhang, L.; Wang, J.; Feng, X.; Dai, J.; Tang, Y., Facile Preparation of Cotton-Derived Carbon Fibers Loaded with Hollow Fe₃O₄ and CoFe Nps for Significant Low-Frequency Electromagnetic Absorption. *Powder Technol.* **2021**, *380*, 134-142.

29. Yin, P.; Zhang, L.; Jiang, Y.; Zhang, Y.; Wang, J.; Feng, X.; Dai, J.; Tang, Y., Recycling of Waste Straw in Sorghum for Preparation of Biochar/(Fe, Ni) Hybrid Aimed at Significant Electromagnetic Absorbing of Low-Frequency Band. *Journal of Materials Research and Technology* **2020**, *9* (6), 14212-14222.

Chapter 4. Boron Nitride Incorporated 1D-2D FeCo Nanobelts

4.1. Introduction

4.1.1. Synthesis of FeCo Nanobelts: Planetary Ball-Mill

In this Chapter, additional shape-modulation is carried out in order to raise the complex permeability value of the as-synthesized FeCo nanochain, where planetary ball-milling is used. Planetary ball-milling is used to grind and mix materials on a small scale.¹ In this case, thermal-plasma synthesized FeCo nanochains are flattened through ball-milling, forming a 2-dimensional belt-like structure (FeCo nanobelt).² In a planetary ball mill, the grinding jars are arranged eccentrically on a sun wheel, which rotates in the opposite direction to the grinding jar. This causes the balls inside the jars to move in a circular trajectory, impacting and grinding the materials present in the jars. The combination of rotational and centrifugal forces generated by the planetary motion of the mill leads to high-energy impacts between the balls and the materials, resulting in effective grinding, mixing, and alloying.³⁻⁵

Planetary ball-milling offers several advantages over other traditional methods. It allows for efficient grinding of particles of different sizes. It is also very simple and easy to use and suitable for materials of all degree of hardness. It can also be used for both wet and dry grinding. Such ball-milling can contribute to flattening materials with high aspect ratio, such as nanorods and fibers. The high-energy impacts in planetary ball-mills can promote flattening. The powder particles are flattened by the compressive forces caused by the impact of the balls.³ The high

kinetic energy of the milling balls results in intense collisions and deformation of the particles. When a ball impacts a particle or cluster, it exerts a significant force on the contact area, causing plastic deformation. This deformation can lead to changes in the shape of the particle or cluster, including flattening and elongation.⁶

4.1.2. Shape Anisotropy of FeCo Nanobelts

Figure 4.1 shows an overview of the newly developed nanomaterial-processing technologies used to fabricate EMW-absorbing membranes. The thermal plasma technique explored in this work allows large-scale production of one-dimensional FeCo nanochains with high magnetic performance (**Figure 4.1 (a)**). Fe and Co precursor powders were injected into the thermal plasma system, which vaporized while passing through the hot section. The nucleation and diffusion growth of the FeCo nanoparticles occurred in the high-temperature chambers. Subsequently, collisions and surface consolidation occurred between the FeCo nanoparticles, forming FeCo alloys with a nanochained structure. In the second step, the as-synthesized FeCo nanochains were flattened via planetary ball milling to achieve shape anisotropy. Such shape modulation is an effective method for enhancing complex permeability. The dependence of the shape anisotropy of magnetic materials can be explained by the relationship between complex permeability and ferromagnetic resonance (FMR). FMR is derived from the natural resonance of the magnetic moment under an external field. At a specific FMR frequency (f_{FMR}), the real part of the complex permeability significantly drops while the imaginary part increases and reaches its maximum peak, resulting in maximum energy loss.[#] Kittel equation defines the effect of shape anisotropy on FMR by equation 7. The complicated Kittel equation can be rewritten as

$$f_{\text{FMR}} = \frac{\gamma}{2\pi} \mu_0 \sqrt{H_\theta H_\phi} \quad (9)$$

Where H_θ is the effective field in-plane with the FMR excitation plane, and H_ϕ is the effective field out-of-plane. Snoeks' limit also relates the complex permeability and the FMR by the following equation 6. However, according to the equation, there

is a trade-off between the complex permeability and FMR as they cannot achieve a high value simultaneously. Consequently, magnetic materials with weak anisotropy cannot perform well in the high-frequency range. However, Snoek's limit can be exceeded by introducing shape anisotropy as mentioned in equation 8. As the shape was modulated, the demagnetizing factors differed for each material according to the magnetic dependence on the easy axis, as shown in **Figure 4.1 (b)**. The series of FE-SEM images shown in Figure 1c and d capture the FeCo nanochains and flattened FeCo nanobelts, demonstrating that the rod-like nanochains were effectively flattened out into ribbon-like nanobelts.

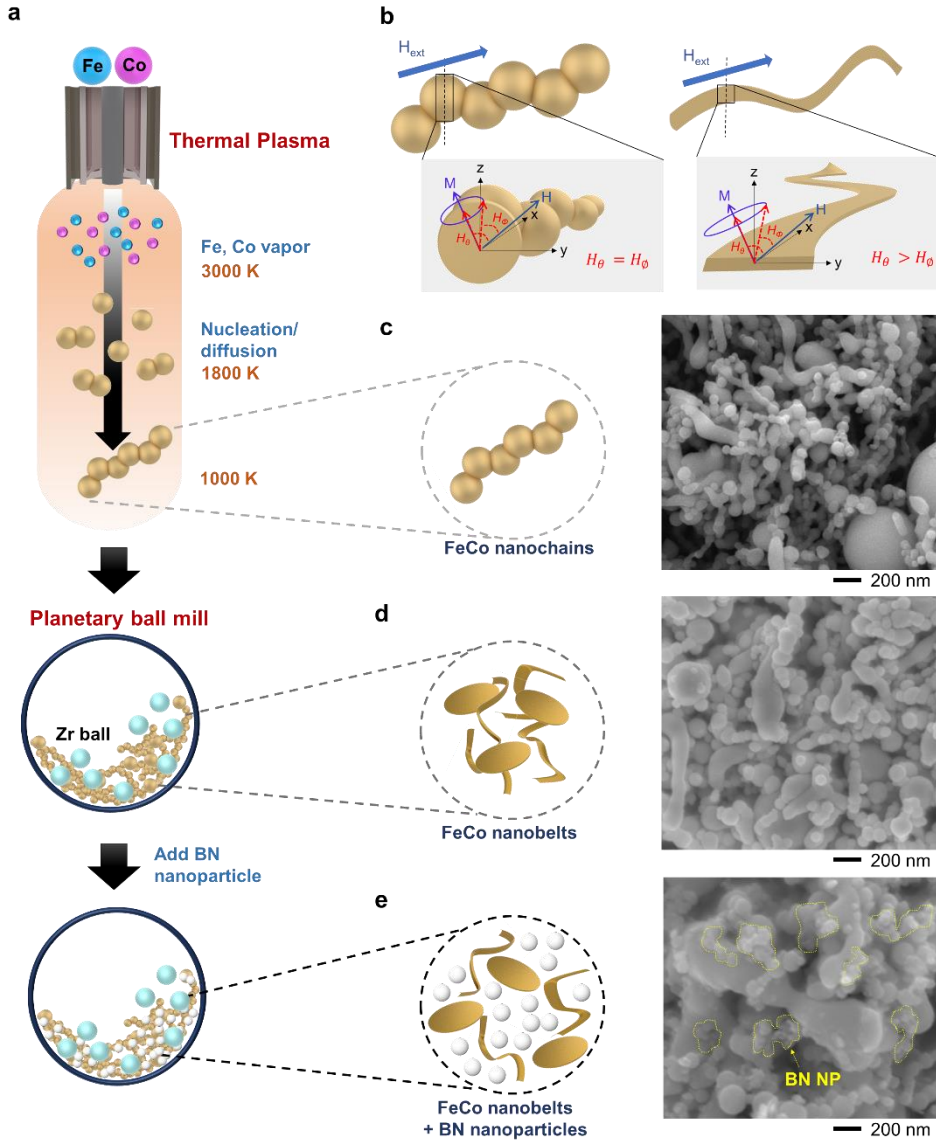


Figure 4.1. Nanomanufacturing strategy of the FCBN. (a) Schematics showing the shape modulation process to fabricate the FCBN, where one-dimensional FeCo nanochains are synthesized with a high-temperature thermal plasma system. Subsequently, the BN nanoparticles are incorporated with the FeCo nanobelts manufactured through a planetary ball mill. (b) Illustration to compare the effect of shape anisotropy in between the FeCo nanochains and FeCo nanobelts. SEM images (right) and corresponding illustrations (left) of (c) FeCo nanochains, (d) nanochains ball-milled into FeCo nanobelts, (e) ball-milled FeCo nanobelts with the addition of BN nanoparticles.

4.2. Experimental Section

4.2.1. Materials

The Fe and Co powders were purchased from Taewon Scientific Co., Ltd., South Korea. Boron nitride nanoparticles (h-BN, 99.8 %, 40 nm) were purchased from Unitech Corporation. Isopropyl alcohol (IPA, C₃H₈O, 99.5%) was purchased from Samchun Chemicals. Thermoplastic urethane TPU (A-9410) was purchased from Songwon Industrial Chemical Co., Ltd., Korea.

4.2.2 Preparation of FeCo nanochains, FeCo nanobelts, and FCBN

The FeCo nanochains were fabricated using a thermal plasma system, TEKNA PL-35LS (Tekna Plasma Systems, Inc.). The Fe and Co precursor powders were mixed at a ratio of 6:4 given that, compared with other mixing ratios, it achieves the highest complex permeability value. The mixed powder was injected into the thermal plasma system through a feeder at a rate of 5 g/min. The powder vaporized as it reached the hot zone of the plasma chamber with the aid of a carrier gas. The vaporized powder then passed through a cooler section of the system, which was cooled by a quenching gas. The powder underwent nucleation and diffused into a nanochain morphology as it passed through different sections of the system.

Planetary ball milling (Fritsch, Pulverisette 6) was used to flatten the as-synthesized FeCo nanochains into nanobelts. Zr balls of size 6 mm were used with a 1:30 powder-to-ball ratio and ground in IPA at 250 rpm for 24 h. The ball-milled FeCo nanobelts were collected with an Nd magnet and washed with ethanol at least three times. The collected FeCo nanobelts were dried in a glove box overnight.

BN nanoparticles (10 and 30 wt%) were added to the FeCo and IPA

solutions and ball-milled under the same conditions as those mentioned earlier. The ball-milled FeCo nanobelt + BN nanoparticle 10 and 30 wt% (FCBN (10 wt%, 24 h), FCBN (30 wt%, 24 h)) solutions were collected via overhead stirring while heating the solution at 100 °C. Once all the alcohol had evaporated, the powder was collected and dried in a glove box overnight.

In addition, we prepared FeCo/Tetraethyl orthosilicate (TEOS) to compare the thermal conductivity values. Solutions of NH₄OH-H₂O and TEOS-absolute ethyl alcohol were prepared and magnetically stirred for 15 min at 60 °C. The two solutions were then mixed and the prepared FeCo nanochains were added to the solution and mechanically stirred for 3 h at room temperature. FeCo/TEOS was obtained after washing with ethanol and drying at 60 °C in a vacuum oven overnight.

4.2.3 Fabrication of FCBN-TPU EMW absorbing membrane

The FeCo nanochains, FeCo nanobelts, and FCBN (x, 24 h) (x = 10, 30 wt%) powders were mechanically mixed with solvent-dissolved TPU using a planetary mixer (Thinky, ARE-310) with a fixed filler ratio of 50 wt%. The mixture was then cast to a thickness of 120 µm using a doctor blade. The cast films were dried overnight in a convection oven at 110 °C. The obtained film was vacuum-pressed by stacking the film and hot-pressing at 110 °C to achieve a flexible composite film with a thickness of 2 mm. The stacked films were hot pressed for 30 min at 10 MPa. Subsequently, the pressed film was left to cool naturally to room temperature, and the obtained film was used to characterize the electromagnetic parameters.

4.2.4 Characterization

The structural morphology was characterized by field-emission scanning electron microscopy (FE-SEM, JSM-7610F, JEOL) and field-emission transmission electron microscopy (FE-TEM, Talos F200X, Thermo Fisher Scientific). The crystal structure and elemental composition were observed by X-ray diffraction (XRD, Rigaku D/Max-2500VL/PC). Thermal conductivity was evaluated using a laser flash analyzer (LFA 467 Hyperflash, Netzsch). The magnetic properties were measured using a vibrating sample magnetometer (VSM, EZ9, Microsense). The electromagnetic properties, complex permeability, and permittivity were investigated using a vector network analyzer (VNA, N5222B, Keysight). For the frequency range 0.5–18 GHz, a Keysight 85051 B verification kit and a 10 cm coaxial airline were utilized with the VNA. The specimen was processed into a donut-shaped shape with an outer diameter of 7 mm, inner diameter of 3.04 mm, and thickness of 2 mm. The bending test was performed using an order-made fiber-bending machine (Science Town, Korea) with a curvature of 1 mm.

4.3. Results and Discussion

4.3.1. Structural Morphology Characterization of FeCo Nanobelt and FeCo/BN Nanobelt (FCBN)

While enhancing the complex permeability of the FeCo nanochains through shape modulation is the main goal, controlling the complex permittivity is another vital step. The flattening process for FeCo nanochains increases the complex permeability; however, it also leads to a tradeoff with the complex permittivity. Generally, the planetary mixer technique leads to unwanted interconnections of the nanomaterials because of the percolation model by Rajagopal and Satyam, which increases the electrical conductivity, and thus, contributes to increased complex permittivity.⁷ To optimize the complex permittivity in magnetic absorbing materials, dielectric materials such as carbon, ceramics, and polymers are incorporated simultaneously.⁸⁻¹⁰ In our study, we employed BN nanoparticles with high intrinsic thermal conductivity to fabricate a chemically and thermally superior EMW-absorbing membrane. BN nanoparticles were simultaneously ball-milled with the FeCo nanochains. The small BN nanoparticles were well dispersed between the FeCo nanobelts to prevent interconnection between the nanobelts, thereby decreasing the electrical conductivity.

Figure 4.2 presents the structural, thermal, and magnetic characteristics of the manufactured FeCo nanomaterials. Morphological observations revealed numerous chain-shaped FeCo chains in the linear direction (**Figure 4.2 (a)**). The flattening process of the FeCo chains in the TEM image in **Figure 4.2 (b)** leads to a structural change from diffused nanoparticles to belt-like nanostructures. Finally, BN nanoparticles as a dielectric material were fully intercalated throughout and between

the FeCo nanobelts owing to interfacial polarization (**Figure 4.2 (c)**). The surface charge of the FeCo nanobelts became relatively positive, whereas the BN nanoparticles had negative charges, which resulted in highly reliable and successful absorption of BN nanoparticles on the surface of the FeCo nanobelts. The EDS analysis in **Figure 4.3** also demonstrates the fully intercalated BN nanoparticles throughout the FeCo nanobelts. TEM imaging and the measured size histogram displayed in **Figure 4.4** show that the prepared BN nanoparticles have an average dimension of 30 nm.

As shown in **Figure 4.5**, the XRD data reveal that the crystal structures of the FeCo nanochains and nanobelts are indicated by two sharp peaks at 44.8° and 65.2° (matched with JCPDS #44-1433). FCBN (BN nanoparticle content of 10 wt%) shows an additional weak peak at 26.5° , which is caused by the BN nanoparticles (reference: JCPDS #85-1068).

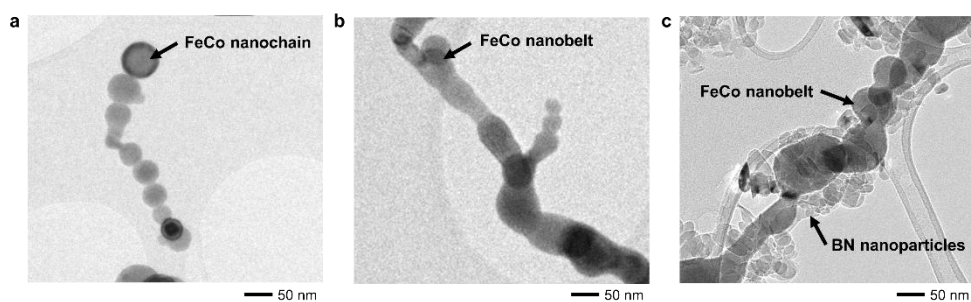


Figure 4.2. Structural characterization of the manufactured FeCo nanomaterials. TEM images of (a) as-synthesized FeCo nanochain, (b) ball-milled FeCo nanobelt, and (c) FeCo nanobelts intercalated with boron nitride nanoparticles.

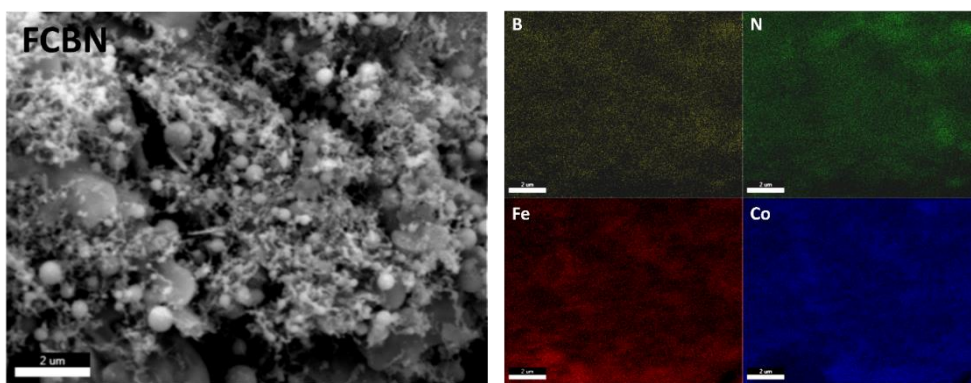


Figure 4.3. SEM image of FCBN and their corresponding EDS mapping for boron (B), nitrogen (N), iron (Fe), and cobalt (Co) atoms. BN nanoparticles are fully intercalated between the FeCo nanobelts.

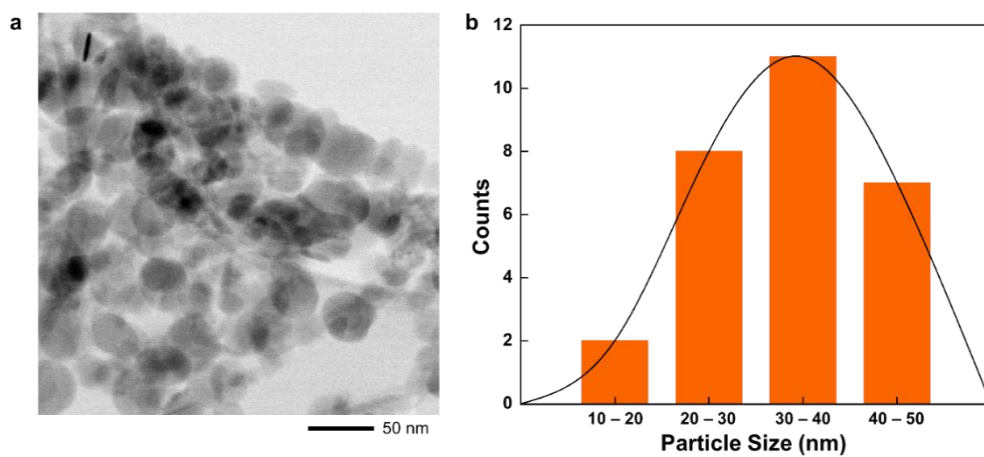


Figure 4.4. (a) TEM image of boron nitride nanoparticles. (b) Measured size histogram of boron nitride nanoparticles show that the nanoparticles have an average dimension of 30 nm.

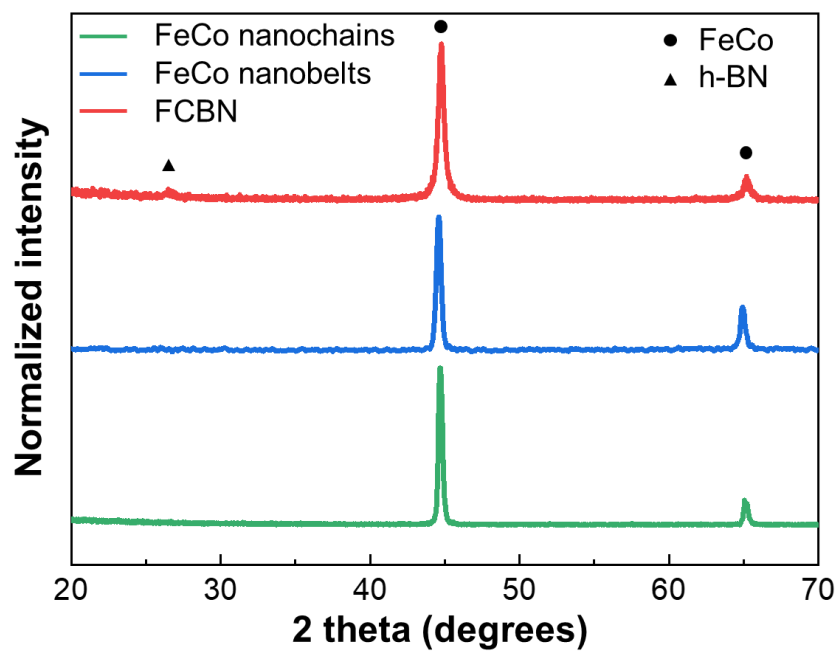


Figure 4.5. XRD analysis of three different samples, including the FeCo nanochains, FeCo nanobelts, and FCBN.

4.3.2. Thermal and Magnetic Properties of FeCo Nanobelts and FCBN

To verify the superior heat dissipation capability of BN nanoparticles, we conducted thermal conductivity measurements (**Figure 4.6**). The incorporation of the BN nanoparticles at 10 wt% improves the thermal conductivity from 0.34 W/(m·K) with no BN up to 0.62 W/(m·K). To compare the thermal conductivity, tetraethyl orthosilicate (TEOS), which is a representative dielectric material for magnetic-based EMW absorbers,¹¹ was coated on the FeCo nanochains. FeCo/TEOS captured a uniform SiO₂ layer with a thickness of 20 nm; however, its thermal conductivity dramatically decreased to 0.16 W/(m·K). The results indicate that BN nanoparticles are helpful in enhancing the thermal conductivity of the composites. The magnetic properties of the four different samples were evaluated using VSM hysteresis loops, as shown in **Figure 4.7**. The saturation magnetization (M_s) before and after the flattening process showed a negligible decrease, below 3%. The introduction of non-magnetic BN nanoparticles caused a reduction in M_s owing to the incorporation ratio (BN nanoparticles with 10 wt% content).

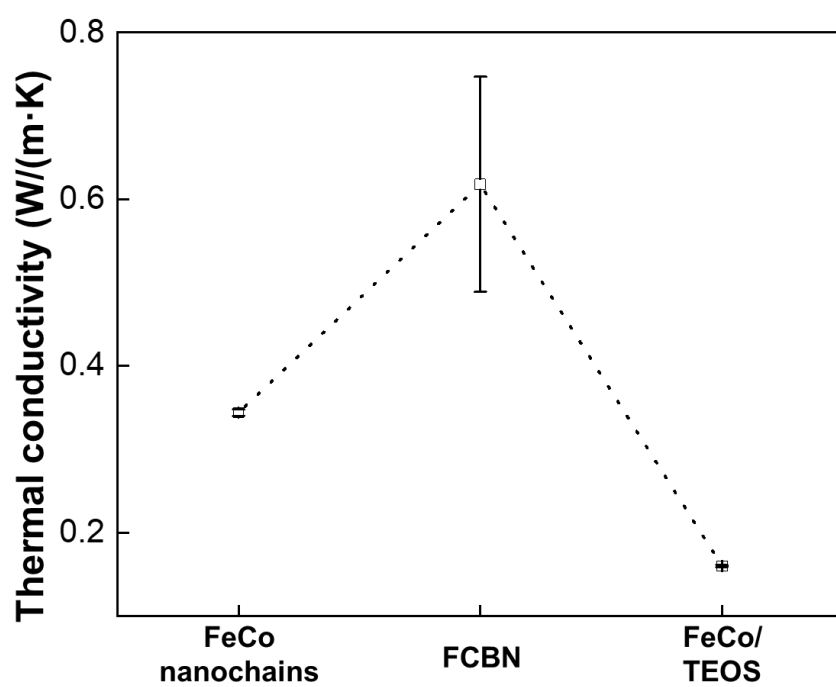


Figure 4.6. Thermal conductivity measurement of three different samples, including the FeCo nanochains, FeCo nanobelts, and FCBN.

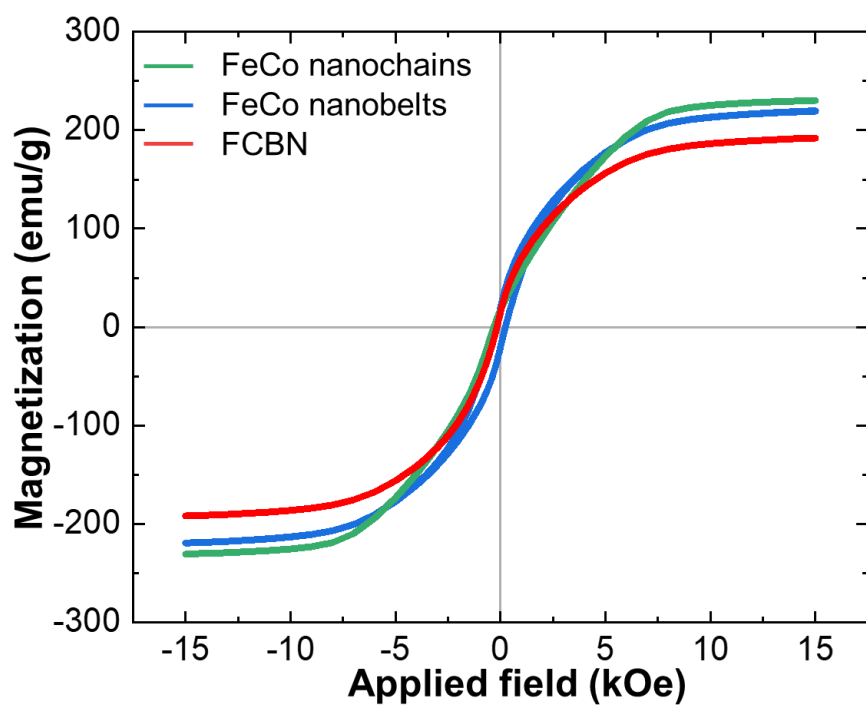


Figure 4.7. Magnetic hysteresis loop data of three different samples, including the FeCo nanochains, FeCo nanobelts, and FCBN.

4.3.3. Electromagnetic Properties of FeCo Nanochains, Nanobelts, and FCBN

Figure 4.8 shows the overall characteristics of the EMW absorbance at the S (2–4 GHz), C (4–8 GHz), X (8–12 GHz), and Ku (12–18 GHz) band regions. First, the permeability of FeCo nanochains, FeCo nanobelts, and FCBN were investigated, as shown in **Figure 4.8 (a)**. The real part (μ') of the complex permeability corresponds to the magnetic storage ability, whereas the imaginary part (μ'') term is a crucial parameter for the magnetic loss. The slight fluctuation of the plot arises from the delayed response of the dipole polarization field changes and the air gap between the sample and the holder.¹²⁻¹⁴ FeCo nanochains present a high μ' value of 1.56 and an increasing trend for μ'' , ranging from 0.28 to 0.44. The structural anisotropy of the one-dimensional FeCo nanochain affects the magnetic loss, originating from natural resonance loss.¹⁵ Subsequent shape modulation enhances the permeability, with μ' and μ'' values that reach 2.15 and a range of 0.61–0.84, respectively. The μ' value, however, drops rapidly with increasing frequency, falling below the values of the FeCo nanochains starting from 12.3 GHz. Such a rapid decrease could be explained by the skin-depth (δ) effect, where the skin depth (δ) is inversely proportional to the electrical conductivity, according to the following equation:¹⁶

$$\delta = \frac{1}{\sqrt{\pi f \mu \sigma}} \quad (10)$$

indicating that δ is related to the frequency (f), permeability (μ), and conductivity (σ). With the flattening technique of the FeCo nanochains, a stronger electrical network is formed. The increase in the electrical conductivity is accelerated with a decrease in the skin depth of the absorber at high frequencies, resulting in a smaller

volume fraction of magnetic materials to interact with the EMW. To prevent electrical connection between the networks of the FeCo nanochains, we added BN nanoparticles as the dielectric material. The insulating effect makes it possible to maintain high permeability in the high-frequency region. These tendencies, in accordance with the structural change, are also confirmed by the real part (ϵ') and imaginary part (ϵ'') of the complex permittivity graph, as shown in **Figure 4.8 (b)**. The ϵ' of the FeCo nanochains increases dramatically to approximately 32 for FeCo nanobelts owing to the existence of electrical networks. However, such a high ϵ' value is not favorable to reflection loss for effective impedance matching. The introduction of BN nanoparticles enables the complex permittivity to decrease to approximately 11.6, indicating that BN nanoparticles are highly suitable for decreasing the electrical pathway.

To verify the validity of Snoek's law, a comparative analysis was conducted on the real and imaginary elements of the complex permeability of FeCo nanochain, FeCo nanobelts, and FCBN within the low frequency range (see **Figure 4.9**). In **Figure 4.9 (a)**, it can be observed that FeCo nanobelts exhibit the highest real permeability value of 3.3 at 0.5 GHz, whereas FeCo nanochains display the lowest value of 1.94. Similarly, when considering the imaginary permeability, FeCo nanobelts also demonstrate the highest value of 0.86, while FeCo nanochains only exhibit a value of 0.49 at 11 GHz (**Figure 4.9 (b)**). This consistent trend of enhanced real and imaginary components of the complex permeability in FeCo nanobelts serves as further validation of Snoek's law.

The loss tangent was calculated from the real and imaginary parts using the measured complex permeability and permittivity, as shown in **Figure 4.10**. The magnetic loss tangent ($\tan\delta_\mu = \mu''/\mu'$) for FCBN shows a higher value all over the

frequency range compared to that for FeCo nanochains, and thus, outstanding EMW absorbing performance can be expected. Meanwhile, the dielectric loss tangent ($\tan\delta_{\varepsilon} = \varepsilon''/\varepsilon'$) for both the FeCo nanochains and FCBN exhibited a similarly low value, and hence, low reflective materials can be achieved. Although a high dielectric loss tangent helps EMW absorption in a similar manner to the magnetic loss tangent, a high dielectric loss tangent usually leads to a high permittivity value and impedance mismatch. A composite membrane with high EMW absorption and low EMW reflection is a key material for EMW absorbers.¹⁷⁻¹⁸

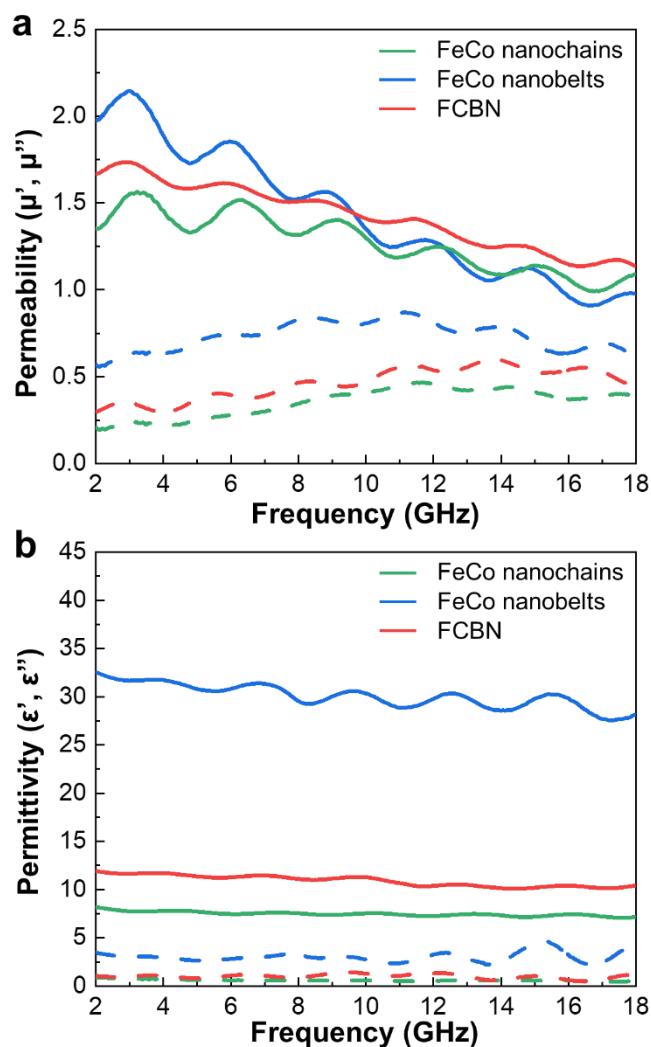


Figure 4.8. Overall characteristics for the EMW absorbance at the S (2–4 GHz), C (4–8 GHz), X (8–12 GHz), and Ku (12–18 GHz) band frequencies. (a-b) Electromagnetic characteristics of (a) complex permeability (μ) and (b) permittivity (ϵ). The samples were prepared with FeCo nanochains, FeCo nanobelts, and FCBN. Solid lines represent the real parts (μ' , ϵ'), whereas the dot lines indicate the imaginary parts (μ'' , ϵ'').

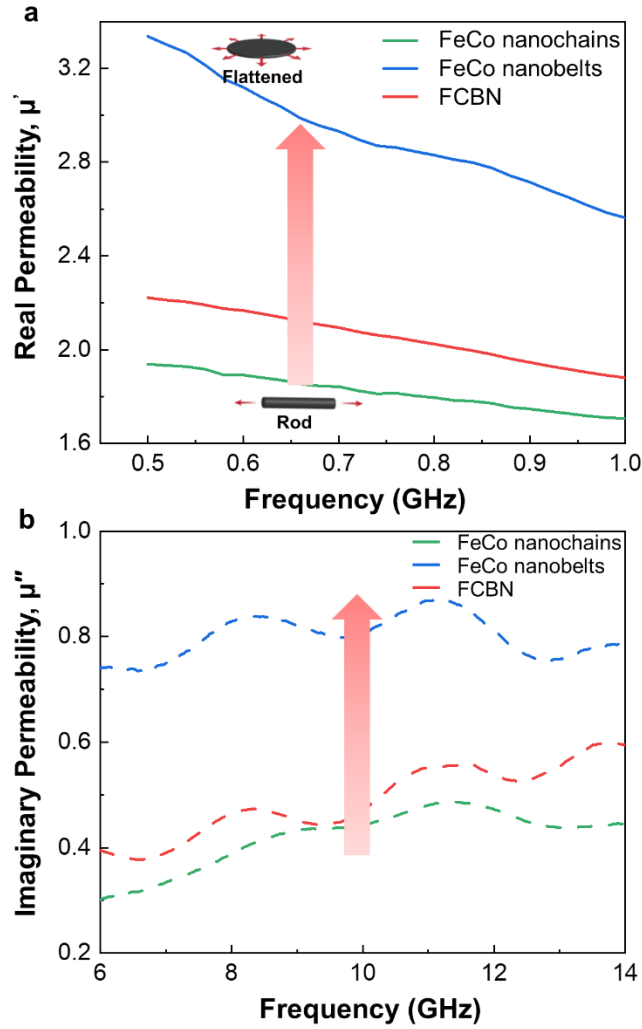


Figure 4.9. Enhancement in (a) real permeability at low frequency range and (b) imaginary permeability of FeCo nanochain, FeCo nanobelts, and FCBN.

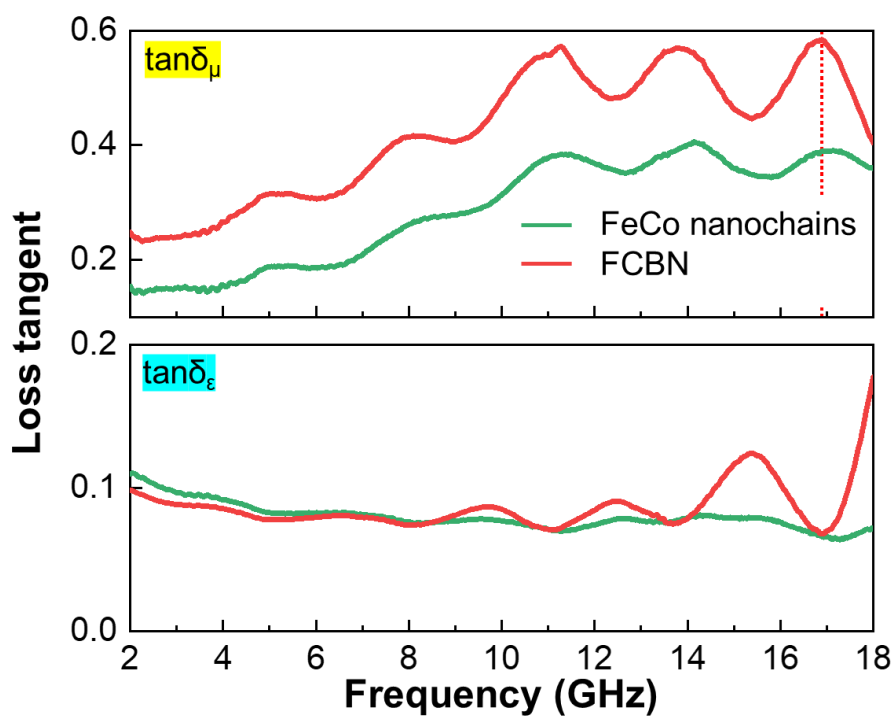


Figure 4.10. Comparison of FeCo nanochains and FCBN represented in the magnetic (δ_μ) and dielectric (δ_ϵ) loss tangent ($\tan \delta_\mu = \mu'' / \mu'$, $\tan \delta_\epsilon = \epsilon'' / \epsilon'$).

4.4.4. Electromagnetic Wave Absorbing Performance: Reflection Loss Calculation

The electromagnetic wave absorbing performance was measured by calculating the reflection loss of FeCo nanochains, FeCo nanobelts, and FCBN at various thicknesses (d) and frequencies (f) via equation 9 and 10. Here, ideal EMW absorbers are thin but have strong EMW absorption and broad absorption bandwidth, with the reflection loss < -10 dB. A reflection loss value exceeding -10 dB is comparable to 90% absorption. **Figure 4.11, 4.12, 4.13** illustrates the calculated reflection loss of the FeCo nanochains, FeCo nanobelts, and FCBN. The reflection loss of the FeCo nanochains has small peaks, mostly in the Ku band, producing a maximum peak of -32.5 dB at 17 GHz with a thickness of 1.2 mm (**Figure 4.11**). The FeCo nanobelts show shallow and narrow peaks of less than -15 dB because of the increased complex permittivity (**Figure 4.12**). For the mixture of FeCo nanobelts and BN nanoparticles, the microwave absorption performances were evaluated by combining broad effective bandwidths (< -10 dB) with a maximum peak, which reached -42.2 dB at 12.0 GHz (**Figure 4.13**). As illustrated in **Figure 4.14**, the three-dimensional mapping of the reflection loss values for the FCBN present wider and deeper valleys across the 6–18 GHz range compared to those of the composites of the FeCo nanochains and nanobelts in **Figure 4.15**.

Table 4.1 also compares the effective bandwidth (< -10 dB) and reflection loss values at different thicknesses for the FeCo nanochains, FeCo nanobelts, and FCBN. The significant increase in the bandwidth for FCBN with the decreased thickness and the reflection loss values below -20 dB indicate that the introduction of BN nanoparticles enhances impedance matching, thus resulting in wide-band

absorption across the Ku-band (See **Figure 4.16**).

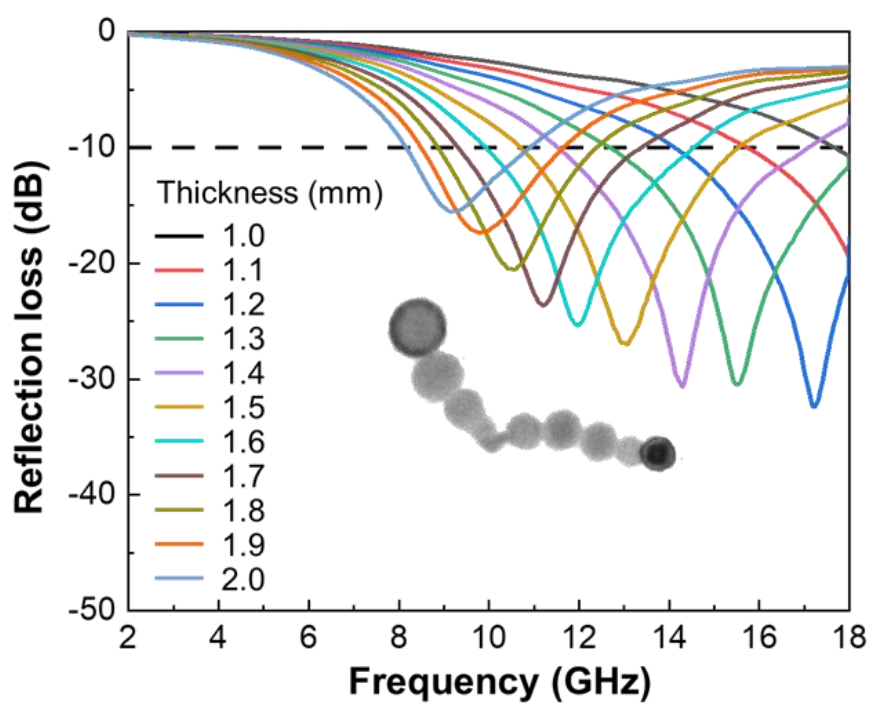


Figure 4.11. EMW absorbing performance of FeCo nanochain at various thicknesses and frequencies and calculated with equations (9-10).

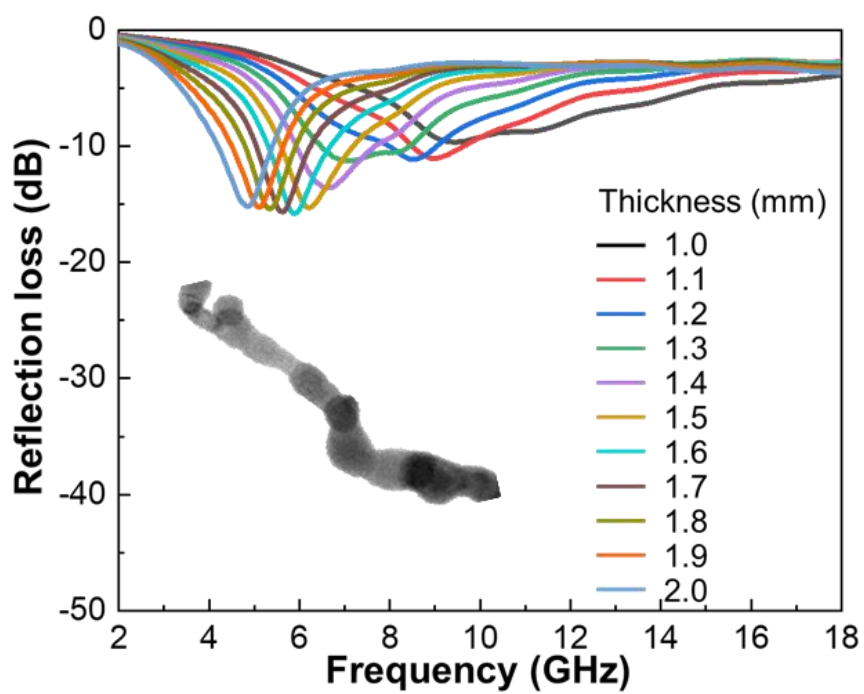


Figure 4.12. EMW absorbing performance of FeCo nanobelt at various thicknesses and frequencies and calculated with equations (9-10).

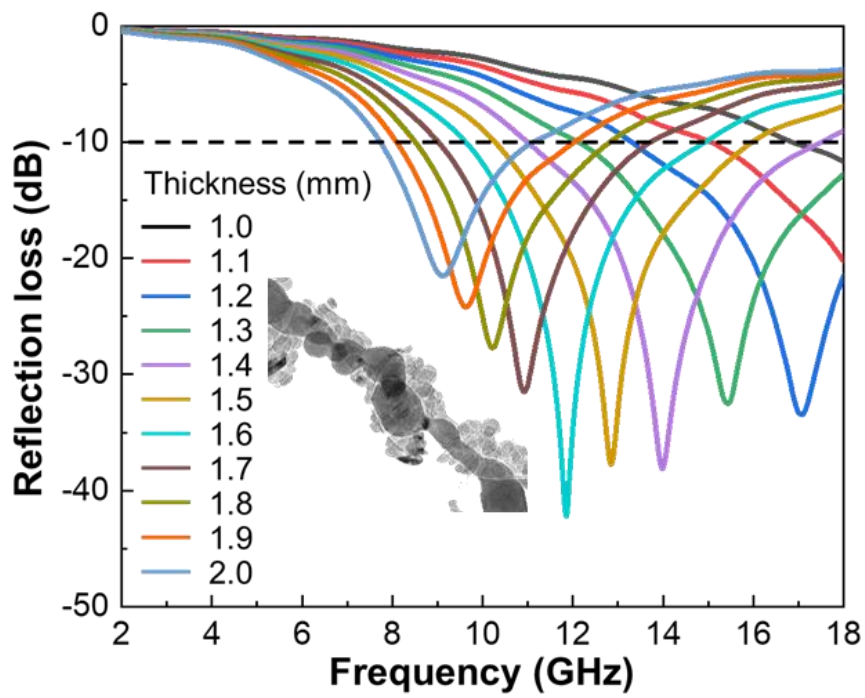


Figure 4.13. EMW absorbing performance of FCBN at various thicknesses and frequencies and calculated with equations (9-10).

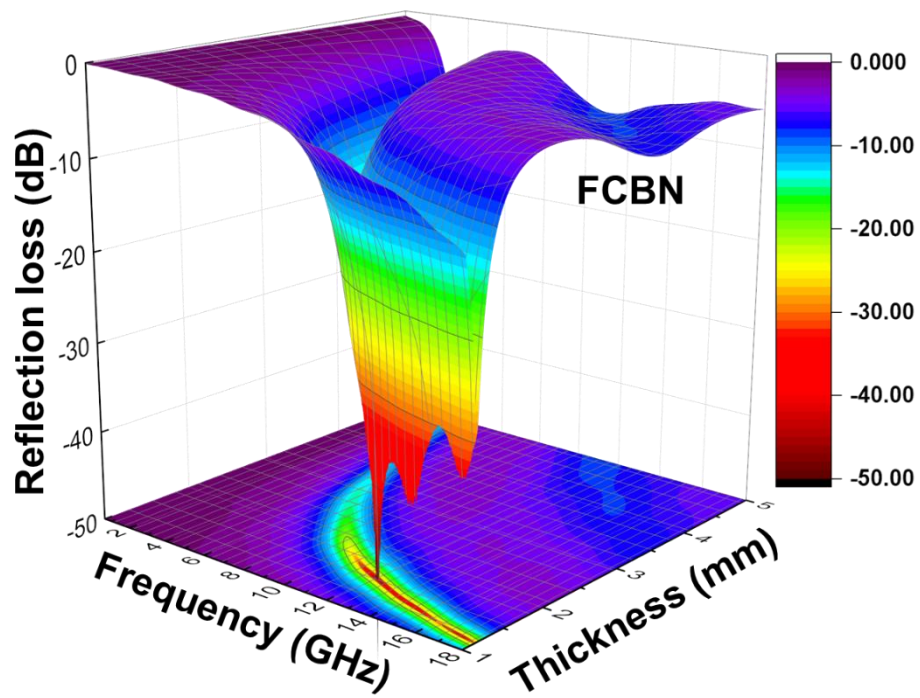


Figure 4.14. Two- and three-dimensional mapping of the overall relationship between reflection loss and frequency up to 18 GHz for FCBN.

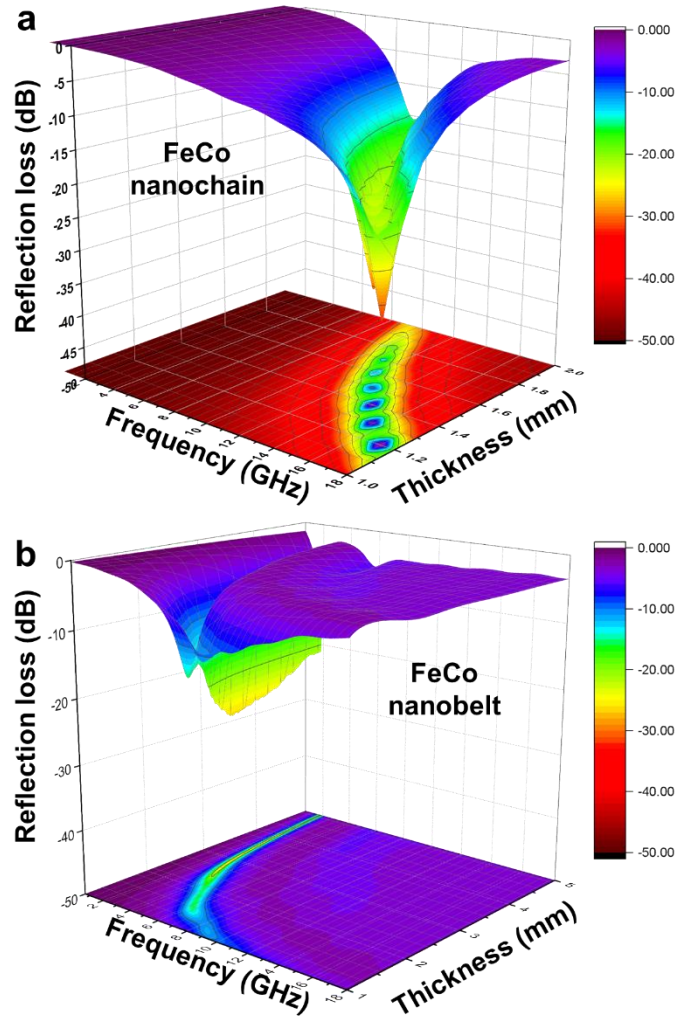


Figure 4.15. Two- and three-dimensional mapping of the overall relationship between reflection loss and frequency up to 18 GHz for (a) FeCo nanochain and (b) FeCo nanobelt.

Table 4.1. Effective bandwidth (< -10 dB) and reflection loss value at different thicknesses of the FeCo nanochain, FeCo nanobelts, and FCBN composite materials.

Thick- ness (mm)	FeCo nanochain		FeCo nanobelt		FCBN	
	Band width	Reflection Loss (dB)	Band width	Reflection Loss (dB)	Band width	Reflection Loss (dB)
2	2.74	-15.54	1.2	-15.2	3.36	-21.53
1.9	3.14	-17.38	1.14	-15.27	3.92	-24
1.8	3.5	-20.54	1.12	-15.38	4.28	-27.7
1.7	4.04	-23.64	1.2	-15.66	4.7	-31.5
1.6	4.58	-25.4	1.38	-15.81	5.3	-42.2
1.5	4.8	-27	1.58	-15.32	5.95	-37.76
1.4	5.52	-30.66	1.72	-13.60	6.4	-38.13

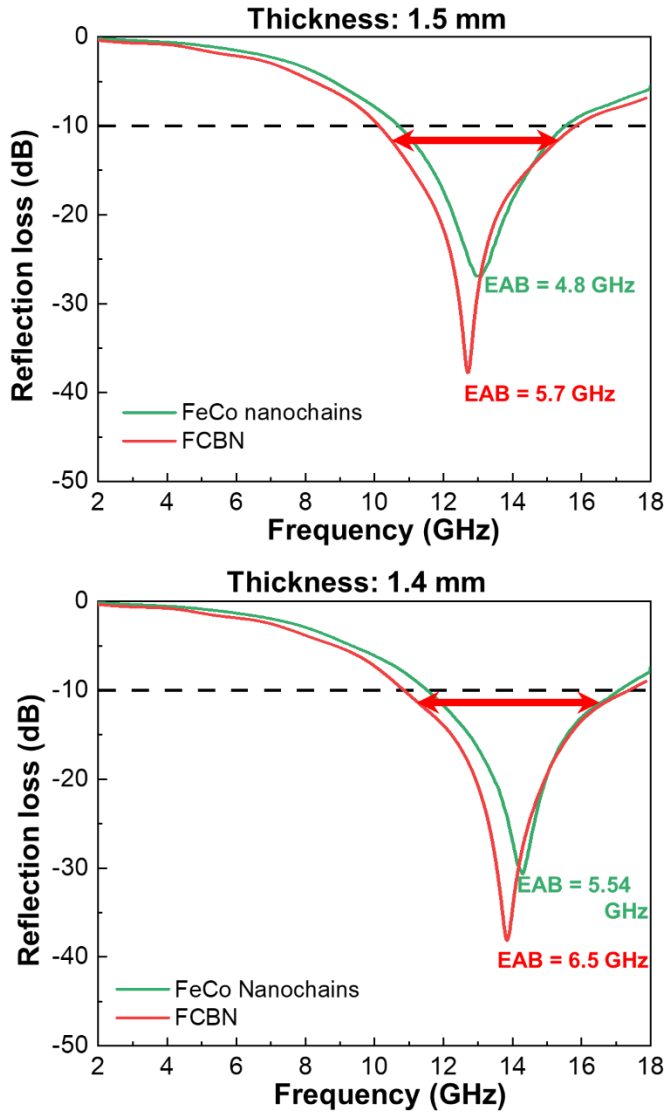


Figure 4.16. Comparison of the bandwidth at thicknesses 1.4 mm and 1.5 mm for FeCo nanochains and FCBN. FCBN shows wider bandwidth than FeCo nanochain for all thicknesses.

4.4.5. Electromagnetic Wave Absorbing Performance: Input Impedance and Attenuation Constant

To better understand the reflection loss performance, the impedance matching of the three different samples was calculated from the ratio of input (Z_{in}) to free-space impedance (Z_0), $Z = |Z_{in}/Z_0|$. EMW absorbers with impedance matching close to 1 are generally known to be good microwave absorbers.¹⁹ **Figure 4.17** shows that the impedance matching for FeCo nanochains reaches 12 GHz once. However, FeCo nanobelts possess a maximum peak of only 0.72 at 6 GHz, implying poor EMW absorbance characteristics. After the addition of BN nanoparticles, the FCBN composite shows the best performance with its maximum peak close to 1 at frequencies of 10.2 and 12.0 GHz; this frequency range is found in the effective bandwidth ($RL < -10.0$ dB) at thickness of 1.6 mm. In addition, the attenuation constant was calculated using the following equation to further describe the loss capacity of EMW absorbing materials:²⁰

$$\alpha = \frac{\sqrt{2}\pi f}{c} \sqrt{(\mu''\varepsilon'' - \mu'\varepsilon') + \sqrt{(\mu''\varepsilon'' - \mu'\varepsilon')^2 + (\mu'\varepsilon'' + \mu''\varepsilon')^2}} \quad (11)$$

The α for all samples increases all over the frequency range as shown in **Figure 4.18**. The FCBN shows highest α values, indicating the highest attenuation ability compared to the FeCo nanochains. The synergetic effect of impedance matching and attenuation ability of FCBN leads to an effective absorption performance.²⁰ In summary, the exceptional absorption performance is the result of the following comprehensive effects: (1) magnetic material loss from shape modulation and (2) interfacial/dipole polarization loss from the inclusion of a dielectric material.²¹⁻²²

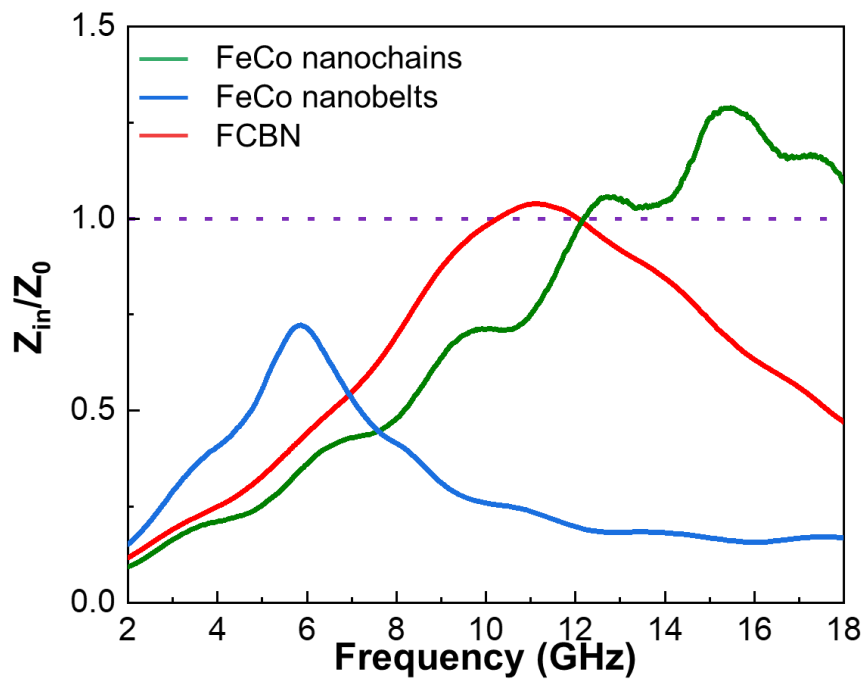


Figure 4.17. Frequency dependence of relative input impedance ($|Z_{in}/Z_o|$) for FeCo nanochains, FeCo nanobelts, and FCBN.

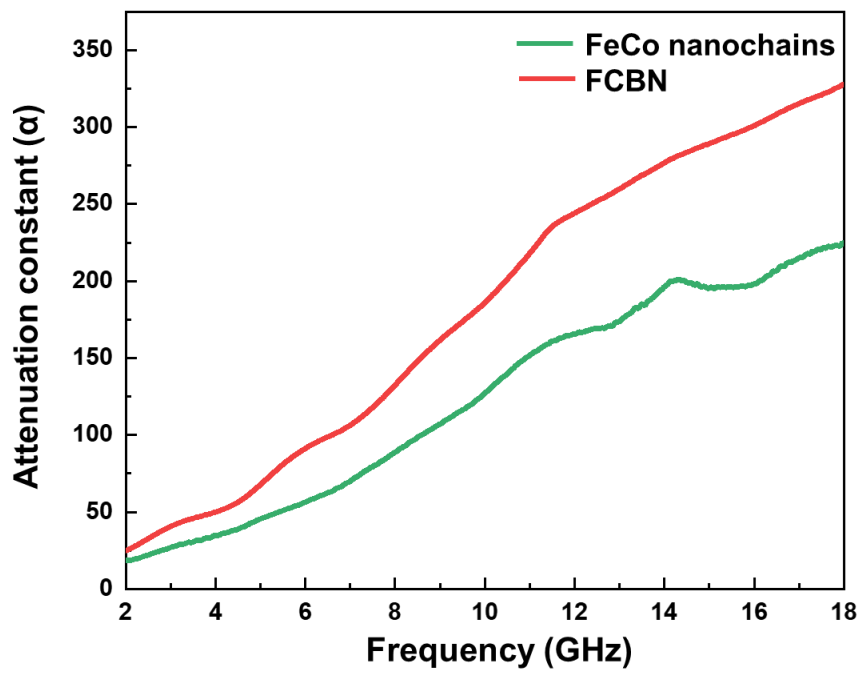


Figure 4.18. Comparison of the attenuation constants (α) between FeCo nanochains and FCBN.

4.4.6. EMW-Absorbing Mechanisms

Figure 4.19 displays the EMW-absorbing mechanisms and the reliability study of the FCBN-TPU composite membrane.²³⁻²⁵ The aforementioned results indicate that these strategies, including shape modulation and BN nanoparticle incorporation into FeCo nanochains, are an effective way to improve EMW absorbance. The schematic shown in **Figure 4.19** reveals the three absorption mechanisms of the FCBN membrane. First, the transformation into a two-dimensional FeCo structure maximizes the natural resonance of the magnetic loss. However, the involuntary electrical networks generated during the shape-modifying process produced the adverse effect of a decrease in the skin-depth, resulting in a volume reduction for eddy current absorption in FeCo nanobelts. To block this additional electrical pathway, we introduced dielectric BN nanoparticles.

The magnetic loss derived from natural resonance and eddy current loss can be interpreted from the eddy current loss coefficient $C_o = \mu''(\mu')^{-2}f^{-1} = 2\pi\mu_0\sigma d^2/3$ where σ is the electrical conductivity and μ_0 is the vacuum permeability.²⁶ The natural resonance occurs in the lower part of the frequency range while the eddy current loss occurs from the constant coefficient values when f is increasing.²⁶⁻²⁷ As shown in **Figure 4.20 (a)**, both FeCo nanochain and FCBN show natural resonance peak below 4 GHz. We additionally calculated the ratio of the eddy current loss coefficient between FCBN and FeCo nanochain to distinguish the difference in eddy current loss as frequency increases (**Figure 4.20 (b)**). Consequently, 20% more eddy current loss can be observed for FCBN compared to FeCo nanochains. Second, the flake-like morphology could promote multiple reflections and scattering of the absorbed EMW within the composite.²⁸

Lastly, the interfacial and dipole polarizations induced on the surface of

FCBN contribute to the dielectric energy loss. Interfacial polarization is generated by the difference in surface charge between the FeCo nanobelts and BN nanoparticles. Moreover, the dipole moments of the BN nanoparticles generated additional polarization. The dielectric loss resulting from interfacial and dipole polarization can be verified from Cole-Cole curves (ϵ' versus ϵ'') representing multiple relaxation mechanism (**Figure 4.21**). Based on the Debye dipolar relaxation, each semicircle in the Cole-Cole curve represent one Debye relaxation process.²⁹ As for FeCo nanochain, approximately 3 semicircles are observed in the Cole-Cole curve. In contrast, the incorporation of BN nanoparticle in FCBN results in more obvious 5 semicircles, indicating that the multiple relaxation process contributes to permittivity enhancement. These polarizations contribute to the conversion of electromagnetic energy into heat energy at a specific frequency for impedance matching.³⁰

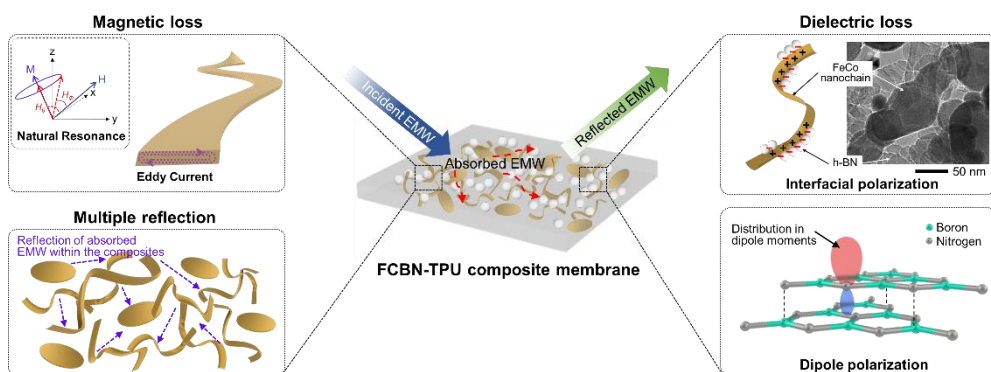


Figure 4.19. Schematic of possible EMW absorption process in FCBN-TPU composite membrane. Three different absorption systems, including the magnetic loss, multiple reflection, and dielectric loss, allow an improved EMW absorbance and successful impedance matching.

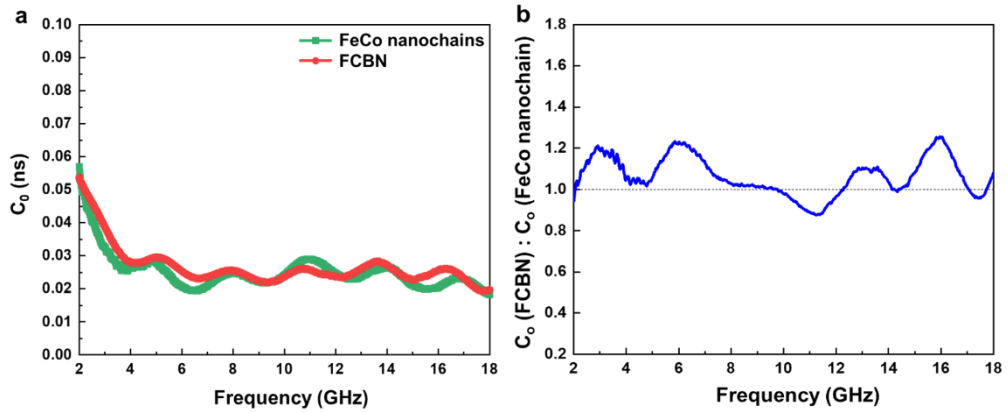


Figure 4.20. Graphs showing (a) $\mu''(\mu')^{-2}f^{-1}$ (eddy current loss) versus frequency of FeCo nanochains and FCBN and (b) ratio of Co value for FCBN and FeCo nanochain versus frequency.

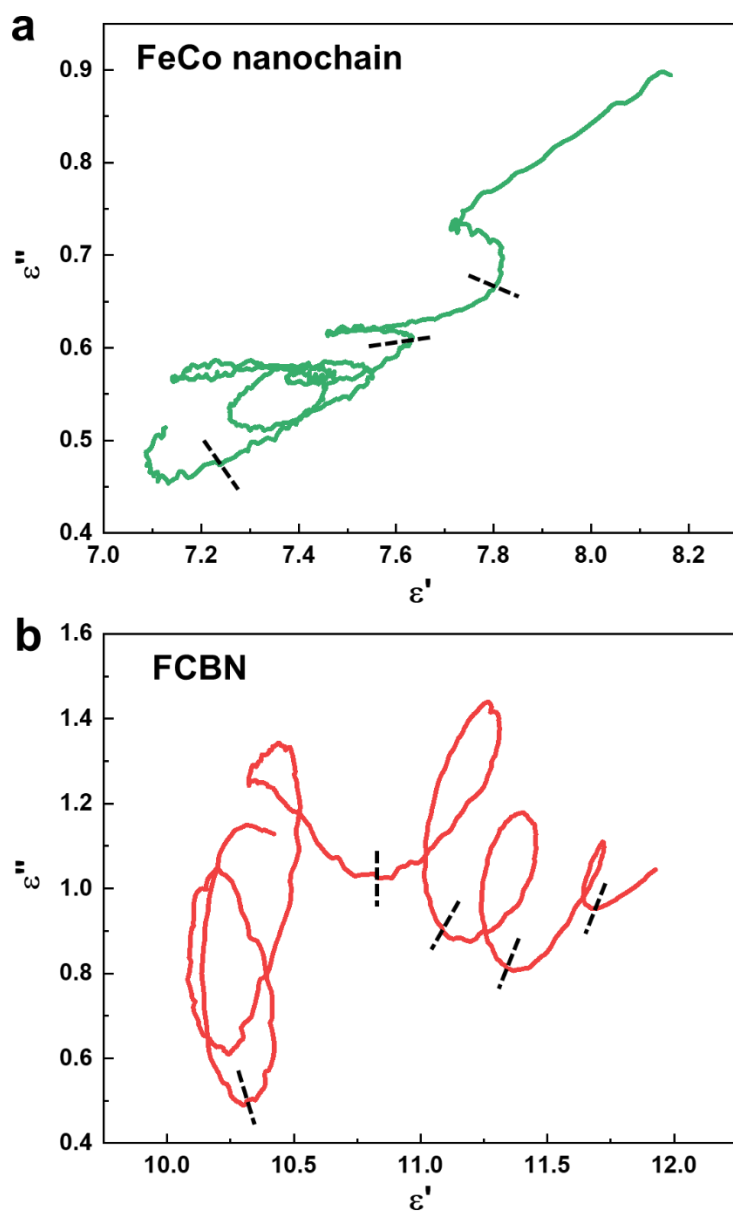


Figure 4.21. Cole-Cole plots of (a) FeCo nanochains and (b) FCBN. The dotted line indicates the semicircles in the Cole-Cole curves.

4.4.7. Reliability Study

To validate the potential of the FCBN membrane as a flexible EMW absorber, we evaluated the mechanical reliability of the manufactured FCBN-TPU membrane upon excessive 90° bending cycles. **Figure 4.22 (a)** shows a thin (1.6 mm) flexible FCBN-TPU composite. The results in **Figure 4.22 (b)** and **(c)** demonstrate that a sample with the FCBN composite has a negligible change in magnetic data, including permeability (μ) and permittivity (ϵ), even after 1,000 cycles. **Table 4.2** compares the measured EMW-absorbing properties of the various types of flaky materials. The FCBN composite not only offers remarkable EMW absorption (−42.2 dB equivalent to a loss of over 99.99%) but also generates a wide electromagnetic wave absorbing bandwidth (EAB), verifying the main advantages of the FCBN membrane presented in this work.

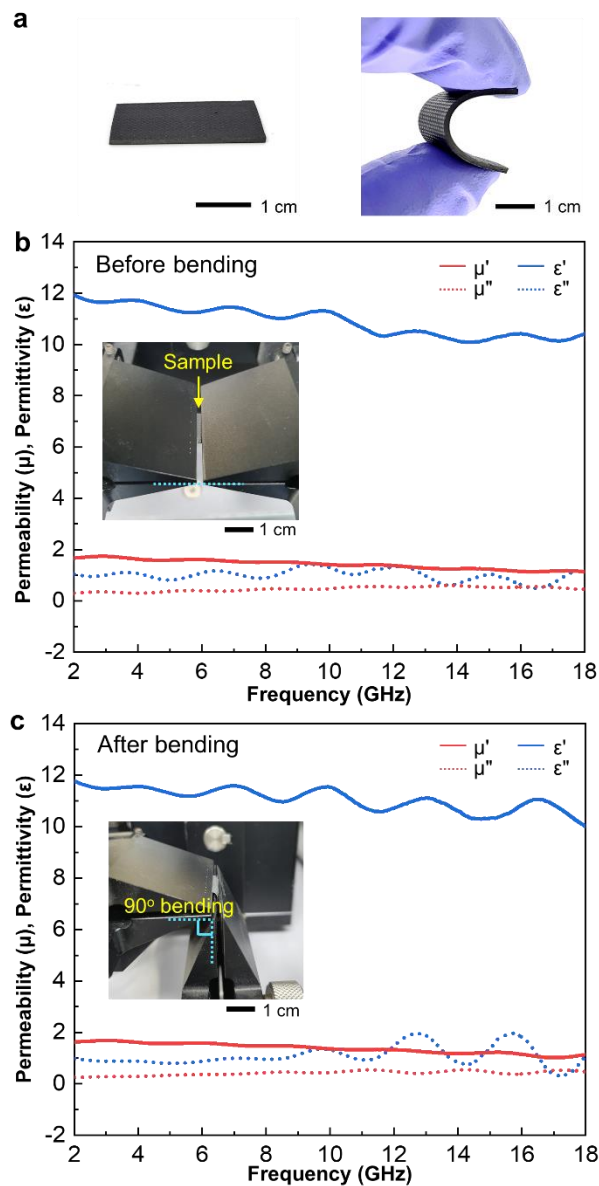


Figure 4.22. (a) Photographs showing the FCBN composite with a dimension of 30 mm in width x 30 mm in height x 15 mm in thickness. The manufactured membrane displays high flexibility. (b-c) Complex permeability and permittivity values measured (b) before and (c) after 1,000-cycle bending. The insert photographs indicate the FCBN-TPU composite membrane loaded into the 90° bending machine.

Table 4.2. Comparison of flaky-shaped materials reported in the literature.

Material	RL_{min} (dB)	Matching frequency (GHz)	EAB (GHz)	Matching thickness to EAB (mm)	Filler ratio (wt%)	Reference
FeCo nanobelts/BN	−42.2	12.0	6 (10– 16)	1.5	50	This work
Flaky CIPs	−17.18	12.5	10 (8– 18)	1.63	50	Ref. ³¹
Co-coated flaky CIPs	−25	10.5	4.2 (8.2– 12.4)	1.5	70	Ref. ³²
Flaky nanocrystalline CIPs	−12	11.5	10 (8– 18)	1.4	18	Ref. ³³
Flake-shaped FeNiMo	−20.4	13.0	2.7 (11.8– 14.5)	2	70	Ref. ³⁴
Flake-shaped Pr _x Ho _{2-x} Fe ₁₇	−41.03	6.88	2 (6– 8)	2	80	Ref. ³⁵

4.4. Conclusion

This Chapter reports the nanomaterial processing of magnetic and dielectric materials to obtain multiple functions of the prepared membrane, including EMW absorption and thermal conductivity. We demonstrate that the structural modulation of FeCo using thermal plasma synthesis and simple mechanical milling provides excellent magnetic complex permeability in the S-, C-, and X-bands. The introduction of BN nanoparticles to the FeCo nanobelts allows the optimization of the complex permittivity, leading to impedance matching and consequently resulting in a high reflection loss value of -42.2 dB at 12.0 GHz with a thickness of only 1.6 mm. The FCBN also shows wider bandwidth at small thicknesses when compared to FeCo nanochain and other works (**Figure 4.23**). Furthermore, the enhanced thermal conductivity of the FCBN membrane results in heat dissipation of the absorbed electromagnetic wave energy. A set of experimental studies validated the mechanical flexibility of EMW absorbers, which enable them to endure harsh dynamic conditions. The FCBN-TPU composite membrane fabricated in this work served as a flexible, thin EMW absorber for transmission technologies in the GHz range.

Lastly, to validate the empirical function generated in Chapter 3, the experimental data was interpreted by assuming a significantly larger aspect ratio for the FeCo nanobelt, such as 10. By assuming the f_{FMR} of the FeCo nanobelt based on the imaginary part of the complex permeability, and by considering μ_i from the equation presented in **Figure 3.25**, the anisotropic function of the FeCo nanobelt was calculated. The results showed a strong agreement with the calculated values, as depicted in **Figure 4.24**. In essence, the anisotropic function was validated using the

calculated values of the FeCo nanobelt, reaffirming the relationship between shape modulation and complex permeability and, consequently, validating Snoek's law once again.

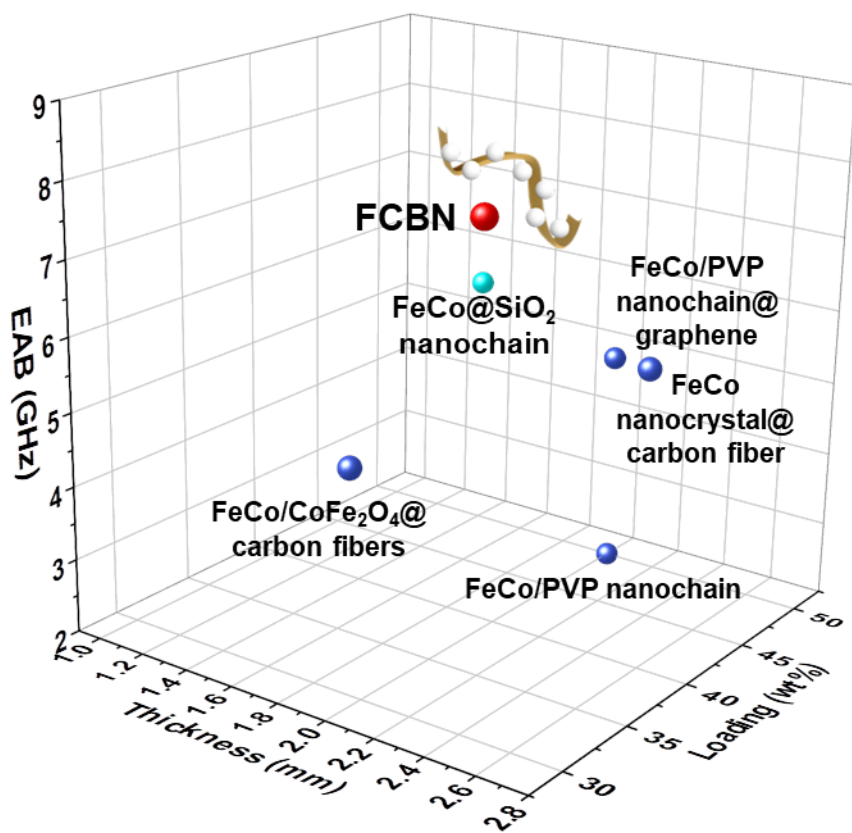
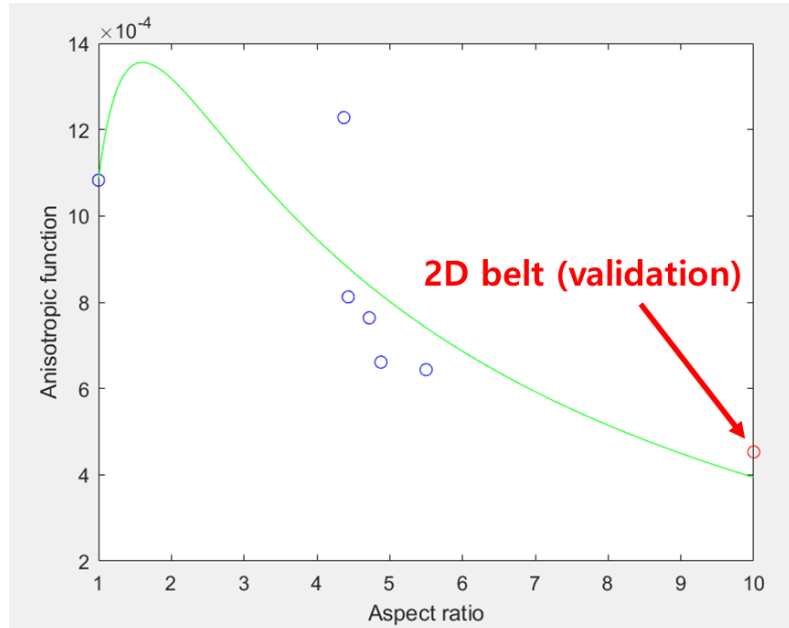


Figure 4.23. 3-D graph showing comparison of this work to other works. FCBN shows the largest bandwidth at small thickness.



Anisotropic Function:

$\frac{\mu_i}{f_{FMR}M_s} = F(AR) = \left(\alpha \frac{\ln(\beta * AR)}{AR} + \gamma \right)$	
Coefficients	value
Alpha	0.0054
Beta	1.6050
Gamma	-0.0015

Figure 4.24. Validation of anisotropic function through the experimental value of FeCo nanobelt.

4.5. References

1. Burmeister, C. F.; Kwade, A., Process Engineering with Planetary Ball Mills. *Chem. Soc. Rev.* **2013**, 42 (18), 7660-7667.
2. Xu, R.; Tan, Z.; Xiong, D.; Fan, G.; Guo, Q.; Zhang, J.; Su, Y.; Li, Z.; Zhang, D., Balanced Strength and Ductility in Cnt/Al Composites Achieved by Flake Powder Metallurgy Via Shift-Speed Ball Milling. *Compos. Part A* **2017**, 96, 57-66.
3. Stolle, A.; Szuppa, T.; Leonhardt, S. E.; Ondruschka, B., Ball Milling in Organic Synthesis: Solutions and Challenges. *Chem. Soc. Rev.* **2011**, 40 (5), 2317-2329.
4. Egorov, I. N.; Santra, S.; Kopchuk, D. S.; Kovalev, I. S.; Zyryanov, G. V.; Majee, A.; Ranu, B. C.; Rusinov, V. L.; Chupakhin, O. N., Ball Milling: An Efficient and Green Approach for Asymmetric Organic Syntheses. *Green Chemistry* **2020**, 22 (2), 302-315.
5. Blázquez, J.; Ipus, J.; Moreno-Ramírez, L.; Álvarez-Gómez, J.; Sánchez-Jiménez, D.; Lozano-Pérez, S.; Franco, V.; Conde, A., Ball Milling as a Way to Produce Magnetic and Magnetocaloric Materials: A Review. *Journal of Materials Science* **2017**, 52, 11834-11850.
6. Bor, A.; Jargalsaikhan, B.; Uranchimeg, K.; Lee, J.; Choi, H., Particle Morphology Control of Metal Powder with Various Experimental Conditions Using Ball Milling. *Powder Technol.* **2021**, 394, 181-190.
7. Guan, Z.-J.; Wang, Z.-Q.; Jiang, J.-T.; Gong, Y.-X.; Yao, Y.-T.; Zhen, L., Flaky Fesi Particles with Tunable Size, Morphology and Microstructure Developing for High-Efficiency and Broadband Absorbing Materials. *J. Magn. Magn. Mater.* **2021**, 527, 167800.

8. Ding, X.; Huang, Y.; Wang, J., Synthesis of Fe₃O₄ Nanocrystals Encapsulated in Carbon Nanospheres/Reduced Graphene Oxide as a Light Weight Electromagnetic Wave Absorbent. *RSC Adv.* **2015**, 5 (80), 64878-64885.
9. Wang, Y.; Luo, F.; Zhou, W.; Zhu, D., Dielectric and Microwave Absorption Properties of TiO₂-Al₂O₃/Silica Coatings at High Temperature. *J. Electron. Mater.* **2017**, 46 (8), 5225-5231.
10. Li, J.; Qi, L.; Li, H., Facile Strategy to Prepare Light-Weight PVA Membrane Based on Schiff Base Derivatives and MWCNTs for Electromagnetic Wave Absorption. *J. Phys. Chem. C* **2016**, 120 (40), 22865-22872.
11. Zhou, L.; Xu, H.; Su, G.; Zhao, L.; Wang, H.; Wang, Z.; Li, Z., Tunable Electromagnetic and Broadband Microwave Absorption of SiO₂-Coated Fe₃O₄ Absorbents. *J. Alloys Compd.* **2021**, 861, 157966.
12. Liu, X.; Cui, C.; Yu, J.; Sun, Y.; Xia, A., Ag₃PO₄ Sub-Microcubic/SrFe₁₂O₁₉ Hexagon Nanoflake Heterostructure for Broadband Electromagnetic Absorber at GHz Frequency. *Mater. Lett.* **2018**, 225, 1-4.
13. Zhou, N.; An, Q.; Xiao, Z.; Zhai, S.; Shi, Z., Solvothermal Synthesis of Three-Dimensional, Fe₂O₃ NPs-Embedded CNT/N-Doped Graphene Composites with Excellent Microwave Absorption Performance. *RSC Adv.* **2017**, 7 (71), 45156-45169.
14. Zhang, N.; Huang, Y.; Liu, X.; Wang, M., High Efficiency Microwave Absorption Nanocomposites of Multiple-Phase Core-Shell CoNi Alloy@C Loaded on RGO Conducting Network. *Compos. Part A* **2018**, 115, 283-293.
15. Pan, J.; Guo, H.; Wang, M.; Yang, H.; Hu, H.; Liu, P.; Zhu, H., Shape Anisotropic Fe₃O₄ Nanotubes for Efficient Microwave Absorption. *Nano Res.* **2020**, 13 (3), 621-629.

16. Chung, D. D. L.; Ozturk, M., Electromagnetic Skin Depth of Cement Paste and Its Thickness Dependence. *J. Build. Eng.* **2022**, *52*, 104393.
17. Zeng, Q.; Chen, P.; Yu, Q.; Chu, H.-r.; Xiong, X.-h.; Xu, D.-w.; Wang, Q., Self-Assembly of Ternary Hollow Microspheres with Strong Wideband Microwave Absorption and Controllable Microwave Absorption Properties. *Sci. Rep.* **2017**, *7* (1), 8388.
18. Shi, X.-L.; Cao, M.-S.; Yuan, J.; Fang, X.-Y., Dual Nonlinear Dielectric Resonance and Nesting Microwave Absorption Peaks of Hollow Cobalt Nanochains Composites with Negative Permeability. *Appl. Phys. Lett.* **2009**, *95* (16), 163108.
19. Liu, L.; He, N.; Sun, J.; Hu, P.; He, R.; Cheng, J.; Tian, W.; Tong, G., Tailoring Impedance Match and Enhancing Microwave Absorption of Fe₃O₄/Bi₂₄Fe₂O₃₉/Bi Hollow Porous Microrods by Controlling Their Composition. *Prog. Nat. Sci.* **2018**, *28* (5), 575-583.
20. Liu, R.; Du, G.; Liao, B.; Xiao, W.; An, Z.; Zhang, J., Simultaneous Dual Pyrolysis Synthesis of Heterostructured Feco/C Porous Hollow Microspheres for Highly Efficient Microwave Absorption. *J. Mater. Chem. A* **2022**, *10* (3), 1547-1559.
21. Yang, H.; Cao, M.; Li, Y.; Shi, H.; Hou, Z.; Fang, X.; Jin, H.; Wang, W.; Yuan, J., Enhanced Dielectric Properties and Excellent Microwave Absorption of Sic Powders Driven with Nio Nanorings. *Advanced Optical Materials* **2014**, *2* (3), 214-219.
22. Yang, H.-J.; Cao, W.-Q.; Zhang, D.-Q.; Su, T.-J.; Shi, H.-L.; Wang, W.-Z.; Yuan, J.; Cao, M.-S., Nio Hierarchical Nanorings on Sic: Enhancing Relaxation to Tune Microwave Absorption at Elevated Temperature. *ACS Appl. Mater. Interfaces* **2015**, *7* (13), 7073-7077.
23. Tang, L.; Wang, J.; Zhang, B.; Li, C.; Jin, H., Remarkable Microwave

Heating Performance of Mwcnts/Polypropylene Composites Verified by Electromagnetic-Thermal Coupling Experiment and Simulation. *Compos. Sci. Technol.* **2022**, *223*, 109428.

24. Wu, Q.; Wang, J.; Jin, H.; Dong, Y.; Huo, S.; Yang, S.; Su, X.; Zhang, B., Facile Synthesis of Co-Embedded Porous Spherical Carbon Composites Derived from Co₃O₄/Zif-8 Compounds for Broadband Microwave Absorption. *Compos. Sci. Technol.* **2020**, *195*, 108206.

25. Zhang, B.; Wang, J.; Wang, T.; Su, X.; Yang, S.; Chen, W.; Wang, J.; Sun, J.; Peng, J., High-Performance Microwave Absorption Epoxy Composites Filled with Hollow Nickel Nanoparticles Modified Graphene Via Chemical Etching Method. *Compos. Sci. Technol.* **2019**, *176*, 54-63.

26. Zhao, Y.; Liu, L.; Jiang, K.; Fan, M.; Jin, C.; Han, J.; Wu, W.; Tong, G., Distinctly Enhanced Permeability and Excellent Microwave Absorption of Expanded Graphite/Fe₃O₄ Nanoring Composites. *RSC Adv.* **2017**, *7* (19), 11561-11567.

27. Wang, F.; Gu, W.; Chen, J.; Wu, Y.; Zhou, M.; Tang, S.; Cao, X.; Zhang, P.; Ji, G., The Point Defect and Electronic Structure of K Doped LaCo_{0.9}Fe_{0.1}O₃ Perovskite with Enhanced Microwave Absorbing Ability. *Nano Res.* **2022**, *15* (4), 3720-3728.

28. Zhang, Y.; Piao, M.; Zhang, H.; Zhang, F.; Chu, J.; Wang, X.; Shi, H.; Li, C., Synthesis of Mesoporous Hexagonal Cobalt Nanosheets with Low Permittivity for Enhancing Microwave Absorption Performances. *J. Magn. Magn. Mater.* **2019**, *486*, 165272.

29. Tong, G.; Liu, Y.; Cui, T.; Li, Y.; Zhao, Y.; Guan, J., Tunable Dielectric Properties and Excellent Microwave Absorbing Properties of Elliptical Fe₃O₄

Nanorings. *Appl. Phys. Lett.* **2016**, *108* (7), 072905.

30. Ren, S.; Yu, H.; Wang, L.; Huang, Z.; Lin, T.; Huang, Y.; Yang, J.; Hong, Y.; Liu, J., State of the Art and Prospects in Metal-Organic Framework-Derived Microwave Absorption Materials. *Nanomicro Lett.* **2022**, *14* (1), 68.
31. Xu, Y.; Yuan, L.; Wang, X.; Zhang, D., Two-Step Milling on the Carbonyl Iron Particles and Optimizing on the Composite Absorption. *J. Alloys Compd.* **2016**, *676*, 251-259.
32. Zhou, Y.; Zhou, W.; Li, R.; Mu, Y.; Qing, Y., Enhanced Antioxidation and Electromagnetic Properties of Co-Coated Flaky Carbonyl Iron Particles Prepared by Electroless Plating. *J. Alloys Compd.* **2015**, *637*, 10-15.
33. Wang, W.; Guo, J.; Long, C.; Li, W.; Guan, J., Flaky Carbonyl Iron Particles with Both Small Grain Size and Low Internal Strain for Broadband Microwave Absorption. *J. Alloys Compd.* **2015**, *637*, 106-111.
34. Yang, R. B.; Liang, W. F., Microwave Absorbing Characteristics of Flake-Shaped Fenimo/Epoxy Composites. *J. Appl. Phys.* **2013**, *113* (17), 17A315.
35. Luo, J.; Pan, S.; Qiao, Z.; Cheng, L.; Wang, Z.; Lin, P.; Chang, J., Electromagnetic and Microwave Absorption Properties of the Flake-Shaped Pr-Ho-Fe Alloys in the C-Band. *J. Electron. Mater.* **2018**, *47* (1), 751-759.

Chapter 5. Boron Nitride Incorporated 0D-1D@3D FeCo Nanoparticles

5.1. Introduction

5.1.1. Limitation of Loading Factor of Nano-Filler Material in EW absorbers

Filler materials in composites from EW absorbers are used to enhance the electromagnetic wave absorption properties of the material.¹ These fillers play a crucial role in attenuating or absorbing EM radiation, converting it into heat energy. The filler material is dispersed within a matrix material, which is typically a polymer or a resin. It is crucial to achieve a uniform distribution of the filler particles within the matrix to maximize the absorption efficiency. The loading ratio of the filler material is adjusted to optimize the absorption properties of the composite. An optimal loading ratio can improve the absorber's electromagnetic absorption.²⁻⁴

As mentioned in Part 1, nanomaterials are widely used in EWAM applications owing to its small particles size, which leads to a large surface area with large quantity of active chemical sites. Subsequently, generating more dielectric and magnetic interaction. However, nanomaterials have high viscosity due to their small size and large surface area-to-volume ratio.⁴ Due to the high viscosity, the EWAM/resin composite faces difficulty when casted as a film.⁵ When casting the composite, ability of the material to flow into the mold and fill complex geometries is crucial. However, the high viscosity of nanomaterials can impede their flow, making it difficult to achieve uniform distribution within the composite matrix or to fill intricate mold features completely. For example, when FeCo nanochain and nanobelt is used as EWAM in Chapter 3 and 4, the nanosized FeCo filler material is

mechanically mixed with a thermoplastic urethane (TPU) solution, subsequently cured and casted as a composite film. Currently, the maximum loading ratio of the FeCo nanomaterial (nanochain, nanobelt) is set as 50 wt% because beyond this value, the casting of the composite material becomes very difficult (See **Figure 5.1**). As the casting process becomes more demanding as the viscosity increases, it is necessary to modify the nanomaterial fabrication process or use alternative techniques to overcome the challenge. Shape modulation of the nanomaterial is one method to help reduce the viscosity and will be discussed in this Chapter.

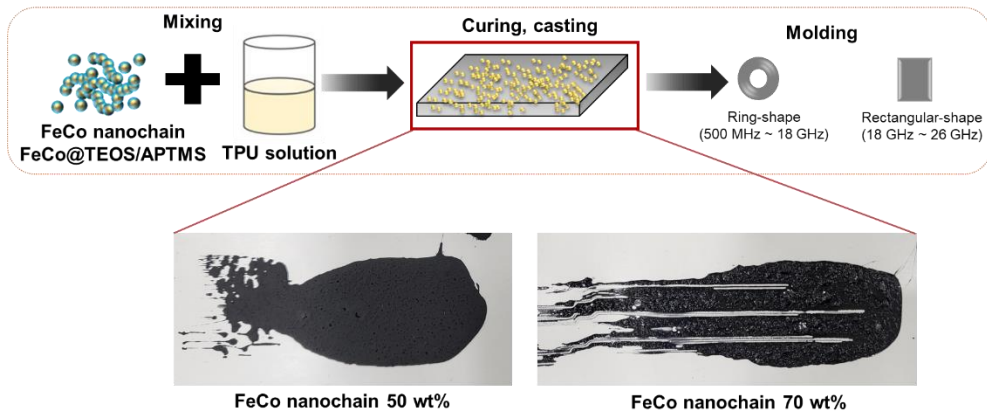


Figure 5.1. EW absorbing composite (FeCo/TPU) fabrication process. Composite with 50 wt% FeCo nanochain well-casted compared to inhomogeneous casting of 70 wt% composite.

5.1.2. Synthesis of Shape-Modulated FeCo Particles: Ultrasonic Spray Pyrolysis

Ultrasonic spray pyrolysis (USP) is a technique used to produce micro- and nanoparticles through the process of atomization pyrolysis, and deposition.⁶ It involves the use of ultrasonic waves to generate a fine mist or aerosol of precursor solution, which is then subjected to high temperatures to induce chemical reactions and solid-state formation.⁷ As of the mechanism, a precursor solution is prepared by dissolving the desired chemicals or compounds in a suitable solvent (See **Figure 5.2**). This solution typically contains metal salts or organic compounds. The precursor solution is loaded into a nebulizer or an ultrasonic atomizer. Ultrasonic waves are generated that propagate through the solution, causing the rapid formation and collapse of bubbles. This phenomenon leads to the atomization of the liquid, creating a fine mist or aerosol of droplets. The aerosol travels through the hot chamber, and the solvent quickly evaporates from the droplets due to the elevated temperatures. Simultaneously, chemical reactions occur within the droplets, driven by the heat. These reactions result in the decomposition of the precursor compounds and the formation of solid particles. The solid particles formed during the pyrolysis process are carried by a gas stream and deposited onto a suitable substrate.⁸⁻¹⁰

Ultrasonic spray pyrolysis offers several advantages, including the ability to control particle size, composition, and morphology by adjusting parameters such as precursor concentration, solution flow rate, furnace temperature, and carrier gas flow.¹¹⁻¹³ Among them, adjusting the type of precursor used is one method for shape modulation of particles.¹⁴⁻¹⁵ The choice of precursor can significantly influence the morphology, size, and composition of the particles formed during the pyrolysis process. By selecting different precursor compounds or mixtures, variations in the

chemical reactions, decomposition pathways, and phase transformations occurring during pyrolysis can be introduced. This, in turn, can lead to the formation of particles with different shapes, sizes, and structures.¹⁶ Among the many ways of precursor selection, selecting precursors with different reactivities can impact the kinetics and thermodynamics of the pyrolysis process.¹⁷ Some precursors may decompose more readily or at lower temperatures, leading to rapid reactions and the formation of unique morphologies. By using precursors with varying reactivity, pyrolysis conditions can be tailored to achieve specific particle shapes and sizes.

In this Chapter, three different types of metal salt precursors are used for FeCo particles formation, including Fe/Co Nitrate, Fe/Co Chloride, and Fe/Co Acetate. When three of these different precursors are inserted into the USP system, FeCo particles are formed with very different morphology (See **Figure 5.3**).

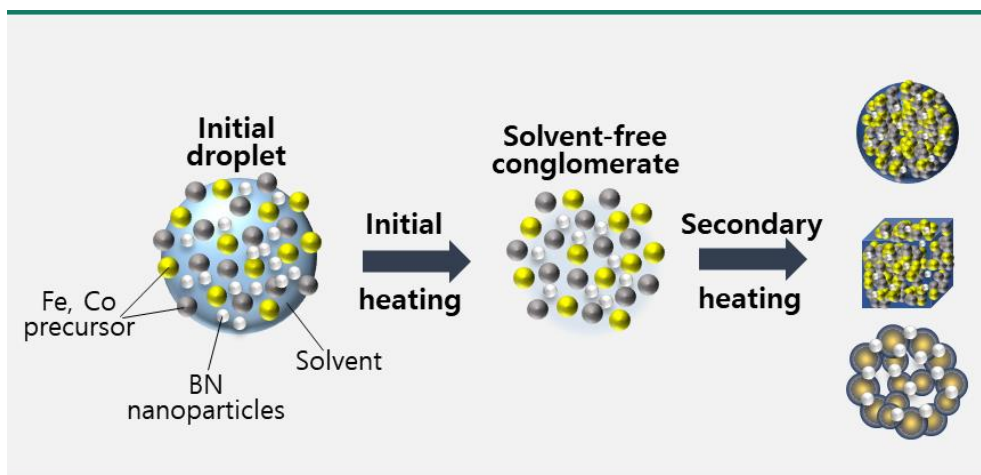


Figure 5.2. Schematic illustration of formation of FeCo/BN particles from three different precursors including Fe/Co Nitrate, Fe/Co Chloride, and Fe/Co Acetate via Ultrasonic Spray Pyrolysis. Droplets of aerosol carried by carrier gas into hot chamber and droplets are dried, contracted, precipitated, thermolized and sintered.

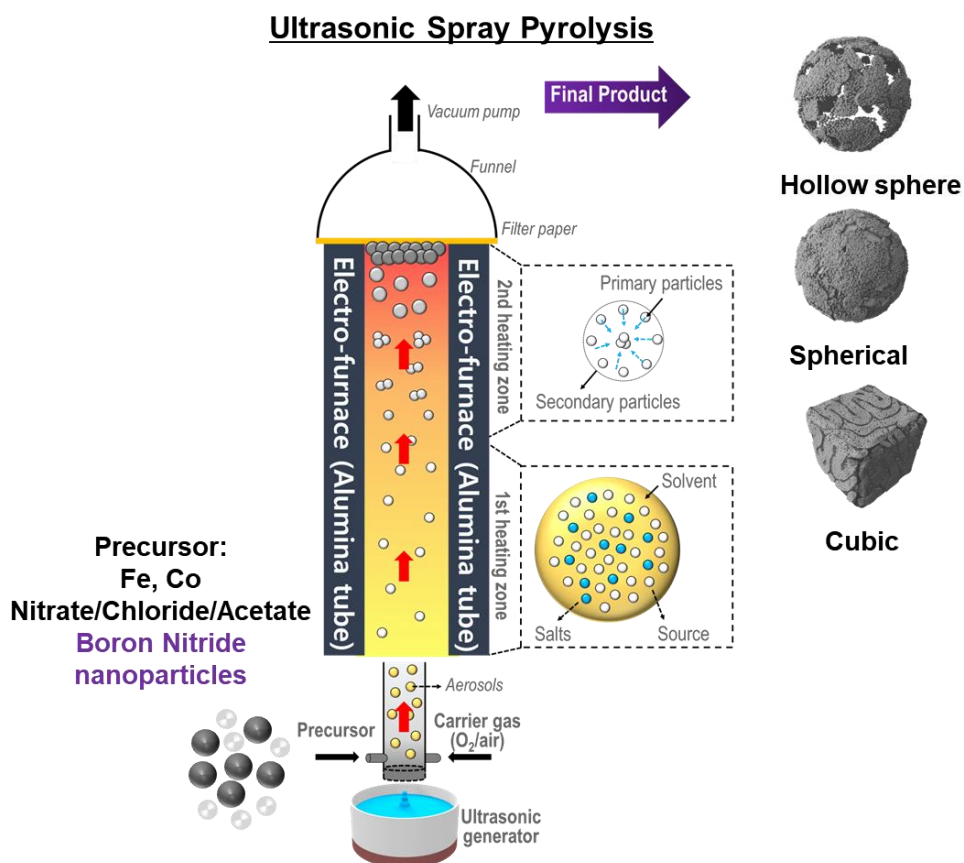


Figure 5.3. Schematic illustration of overall process of Ultrasonic Spray Pyrolysis involving the three different precursors, Fe/Co Nitrate, Fe/Co Chloride, and Fe/Co Acetate, where spherical, cubic, and hollow-sphere particles are formed respectively.

5.2 Experimental Section

5.2.1. Materials

Fe (III) nitrate nonahydrate ($\text{Fe}(\text{NO}_3)_3 \cdot 9\text{H}_2\text{O}$, ACS reagent, $\geq 98\%$), Co(II) nitrate hexahydrate ($\text{Co}(\text{NO}_3)_2 \cdot 6\text{H}_2\text{O}$, ACS reagent, $\geq 98\%$), Fe (II) acetate ($\text{Fe}(\text{CO}_2\text{CH}_3)_2$, 95%) were purchased from Sigma-Aldrich. Fe (II) chloride tetrahydrate ($\text{FeCl}_2 \cdot 4\text{H}_2\text{O}$, 99%), Co (II) chloride hexahydrate ($\text{CoCl}_2 \cdot 6\text{H}_2\text{O}$, 97%), and Co (II) acetate tetrahydrate ($(\text{CH}_3\text{COO})_2\text{Co} \cdot 4\text{H}_2\text{O}$, 97%) were purchased from Samchun Chemicals. Boron nitride nanoparticles (h-BN, 99.8 %, 40 nm) were purchased from Unitech Corporation. Thermoplastic urethane TPU (A-9410) was purchased from Songwon Industrial Chemical Co., Ltd., Korea.

5.2.2. Synthesis of FeCo spherical, cubic, and hollow-spherical particles via ultrasonic spray pyrolysis

The concentration of the precursor solutions was uniformly set at 0.2 M. To prepare the nitrate precursor solution, 4.04 g of $\text{Fe}(\text{NO}_3)_3 \cdot 9\text{H}_2\text{O}$ and 2.91 g of $\text{Co}(\text{NO}_3)_2 \cdot 6\text{H}_2\text{O}$ were magnetically stirred and dissolved in 50 mL of distilled (DI) water. The same procedure was repeated for the chloride and acetate precursors, and specific details can be found in **Table 5.1**. The dissolved solutions were loaded into a 50 mL syringe and pumped at a speed of 0.4 mL/min into a glass quartz which was subsequently sprayed into the USP system using an ultrasonic nebulizer. The aerosol droplets generated from the nebulizer was carried through the system with the aid of carrier gas. Mixed gas (H_2 10% + Ar 90%) was used with a flow rate of 5 L/min. The two thermal zones within the reaction chamber were preheated, with the first heating zone reaching a temperature of 200 °C and the second heating zone reaching 900 °C.

The synthesized FeCo particles were collected in the collecting zone using a filter paper.

5.2.3. Synthesis of FeCo/BN spherical, cubic, and hollow-spherical particles via ultrasonic spray pyrolysis

The fabrication of FeCo/BN particles utilized the same method as described in Section 5.2.2, wherein the BN nanoparticle solution was loaded into the USP system concurrently with the FeCo precursor solutions. To prepare the BN nanoparticle solution, 0.08 g of BN nanoparticles were dissolved into 50 mL of DI water. The BN nanoparticle solution was tip sonicated for 1 hour at 30% amplitude. The solution containing dispersed BN nanoparticles was transferred into a 50 mL syringe and pumped simultaneously with the FeCo precursor solution at a rate of 0.4 mL/min. The same heating temperature and carrier gas employed in Section 5.2.2 were used. The synthesized FeCo/BN particles were collected in the collecting zone using a filter paper.

5.2.4. Fabrication of FeCo/BN/TPU EW Absorbing Composite

The FeCo spherical, cubic, and hollow-spherical powders and FeCo/BN spherical, cubic, and hollow-spherical powders were mechanically mixed with TPU dissolved in a solvent using a planetary mixer (Thinky, ARE-310). The mixture maintained a fixed ratio of 50% filler to total weight. Next, the mixture was casted using a doctor blade to achieve a uniform thickness of 120 μm . The cast films were dried overnight in a convection oven at 110°C. Afterwards, the film was vacuum-pressed by stacking and hot-pressing at 120°C to produce a flexible composite film

with a thickness of 1 mm. The stacked films were subjected to hot pressing at a pressure of 10 MPa for 30 minutes. Following the pressing, the film was allowed to cool naturally to room temperature. The resulting film was then used for characterizing the electromagnetic parameters.

5.2.5. Characterization

The structural morphology was characterized by field-emission scanning electron microscopy (FE-SEM, JSM-7610F, JEOL) and field-emission transmission electron microscopy (FE-TEM, Talos F200X, Thermo Fisher Scientific). The crystal structure was analyzed by X-ray diffraction (XRD, Rigaku D/Max-2500VL/PC). The magnetic properties were measured using a vibrating sample magnetometer (VSM, EZ9, Microsense). Thermal conductivity was assessed using a laser flash analyzer (LFA 467 Hyperflash, Netzsch). The electromagnetic properties (complex permeability and complex permittivity) were investigated by vector network analyzer (VNA, N5222B, Keysight). To cover the frequency range of 0.5–18 GHz, a Keysight 85051 B verification kit and a 10 cm coaxial airline were employed alongside the VNA (Vector Network Analyzer). The specimen was shaped into a donut with an outer diameter of 7 mm, inner diameter of 3.04 mm, and a thickness of 1 mm. For the frequency range of 18-26 GHz, the N5222B was coupled with the Keysight K11644A calibration kit and a WR-42 waveguide. Rectangular specimens measuring $10.7 \times 4.3 \times 1.0 \text{ mm}^3$ were used for the measurements. The viscosity measurements of FeCo/TPU composites were carried out using a Discovery HR-3 hybrid rheometer (TA Instrument, USA). The rheometer utilized a 20 mm parallel plate geometry. The viscosity was measured at room temperature, with a shear rate ranging from 10^{-3} to 10^3 s^{-1} , and a gap size of 300 μm . The zero-rate viscosity and

infinite-rate viscosity were calculated using the Carreau-Yasuda model^{##}.

Table 5.1. Table showing variables for each precursor material.

Samples	FeCo-Nitrate		FeCo-Chloride		FeCo-Acetate	
Precursors	$\text{Fe}(\text{NO}_3)_3 \cdot 9\text{H}_2\text{O}$	$\text{Co}(\text{NO}_3)_2 \cdot 6\text{H}_2\text{O}$	$\text{FeCl}_2 \cdot 4\text{H}_2\text{O}$	$\text{CoCl}_2 \cdot 6\text{H}_2\text{O}$	$\text{Fe}(\text{CO}_2\text{CH}_3)_2$	$(\text{CH}_3\text{COO})_2\text{Co} \cdot 4\text{H}_2\text{O}$
Molar Concentration (M)	0.2	0.2	0.2	0.2	0.2	0.2
Mass (g)	4.04	2.91	1.99	2.38	1.74	2.49
DI water (mL)	50	50	50	50	50	50

5.3 Results and Discussion

5.3.1. Structural Morphology Characterization of FeCo and FeCo/BN Particles

The experimental verification of the preparation and fabrication process of the FeCo/TPU EW absorber composite began with the synthesis of shape-modulated FeCo particles. The FeCo particles, synthesized using three distinct precursor solutions (nitrate, chloride, and acetate), exhibited significantly varied structures, as depicted in **Figure 5.4**. FeCo nitrate possesses a spherical structure, as observed in **Figure 5.4 (a)**. In contrast, FeCo chloride displays a cubic structure as depicted in **Figure 5.4 (b)**. FeCo acetate, on the other hand, exhibits a hollow-spherical structure composed of longer one-dimensional rod-like sub-particles as shown in **Figure 5.4 (c)**. The distinct variations in particle shape can be attributed to the varying reactivities of the different precursor solutions, which influence the kinetics and thermodynamics of the pyrolysis process.¹⁸⁻¹⁹ The chemical reactivity of each precursor solution will be explored and discussed in Section 5.3.2.

The low-magnification SEM images of the three samples provide an overview of their respective structural morphologies, as depicted in **Figure 5.4 (d)** to **(f)**. The particles of FeCo nitrate and FeCo chloride appear to be well-separated from one another, occupying sufficient individual space. In contrast, the particles of FeCo acetate exhibit an interconnected appearance, forming a network-like structure. The presence of this network-like structure may result in an increase in electrical conductivity, consequently leading to an elevation in complex permittivity. When an EWAM exhibits a high complex permittivity, it can lead to impedance mismatching, which subsequently results in poor absorption performance. Therefore, it is crucial

to control and reduce the value of the complex permittivity by introducing an appropriate dielectric material. Furthermore, heat dissipation is another crucial factor to consider during the fabrication of EW absorbers. Prolonged exposure to EM radiation without effective dissipation of the generated heat from absorbed EM radiation can have a negative impact on the lifetime and performance of the absorber. Thus, the inclusion of a dielectric material possessing both high dielectric constant and thermal conductivity can effectively address the aforementioned issues. To accomplish this, the fabrication of FeCo particles incorporates the introduction of BN nanoparticles. The inclusion of BN nanoparticles in each FeCo particle can be confirmed by examining the EDS analysis provided in **Figure 5.5**. As illustrated in the figure, all three samples (FeCo/BN nitrate, FeCo/BN chloride, and FeCo/BN acetate) exhibit elemental mapping results for Fe, Co, and N. The N mapping reveals that the BN nanoparticles were successfully deposited onto the surface of the FeCo particles. In particular, for FeCo acetate, the BN particles are not only observed on the particle's surface but also found to be intercalated between the rod-like sub-particles. The presence of these intercalated BN particles can significantly contribute to reducing the electrical conductivity of the FeCo particles while also enhancing heat dissipation across all regions.

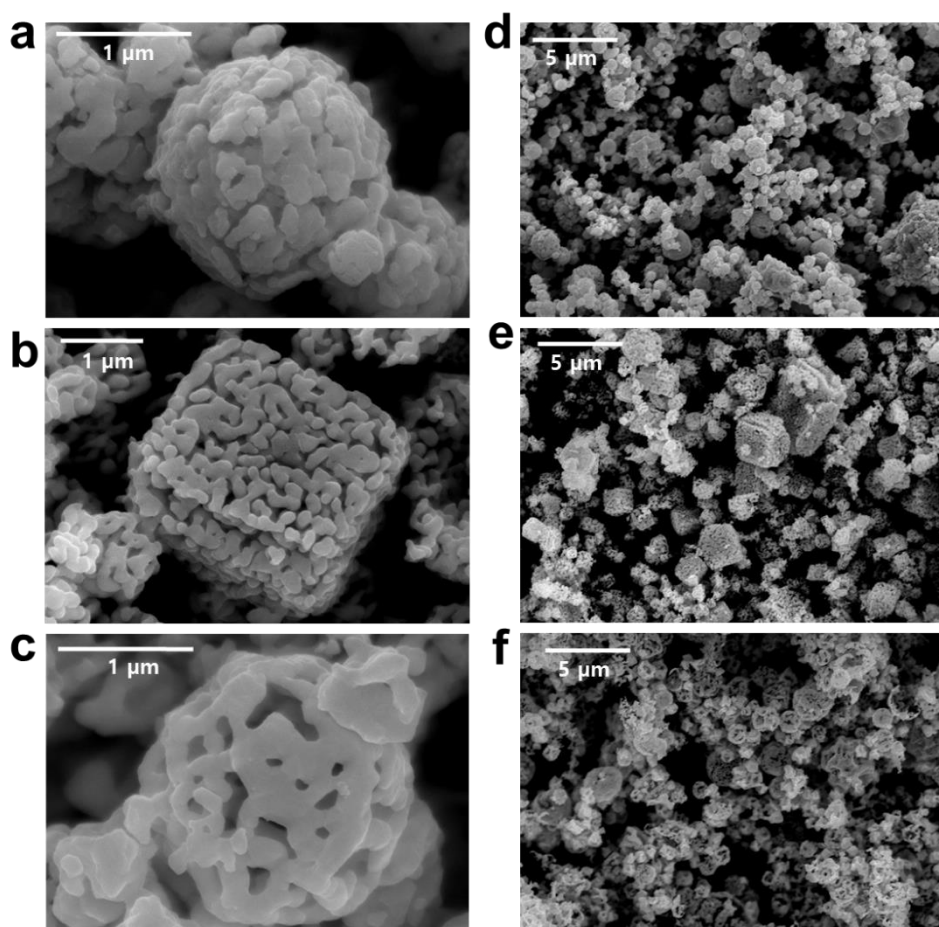


Figure 5.4. Structural characterization of as-synthesized FeCo. (a-c) High magnification SEM images of one particle and (d-f) Low magnification SEM images of overview of FeCo-Nitrate, FeCo-chloride, and FeCo-Acetate respectively.

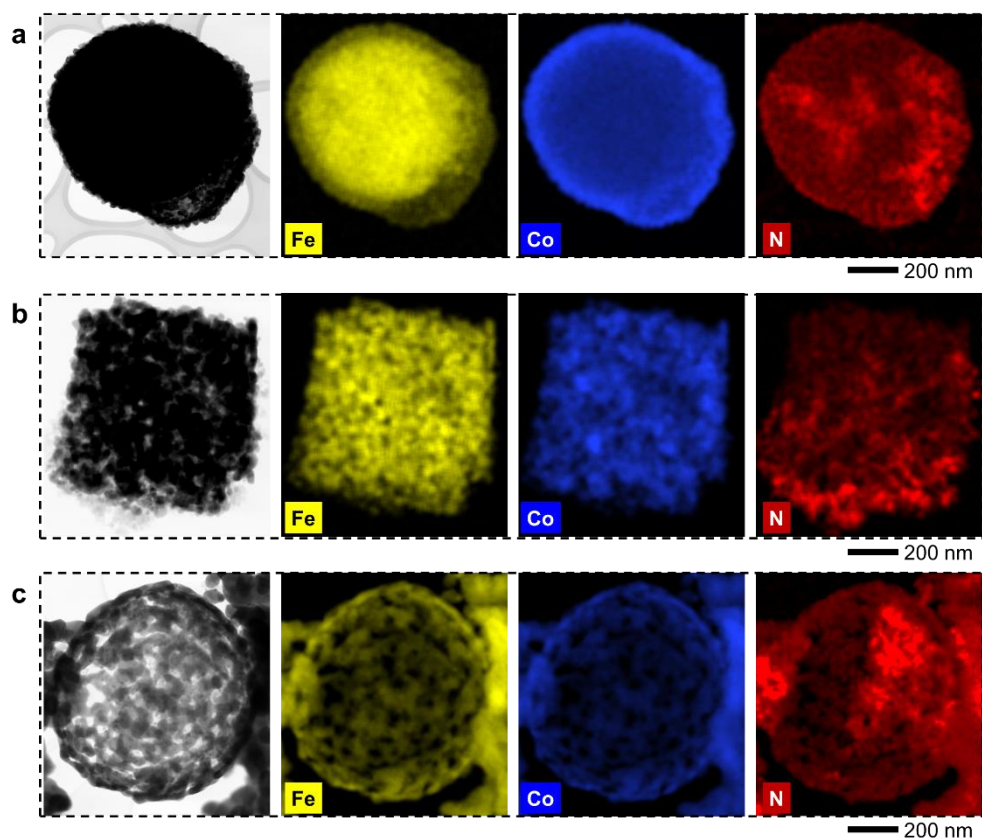
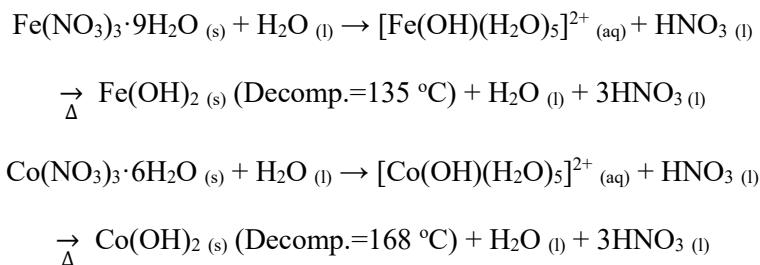


Figure 5.5 TEM observation images, and corresponding elemental mapping of iron, cobalt, and nitrogen: (a) FCBN-Nitrate, (b) FCBN-Chloride, and (c) FCBN-Acetate particles.

5.3.2. Theoretical Consideration of Relationship Between Precursor Material and Shape Modulation

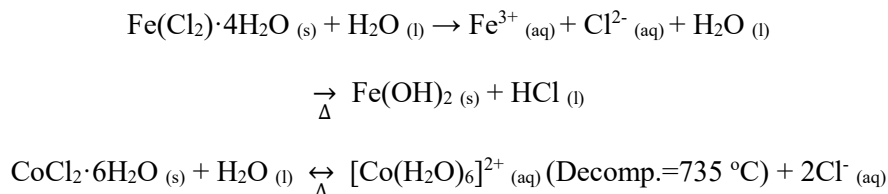
As discussed in Section 5.3.1, the significant variation in the shapes of the FeCo particles is likely attributed to the differing reactivity of each precursor solution. Regarding the aqueous FeCo nitrate solution, the metal ions and nitrate anions are initially dissolved in water (See **Figure 5.6 (a)**). During the initial heating at 200 °C, the solvent begins to evaporate, initiating the nucleation of metal particles and forming intermediate hydroxide particles of Fe(OH)₂ and Co(OH)₂. The chemical reaction is depicted below:



The hydroxides of Fe and Co have relatively low decomposition temperatures of 135°C and 168°C respectively. As a result, when they are introduced into the primary heating zone, the hydroxides break down. Upon entering the secondary heating zone, the process of nucleation and growth of metal particles occurs, followed by the subsequent sintering of these particles. This sintering process serves to minimize surface energy and results in the formation of spherical particles as illustrated in the **Figure 5.6 (a)**.²⁰

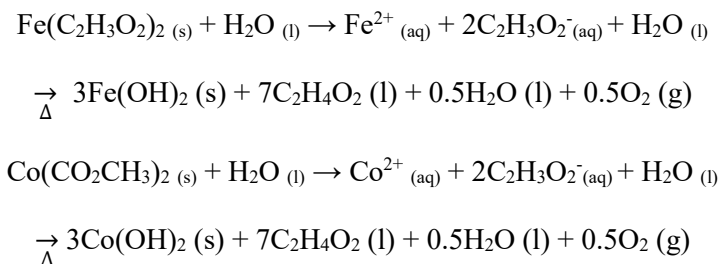
The behavior of the aqueous FeCo chloride solution differs significantly from that of the nitrate solution. The metal ions and Cl anions are initially dissolved in water (See **Figure 5.6 (b)**). During the initial heating process at 200 °C, the solvent evaporates, resulting in the formation of Fe(OH)₂ particles from the Fe cations. In

contrast, CoCl_2 exhibits a reversible reaction when subjected to heat. The chemical reaction is depicted below:



When the dissociated $[\text{Co}(\text{H}_2\text{O})_6]^{2+}$ aqueous solution is heated, it undergoes a reversible reaction. However, the solid state of CoCl_2 has a significantly high decomposition temperature of $735\text{ }^\circ\text{C}$. As a result, the CoCl_2 particles are able to maintain their cubic structure when subjected to the secondary heating zone as illustrated in **Figure 5.6 (b)**.

Lastly, the FeCo acetate particles undergo a similar reaction in which they form Fe and Co hydroxides. However, in addition to the hydroxides, the reaction also produces oxygen gas, as shown in the following chemical equation:



Due to the presence of generated oxygen gas, the FeCo acetate particles exhibit the formation of hollow shells while maintaining their spherical shape. The gas causes fractures within the particles, resulting in hollow structures that contain macropores or "blow-outs" as illustrated in **Figure 5.6 (c)**.²¹

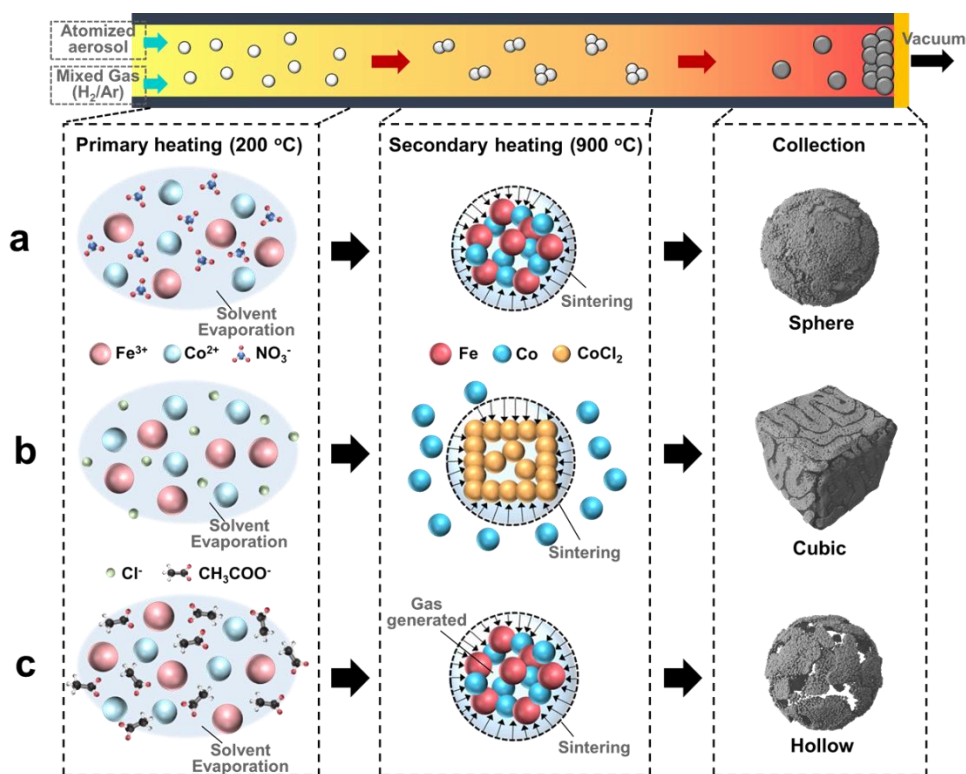


Figure 5.6. Manufacturing strategy for the shape-modulated FeCo particles. (a-c) Schematics demonstrating a series of shape-modulation processes produced from the different metal salt precursors. (a) Sphere-shaped FeCo particle manufactured through the aerosol reaction of iron nitrate and cobalt nitrate. (b) FeCo cube particle synthesized from the pyrolysis process of iron chloride and cobalt chloride. (c) FeCo hollow sphere particle using iron acetate and cobalt acetate.

5.3.3. Crystallographic and Magnetic Properties of FeCo Particles

X-ray diffraction (XRD) analysis was conducted to investigate the crystallographic properties of the FeCo samples obtained from nitrate, chloride, and acetate precursors. As depicted in **Figure 5.7**, all three samples exhibit distinct and pure FeCo body-centered cubic (BCC) peaks at 44.8° , 65.2° , and 82.6° . No additional peaks are observed in the spectra, indicating that the collected samples solely consist of pure FeCo particles without any other impurities.

The magnetic properties of the aforementioned three samples were also investigated using VSM (Vibrating Sample Magnetometer) to measure their hysteresis loops. As anticipated, all three samples exhibited remarkably high M_s values of 213.2, 214.7, and 219.9 emu/g (See **Figure 5.8**). Given the already elevated values of all three samples, the slight difference between them can be considered negligible.

Based on the XRD and VSM analysis, it is evident that all three samples exhibit identical crystallographic features and magnetic properties. This suggests that the sole distinction between them lies in their respective shapes. The impact of these particle shape differences can be explored by investigating the electromagnetic properties of the samples.

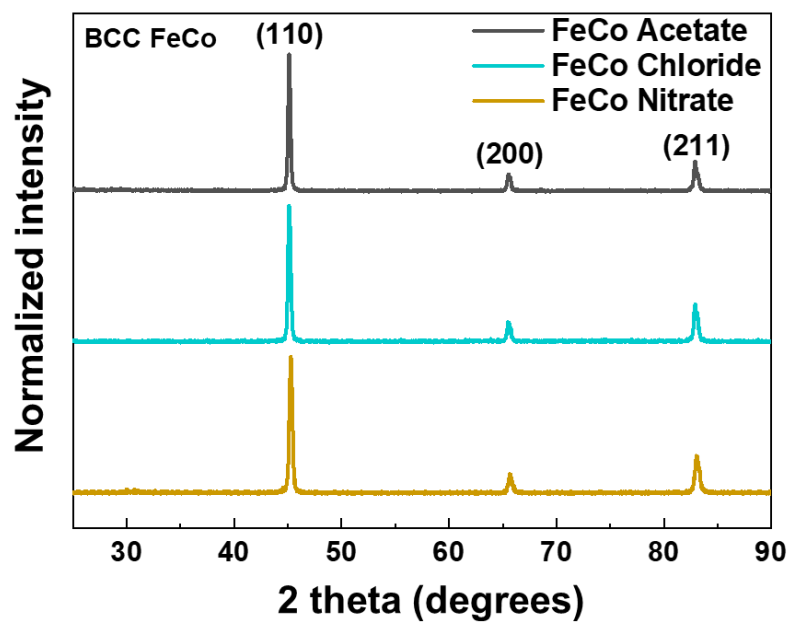


Figure 5.7. Characterization results from XRD analysis. XRD data captures the pure FeCo body-centered cubic (BCC) peaks at 44.8°, 65.2°, and 82.6°.

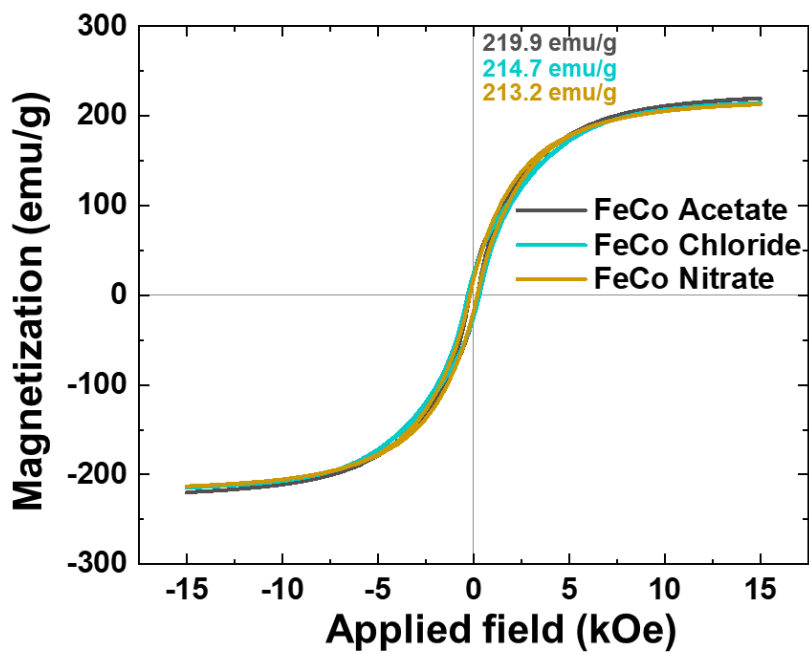


Figure 5.8. Magnetic hysteresis loop data of the three different samples, including FeCo-Nitrate, FeCo-Chloride, and FeCo-Acetate.

5.3.4. Thermal Properties of FeCo/BN Particles

In order to assess the influence of BN on the thermal conductivity of the FeCo/BN/TPU composite, the thermal properties of FeCo nitrate, chloride, and acetate particles incorporating BN were examined. The disparity in thermal conductivity measurements between the FeCo/BN/TPU composites prior to and after the addition of BN nanoparticles was assessed and is illustrated in **Figure 5.9**. As depicted in the figure, the inclusion of BN nanoparticles remarkably enhances the thermal conductivity of the FeCo/TPU composite for all three samples. The thermal conductivity value enhances by 29.1%, 31.4%, 13.4% for FeCo-Nitrate/BN/TPU, FeCo-Chloride/BN/TPU, and FeCo-Acetate/BN/TPU respectively, indicating that the incorporation of BN nanoparticles has played a crucial role in enhancing the thermal properties of the composites. The thermal conductivity values increase by 29.1%, 31.4%, and 13.4% for FeCo-Nitrate/BN/TPU, FeCo-Chloride/BN/TPU, and FeCo-Acetate/BN/TPU, respectively. This clearly indicates that the addition of BN nanoparticles has played a vital role in enhancing the thermal properties of the composites.

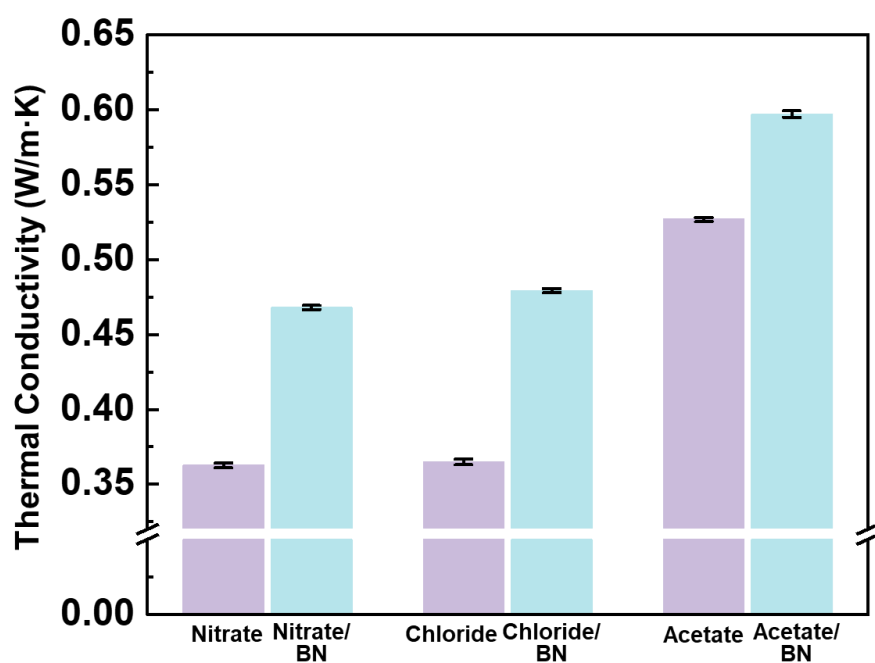


Figure 5.9. Thermal conductivity measurement of the three different as-synthesized FeCo particles and the BN-incorporated samples.

5.3.5. Electromagnetic Properties of FeCo and FeCo/BN Particles: Complex Permeability and Permittivity Spectra

The complex permeability and permittivity values were measured for the three distinct FeCo particle samples to assess the influence of their shape differences on the electromagnetic properties (See **Figure 5.10**). The complex permeability values, illustrated in **Figure 5.10 (a)**, reveal a significant disparity in the real part (μ') and the imaginary part (μ'') among the three samples. Among the three samples, FeCo-Acetate and FeCo-Chloride exhibit the highest complex permeability values, while FeCo-Nitrate demonstrates the lowest value. This outcome aligns well with the observed shape differences in the three samples, indicating a consistent and meaningful relationship between shape variation and complex permeability. Due to the spherical shape of FeCo-Nitrate particles, they lack anisotropy. According to Snoek's law, isotropic materials tend to exhibit lower complex permeability values. However, FeCo-Chloride has anisotropy features owing from its cubic structure and FeCo-Acetate particles consist of 1-dimensional rod-like sub-particles, which serves as the primary reasons for their elevated complex permeability values. According to Equation (8) of Snoek's law, materials that possess anisotropy have a greater effective magnetic field aligned with the easy axis compared to the effective field along the hard axis. This leads to an increase in the complex permeability values. The presence of anisotropic cubic structure in FeCo-Chloride and 1-dimensional rod-like sub-particles in FeCo-Acetate leads to the generation of effective fields associated with the anisotropy of the particles. This phenomenon consequently elevates the complex permeability values for these particles.

On the other hand, the complex permittivity exhibits a slightly different pattern compared to the complex permeability values (See **Figure 5.10 (b)**). The

complex permittivity values of FeCo-Nitrate and FeCo-Chloride particles are noticeably lower compared to FeCo-Acetate. This distinction is likely attributed to the overall morphology of the three different samples. As mentioned in Section 5.3.1, FeCo-Chloride and FeCo-Nitrate particles appear to be well-separated from one another, occupying sufficient individual space. In contrast, the particles of FeCo acetate exhibit an interconnected appearance, forming a network-like structure, which is the primary reason for the higher complex permittivity value observed in FeCo-Acetate. Materials with high connectivity exhibit increased electrical conductivity, which subsequently results in an elevation of the complex permittivity. Having an excessively high complex permittivity is unsuitable for impedance matching, which can lead to poor absorbing performance. Therefore, it is necessary to moderately decrease the complex permittivity value by incorporating dielectric materials, such as BN nanoparticles, for improved impedance matching.

Following the introduction of BN nanoparticles, a subsequent investigation was conducted to re-evaluate the complex permeability and permittivity values. As depicted in **Figure 5.11 (a)**, there is no significant change observed in the complex permeability values for the three FeCo/BN particles in comparison to the as-synthesized FeCo particles. While FeCo/BN-Chloride and FeCo/BN-Acetate particles maintain their high complex permeability values, the FeCo/BN-Nitrate particles remain in the lower range. In terms of complex permittivity values (**refer to Figure 5.11 (b)**), no notable change is observed in the FeCo/BN-Nitrate particles. However, there is a slight reduction in the complex permittivity value for FeCo/BN-Chloride particles, while a significant decrease is observed for FeCo/BN-Acetate particles. Therefore, it can be inferred that BN nanoparticles have effectively contributed to the reduction of the complex permittivity values of the FeCo particles.

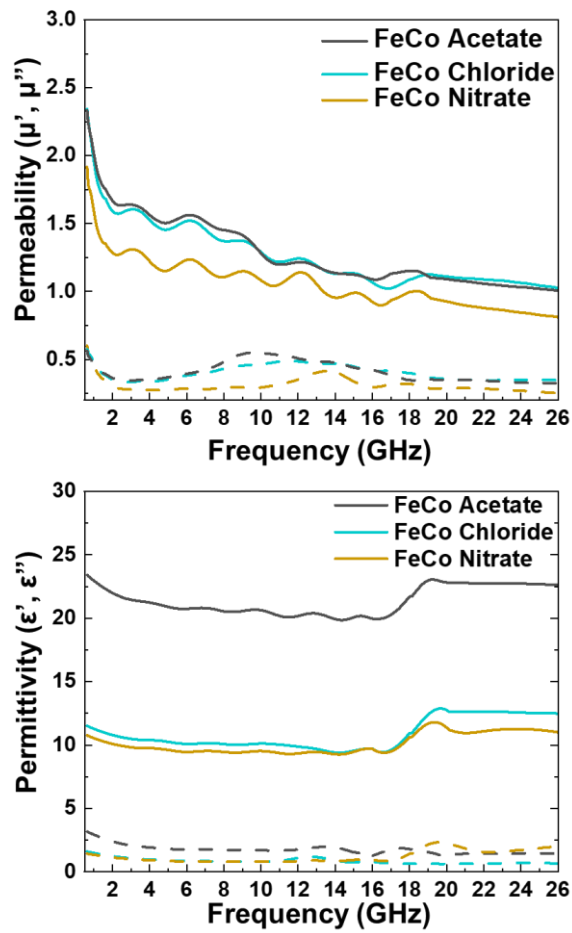


Figure 5.10. Electromagnetic characterization of the as-synthesized FeCo particles. (a) Complex permeability and (b) complex permittivity for FeCo-Nitrate, FeCo-Chloride, and FeCo-Acetate.

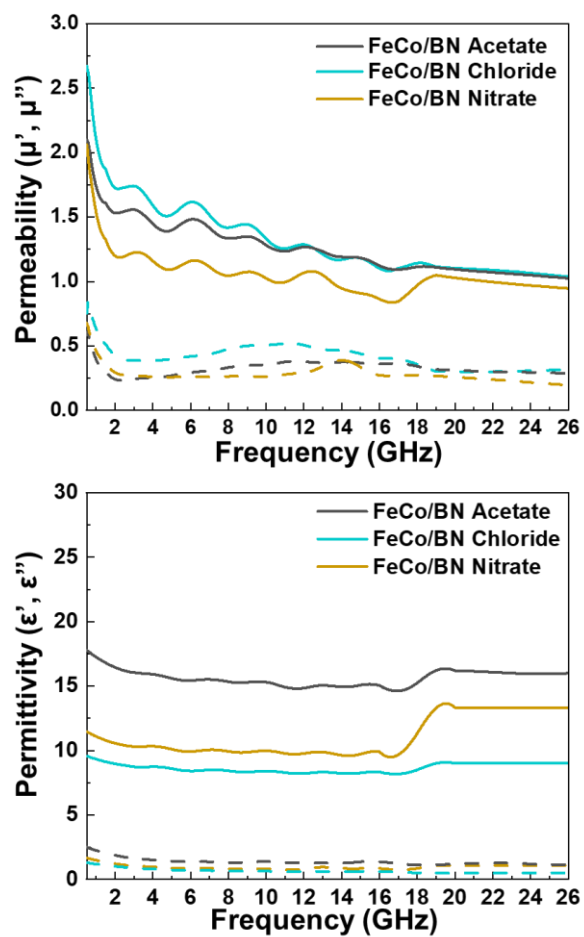


Figure 5.11. Electromagnetic characterization of the as-synthesized FeCo particles. (a) Complex permeability and (b) complex permittivity for FeCo/BN-Nitrate, FeCo/BN-Chloride, and FeCo/BN-Acetate.

5.3.6. Electromagnetic Wave Absorbing Performance: Reflection Loss Calculation and EAB

To assess the absorbing performance of the three FeCo/BN/TPU composites, the reflection loss calculation was conducted using equations (9) and (10). The reflection loss calculations were performed across the entire frequency range, ranging from 2 GHz to 26 GHz, with varying thicknesses between 1.0 mm and 2.0 mm (See **Figure 5.12**). In this context, we focus on thinner thicknesses and wide effective absorption bandwidth (EAB) for discussion, as the objective is to develop wide-band absorbing materials that are thin and lightweight. As depicted in **Figure 5.12(a)**, the absorption peaks of FeCo/BN-Nitrate composites predominantly exceed -20 dB within the range of thin thicknesses, specifically from 1 mm to 1.5 mm. However, it is worth noting that the EABs are relatively narrow, measuring only 4.40 GHz, 2.54 GHz, 1.32 GHz, and 1.32 GHz for thicknesses of 1 mm, 1.1 mm, 1.2 mm, and 1.3 mm, respectively. In contrast, the FeCo/BN-Acetate particles exhibit significantly higher absorption peaks exceeding -20 dB across all thicknesses (See **Figure 5.12 (b)**). At a thickness of 1.5 mm, the FeCo/BN-Acetate particles exhibit an impressive maximum absorption peak, reaching as low as -46.37 dB. The FeCo/BN-Acetate particles also demonstrate enhanced performance in terms of EABs at thin thicknesses compared to the FeCo/BN-Nitrate particles. Specifically, the FeCo/BN-Acetate composites exhibit significantly wider EABs across thicknesses ranging from 1.0 mm to 1.3 mm. The EABs measure 4.42 GHz, 4.60 GHz, 5.04 GHz, and 3.84 GHz for thicknesses of 1 mm, 1.1 mm, 1.2 mm, and 1.3 mm, respectively. Despite the generally spherical shape of both particles, the disparity in reflection loss values and bandwidths can be attributed to their distinct structures. The FeCo/BN-Acetate composite, for instance, is composed of 1-

dimensional sub-particles that exhibit anisotropic properties, contributing to the observed differences. The presence of anisotropic features in FeCo/BN-Acetate particles led to significantly higher complex permeability values compared to FeCo/BN-Nitrate particles. Additionally, the incorporation of BN nanoparticles into FeCo-BN/Acetate particles caused a considerable decrease in complex permittivity values. This resulted in a successful impedance matching, ultimately leading to outstanding absorption performance. Moreover, the hollow structure of FeCo/BN-Acetate allows for the capture of EM radiation within the shell, leading to multiple reflections. Consequently, this unique characteristic contributes to the excellent absorption performance exhibited by the material. In the case of FeCo/BN-Chloride particles, the absorption peaks only slightly exceed -20 dB when the thickness ranges from 1.6 mm to 2.0 mm (refer to **Figure 5.12 (c)**). However, when the thickness is reduced to the range of 1.0 mm to 1.4 mm, the absorption peaks fail to surpass -20 dB entirely, indicating the poorest absorption performance. The poor absorption performance of FeCo/BN-Chloride can likely be attributed to impedance mismatching, primarily due to its lowest complex permittivity value. When the permittivity value is excessively low, it results in impedance mismatching, necessitating a thicker thickness for effective performance of the EWAM composite. Hence, considering that FeCo/BN-Chloride possesses an anisotropic structure, it can potentially function as an effective EWAM if the permittivity value is appropriately adjusted to achieve impedance matching. The overall reflection loss values and EABs are summarized in **Table 5.2**.

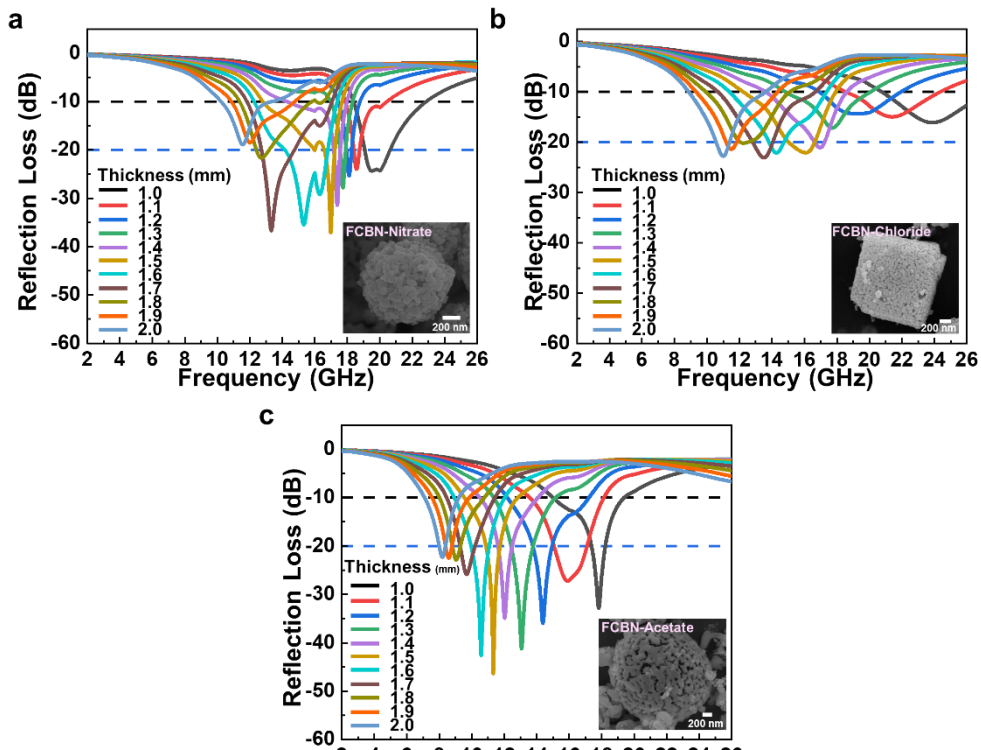


Figure 5.12. EMW absorption characteristics at the S (2 – 4 GHz), C (4 – 8 GHz), X (8 – 12 GHz), Ku (12 – 18 GHz), and K (18 – 26 GHz) band frequencies. (a-c) 2-D mappings of reflection loss calculation at the various thickness of EMW absorbing membranes manufactured by (a) FeCo/BN-Nitrate, (b) FeCo/BN-Chloride, and (c) FeCo/BN-Acetate particles.

Table 5.2. Effective bandwidth (<-10 dB) and reflection loss value (<-20 dB) at different thicknesses of the EMW absorbing membranes manufactured by FeCo/BN-Nitrate, FeCo/BN-Chloride, and FeCo/BN-Acetate.

Thick- ness (mm)	FCBN-Nitrate		FCBN - Chloride		FCBN-Acetate	
	Band width (GHz)	Reflection Loss (dB)	Band width (GHz)	Reflection Loss (dB)	Band width (GHz)	Reflection Loss (dB)
1.0	4.40	-24.38	-	-	4.42	-32.86
1.1	2.54	-23.99	-	-	4.60	-27.25
1.2	1.32	-25.33	-	-	5.04	-35.98
1.3	1.32	-27.83	-	-	3.84	-41.24
1.4	3.7	-31.45	4.96	-21.07	3.62	-34.90
1.5	4.88	-37.13	5.66	-22.08	3.34	-46.37
1.6	5.10	-35.52	5.94	-22.13	3.12	-42.64
1.7	5.22	-36.75	5.98	-23.08	3.00	-25.85
1.8	4.42	-21.67	5.14	-20.17	2.78	-22.87
1.9	-	-	4.98	-21.38	2.32	-22.50
2.0	-	-	4.72	-22.78	2.14	-22.31

5.3.7. Investigation of Loading Factors for FeCo Nanochain, FeCo Spherical Particle, and FeCo Hollow-Spherical Particle

As previously mentioned, the loading factor of filler material in EW absorbers plays a crucial role in enhancing the complex permeability. However, the high viscosity of nanomaterial imposes a constraint on the maximum loading factor achievable for the filler material in the composite. Typically, the most common loading factor is 50 wt%, given this limitation. In order to address this issue, hollow-spherical FeCo-Acetate particles were fabricated as part of this study. These particles offer a significant advantage by combining anisotropic 1-dimensional sub-particles with a spherical shape. As a result, it became possible to maintain a high complex permeability while substantially reducing the viscosity of the material. To demonstrate the superior performance of FeCo-Acetate in comparison to other materials, an investigation was conducted to analyze their loading factor as filler materials, as depicted in **Figure 5.13**. **Figure 5.13 (a)** displays the microstructure of three particles: FeCo nanochain, FeCo-Nitrate spherical particle, and FeCo-Acetate hollow-spherical particle. When the three particles are blended with TPU resin at a loading factor of 50 wt%, the resulting composites for all three samples exhibit excellent flow stability (refer to **Figure 5.13 (b)**). This attribute is a key reason for the widespread adoption of the 50 wt% loading factor in practice. However, when the loading factor is increased up to 70 wt%, the flow of the composite containing FeCo nanochain and FeCo-Nitrate particles becomes noticeably thick and viscous (see **Figure 5.13 (c)**). In contrast, the composite with FeCo-Acetate particles maintains its stable flow characteristics under the same conditions. In order to quantitatively evaluate the difference in viscosity among the three particles, viscosity

characteristics were also assessed.

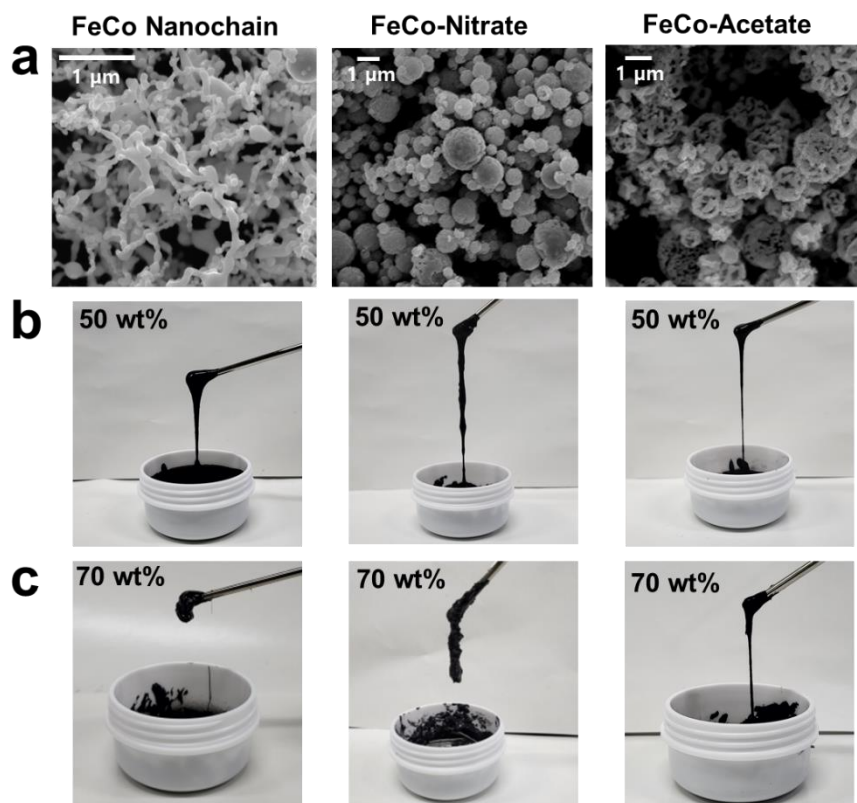


Figure 5.13. Overall microstructure and flow characteristics of FeCo nanochain, FeCo-Nitrate, and FeCo-Acetate shown by (a) SEM images and (b) photos of uncured FeCo/TPU composites.

5.3.8. Bulk Density and Viscosity Measurements of FeCo Nanochain, FeCo Spherical Particle, and FeCo Hollow-Spherical Particle

Viscosity refers to the property that measures the fluid's thickness or thinness. Density, on the other hand, quantifies the spacing between particles. When powders with low density are transformed into a fluid, they tend to exhibit high viscosity, and conversely, powders with high density result in lower viscosity. This phenomenon is evident in **Figure 5.14 (a)** and **(b)**. As illustrated in **Figure 5.14 (a)**, FeCo nanochain exhibits the smallest bulk density owing to the small size of its particles and their high aspect ratio. Conversely, FeCo-Nitrate demonstrates the highest bulk density due to its spherical-shaped particles. Notably, FeCo-Acetate showcases a bulk density value that falls right between the two particles, precisely aligning with the shape modulation achieved by the hollow-spherical structure (similar to FeCo-Nitrate) combined with 1-dimensional sub-particles (similar to FeCo nanochain).

The viscosity measurements clearly conform with the observed trend in bulk density values (refer to **Figure 5,14 (b)**). As the shear rate increases, FeCo nanochain exhibits the highest viscosity value, whereas FeCo-Nitrate demonstrates the lowest viscosity value. Once again, the viscosity of FeCo-Acetate falls between these two samples. Hence, it becomes evident that the successful reduction in viscosity was achieved solely through shape modulation while preserving the high complex permeability value, despite employing the exact same elements in the fabrication process.

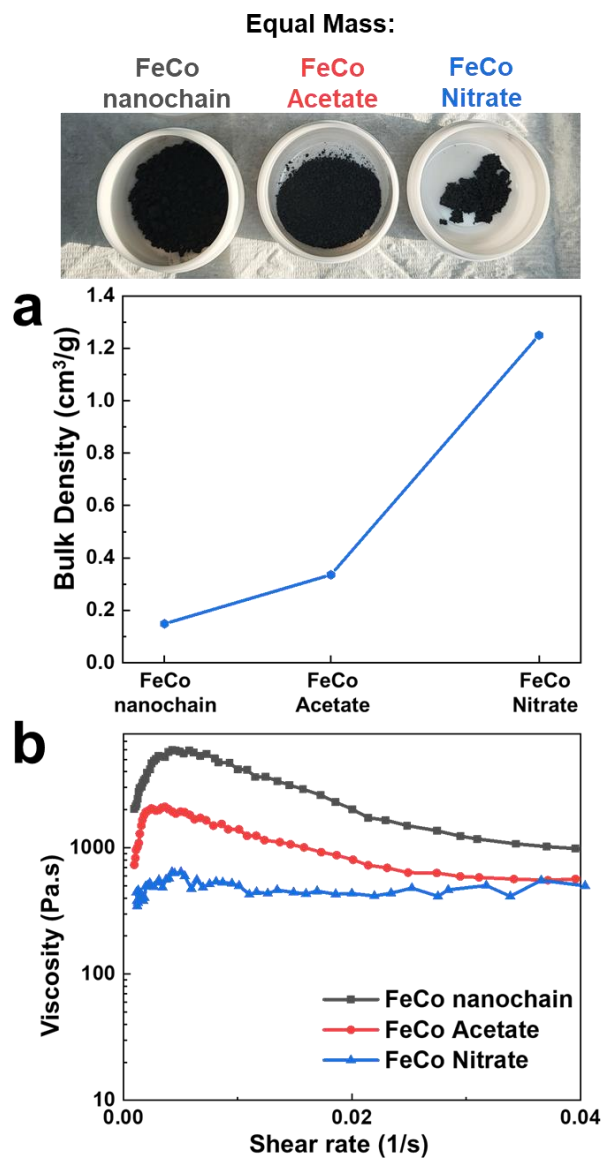


Figure 5.14. Physical characteristics of FeCo nanochain, FeCo-Acetate, FeCo-Nitrate analyzed by (a) Bulk density measurements and (b) Viscosity measurements.

5.4.9. Electromagnetic Properties of FeCo Hollow-Spherical Particles of 70 wt% Loading Factor

Due to its lower viscosity value compared to FeCo nanochain, it was feasible to incorporate FeCo-Acetate into a composite material with TPU at a loading ratio of 70 wt%. The feasibility of casting the un-cured FeCo-Acetate/TPU (70 wt%) composite into a film facilitated the subsequent evaluation of its electromagnetic properties (see **Figure 5.15**). The complex permeability and complex permittivity values of FeCo-Acetate/TPU (70 wt%) increased proportionally with the increase in filler material content. The increase in complex permeability is a positive indication. However, the increase in complex permittivity can result in impedance mismatching. Therefore, for future endeavors, careful design of FeCo-Acetate may be necessary to regulate the complex permittivity. By doing so, this particle has the potential to become an optimal material for EW absorbers.

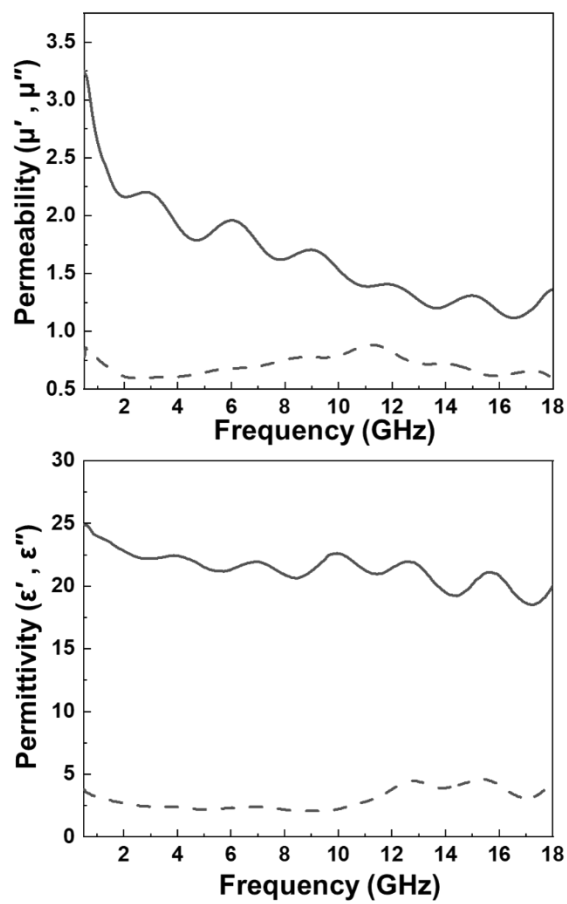


Figure 5.15. Electromagnetic characterization of FeCo-Acetate/TPU (70 wt%).

5.4. Conclusion

In conclusion, filler materials in composites from electromagnetic wave (EW) absorbers are essential for enhancing the absorption properties of the material by attenuating or absorbing electromagnetic radiation and converting it into heat energy. Achieving a uniform distribution of filler particles within the matrix is crucial for maximizing absorption efficiency. The loading ratio of the filler material can be adjusted to optimize the absorption properties of the composite. Nanomaterials, due to their small particle size and large surface area, are commonly used in EW absorber composites, but their high viscosity poses challenges in casting as a film. Ultrasonic spray pyrolysis (USP) is a promising technique for producing shape-modulated particles by controlling parameters such as precursor concentration, solution flow rate, furnace temperature, and carrier gas flow. Different precursor compounds can be selected to influence the particle shape, size, and composition. In this study, three metal salt precursors (FeCo-Nitrate, FeCo-Chloride, and FeCo-Acetate) were used to synthesize FeCo particles with different morphologies. The introduction of boron nitride (BN) nanoparticles helped reduce the complex permittivity. The X-ray diffraction analysis confirmed the pure FeCo composition, and the magnetic properties showed similar behavior for all samples. The addition of BN nanoparticles significantly improved the thermal conductivity of the FeCo/TPU composite. The complex permeability and permittivity measurements demonstrated the influence of particle shape on electromagnetic properties of the three different particles, FeCo/BN-Nitrate, FeCo/BN-Chloride, and FeCo/BN-Acetate. The FeCo/BN-Acetate material displayed superior absorption performance and low viscosity owing to its shape modulation. These findings highlight the importance of shape

modulation and the incorporation of suitable additives for optimizing the electromagnetic absorption performance of composites. Further research and optimization of fabrication processes can lead to the development of advanced EW absorber materials with enhanced properties for various applications.

5.5. References

1. Yusuf, J. Y.; Soleimani, H.; Sanusi, Y. K.; Adebayo, L. L.; Sikiru, S.; Wahaab, F. A., Recent Advances and Prospect of Cobalt Based Microwave Absorbing Materials. *Ceram. Int.* **2020**, *46* (17), 26466-26485.
2. Munir, A., Microwave Radar Absorbing Properties of Multiwalled Carbon Nanotubes Polymer Composites: A Review. *Adv. Polym. Tech.* **2017**, *36* (3), 362-370.
3. Wang, Y., Microwave Absorbing Materials Based on Polyaniline Composites: A Review. *International journal of materials research* **2014**, *105* (1), 3-12.
4. Singh, A.; Sambyal, S.; Singh, V., Recent Advances in Graphene Oxide-Ferrite Hybrid Framework as Radar Absorbing Material. *Recent Advances in Graphene Nanophotonics* **2023**, 263-286.
5. Rakha, S. A.; Khurram, A.; Ali, N.; Munir, A.; Iqbal, A.; Subhani, T.; Gul, I., Preparation of Microwave Absorbing E-Glass/Epoxy Nanocomposites with Low Content of Binary Carbon Nanofillers. *Adv. Polym. Tech.* **2015**, *34* (4).
6. Ardekani, S. R.; Aghdam, A. S. R.; Nazari, M.; Bayat, A.; Yazdani, E.; Saievar-Iranizad, E., A Comprehensive Review on Ultrasonic Spray Pyrolysis Technique: Mechanism, Main Parameters and Applications in Condensed Matter. *J. Anal. Appl. Pyrolysis* **2019**, *141*, 104631.
7. Majerič, P.; Rudolf, R., Advances in Ultrasonic Spray Pyrolysis Processing of Noble Metal Nanoparticles. *Materials* **2020**, *13* (16), 3485.
8. Jung, D. S.; Park, S. B.; Kang, Y. C., Design of Particles by Spray Pyrolysis and Recent Progress in Its Application. *Korean J. Chem. Eng.* **2010**, *27*, 1621-1645.
9. Workie, A. B.; Ningsih, H. S.; Shih, S.-J., An Comprehensive Review on

the Spray Pyrolysis Technique: Historical Context, Operational Factors, Classifications, and Product Applications. *J. Anal. Appl. Pyrolysis* **2023**, 105915.

10. Leng, J.; Wang, Z.; Wang, J.; Wu, H.-H.; Yan, G.; Li, X.; Guo, H.; Liu, Y.; Zhang, Q.; Guo, Z., Advances in Nanostructures Fabricated Via Spray Pyrolysis and Their Applications in Energy Storage and Conversion. *Chem. Soc. Rev.* **2019**, 48 (11), 3015-3072.

11. Jung, D. S.; Ko, Y. N.; Kang, Y. C.; Park, S. B., Recent Progress in Electrode Materials Produced by Spray Pyrolysis for Next-Generation Lithium Ion Batteries. *Adv. Powder Technol.* **2014**, 25 (1), 18-31.

12. Jamkhande, P. G.; Ghule, N. W.; Bamer, A. H.; Kalaskar, M. G., Metal Nanoparticles Synthesis: An Overview on Methods of Preparation, Advantages and Disadvantages, and Applications. *Journal of drug delivery science and technology* **2019**, 53, 101174.

13. Castañeda, L., Use of Ultrasonic Spray-Pyrolysis Process: A Brief Review. *Ultrasonics: Theory, Techniques and Practical Applications* **2013**, 47-72.

14. Suh, W. H.; Suslick, K. S., Magnetic and Porous Nanospheres from Ultrasonic Spray Pyrolysis. *J. Am. Chem. Soc.* **2005**, 127 (34), 12007-12010.

15. Wang, W.-N.; Purwanto, A.; Lenggono, I. W.; Okuyama, K.; Chang, H.; Jang, H. D., Investigation on the Correlations between Droplet and Particle Size Distribution in Ultrasonic Spray Pyrolysis. *Ind. Eng. Chem. Res.* **2008**, 47 (5), 1650-1659.

16. Tiyyagura, H. R.; Majerič, P.; Anžel, I.; Rudolf, R., Low-Cost Synthesis of Aunps through Ultrasonic Spray Pyrolysis. *Materials Research Express* **2020**, 7 (5), 055017.

17. Duret, A.; Grätzel, M., Visible Light-Induced Water Oxidation on

Mesoscopic A-Fe₂O₃ Films Made by Ultrasonic Spray Pyrolysis. *J. Phys. Chem. B* **2005**, *109* (36), 17184-17191.

18. Djelloul, A.; Bouzid, K.; Guerrab, F., Role of Substrate Temperature on the Structural and Morphological Properties of ZnO Thin Films Deposited by Ultrasonic Spray Pyrolysis. *Turkish Journal of Physics* **2008**, *32* (1), 49-58.

19. Ebin, B.; Gençer, Ö.; Gürmen, S., Simple Preparation of CuO Nanoparticles and Submicron Spheres Via Ultrasonic Spray Pyrolysis (Usp). *International Journal of Materials Research* **2013**, *104* (2), 199-206.

20. Majerič, P.; Jenko, D.; Friedrich, B.; Rudolf, R., Formation of Bimetallic Fe/Au Submicron Particles with Ultrasonic Spray Pyrolysis. *Metals* **2018**, *8* (4), 278.

21. Dunkle, S. S.; Helmich, R. J.; Suslick, K. S., BiVO₄ as a Visible-Light Photocatalyst Prepared by Ultrasonic Spray Pyrolysis. *J. Phys. Chem. C* **2009**, *113* (28), 11980-11983.

Part III

Conclusion

Chapter 6. Concluding Remarks

The aim of this research was to investigate the relationship between complex permeability and soft magnetic materials through various shape-modulation techniques applied to FeCo alloys. Shape modulation was identified as a crucial factor for enhancing complex permeability and was validated in this study using Snoek's Law. While previous studies have attempted shape modulation of FeCo powders into a chain-like structure using wet-chemical methods, it was found that these approaches had limitations in achieving one-dimensional structures with securely bonded or firmly attached particles. The objective of this study was to explore the correlation between shape modulation of magnetic materials and complex permeability, with a specific focus on achieving a broadband EWAM and identifying the optimal structure for maximum loading as a filler material in composites. By gaining a better understanding of this relationship, this research may pave the way for the development of novel strategies to shape-modulate FeCo alloys for applications in electromagnetic wave absorbers.

Here is a summary of this research:

1. The enhancement of complex permeability in FeCo alloys was pursued by considering Snoek's limit. Various shape-modulation techniques were employed to enhance both the initial permeability and the ferromagnetic resonance frequency (f_{FMR}), aiming to improve the complex permeability value.
2. To overcome the issue of high viscosity associated with nanomaterials used as filler in EW absorbing composites,

shape modulation of FeCo alloy was employed while preserving its high complex permeability.

3. To regulate the complex permittivity and improve the absorbing performance of shape-modulated FeCo electromagnetic wave (EW) absorbing composites, BN nanoparticles were incorporated into the FeCo alloys.
4. Overall, among the examined structures, FeCo nanobelts exhibited the highest initial permeability value and f_{FMR} , followed by FeCo nanochains and FeCo hollow-spheres.

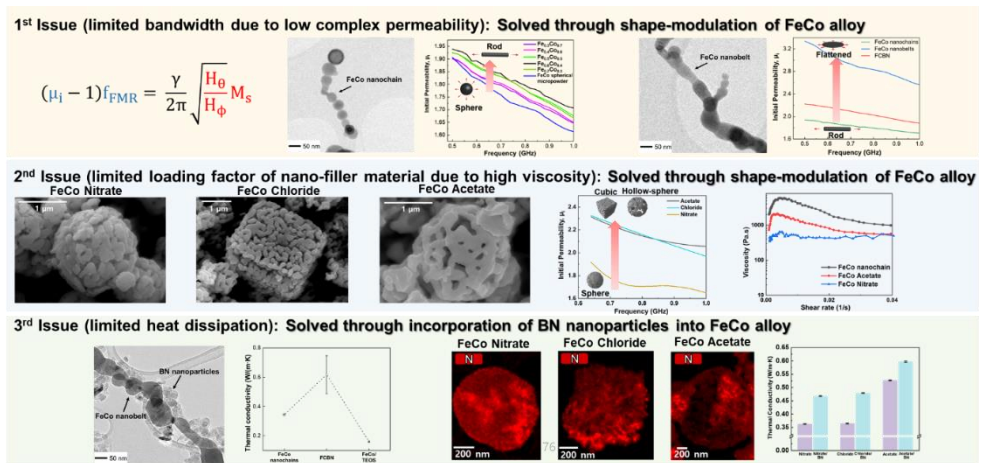


Figure 6.1. Summary of results in Chapter 3, 4, and 5.

국문 초록

무선 전송 및 항공우주 기술의 발전으로 인해 전자기파(EMW)는 민간 및 군사 분야에서 널리 사용되고 있다. 일상에서 사용되는 무선 통신의 편리함에도 불구하고, 아직까지도 EMW의 신호 간섭 및 오염으로 인해 데이터 전송의 신뢰성이 저하되고 사람의 건강이 위협받는 문제가 발생하고 있다. 이러한 문제들을 해결하기 위해 전자파 흡수체에 대한 수요가 증가하고 있다. 소형화된 전자기기나 항공 우주 기술을 고려할 때, 전자파 흡수 재료는 유연성과 가벼운 무게를 갖추어야 하며, 흡수된 EMW 에너지의 열 전도를 위해 높은 열전도성을 나타내야 한다. 이러한 전자파 흡수 재료는 광대역 주파수 범위에서 강한 전자파 흡수를 요구한다. 설계된 전자파 주파수 대역에서의 흡수를 위해서는 목적에 따라 적절한 흡수 재료를 선택해야 한다.

본 연구는 다양한 형상 제어 기법을 적용한 FeCo 합금을 통해 복소 투자율과 연자성 소재간의 관계를 탐구하기 위해 수행되었다. 형상 제어는 Snoek의 법칙을 통해 복소 투자율을 향상시키는 중요한 요소로 확인 되었다. 이전의 연구들이 사용한 wet-chemical 방법인 FeCo 합금의 형상 제어 시도는 견고하게 결합된 입자를 가진 1차원 구조를 달성 하는 데 제한이 있었다.

이 연구의 목표는 복소 투자율을 향상시키고, ferromagnetic resonance frequency (f_{FMR})을 개선하기 위해 Snoek's limit을 고려하는 동안, 광대역 전자파 흡수 재료를 개발하는 것이다. 또한, 높은 점도를 가진 나노소재로 인한 복합재의 한계를 해결하기 위해 FeCo 합금의 형상 제어를 사용하면서 높은 복소 투자율 또한 유지 할 수 있었다. BN 나노입자를 첨가함으로써 형상 제어된 FeCo 전자파 흡수재의 복소 유전율과 열전도도를 조절 할수 있었다. 제조 된 합금 중에서 Co 나노벨트가 가장 높은 초기 투자율과 f_{FMR} 을 나타내었으며 그 다음으로 FeCo 나노체인과 FeCo hollow-spherical이 높은 복소 투자율을 나타냈다.

1부에서는 전자파 흡수 재료에 대한 기본적인 이론들을 정리 하였다. 그 중에서도 초기 투자율과 f_{FMR} 을 향상 시키기 위한 형상 제어라는 중요한

기법에 대해 강조한다. 또한, 나노소재의 고 점도로 인해 전자파 흡수 복합재에서 충전재료로의 사용이 제한되는 등 해당 분야에서 마주치는 추가적인 문제에 대해서도 논의 한다. 전자파 흡수체의 제한된 열 방출 능력에 대해서도 논의 한다. 2부에서는 이러한 도전을 극복하기 위한 해결책을 제시하고 있다.

2부에서는 1부에서 논의된 문제들을 해결하기 위한 새로운 방법들을 제시한다. 제3장에서는 형상 제어 기술이 소개가 되며, 이를 통해 FeCo 합금이 열플라즈마 기법을 사용하여 일차원 구조로 변형 되어 흡수체의 성능을 향상 시키는 방법이 소개 된다. 제4장에서는 제3장에서 소개된 형상제어 접근법을 확장하여 이차원의 FeCo 합금을 제조함으로써 재료의 흡수 성능을 더욱 향상 시킨다. 그리고, BN 나노입자를 전자파 흡수체에 첨가함으로써 열 방출 문제를 해결하는 방법도 제시한다. 마지막으로, 제4장에서는 고점도 나노소재의 문제에 대응하기 위해 hollow한 구조를 가진 구형 FeCo 합금을 제조하는 추가적인 형상 제어 방법을 제시한다.

요약하면, 이 연구는 형상 제어와 복소 투자율 간의 관계를 조사하고, 광대역 전자파 흡수 재료를 개발하며, 복합체에서 사용될 수 있는 최적의 입자 구조를 제조하기 위한 가이드라인을 제시하였다. Snoek's limit을 고려하여 초기 투자율과 f_{fMR} 을 향상 시키는 전략이 적용 되었으며, 이 연구는 FeCo 합금의 형상 제어 기술에 대한 통찰력을 제공하며, 전자파 흡수체 응용 분야에서의 발전 가능성을 열어준다.